UNIVERSITY OF SOUTHAMPTON

FACULTY OF ENGINEERING AND THE ENVIRONMENT

Water and Environmental Engineering Aerodynamics and Flight Mechanics

Turbulent flows interacting with groups of obstacles

by

Sonia Taddei

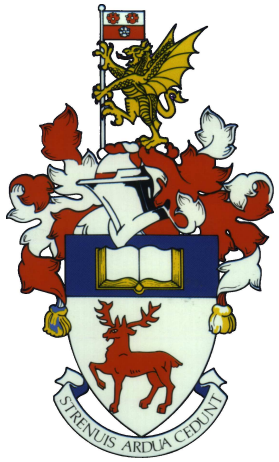

Thesis for the degree of Doctor of Philosophy

June 2016

UNIVERSITY OF SOUTHAMPTON

ABSTRACT

FACULTY OF ENGINEERING AND THE ENVIRONMENT
Water and Environmental Engineering Aerodynamics and Flight Mechanics

Doctor of Philosophy

TURBULENT FLOWS INTERACTING WITH GROUPS OF OBSTACLES

by Sonia Taddei

This thesis presents extensive experimental data that systematically examines the wakes and the drag forces of canopy patches with different densities, immersed in turbulent boundary layers. The patches are circular (with outer diameter D) and are made of several identical circular cylinders (height, H and diameter, d). The bulk aspect ratio of all the patches ($AR = H/D$) was fixed at 1 and the patch density ($\phi = N_c d^2/D^2$) is altered by varying the number of cylinders (N_c) in the patch. Drag measurements show that the patch drag coefficient increases with increasing density. The drag coefficient of the highest investigated density ($\phi \approx 0.25$) is greater than the drag coefficient of a solid patch (i.e. $\phi = 1$, which is a solid cylinder with $AR = 1$). PIV measurements were carried out along streamwise-wall-normal ($x - y$) plane along the centreline of patch and in the streamwise-spanwise ($x - z$) plane at its mid height (i.e. $y = H/2$). Mean velocity fields show that the porosity of the patch promotes bleeding along all directions. It was observed that bleeding along the vertical/horizontal direction increases/decreases with increasing ϕ. Furthermore, it was also observed that bleeding along the lateral direction dictates the point of flow separation along the sides of the patch and makes it independent of ϕ. All these aspects make wakes for porous patches markedly different from their solid counterpart and provide a basis to explain the observed trends in the drag coefficient. The wakes generating behind three-dimensional porous patches can be divided in two distinct regions: the very near wake, where the wake properties are constant along the height of the model, as a first approximation, and the near wake, where the velocity profiles for different patches collapse, regardless of patch density. Scaling laws and parameters for the velocity profiles are introduced. Subsequently, an analysis of the trend of these parameters with ϕ and y is carried out and, where possible, a predictive model is evaluated. The wakes are also found to be self similar at the mid height horizontal plane, if scaled with appropriate scaling parameters, and the trend of these parameter with patch density is analysed. The analysis of fluctuating quantities confirms the presence of two distinct regions in the patches' wakes, and suggests the presence of an alternate vortex street whose intensity and coherence increases with increasing patch density.

Contents

List of Figures

List of Tables

Declaration of Authorship

I, Sonia Taddei , declare that the thesis entitled *Turbulent flows interacting with groups of obstacles* and the work presented in the thesis are both my own, and have been generated by me as the result of my own original research. I confirm that:

- this work was done wholly or mainly while in candidature for a research degree at this University;
- where any part of this thesis has previously been submitted for a degree or any other qualification at this University or any other institution, this has been clearly stated;
- where I have consulted the published work of others, this is always clearly attributed;
- where I have quoted from the work of others, the source is always given. With the exception of such quotations, this thesis is entirely my own work;
- I have acknowledged all main sources of help;
- where the thesis is based on work done by myself jointly with others, I have made clear exactly what was done by others and what I have contributed myself;
- parts of this work have been published as: Taddei, S., Manes, C., and Ganapathisubramani, B. (2016). Characterisation of drag and wake properties of canopy patches immersed in turbulent boundary layers. *Journal of Fluid Mechanics*, 798:27–49.

Signed: .....

Date .....

Acknowledgements

First, and foremost, I would like to express my deepest gratitude to my supervisors Prof. Costantino Manes and Prof. Bharath Ganapathisubramani for their help and unconditioned support throughout all the time of this work. I consider myself extremely lucky and honoured to have been able to work with both of them. I am grateful for the time and patience they invested on me, providing inspiration, motivation and guidance in any single moment, and expecially in the darkest ones. This work would not have been possible without them.

I am also grateful to Dr. Christina Vanderwel for the enthusiasm and support from the very first moment she arrived at the University of Southampton. She helped me to understand the value and quality of my work, not to mention all the discussions, suggestions and precious advices she shared with me. I also want to express my gratitude to Dr. Roeland de Kat, for teaching me how to deal with PIV experiments, and for always being ready to answer to all my questions and doubts.

I must also acknowledge my sponsors for their support, without which I could not have completed this research. I want to thank the Engineering and Physical Sciences Research Council (EPSRC) and the European Research Council (ERC), for their financial support over the past three years.

A great thank you goes to all my research group and to all the people I met during the time I spent in Southampton. Each and every one of them contributed in many different ways to share the path that led up to this point.

Finally, I would like to thank my family for being by my side, even if they were so far away.

Nomenclature

Upper-case Greek symbols

ΔU	$U_2 - U_1$
ΔU_+	roughness function
ΔU_0	maximum velocity deficit at the mid height plane($U_{H/2} - U_0$)
$\Delta U_{0,max}$	maximum velocity deficit along the centreline at mid height plane ($U_{H/2} - U_{min}$)
ΔU_{bulk}	global velocity deficit ($U_{bulk} - U_y$)
ΔU_{max}	maximum velocity deficit
ΔU_y	local velocity deficit ($U_{y\infty} - U_y$)
Π	wake strength parameter

Lower-case Greek symbols

α	boundary layer power law exponent
δ	boundary layer thickness
δ_{sl}	characteristic width of the shear layer
ϵ_A	error on the generic quantity A
κ	von Karaman constant
ν	kinematic viscosity of the fluid
μ	viscosity of the fluid
ϕ	obstacle density (total base area of the obstacles/total base area of the array)
ρ	fluid density
σ_i	variance of the i-th fluctuating velocity component ($i = u, v, w$)
τ_w	wall shear stress
ω_i	vorticity in i-th direction ($i = x, y, z$)
$\omega_{yMAX} D/U_\infty$	maximum value of the lateral shear layer vorticity at $x/D = 0.75$
$\omega_{zMAX} D/U_\infty$	minimum value of the top shear layer vorticity at $x/D = 0.75$

Upper-case Roman symbols

AR	aspect ratio of a cylinder (H/D)
B	base length of one spire
C_D	drag coefficient
C_{Di}	average drag coefficient for the cylinders within the patch
C_{Dbulk}	drag coefficient non-dimensionalised with U_{bulk} ($F_D/(1/2\rho U_{bulk}^2 DH)$)

C_{Dmax}	maximum value of the drag coefficient
C_{D_H}	drag coefficient non-dimensionalised with $U_H\ F_D/(1/2\rho U_H^2 DH)$
C_f	bed friction coefficient
C_i	model reference name, i =7, 20, 39, 64, 95 number of obstacles
D	base dimension of an obstacle along z
	external diameter of the patch
F_D	total drag of the patch
H	height of an obstacle
	height of one spire
L	streamline distance between two rows of roughness elements
L_i	lengths related to the roughness dimensions and relative positioning
L_{i+}	inner scaling of L_i ($L_i u_\tau/\nu$)
L_1	length of the steady region
L_2	length of the recovery region
L_{min}	x location of U_{min} along the centreline
L_r	length of the recovery region along x non-dimensionalised with D
L_w	wake formation length
M	half distance of two roughness elements in spanwise direction
N_c	number of cylinders in the patch
Re	Reynolds number
St	Strouhal number
T	ambient temperature
U	mean streamwise velocity component
$\overline{U}$	$(U_1 + U_2)/2$
U_∞	free stream velocity
U_0	steady velocity value within a rectangular patch
	minimum U long the profiles at the mid-height plane
U_1	streamwise mean velocity in the steady region
U_2	streamwise mean velocity outside the wake of the array
U_δ	velocity at $y = \delta$
U_τ	friction velocity ($\sqrt{\tau_w/\rho}$)
U_{bTE}	mean streamwise bleeding velocity at the trailing edge ($x/D = 0.52$)
U_{bulk}	bulk velocity impinging on the patch ($U_{bulk} = 1/H \int_0^H U dy = 0.59 U_\infty$)
U_e	mean velocity outside of the patch
	bleeding velocity at mid-height at $x/D = 0.6$
U_H	incoming boundary layer velocity at $y = H$
$U_{H/2}$	incoming flow velocity at $y = H/2$
U_{in}	average velocity immediately upstream of the patch ($1/(H-2d) \int_d^{H-d} U(x/D = -0.55) dy$)
U_{min}	minimum velocity value along the centreline
U_{out}	average velocity immediately downstream of the patch ($1/(H-2d) \int_d^{H-d} U(x/D = 0.55) dy$)
U_p	average flow velocity within the canopy

U_{ref}	reference velocity, from the Pitot-static tube
U_y	longitudinal velocity component at a certain y location
V_{bTE}	mean vertical bleeding velocity at the trailing edge (x/D = 0.52)
$U_{y\infty}$	boundary layer velocity at different y coordinates
V	mean veritcal velocity component
W	mean lateral velocity component
Y	displaced height ($y - d$)
Y_+	inner scaling of Y ($Y u_\tau/\nu$)

Lower-case Roman symbols

a	frontal area per unit volume of the patch (nd)
	roughness element streamline length
b	base length of one splitter plate
	roughness element spanwise length
d	zero-plane displacement
f	frequency
$f\#$	aperture number
h	roughness height
	water depth
	height of a splitter plate
h_+	roughness Reynolds number (hu_τ/ν)
i	distance between two spires
k	constant in L_{min} fitting
l	length of a roughness distribution
m	constant in L_{min} fitting
n	number of cylinders per unit planar area ($N_c/(\pi D^2/4)$
p	ambient pressure
p_∞	total pressure
p_s	static pressure
q	constant in L_{min} fitting
u	fluctuating streamwise velocity component
v	fluctuating vertical velocity component
w	fluctuating lateral velocity component
x	stremwise coordinate
x_0	virtual origin of the wake
x_D	interior adjustment length
x_{rb}	streamwise coordinate of the centre of the recirculation bubble
y	vertical coordinate
y_0	roughness length
y_*	threshold limit for L_{min} change in trend
$y_{\omega_{zMAX}}$	vertical coordinate of $\omega_{zMAX} D/U_\infty$

z	lateral coordinate
$z_{1/2}$	wake half width, z location where the velocity deficit is half of its maximum value
z_{peak}	position of the peak of σ_U

Acronyms

ABL	atmospheric boundary layer
ABS	Acrylonitrile Butadiene Styrene
DFT	discrete Fourier transform
FOV	field of view
GPU	graphics processing unit
OHR	overheat ratio of a hot wire
PIV	particle image velocimetry
PSD	power spectral density
UPS	uninterrupted power supply

Chapter 1

Introduction

1.1 Overview

The interaction between flows and isolated groups of obstacles is widely encountered in Environmental Fluid Mechanics. Many examples of these interactions can be cited, including atmospheric boundary layers impinging on forests or wind farms, marine boundary layers over aquatic vegetation and offshore structures, or over turbines in tidal channels. All these different groups of obstacles can be referred as arrays. It is evident from the examples above, that such arrays can have very different shapes and characteristics and their effects on an incoming flow can be disparate, as well as the effects of the flow over the obstacles themselves.

Turbulent flows interacting with groups of obstacles have been widely investigated in the past, both for research purposes and for industrial applications, and there are many studies reporting all the results and achievements reached with these investigations. However, the literature pertaining to this topic is largely incomplete. In particular, it lacks almost completely the study of arrays of finite obstacles impinged by thick turbulent boundary layers (hereafter, for simplicity, we will refer to this class of flows as 3-D flows). On the contrary, the case of arrays of two-dimensional obstacles impinged by turbulent boundary layers with thickness equal or lower than the height of the obstacles has been largely addressed (hereafter, for simplicity, we will refer to this class of flows as 2-D flows). A typical example of 2-D flows involves open channel flows impinging canopy patches piercing the free surface.

There are a few studies that addressed the case of 2-D flows (Ball et al., 1996, Chang and Constantinescu, 2015, Chen et al., 2012, Nicolle and Eames, 2011, Rominger and Nepf, 2011, Tanino and Nepf, 2008, Zong and Nepf, 2012). However, in these studies the flow characteristics can be considered 2-D, and only the density of the cylinders in the array was varied. On the opposite side, the literature related to 3-D flows is very limited. There are some experimental studies and numerical simulations presented by Davidson et al. (1996), Princevac et al. (2010) and Gu et al. (2011). These papers highlight the main characteristics of the 3-D flow and the differences

with the 2-D cases, but none of them goes into a deep and systematic investigation. All the results are limited to one single array of obstacles without taking into account, for example, the effects of shape and density of the obstacles within the array.

The 3-D configuration is probably encountered more often in engineering applications and the natural environment than its 2-D counterpart (wind farms, marine turbines in tidal channels, and vegetated patchy beds are very commonly submerged within a turbulent boundary layer) and hence deserves to be investigated in as much detail. The height difference between the boundary layer and the obstacles promotes the formation of an additional shear layer which induces strong 3-D features to the mean flow, whose effects on drag and wake development need to be clarified and this is the primary goal of this thesis.

1.2 Motivation

Depending on the case, the reasons for studying the interaction between turbulent flows and isolated groups of obstacles can have different objectives, which can be associated with three main research questions: (i) what are the forces exerted on the array by the flow? (ii) what is the average time that the fluid spends among the obstacles? (iii) how can the wake of the array be characterized?

Question (i) is relevant in the context of renewable energies, in particular for tidal or wind farms. Garrett and Cummins (2005) and many others (see for example Myers and Bhaj, 2012, Vennell, 2010, 2011) have pointed out that the prediction of the energy that can be extracted from a tidal or wind farm is strongly related to the drag of the "total farm". The ability to predict the forces that act over arrays of obstacles is also relevant for the study of wind flows over patches of vegetation, for example to characterise wind resistance and wind-firmness during storms (Cucchi and Bert, 2003, Rudnicki et al., 2001). Finally, addressing this question is of fundamental importance to predict wind loads on groups of tall buildings, with a view to providing a more detailed and safer design.

Question (ii) is relevant in those fields that study mass-transfer processes between patches of vegetation (e.g. forests or aquatic plants) and the surrounding environment (see for example Irvine et al., 1997, Cassiani et al., 2008 and Huang et al., 2011 for forests and atmosphere, and Folkard, 2011 or Zong and Nepf, 2012 for water flows). Another application is related to pollutant dispersion in cities or industrial areas (see Britter and Hanna, 2003).

Finally, question (iii) is of particular interest to determine the effects of the obstacles on the surrounding environment. Being able to quantify the wake characteristics of an array of obstacles, will lead to model properly, for example, how tidal turbine arrays influence sediment transport and other ecologically relevant mass transfer processes (Blunden, 2009), in the vicinity of tidal farms.

This thesis addresses mainly questions (i) and (iii).

1.3 Aims and objectives

The main aim of this thesis is to carry out extensive and detailed wind tunnel experiments of thick turbulent boundary layers interacting with three-dimensional arrays of obstacles with different densities. The focus of these experiments is mainly on investigating wake development and drag forces of the arrays.

More in detail, the objectives of this research are the following:

1. quantify the drag coefficient of three-dimensional patches of obstacles, and its dependence on patch density;
2. characterisation of the main phenomena which influence the wake structure and, therefore, affect the drag forces;
3. investigation of the influence of the ratio between boundary layer thickness and patch height on the drag coefficient of the arrays;
4. identification and quantification of relevant lengthscales and velocity scales characterizing the wake and analysis of their dependence on the patch density;
5. parametrization of drag forces as a function of patch properties;
6. analysis of velocity fluctuations to infer properties of the instantaneous wake structure.

The drag forces and the wake development are deeply interlinked, and the first objective is to characterise how the drag force exerted on the patch, and therefore its wake, is affected by patch density. The focus will be on the main phenomena characterising the wake of porous patches, and how their wakes differ from solid cases. A deep analysis of the wake properties and characteristic lengthscales and velocity scales provides the possibility to predict the wake development downwind of patches of obstacles just by knowing their geometrical parameters. The analysis of the fluctuating quantities gives an insight to the dynamics of the wake, and therefore on the instantaneous structure of the wake itself. In order to accomplish these objectives, the combination of different experimental techniques is required. Direct force measurements are carried out to characterise the drag coefficient and its variation with patch density. Particle Image Velocimetry (PIV) measurements are taken at different locations to characterise the velocity fields. Hot wire measurements are carried out to estimate the dominant frequencies in the wake fluctuations and hence to help infer the wake in terms of coherency and characteristic lengthscale of coherent structures generated by the arrays at different densities. The results emerging from these measurements, contribute to addressing the gap in literature concerning the wake and drag characterisation of three-dimensional patches immersed in a turbulent boundary layer, that was never addressed before.

1.4 Thesis outline

A literature review of the main characteristics of turbulent boundary layers, and their interactions with single and groups of obstacles is presented in Chapter 2. Chapter 3 describes the experimental facilities where the experiments were taken, provides the design and characterisation of the flow conditioning used to generate a suitable turbulent boundary layer and presents the methodology and setup of all the measurements. The drag coefficient of patches with different obstacle densities, and their relation with wake properties are presented in Chapter 4, and the development of the wake along the height of the patch is given in Chapter 5. Self-similarity properties of the wake are discussed in Chapter 6, together with the identification of characteristic length and velocity scales, and their dependence on patch density. Chapter 7 describes an analysis of fluctuating quantities in order to capture the wake's instantaneous dynamics. A summary of the major findings and conclusions, together with future works that still needs to be addressed are discussed in Chapter 8. The Appendices provides additional results that were not included in the previous chapters. In particular, Appendix A contains further characterisation of the incoming boundary layer; Appendix B shows all the spectra taken along the wake of all the patches at different velocity, density, height and boundary layer thickness; Appendix C contains additional PIV plots; Appendix D describes a more detailed comparison between 2-D and 3-D cases and Appendix E provides a comparison between horizontal and vertical measurements at the centreline of the patches' wakes.

1.5 Novel contributions and publications

Parts of this work are discussed in the following publication:

Taddei, S., Manes, C., and Ganapathisubramani, B. (2016). Characterisation of drag and wake properties of canopy patches immersed in turbulent boundary layers. *Journal of Fluid Mechanics*, 798:27fi?!49.

In addition, some elements of this work have been presented at the following conferences:

Taddei, S., Manes, C., and Ganapathisubramani, B. (2014). Turbulent flows interacting with groups of obstacles. In *67th Annual Meeting of APS Division of Fluid Dynamics, San Francisco, California, November 23-25*

Taddei, S., Manes, C., and Ganapathisubramani, B. (2015). Turbulent flows interacting with groups of obstacles. In *ERCOFTAC SIG44-42 Workshop, "Multiscale-forced Turbulent Flows: fundamentals and applications", Sheffield, UK, September 7-8*

Chapters 5, 6 and 7 will form the basis for another journal publication, which is in progress at the moment of this writing.

Chapter 2

Literature review

In this Chapter, a brief review of the main topic of this research is given. Since an important part of the experimental campaign involves creating thick turbulent boundary layers by means of roughness elements and vortex generators, a brief review of rough-wall boundary layer theory is given in the first section. Section 2.2 addresses the interactions between turbulent flows and singles and patches of obstacles, respectively, and represents the main core of this Chapter.

2.1 Rough-wall boundary layer theory

Turbulent boundary layers developing over a smooth surface have been widely investigated both theoretically and experimentally. These studies can be applied, for example, in field such as naval or aeronautical engineering, for what concerns the flow over the hull of ships or the wings of an airplane. The literature regarding boundary layers developing over rough walls has been developed more recently, despite the applications of this kind of flow being larger and very often encountered in nature. The presence of roughness elements, as obvious, leads to a more complicated development of the flow, and this is why this field is less understood with respect to the smooth case.

In general turbulent boundary layers (whether over smooth or rough walls) can be divided in two overlapping main regions: an outer layer and an inner layer. The characteristic length and velocity scales of the outer layer are δ and U_τ, respectively, where δ is the boundary layer thickness and U_τ the friction velocity ($U_\tau^2 = \tau_w/\rho$, with τ_w being the wall shear stress and ρ the density of the fluid). For the inner layer the scaling parameters are U_τ and a set of length scales related to the wall-surface. These are the viscous length scale (i.e. ν/U_τ, where ν is the kinematic viscosity of the fluid), the roughness height (i.e. h), and other length scales associated with roughness size and relative positioning (L_i). For the case of an aerodynamically smooth surface the only relevant length scale is ν/U_τ only.

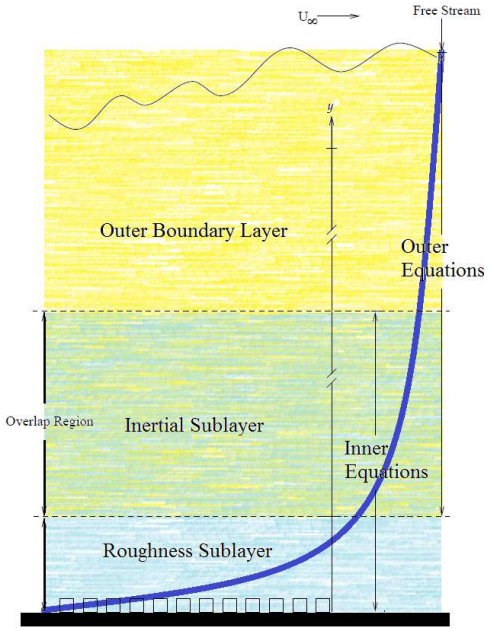

Figure 2.1: Schematic representation of the splitting of rough wall boundary layer in different flow regions.

Within the inner layer, the very near wall region is often referred to as the viscous or roughness sub-layer for the case of smooth or rough walls, respectively. Away enough from the wall and from the boundary layer top, the inner and the outer layer overlap in a region called the inertial (or logarithmic) layer, where the only relevant length scale is the distance from the wall surface. All these regions are represented in Figure 2.1 and will be briefly described in the following sections.

In this thesis (x, y, z) refer to as the longitudinal, vertical and lateral coordinates, (U, V, W) and (u, v, w) denote the mean and fluctuating components of the velocity, respectively along x, y and z. A schematic representation of the setup and the coordinate system is given in Figure 2.2.

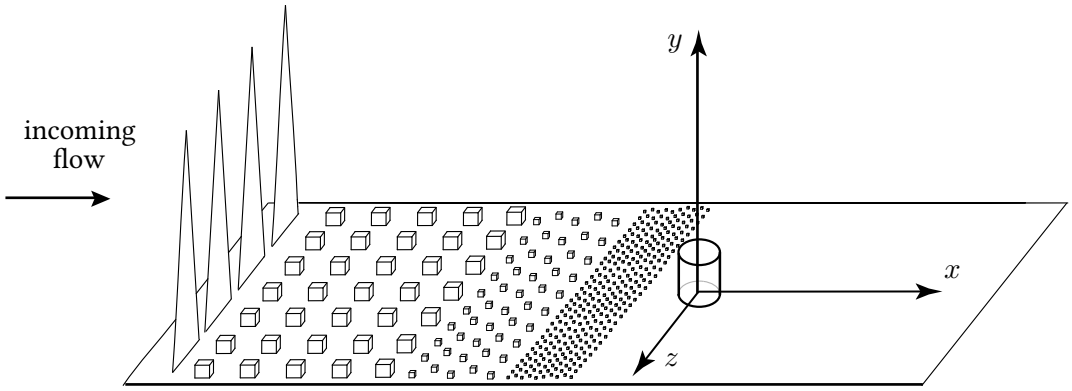

Figure 2.2: Schematic representation of the coordinate system.

2.1.1 The roughness sub-layer

The roughness sub-layer is the flow region embedded within the wall up to the inertial sub-layer. A first estimation of its extent is given by Raupach et al. (1991) who suggest that this layer is enclosed within the region $0 < y < 2h - 5h$, where h is the characteristic height of the roughness elements. Some studies report that the upper limit is closer to $2h$ than $5h$. For cubic roughness elements, Cheng and Castro (2002) found a value of $1.8 - 1.85h$ and they showed that such values are almost independent of roughness type and flow direction.

This flow region presents no universal features since it is strongly heterogeneous and influenced by local roughness properties. Some authors (e.g Florens et al., 2013, Raupach et al., 1991, among others) attempted to provide a characterization of mean velocity profiles that can be encountered, but this topic goes beyond the purpose of this thesis and therefore it is not discussed further.

2.1.2 The inertial sub-layer

The inertial sub-layer extends approximatively from the end of the roughness sub-layer up to $y < 0.2\delta - 0.3\delta$ (Pope, 2011). In this region, as will be evident below, the flow depends only on one length scale, since it is placed at the overlap between the inner and the outer layer.

It is not trivial to define the origin of the vertical coordinate for a rough wall since the roughness itself moves the flow upwards. Hence, it is necessary to define a displaced height $Y = y - d$, where d can be somewhat regarded as the "fluid dynamic" height origin. It has been speculated that this elevation can be regarded as the mean height of momentum extraction by the surface and it is a property of the roughness geometry ($0 < d < h$ and $d = 0$ for smooth walls, Jackson, 1981).

The mean velocity profile $U(Y)$ can be derived by a classical asymptotic matching process (Raupach et al., 1991). As has already been observed, in the outer layer the mean velocity $U(Y)$ depends only on δ and U_τ (and, obviously, Y) and this leads to the *velocity-defect law*

$$\frac{U(Y) - U_\infty}{U_\tau} = G(\eta) = G\left(\frac{Y}{\delta}\right), \tag{2.1}$$

where $\eta = Y/\delta$ and U_∞ is the free stream velocity. Furthermore, δ is here considered as the distance from the wall where the mean velocity reaches 99% of its free stream value.

Analogously, within the inner layer, $U(Y)$ depends on Y, U_τ, the length scales of the surface, L_i (there can be more than one, depending on the surface) and h, and this leads to the *law of the wall*

$$\frac{U(Y)}{U_\tau} = F\left(Y_+, h_+, L_{i+}\right), \tag{2.2}$$

where the + subscript indicates a normalization with the viscous length scale ν/U_τ. In particular, h_+ is an indicator of the "roughness" of the flow, and it is called the roughness Reynolds number: a flow can be considered "smooth" if $0 < h_+ < 5$, while it can be considered "fully rough" if $h_+ > 70$.

In the overlap region equations 2.1 and 2.2 must be valid simultaneously, which means that the only independent variable can be Y and that

$$\frac{U(Y)}{U_\tau} = G\left(\frac{Y}{\delta}\right) + \frac{U_\infty}{U_\tau} = F\left(\frac{YU_\tau}{\nu}\right). \tag{2.3}$$

Also the derivative with respect to Y must be valid in the same layer. Differentiating equation 2.3 with respect to Y leads to

$$\frac{1}{U_\tau}\frac{dU}{dY} = \frac{1}{\delta}\frac{dG}{d\eta} = \frac{U_\tau}{\nu}\frac{dF}{dY_+}. \tag{2.4}$$

Finally, multiplying all terms in equation 2.4 by Y we obtain

$$\frac{Y}{U_\tau}\frac{dU}{dY} = \eta\frac{dG}{d\eta} = Y_+\frac{dF}{dY_+} = \frac{1}{\kappa}, \tag{2.5}$$

where κ is the von Karman constant, here taken as to 0.41. Each term of equation 2.5 must be equal to a constant because they cannot depend on any other variable (see for example Monin and Yaglom, 1971, for further reference). Integrating equation 2.5 yields the well known *logarithmic law*

$$\frac{U}{U_\tau} = \frac{1}{\kappa}\ln Y_+ + C, \tag{2.6}$$

where $C = A$ is a constant for a smooth-wall boundary layer, and $C = A - \Delta U_+(h_+, L_{i+})$ for a rough wall boundary layer, where ΔU_+ is called the *roughness function* and quantifies the effects of the roughness on the boundary layer (ΔU_+ increases as the roughness Reynolds number (h_+) increases).

A more common way to express the log-law is

$$\frac{U}{U_\tau} = \frac{1}{\kappa}\ln\left(\frac{Y}{y_0}\right) = \frac{1}{\kappa}\ln\left(\frac{y-d}{y_0}\right), \tag{2.7}$$

where y_0 is called *roughness length* and it incorporates all the roughness effects that were represented previously by ΔU_+ and they are related by

$$\ln\frac{y_0}{h} = -\kappa\left(A - \Delta U_+(h_+, L_{i+})\right) - \ln h_+. \tag{2.8}$$

A necessary condition for the logarithmic layer to exist is that $\delta \gg (\nu/U_\tau, h, L_i)$. This guarantees that the overlapping region between the outer layer and the inner layer is large enough to meet the assumptions that were initially made.

2.1.3 The outer layer

The outer layer includes the log-law region, and spreads along all the upper part of the boundary layer. The governing equation for this region consists of the log-law, with an additional term called the *law of the wake* (Pope, 2011).

$$\frac{U}{U_\tau} = \frac{1}{\kappa}\ln\left(\frac{Y}{y_0}\right) + \frac{\Pi}{\kappa}w\left(\frac{Y}{\delta}\right). \tag{2.9}$$

The Coles wake function $w(y/\delta)$ is assumed to be universal (although the literature presents contradictory results and the question remains open), at least for zero-pressure-gradient flows, and it satisfies the conditions $w(0) = 0$, $w(1) = 2$ and also $\int_0^\infty w\, d(Y/\delta) = 1$ (Coles, 1956). Π is called the wake strength parameter and it is flow dependent. Nevertheless, Castro (2007) demonstrated that a constant value of 0.7 fits well data from different types of roughness, and the correlations that have been calculated there, are not very sensitive to changes in Π.

Another way to write equation 2.9 is using the velocity-defect form:

$$\frac{U_\infty - U}{U_\tau} = -\frac{1}{\kappa}\ln\left(\frac{Y}{\delta}\right) + \frac{\Pi}{\kappa}\left(2 - w\left(\frac{Y}{\delta}\right)\right). \tag{2.10}$$

It is noteworthy that plotting data in the velocity-defect form shows a collapse of mean profiles within the outer layer regardless of the nature of the wall surface, i.e. being smooth or rough (Connelly et al., 2006). This is one of the main implications of the so-called *outer layer* or *wall similarity hypothesis*, initially made by Townsend (Townsend, 1961) and then verified by many authors (see e.g. Flack et al., 2007, Raupach et al., 1991). This hypothesis is stated in Raupach et al. (1991) as following:

> *Outside the roughness sub-layer, the turbulent motions in a boundary layer at high Reynolds number are independent of the wall roughness and the viscosity, except for the role of the wall in setting the velocity scale U_τ, the height $Y = y - d$ and the boundary layer thickness δ.*

Provided that the Reynolds number is sufficiently large, this implies not only the collapse of the velocity-defect law, but also that each of the profiles of $\overline{u^2}$, $\overline{v^2}$, $\overline{w^2}$ and $\overline{uv}$ (or any other velocity statistics) collapse to one curve if U_τ and δ are used as scaling parameters. In the literature there are many experimental studies that support this hypothesis, see, for example, Flack et al. (2005) or Castro (2007).

2.2 The interaction between obstacles and turbulent boundary layers

This section is divided into two parts. The first part addresses the flow characteristics resulting from the interaction between a turbulent boundary layer and a single obstacle. The second part covers the literature pertaining to groups of obstacles and porous obstructions.

2.2.1 Single obstacle

There are several studies in literature that address the problem of understanding the physics of the vortex structures in the wake of a finite obstacle, and a complete summary of these studies can be found in Sumner (2013). In general, the flow behind a single, finite obstacle in cross flow is deeply influenced by the characteristics of the incoming flow and by the geometry of the obstacle itself.

One of the main parameters that affects the flow behind a finite obstacle is the aspect ratio (i.e. AR, defined as the ratio between the height of the obstacle H and its base dimension D along the z direction). In particular, many studies have reported the existence of a critical aspect ratio, below which the flow behind the obstacle changes its structure from the well known von Karman antisymmetric vortex street, for AR above the critical value, to a "arch-type" wake with symmetrical vortices, for AR lower than the critical value (see for example Adramola et al., 2006, Okamoto and Yagita, 1973, Sakamoto and Arie, 1983, Sumner et al., 2004, Wang et al., 2006). The value of the critical aspect ratio ranges from 1 to 7, depending on the study, and it is probably sensitive to the experimental setup and conditions. The influence of the aspect ratio is schematically represented in Figure 2.3.

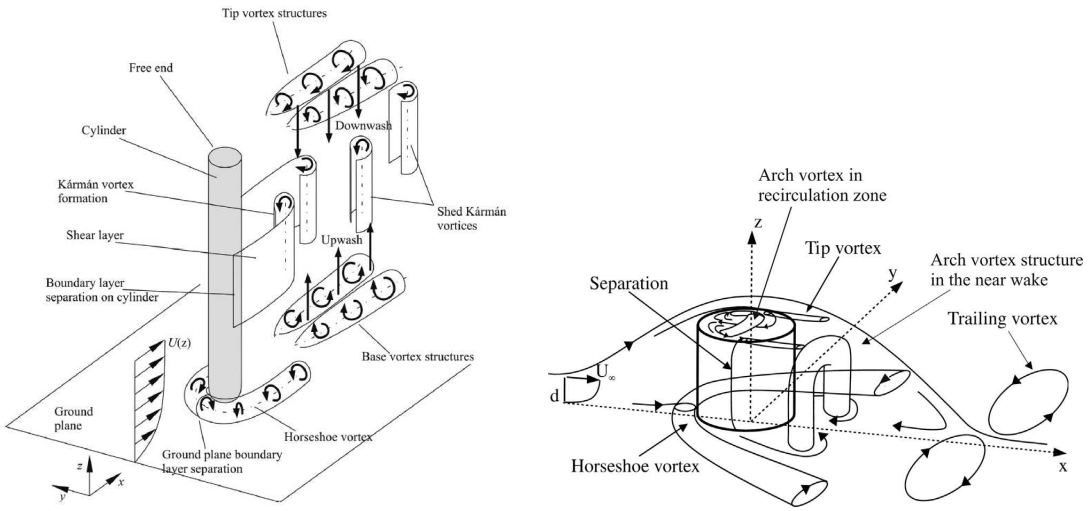

(a) High aspect ratios (Einian et al., 2010). (b) Low aspect ratios (Pattenden et al., 2005).

Figure 2.3: Schematic representation of the flow behind a finite obstacle for different aspect ratios.

In both configurations, a horseshoe vortex forming at the base of the obstacle and a tip vortex forming at the top are present. For cylinders with high aspect ratio the effects of the tip vortices are confined to the top region and a von Karman vortex street forms along the middle span of the body. The pair of counter rotating tip vortices dominates the wake of the obstacle for low aspect ratios and the downwash due to these vortices inhibits the vortex shedding from the side of the body. Furthermore, for high ARs, a base vortex system consisting of a counter rotating pair of vortices is observed in the lower part of the wake and these vortices induce an upwash velocity in this region. These structures were firstly observed by Tanaka and Murata (1999): they are not present in the cases with low AR. Similar results were observed also by Sumner et al. (2004), Wang et al. (2004), Adramola et al. (2006) and Wang and Zhou (2009).

Tanaka and Murata (1999) also plotted what they called the "vortex lines" (which were calculated for the vorticity vectors using the same method used to calculate streamlines for the velocity vectors). These lines basically represent the time-averaged configuration of the composition of the overall vorticity structures present in the wake as shown in Figure 2.4. The vortex lines are composed of two main parts: the "legs", which elongate along the vertical direction and the "heads", that join the two legs in the upper part of the wake. The evolution of these lines downstream changes with the aspect ratio of the cylinder: for low AR the heads bend downwards and the legs stretch in the spanwise direction, resulting in a three-dimensional configuration, while for higher AR the configuration is more steady and nearly two-dimensional and there is just a small bending of the legs along the vertical axis. In any case the structure observed in this study is always of the "arch-type", regardless of the aspect ratios.

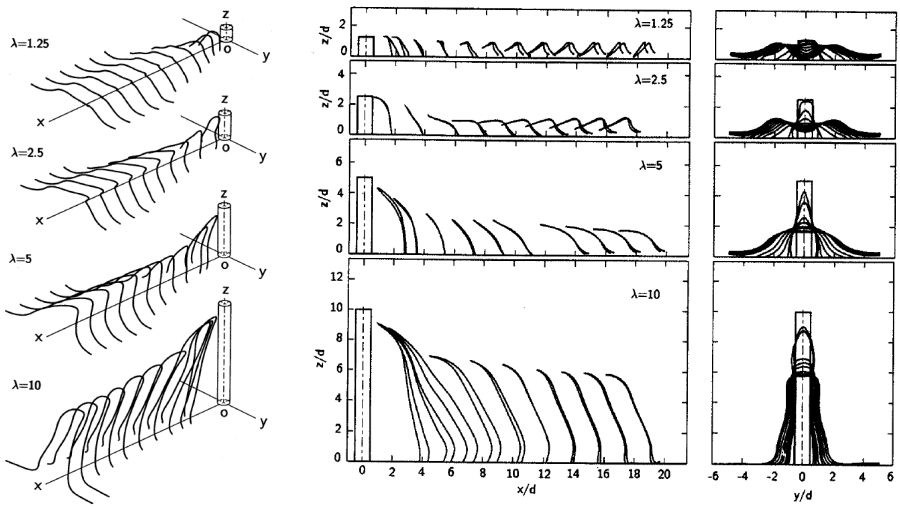

Figure 2.4: Vortex lines behind finite cylinders of different AR and their projections (Tanaka and Murata, 1999).

Wang and Zhou (2009) observed that a symmetric configuration of vortices shed from the side of the obstacle is also present for high AR, but less frequent than in the case of low AR. Based

on this observations and on the study reported in Tanaka and Murata (1999), they propose a new model for the flow behind a finite obstacle that is schematically represented in Figure 2.5.

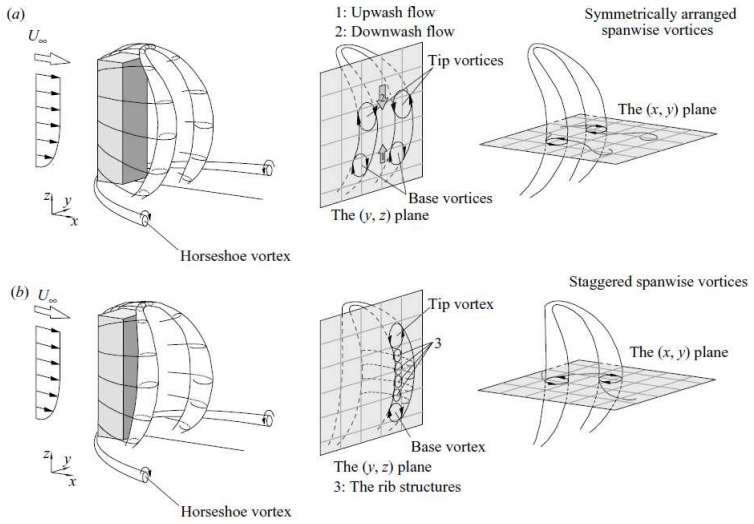

Figure 2.5: Schematic representation of the flow behind a finite obstacle (Wang and Zhou, 2009).

They suggest that spanwise vorticity is shed from both sides of the obstacle (i.e. the "legs"), and connected near the free end (i.e. the "heads"). Due to the downwash at the top and the upwash at the bottom, this "arch-type" vortex structure is inclined upstream, both at the upper and lower parts. This structure switches instantaneously between two different configurations: a symmetric one (Figure 2.5 (a)) and an antisymmetric one (Figure 2.5 (b)), which results in different vorticity distributions in horizontal and vertical planes. In particular, according to this model, the base vortex system and the tip vortex system, are just part of this whole structure, and they appear because of the inclination of the structure itself (see also Figure 2.4). For lower AR the base vortex system disappears due to the strong complexity and three dimensionality of the vortex lines. Finally, Wang et al. (2006) and Wang and Zhou (2009), also showed that the probability of a symmetrical configuration is higher for low AR, while a probability of an antisymmetric configuration is higher for high AR.

In addition to the aspect ratio, there are other parameters that affect the flow around and behind a wall mounted obstacle, namely the nature of the incoming flow (i.e. laminar or turbulent), the shape of the body and its orientation with respect to the incoming flow and the ratio between the obstacle height and the boundary layer thickness (i.e. H/δ). For the sake of a better understanding of the influence of these parameter on the wake, in the following literature review, the tip vortex and the base vortex systems could be referred to as separated systems, even if they could be part of the same vortical structure, as to indicate respectively the upper and lower part of the main "arch-type" vortex.

One of the first attempts to highlight the effects of a finite obstacle on a turbulent incoming flow is from Castro and Robins (1977). They studied the flow around a surface-mounted cube,

both in uniform upstream flow and in a turbulent boundary layer. The main difference between these two cases was found to be that upstream turbulence promotes flow reattachment, both on the top and lateral body surfaces, even for cubes that were taller than the boundary layer, although in that case this reattachment was found to be intermittent. According to this study, the reattachment is strongly related to the turbulence intensity of the upstream flow. In particular they demonstrate that upstream turbulence reduces the size of reversed flow region behind the cylinder and they suggest that the maximum velocity deficit downstream of the cylinder is inversely related to the upstream turbulence intensities.

Another attempt to evaluate the effects of the boundary layer thickness can be found in Sakamoto and Arie (1983), who found an empirical correlation between the Strouhal number measured outside of the wake and H/δ, with different constants depending on the aspect ratio being lower or higher than the critical value. Wang et al. (2006) studied the influence of different boundary layer thicknesses on the wake of a circular cylinder with a fixed aspect ratio. They investigated the influence of δ on the mean and fluctuating velocities in the wake, and they also found out that changes in δ can lead to different symmetric and antisymmetric configuration of the spanwise vortices.

Castro and Robins (1977) also figured out the effects that the orientation of the cube with respect to the incoming flow has on the wake flow. They compared the case with the flow normal to one surface of the cube with the case of the cube facing the flow with one edge. For the second case, it came out that the flow near the body is strongly influenced by the "tip vortices" with the turbulent incoming flow affecting only their decay, and not their formation. It was also reported that these vortices were not present in the case where the cube was facing the flow. Finally, in this case the pressure distributions are similar for both the incoming flows, showing apparently no influence of the upstream turbulence.

The pressure distributions around the cube from Castro and Robins (1977) were found to be less intense in the case of turbulent incoming flow, especially on the downstream surface, due to the reattachment of the flow on the top and side surfaces. The overall distribution shows that the drag of a body immersed in a turbulent flow is reduced, compared to the case of laminar incoming flow. Sumner et al. (2004) measured the mean drag coefficient for each aspect ratio, and they found that the values are almost constant for high aspect ratios, but it reduces in the case of low aspect ratio.

As mentioned previously, in addition to the aspect ratio, the ratio between the cylinder height and the boundary layer thickness also matters for evaluating the flow field and the forces acting on the body. Taniguchi et al. (1981) carried out an extensive experimental investigation with the aim to correlate the drag of a circular cylinder both with the body characteristics as well as the features of the incoming flow. They found that the drag coefficient was almost independent of U_τ/U, and dependent almost only on H/δ and D/δ, where δ is the boundary layer thickness. They found that C_D (i.e. the drag coefficient) was dependent on D only for $H/\delta < 1.1$. They

finally propose an empirical relation to evaluate C_D:

$$C_D = a(H/\delta)^b, \tag{2.11}$$

where a and b are defined as following

$$\begin{cases} a = -0.036(d/\delta) + 0.607 \\ b = 0.559(d/\delta) + 0.254 \end{cases} \text{for } H/\delta < 1.1 \qquad \begin{cases} a = 0.617 \\ b = 0.157 \end{cases} \text{for } H/\delta > 1.1.$$

A good agreement between this law and experimental data is also reported in Iungo et al. (2012).

Finally, Lim et al. (2007) investigated the influence of the Reynolds number on the characteristics of the flow behind a wall mounted cube. The main outcome of this research is that two different classes of bluff bodies can be distinguished. For the first class the mean pressure and velocity fields can be considered independent of Reynolds number (at least for the ranges studied therein) while the fluctuating statistics seem to be dependent on Re. For the second class of bluff bodies, both the mean values and the fluctuating statistics are found to be dependent on Re and this dependence is stronger near the cores of vortex structures.

As can be seen from this brief review, there are many parameters that affect the flow around a wall mounted obstacle and they are not always independent (e.g. the aspect ratio and the ratio between δ and the obstacle height are usually linked). The influence of each of these parameters is far from being well understood, and many other experiments or numerical simulations are required to shed light on the mean and fluctuating flow properties generated by a turbulent boundary layer interacting with a wall-mounted body.

2.2.2 Effects of a turbulent boundary layer on arrays of obstacles

Studies regarding the interactions between a turbulent boundary layer and 3-D isolated groups of obstacles have been carried out just in the last few years. One of the first examples is Davidson et al. (1996). This study presents wind tunnel experiments of turbulent boundary layers interacting with two square arrays of cubic obstacles (staggered configuration, and aligned configuration). The mean flow around the array is divided in five main regions, as show in Figure 2.6.

In region I the flow is undisturbed by the presence of the obstacles. In Region II the streamlines are diverging, since part of the flow goes over the array, and part of it goes into the obstacles, reducing the velocity. In region III mean and fluctuating properties appear to be function of the obstacles' size and spacing. The region above the obstacles (Region IV) is characterized by a strong shear and the development of an internal turbulent boundary layer. Finally, the streamlines converge in Region V, where the fluid is accelerating beyond the array.

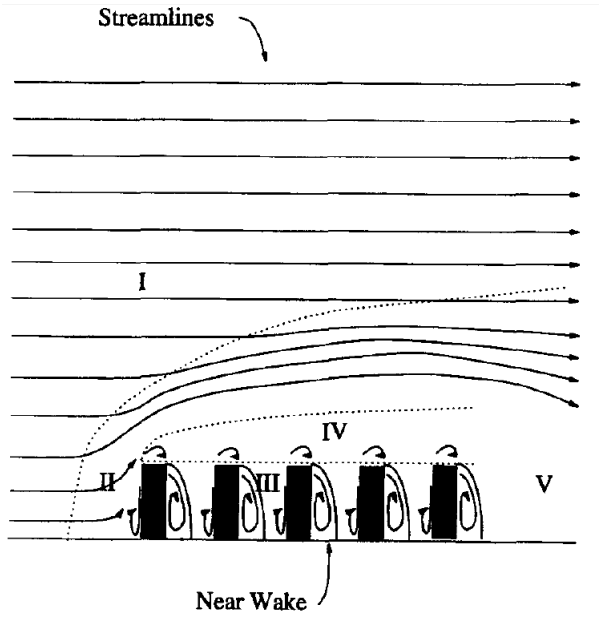

Figure 2.6: Schematic mean flow around an array of obstacles, lateral view (Davidson et al., 1996)

Observing the dispersion of a control plume and with respect to this classification of the flow, they concluded that there are two different mechanisms that affect the behaviour of the flow: the divergence and convergence of streamlines and changes in the nature of turbulence. The trend of the streamlines affects the extent of a control plume, while the turbulence controls the dilution of the plume. These mechanisms are not independent, since the trend of the streamlines influences the structure of the turbulence. In particular, diverging streamlines in Region I increase the height of the plume by approximately 50%, while converging streamlines in Region V are not significant, since the convergence develops over a greater distance. Finally, the measurements within the array indicate that in Region III there is an increasing strength of turbulent velocity fluctuations, which has a little effect on the concentration and spread of the plume.

Another outcome from Davidson et al. (1996) concerns the configuration of the obstacles. If the obstacles are aligned, i.e. there are rows of channels between the cubes, the lateral growth of the control plume is inhibited and the size of the gaps is also inversely correlated with the vertical expansion of the plume, which is also sensitive to the height of the obstacles.

Gu et al. (2011) carried out a Large-Eddy simulation of the same flow configurations as the one analysed by Davidson et al. (1996), with a good agreement between the computational and the experimental results which therefore provides confidence on the reliability of the outcomes from these studies.

Ball et al. (1996) present an experimental study of three different square arrays of staggered circular cylinders immersed in an uniform flow. The height of the cylinders extended for the entire wind tunnel height, and all the configurations had the same overall dimensions but

different densities. In particular, the densities studied in this paper are around 0.02, 0.07 and 0.27, meaning the ratio between the total obstacles base area and the total area of the array. The mean flow for all the arrays was similar, and is summarized in Figure 2.7. As noticed before, the flow diverges approaching the array, and the velocity decreases through the obstacles. Downstream of the array there is a steady region of low velocity and eventually, an unsteady wake resembling a von Karman vortex street.

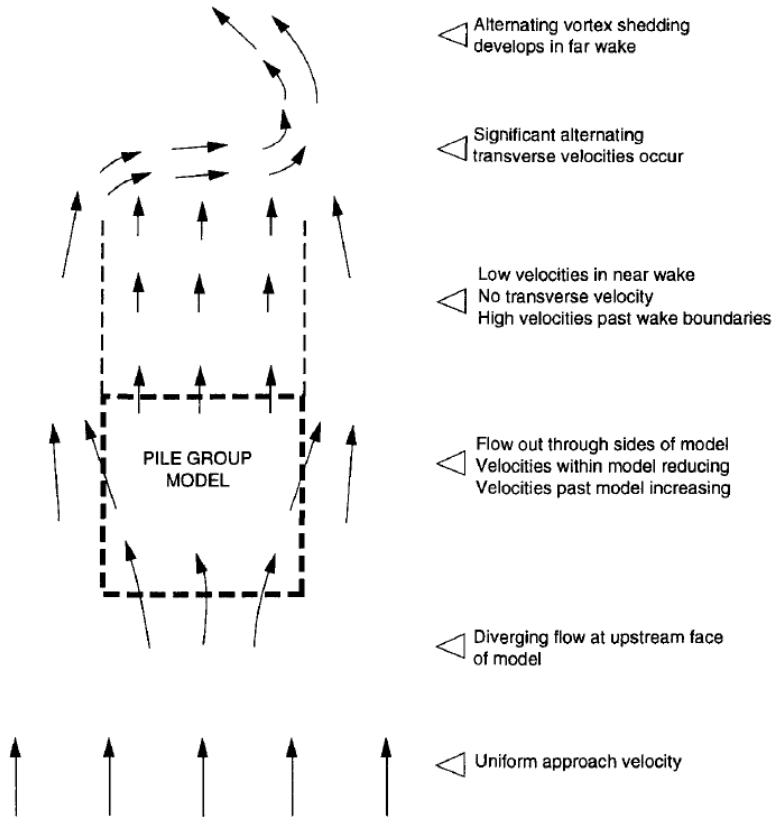

Figure 2.7: Features of the mean flow around a square array of obstacles, top view (Ball et al., 1996).

As the density of the obstacles within the array is increased, the divergence of the flow increases as well. The velocity of the flow outside the wake grows and the velocity inside the wake is reduced. In this way the velocity gradient at the wake boundary is enhanced and results in a reduction of the dimension of the steady region behind the obstacle, i.e. the unsteady wake develops closer to the end of the array.

The flow within the obstacles decreases as the porosity (i.e. opposite of density) decreases and an increase in the mixing of the flow in this region is observed, due to the small scale structures that also depend on the spacing between the obstacles.

The Strouhal numbers of the von Karman vortex street are not affected by changing the spacing between the obstacles, but the shedding appears to be irregular for the lowest density, which suggests that for lower values it could not be present.

Princevac et al. (2010) focused on the flow inside an array of cubical obstacles. In this study, an experimental investigation of two different arrays (3x3 and 5x5 aligned cubes) was carried out, in order to characterize the flow around and through the obstacles. Initially, three different flow regimes are defined, depending on the ratio between the height of the obstacles (H) and the spacing between them (s): if $H/s > 4$, the obstacles behave like isolated elements, if $H/s < 2$ a skimming flow regime is achieved, and for intermediate values interference effects are observed between the obstacles wakes. The experiment was carried out for $H/s = 1$. A qualitatively representation of the results is given in Figure 2.8.

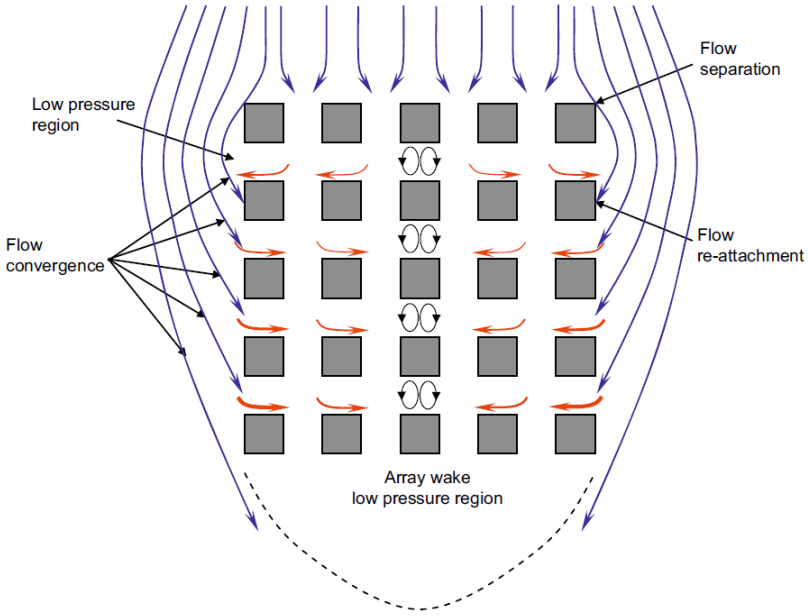

Figure 2.8: Characterization of the mean flow around and inside an array of obstacles (blue arrows represent streamlines, red arrows represent the direction of the lateral channelling) (Princevac et al., 2010).

The main outcome of this study is the observation of a mean flow going into and out of the array. In particular, the flow behind the first row of building was found to be outgoing from the array, while the rest of the gaps are characterized by an incoming flow. The first effect is due to the fact that in proximity to the first row the flow is still affected by the divergence of the incoming flow. Furthermore, the outer flow separates at the leading edge of side buildings, and reattachment occur downstream of the first row, so that a region of low pressure is formed in correspondence of the first gap on both sides of the array, and this enhances the outflow. Around the centre of the array, the streamlines converge back towards the obstacles and this promotes the inflow through the lateral channels. Moreover, the region after the array is characterized by a low pressure due to the wakes of the obstacles, and this helps to draw the fluid inside the array. This last pressure gradient decreases going downstream along the array.

The result obtained by Ball et al. (1996) are studied more accurately by Nicolle and Eames (2011) that extend the range of density going from 0.0159 to 0.3016 (again the ratio between the total obstacles base area and the total base area of the array). Simulations were carried out

for laminar flow and circular arrays at Re_D = 2100, Re_d = 100 for Nicolle and Eames (2011), whereas $Re_D \approx 82000$, $900 < Re_d < 3500$ for Ball et al. (1996), where D is the array dimension along z and d the cylinders diameter. A numerical simulation of 2-D flow over six circular arrays with cylindrical obstacles was been carried out and the main results are represented in Figure 2.9.

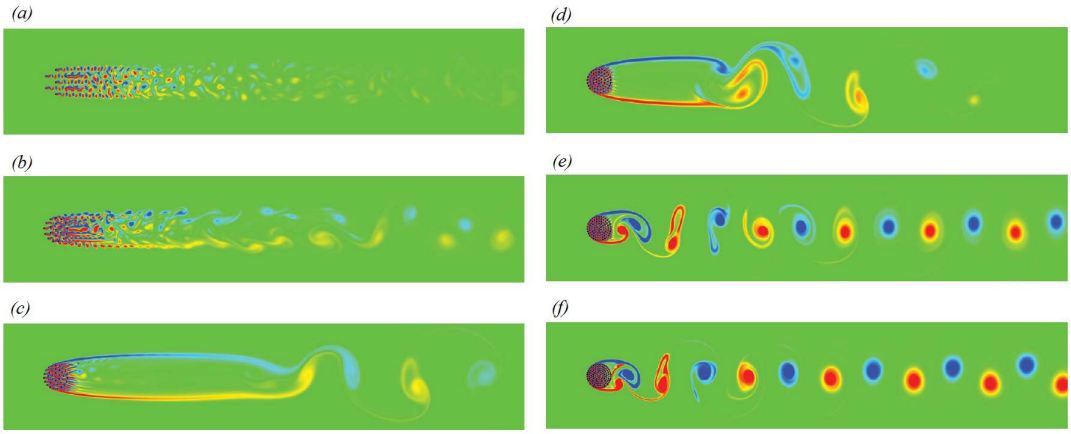

Figure 2.9: Vorticity field for different cylinders densities: (a) 0.0159, (b) 0.0454, (c) 0.0884, (d) 0.1451, (e) 0.2154, (f) 0.3016. Red and blue denote positive and negative vorticity, respectively and green is irrotational flow (Nicolle and Eames, 2011).

From these simulations, three different regimes are identified, depending on the array density (ϕ):

1. $\phi < 0.05$: for such low densities, the forces on each cylinder are comparable to the forces acting on an isolated body. each obstacle releases an identifiable wake, and the interactions between them are negligible within the array. These wakes rapidly annihilate downstream of the array (Figure 2.9, (a), (b)). The drag of the bulk configuration in this range increases as the density of the obstacles increases.

2. $0.05 < \phi < 0.15$: this is the range also studied in Ball et al. (1996). For these values of density the flow is characterized by a steady irrotational region behind the array, delimited by two shear layers that thicken downstream. As soon as the two shear layers become unstable, a von Karman vortex street develops. This region reduces its dimension and the intensity of the vortices increases with the density (Figure 2.9, (c), (d)). The drag of the entire array is higher with respect to the previous regime, but in this range of density seems to be almost constant.

3. $\phi > 0.15$: for higher values of density, the array behaves like a solid body, with a clear vortex shedding behind it (Figure 2.9, (e), (f)). The drag of the array in this range is higher than the previous range and is almost constant, around the same value of a solid body.

These results have been also confirmed by the experimental study from Zong and Nepf (2012). They carried out an investigation of the wake development of three circular arrays with 2-D

cylinders for different densities and different total dimension of the array. They focused on the length scale of the steady region behind the array (i.e. L_1), forming for intermediate values of density. The velocity at the centreline in this region (i.e. U_1) is not affected by the size of the array but only by the porosity, and it is found to be constant along the steady region. A model describing the flow and the length and velocities mentioned above is presented in Figure 2.10.

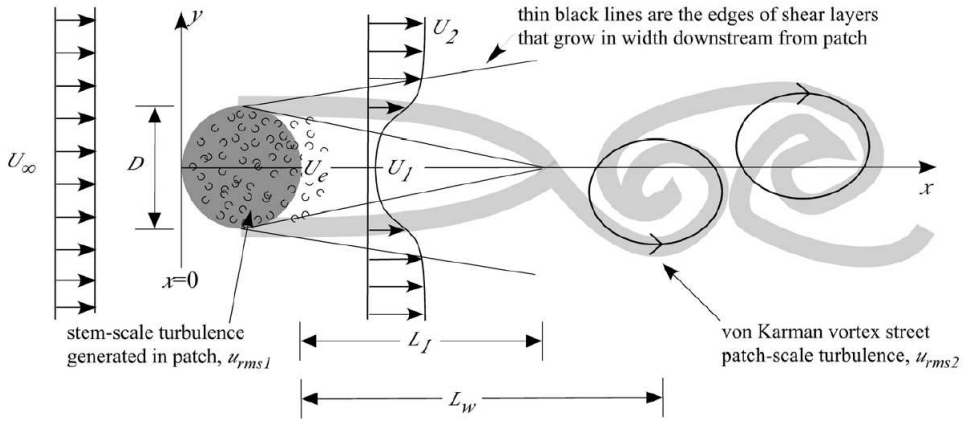

Figure 2.10: Schematic representation of the flow around a circular array of cylinders. The light gray lines represent the dye injections obtained with the flow visualizations in Zong and Nepf (2012) (Chen et al., 2012).

The following observations cam be made from Figure 2.10. First, the velocity of the flow exiting the patch (U_e) is somewhat higher than U_1, because the flow is still adjusting. The intensity of U_e is what determines the presence of small scale turbulence, defining the cylinder Reynolds number as $Re_d = U_e d/\nu$: this velocity decreases with increasing density, and, for higher densities, no small scale turbulence is formed immediately downstream of the patch (see Figure 2.9).

Looking at the mean velocity profiles along the centreline (Figure 2.11), another length scale, L_2, can be defined as what they call the "wake recovery region length" (Zong and Nepf, 2012). Looking at the profiles of the mean U ($\overline{u}$, open circles in the Figure), it is easy to distinguish the steady wake region, as the region were the streamwise velocity is constant and equal to U_1, and a region were this velocity starts to recover along the length L_2. It is also evident how these two lengths increase with a decrease in density (ϕ).

It can also be observed that U_1 decreases as ϕ increases, while the difference between the velocity of the flow out of the steady region and the velocity inside the steady region (i.e. $U_2 - U_1$) increases. This is expected for the increasing blockage of the patch for higher densities, that implies a reduced "bleeding" through the patch. If the velocity gradient in the steady region is not strong enough (i.e. $U_2 - U_1$ not sufficiently high), then the vortex street will not generate. Zong and Nepf (2012) suggested that if $U_1/U_2 < 0.35$ a vortex street can be observed. This is why for lower densities there is no vortex street (see Nicolle and Eames, 2011).

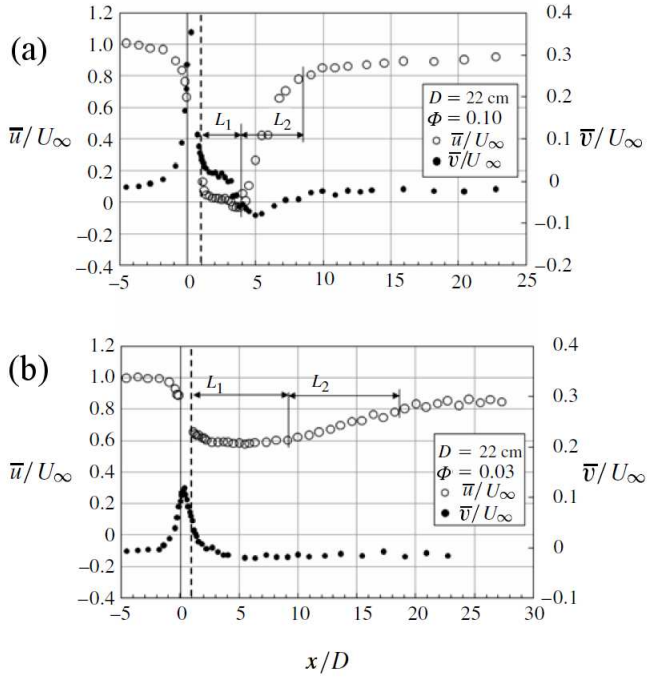

Figure 2.11: Mean velocity (U, V) profiles along the centreline of the patch, for two different densities. (Zong and Nepf, 2012).

Zong and Nepf (2012) deduced that the shear layers at the two sides of the wake keep growing in dimension, until they meet after the distance L_1, at which they start to interact, and their interaction generates the instabilities and the vortex street. Based on the growth rate of the individual shear layer and the patch diameter D, a model to predict the L_1 is also presented as

$$L_1 \approx \frac{D/2}{S}\frac{\overline{U}}{\Delta U}, \tag{2.12}$$

where S is a constant assumed to be equal to 0.1, $\overline{U} = (U_1 + U_2)/2$ and $\Delta U = U_2 - U_1$. This estimation seems to agree well with the experimental values.

The velocity deficit in the steady region is related to the drag of the whole patch, which depends on both D and ϕ. However, Zong and Nepf (2012) show that U_1/U_∞ depends only on ϕ and not on aD, where $a = nd$ is the frontal area per unit volume of the patch ($n = N_c/(\pi D^2/4)$ number of cylinders per bed area, N_c number of cylinders within the patch, $a = \frac{\phi}{d}\frac{4}{\pi}$). This does not account for shielding, especially for low densities arrays. To explain this lack of dependence on aD, they refer to Rominger and Nepf (2011), who studied the evolution of the velocity through a rectangular patch with length much larger than width. They observed that the streamwise velocity starts to decelerate at some point upstream of the patch, and keeps decelerating into the patch over a length x_D (called "interior adjustment length") where it stabilizes along a steady value U_0. Applying a dimensional analysis, they found that the upstream adjustment length scales on the half width of the patch (i.e. $D/2$), while U_0 and x_D depend on the non dimensional parameter $C_{Di}aD$, referred as the patch flow-blockage (where C_{Di} is the average

drag coefficient of the cylinders within the patch). In particular, they estimated the dependence of x_D on $C_{Di}aD$ as:

$$\frac{x_D}{D} \sim \frac{2}{C_{Di}aD}\left[1+\left(\frac{C_{Di}aD}{4}\right)^2\right]^{1/2}. \tag{2.13}$$

For a flow-blockage greater than 4 (which corresponds to $\phi > \frac{\pi}{C_{Di}}\frac{d}{D}$), x_D scales with D only. For lower flow-blockages, x_D scales with $(C_{Di}aD)^{-1}$. That means that, for sufficiently high densities, the velocity inside the array adjusts along a steady value over the length scale D. Since the patch used in Zong and Nepf (2012) is sufficiently dense and provides this length, it can be approximated from Rominger and Nepf (2011) that:

$$\frac{U_1}{U_\infty} = \sqrt{\frac{C_f}{h}\frac{(1-\phi)}{C_{Di}a}} = \sqrt{\frac{C_f}{C_{Di}}\frac{d}{h}\left(\frac{1}{\phi}-1\right)}, \tag{2.14}$$

where C_f is the bed friction coefficient and h is the water depth (they were running experiments in a water channel).

Evaluating the flow-blockage for the patches in Nicolle and Eames (2011) as $C_{Di}aD = (4/\pi)C_{Di}\phi(D/d)$, taking the values of ϕ and D/d provided, and evaluating C_{Di} from Tanino and Nepf (2008), as is done in Chen et al. (2012), a correspondence between the density and the flow-blockage is obtained and shown in Table 2.1. It can be seen that the limit found for $C_{Di}aD$ and ϕ are in

ϕ	0.02	0.45	0.88	0.15	0.21	0.30
$C_{Di}aD$	0.5	1.8	4.5	9.8	24.5	39.5

Table 2.1: Correspondence between Nicolle and Eames (2011) ϕ and $C_{Di}aD$.

good agreement with the results presented in Nicolle and Eames (2011): the first regime identified is for $\phi < 0.5$, that corresponds to $C_{Di}aD < 4$, the second regime is for $0.5 < \phi < 0.15$ that corresponds to $4 < C_{Di}aD < 20$ and the third regime is for $\phi > 0.15$ that corresponds in Chen et al. (2012) to $C_{Di}aD > 20$.

Chen et al. (2012) notice that the deceleration of the velocity within the patch collapses to a single linear slope (see Figure 2.12) when the longitudinal distance x is non-dimensionalised by x_D defined as:

$$x_D = \left[\left(\frac{2(1-\phi)}{C_{Di}a}\right)^2 + \left(\frac{D}{2}\right)^2\right]^{1/2}. \tag{2.15}$$

Based on this observation, they provide a more generalized estimation of U_e/U_∞ as

$$\frac{U_e}{U_\infty} = 1 - \beta\frac{D}{x_D}, \tag{2.16}$$

where β is a constant obtained by fitting the experimental data and estimated to be equal to 0.42. For low flow-blockages ($C_{Di}aD < 4$), $x_D \approx 2(C_{Di}aD)^{-1}$ that reduces 2.16 to $U_e/U_\infty \approx 1 - 0.21C_{Di}aD$. For high flow-blockages ($C_{Di}aD > 4$), $x_D \approx D/2$ and $U_e/U_\infty \approx 0.16$.

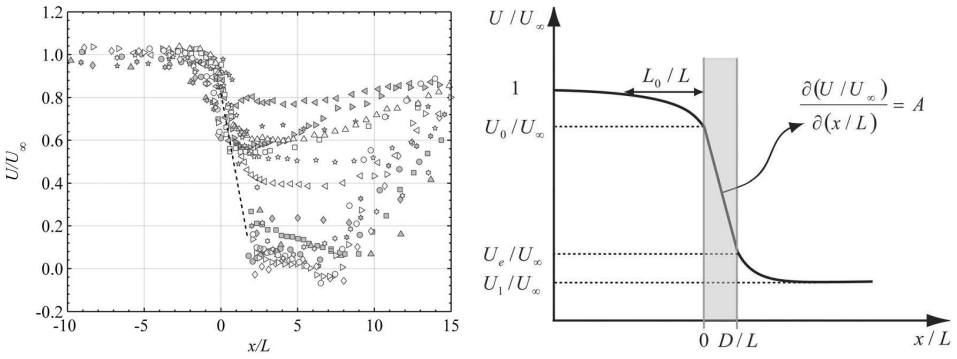

(a) U/U_∞ along the streamwise coordinate, non-dimensionalised by x_D (L in the Figure).

(b) Schematic representation of the evolution of U/U_∞ along the centreline of the streamwise coordinate non-dimensionalised by x_D (L in the Figure).

Figure 2.12: Experimental (a) and schematic (b) representation of the evolution of the velocity at the centreline along the x coordinate (Chen et al., 2012).

Based on the model provided in Figure 2.12(b), it can be assumed that the slope of U/U_∞ immediately downstream of the patch is comparable to the slope of U/U_∞ inside the patch; U_1/U_∞ can be estimated with a relation similar to Equation 2.16. Fitting the experimental data, they obtain a value for β equal to 0.52, that implies, for low-flow blockages $U_1/U_\infty \approx 1 - 0.25 C_{Di} a D$ and for high flow-blockages $U_1/U_\infty \approx 0.03$.

Using these values for U_1 and assuming $U_2 \approx U_\infty$, Equation 2.12 can be written as (Chen et al., 2012):

$$\frac{L_1}{D} = 2.5 \frac{(4 - D/x_D)}{D/x_D}, \tag{2.17}$$

that reduces to:

$$\frac{L_1}{D} = 2.5 \left[\frac{8 - C_{Di} a D}{C_{Di} a D} \right] \qquad \text{for } C_{Di} a D < 4 \tag{2.18}$$

$$\frac{L_1}{D} = 2.5 \qquad \text{for } C_{Di} a D > 4. \tag{2.19}$$

All theoretical predictions presented in Chen et al. (2012) agree well with the experimental results within reasonable uncertainties.

The root mean square of the fluctuating velocity component along x along the centreline is represented in Figure 2.13, and it shows two peaks (Chen et al., 2012, Zong and Nepf, 2012): the first peak occurs immediately behind the patch and corresponds to the turbulence production within the patch, at a scale of the cylinders' diameter d. The second peak occurs at a distance L_w from the end of the patch, and is related to the formation of turbulence at patch-length scales. L_w is called the "wake formation length". For low-blockage patches the first peak is more intense than the second, while the second decreases in magnitude and occurs further downstream (L_w increases, i.e. moves far from the patch). This means that for these patches, the von Karman wake is less intense, and the dominating phenomena is the small scale turbulence shed from the single cylinders. For high-blockage patches, the second peak is more

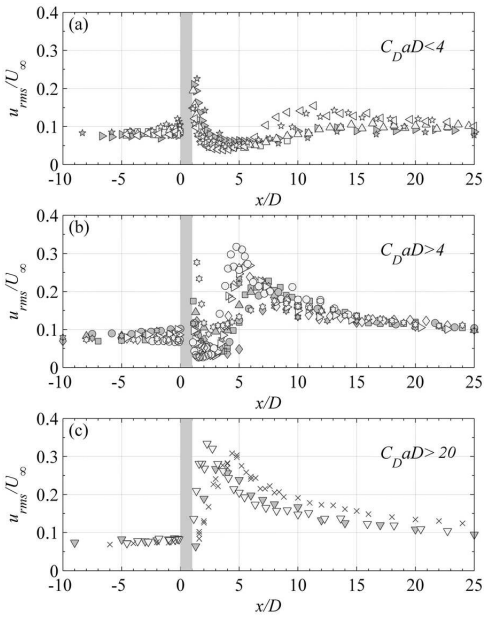

Figure 2.13: Normalised root mean square of the fluctuation of the streamwise velocity component (i.e. $\sqrt{\overline{u^2}}$, u_{rms} in the figure) (for a complete caption see Chen et al., 2012).

intense than the first one, and it occurs more upstream (i.e. L_w reduces), meaning that in this case, the wake is dominated by large scale turbulence, due to the patch-scale vortices. The case with $C_{Di}aD \sim 20$ was found to be the solid body limit in Chen et al. (2012): for all the cases with $C_{Di}aD > 20$ the behaviour is similar to the solid body, e.g. no first peak is detected behind the patch. These considerations can be confirmed also by looking at the power spectra measured on the centreline at two different locations (very close to the patch, and at a distance L_w from the patch) which show a peak at two different frequencies that can be related to the vortex shedding from a cylinder with diameter d and D respectively (Zong and Nepf, 2012).

To conclude, it is worth examining the drag experienced by a patch of obstacles. Nicolle and Eames (2011) showed that, while the average C_{Di} of the cylinders in the patch decreases with increasing density (as also found in Tanino and Nepf, 2008), the drag of the whole array increases with the density (as expected), except for being almost constant in the intermediate regime (i.e. $4 < C_{Di}aD < 20$). Similar results are reported in Chang and Constantinescu (2015) who carried out 3-D LES simulation for laminar flow impinging on 2-D circular patches with different densities and $Re_D = 10,000$, except for two main differences: first, they did not find any plateau in the drag coefficient for intermediate values of density, and second, the coefficient of a solid case was found to be lower than the converging value of patches at higher density. Tanino and Nepf (2008) also provide a model to estimate the mean drag of the cylinders, knowing the density and the Reynolds number based on the time mean and sectional average of the pore velocity and the cylinder diameter. This model has been used above to determine the C_{Di} for the cylinders in Nicolle and Eames (2011).

2.3 Discussion

It appears clear that no systematic investigation for isolated groups of obstacles fully immersed within a turbulent boundary layer has ever been carried out. In particular, there are no studies for three dimensional patches, that examine the influence of the height of the obstacles (relative to the boundary layer thickness) and density of obstacles on the drag of the patch and its wake development.

The main purpose of this research is to contribute to fill this knowledge gap. The main objective is to analyse the effects of a free end on the drag forces and wake properties and development, and to compare these results with two dimensional cases. A study of how the above mentioned parameters affect the total mean drag of the array is completely missing in the literature, and will be addressed in this research. This is of fundamental importance in the context of renewable energy, since the prediction of the drag of a group of obstacles is strongly related to the estimation of the energy that can be extracted from a tidal or a wind farm. Furthermore, the focus will also be on the length scale and the velocities scales defined in Zong and Nepf (2012) and Chen et al. (2012), whether they are still meaningful for 3-D patches, and how they are influenced by the three-dimensionality and the density of the patch. The modelling of the wakes generating downwind of porous patches is an important prerequisite to estimate the total length of the wake and to be able to model its turbulent properties which can influence relevant transport phenomena in aquatic and atmospheric flows.

Drag coefficient-and non dimensional wake time scales (i.e. Strouhal numbers) and length scales clearly depends on the characteristics of the fluid (i.e. fluid density ρ and viscosity μ), on the characteristics of the incoming flow (i.e. friction velocity U_τ, mean velocity U, boundary layer thickness δ, for a naturally grown boundary layer) and on the geometrical length scales that describe the array (i.e. height of the obstacles h, width of one obstacle d, width of the array D, density of the obstacles ϕ). The non dimensional parameters to be investigated can be obtained by means of dimensional analysis and they are: U_τ/U, H/δ, D/δ $(\rho U\delta)/\mu$, d/δ and ϕ.

The experiments presented in this thesis will be carried out with arrays with fixed width D, cylinders with fixed diameter d, three different heights H and two boundary layer thickness δ. Furthermore, U_τ/U is expected to be constant in the incoming turbulent boundary layer, and the changing in U_τ between the two boundary layers are expected not to influence the general results (see e.g. Sakamoto and Arie, 1983). Therefore, the experiments will be focused on the investigation of the relations between the drag and the wake properties with H/δ, $(\rho UD)/\mu$ and ϕ.

Such experiments have never been carried out in this detail, and the results will lead to a better comprehension of the changes in the flow due to the array. A deeper understanding in the physics will lead to the development of improved modelling tools to address the fluid dynamic issues associated with this class of flows.

Chapter 3

Experimental procedures

This Chapter describes briefly the facilities that were used for this project. Firstly, a description of the wind tunnel is presented, to characterize the main properties of this facility. Second the design and testing of the flow conditioning in the wind tunnel is described, in order to characterize the incoming flow. Third, the design and development of the patches is presented. Then the setup and measurements characteristics of two PIV campaigns are presented, on the horizontal mid plane of the models and along the vertical plane at the centreline of the models. Then, the drag measurements setup and characteristics are reported and finally the setup of velocity measurements of the wake fluctuations is described.

3.1 Wind tunnel

All the measurements were undertaken in an open-circuit wind tunnel, at the University of Southampton. This is a suction wind tunnel with a working section of 0.6 m x 0.9 m x 4.5 m in length and a maximum velocity of 30 m/s.

3.2 Flow conditioning methodology and results

3.2.1 Flow conditioning setup

Flow conditioning was designed in order to develop a thick boundary layer where the obstacles are fully immersed within the inertial-logarithmic region of the boundary layer. The rationale behind this choice relies on the observation that in many engineering applications, this is one of the most common conditions, as in the case of atmospheric boundary layers flowing over wind farms or patches of vegetation.

The design of flow conditioning exploited the wealth of knowledge developed in the field of wind engineering where experimental studies traditionally require the generation of thick

boundary layers resembling the adiabatic Atmospheric Boundary Layer (ABL). The generation of an ABL was studied firstly in the early 50s and many different techniques, active and passive, were attempted and developed in order to generate suitable velocity profiles with suitable velocity statistics.

One of the main contribution in this field can be found in Armitt and Counihan (1968) and Counihan (1969). In these studies turbulence is generated for the first time using triangular and elliptical spires located at the entrance of the test section, followed by smaller roughness elements. This method was improved in Irwin (1981), among others. This last study is the one that was followed to design a suitable flow conditioning, knowing the dimensions of the test section. The work presented in Marrè-Brunenghi (2009) was also used to design the setup. In this last work different combinations of roughness elements and vortex generators were tested, and their effects on the flow were reported.

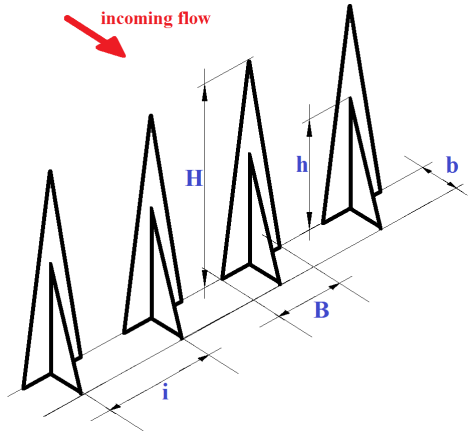

Figure 3.1: Spires configuration and dimensions.

An empirical relationship to evaluate the spires' dimensions is proposed in Irwin (1981), where the desired boundary layer thickness and the exponent for a power law description of the boundary layer ($U/U_\delta = (y/\delta)^\alpha$, U_δ being the velocity at $y = \delta$) must be given as input, as well as the test section height. A boundary layer thickness of 0.35 m was chosen and the spires dimensions were calculated for a range of exponents going from 0.10 (almost smooth surface) up to 0.5 (very rough surface). Some of the results for the height of the spires, H and the base, B are shown in Table 3.1 for some values of the power law exponent, α. The dimensions are also shown in Figure 3.1.

α	H **(mm)**	B **(mm)**
0.10	463	36
0.20	442	56
0.30	423	68
0.40	405	73
0.50	389	74

Table 3.1: Spires' dimensions at different α.

Finally, a value of $\alpha = 0.28$ was chosen (since it is a common value used for urban-type surfaces), and the corresponding dimensions of the spires are $H = 427$ mm and $B = 66$ mm. The dimensions of the splitter plates are $h = 300$ mm and $b = 105$ mm. From Irwin (1981), the spacing i of the spires should be half of their height, but Marrè-Brunenghi (2009) showed that for an increase in the distance, the resulting profile has a bigger logarithmic region, so a spacing of 243 mm was chosen. Spires were cut from a wooden board with a thickness of 6 mm.

The roughness proposed by Irwin (1981) was implemented using a continuous distribution of equal cubical elements that were glued on the floor of the wind tunnel. Marrè-Brunenghi (2009) suggested that a non-uniform distribution of roughness elements is more suitable to simulate the ABL. In particular, a decrease in the roughness element dimension along the test section allows a better behaviour of the flow. With a suitable scaling of one of the configurations presented in this last study, the roughness elements were chosen to be distributed as shown in Figure 3.2.

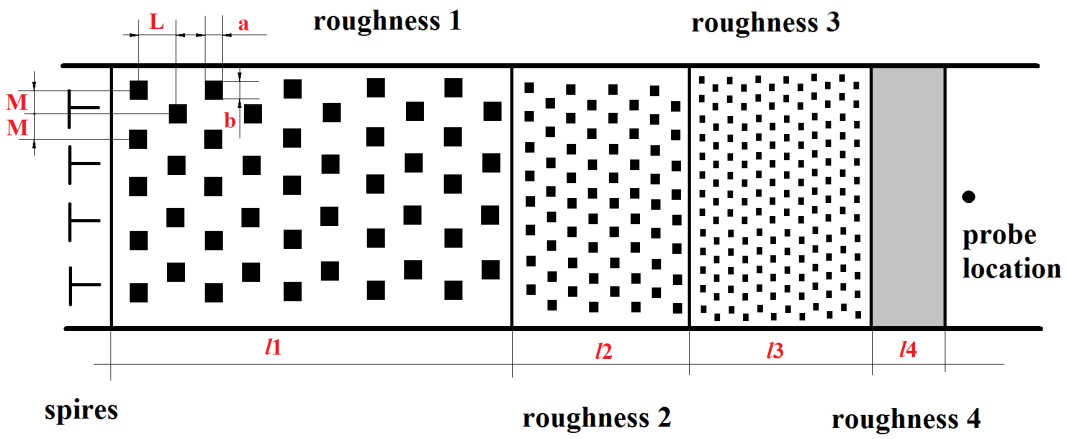

Figure 3.2: Schematic representation of the roughness distribution. The flow goes from left to right.

Type	a (mm)	b (mm)	L (mm)	M (mm)	l (mm)
roughness 1	32	32	160	80	~ 1550
roughness 2	16	16	80	40	~ 380
roughness 3	16	7	80	40	~ 370
roughness 4	-	-	-	-	300

Table 3.2: Roughness element and distribution properties.

Four decreasing types of roughness elements were chosen. The first three types of elements are realized using different Lego blocks assembly to form a staggered cubes pattern, and all roughness properties shown in Figure 3.2 are listed in Table 3.2. The part indicated with "roughness 4" in the figure, was realized with a carpet floor.

In Figure 3.3, a picture of one element used for each of the three different types of roughness is given. A picture of the roughness distribution and of the whole setup is given in Figure 3.4.

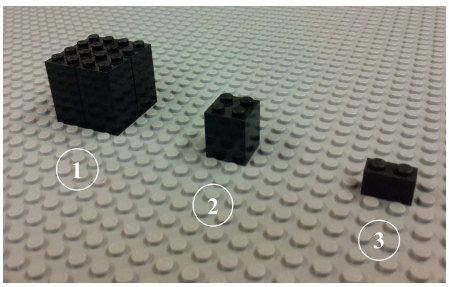

Figure 3.3: Roughness elements for different roughness type.

To obtain a second turbulent boundary layer, the spires were removed, leaving only the roughness distribution, in order to test the influence on drag of the ratio H/δ, H height of the model, δ boundary layer thickness.

Figure 3.4: Flow conditioning setup: only roughness (left), roughness and spires (right).

3.2.2 Hot-wire setup for flow conditioning

A first set of measurements was carried out using a single-wire probe with a resistance of 14.1Ω. The probe was mounted on a traverse system using a probe support and a probe holder and connected to a Newcastle hot-wire system to collect the data and to control the voltage signal. This system was then connected to a data acquisition board (NI USB-6251 BNC from National Instruments), which was finally connected to a laptop. All the data were acquired using a custom Virtual Instrument (i.e. VI) built in LabView environment and postprocessed using Matlab.

The overheat ratio (OHR) was set to 1.7, a common value for hot-wire measurements in air. It was not possible to set up a gain and an offset, or filter in the Newcastle anemometer, so no signal conditioning was applied.

In order to estimate the sampling frequency, and to check if the Newcastle system was properly set up, a square wave test was carried out at the highest expected velocity and connecting the probe to an oscilloscope. The frequency response of the wire was calculated from the time

response of the wire that turned out to be 0.08 ms, for a cut-off frequency of $\sim 10,000$ Hz. For this reason a sampling frequency of $20,000$ Hz was chosen for the acquisition. The same procedure was carried out for all the hot wire measurements that were taken.

A velocity calibration against a Pitot-static tube was carried out twice a day, once at the starting of the measurements, and once at the end. The calibration was taken for 16 values of the velocity, ranging from about 2 m/s to about 23.5 m/s, logarithmically spaced. An example of the two obtained calibration curves, with the corresponding calibration points, is given in Figure 3.5. A polynomial law was used to obtain the calibration coefficients and depending on when the acquisition was made (e.g. morning or afternoon), a choice between one of these curves or an average of them was used to convert the acquired voltage to a value of velocity.

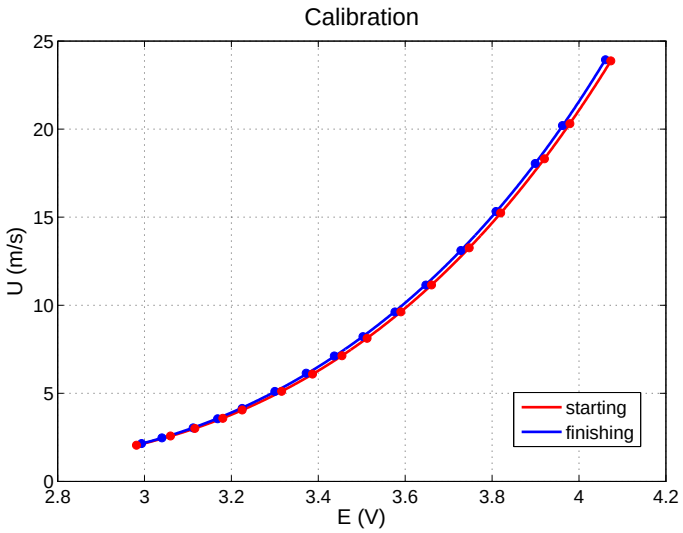

Figure 3.5: Two calibration curves, for the measurements during a single day.

The hot wire was moved vertically by means of a traverse system that was controlled from a computer. The traverse system allows an automatic control of the motion along y and z directions. There is no automatic control for the traverse movement in the x direction.

The reference velocity of the tunnel was acquired using the same Pitot-static tube used for the calibration. It was mounted on the top of the tunnel, trying to find a suitable position that was not affected by the turbulence generated by the spires, or the top wall. A position of 400 mm from the test section floor was suitable to meet these requirements.

A second set of experiments was carried out to measure the mean velocity profile for the configuration without the spires. A single wire probe was used, mounted on the same traverse system of the first set of experiments. The probe was connected to the Newcastle hot-wire system, and the output was connected to the data acquisition board (NI USB-6212 BNC from National Instruments). The data was acquired using a code built in Matlab environment. Ambient temperature and pressure were respectively acquired with the same board, and recorded manually, by mean of a weather station. For this third setup, all the electrical equipment was connected to an UPS (Uninterrupted Power Supply), in order to reduce electrical noise.

The OHR was set equal to 1.8, the sampling frequency was set again on 20 kHz and gain and offset were set to 16 and -2, respectively.

The calibration was performed once a day for 15 velocities ranging from 1.3 m/s to 28.7 m/s .

3.2.3 Hot-wire measurements for flow conditioning

The first set of experiments aimed to characterize the vertical velocity profile (i.e. along y). Each profile was characterized by 20 points logarithmically spaced along the y direction. The profiles were acquired for 5 different locations along the z direction, namely the centreline of the test section, ± 25 mm and ± 50 mm from the centreline. The profile along the centreline was acquired for two different values of the freestream velocity, namely 10 m/s and 20 m/s, while the lateral profiles were acquired only for a freestream velocity of 20 m/s.

Each acquisition was taken for 2 minutes, at $20,000$ Hz, and for each point both the single hot-wire and the Pitot-static velocities were acquired simultaneously. The ambient temperature and pressure were manually noted, using a weather station as a reference.

The acquisition of the reference velocity was made using the Pitot-static tube, located almost at the same x position of the hot-wire. It was mounted at a height of about 400 mm from the floor, and about 300 mm in the z direction. It was connected to an FC012 micromanometer from Furness, whose range of voltage is $0 - 5$ V, and it is able to detect a pressure difference ranging from 0 to 19.99 mmH_2O for a first resolution and from 0 to 199.9 mmH_2O for a second resolution. The resolution can be set up externally by the user, using a switch. The acquired voltage was related to the pressure difference, and the velocity was obtained by

$$U = \sqrt{\frac{2(p_\infty - p_s)}{\rho}}, \tag{3.1}$$

where p_∞ is the total pressure and p_s is the static pressure. The fluid density was evaluated from the pressure (p) and the temperature (T) from the weather station with the following equation

$$\rho = \frac{p}{287.05(T + 273)}. \tag{3.2}$$

The second set of experiments aimed to characterize the velocity profile for a configuration without the spires. Each profile was characterized by 29 points logarithmically spaced along the y direction. The profiles were acquired only at $z = 0$ and for two values of the freestream velocity, namely 10 m/s and 20 m/s.

Each acquisition was taken for 2 minutes, at $20,000$ Hz and the freestream velocity was acquired via a Pitot-static tube, as it was in the first set of experiments and acquired simultaneously with the hot wire and the temperature. The ambient pressure was manually noted from the weather station.

3.2.4 Incoming boundary layer (with spires) results

3.2.4.1 Velocity profiles

All the velocity profiles, non dimensionalised by the Pitot-static velocity (U_{ref}), are presented in Figure 3.6. It is evident that the mean flow is almost symmetric with respect to the centreline.

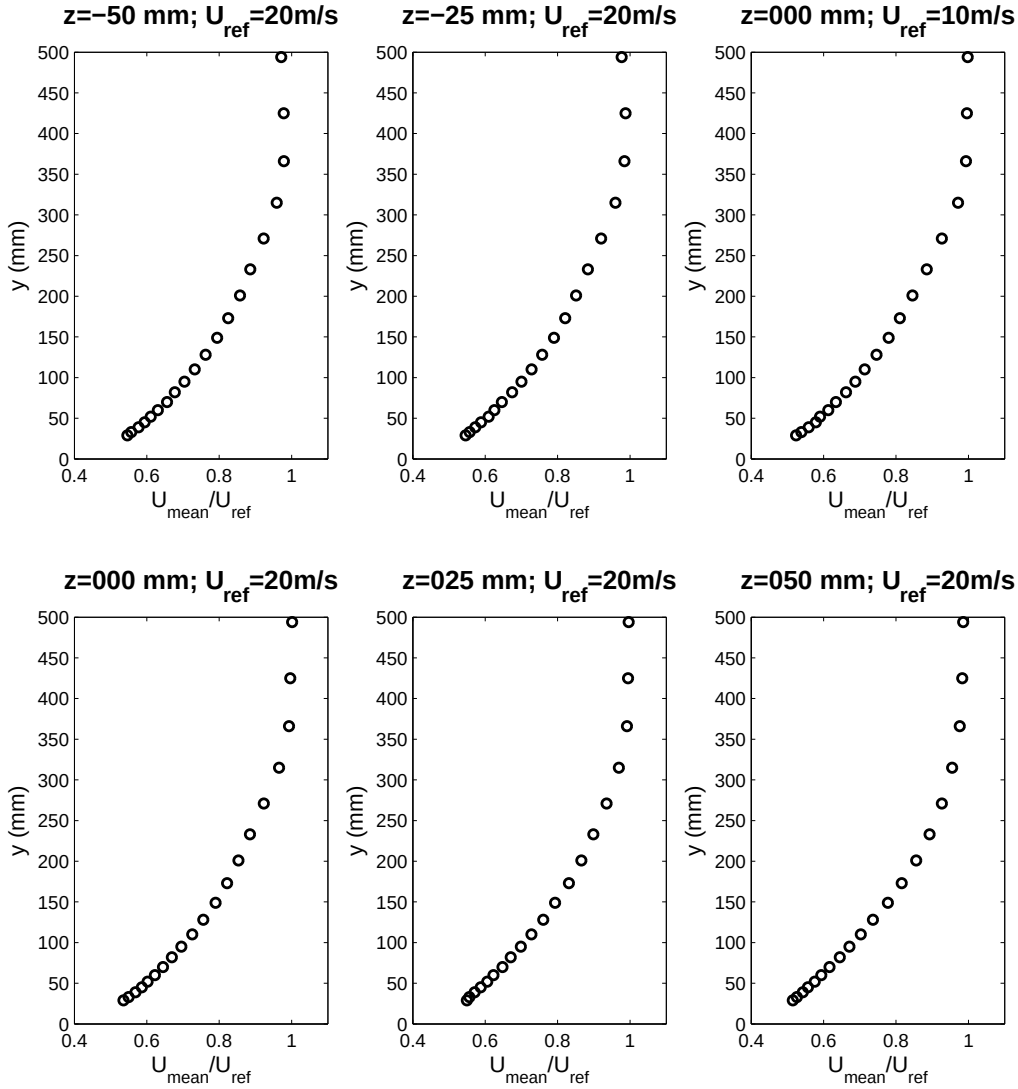

Figure 3.6: Velocity profiles for different z: ± 50 mm, ± 25 mm, 0 mm (centreline). The central profile is represented for two different reference velocities (U_{ref}): 10 m/s and 20 m/s

The standard deviations of the longitudinal velocity at each point, σ_u, are plotted in Figure 3.7. These seem to have almost the same behaviour and magnitude for each transverse location. In each case they start from the maximum value of $\sim 0.1U_{ref}$, maintain this value up to about 100 mm ($\sim 28\%$ of δ) and then decrease to 0. They all are $< 0.02U_{ref}$ above $y \simeq 350$ mm ($\sim \delta$).

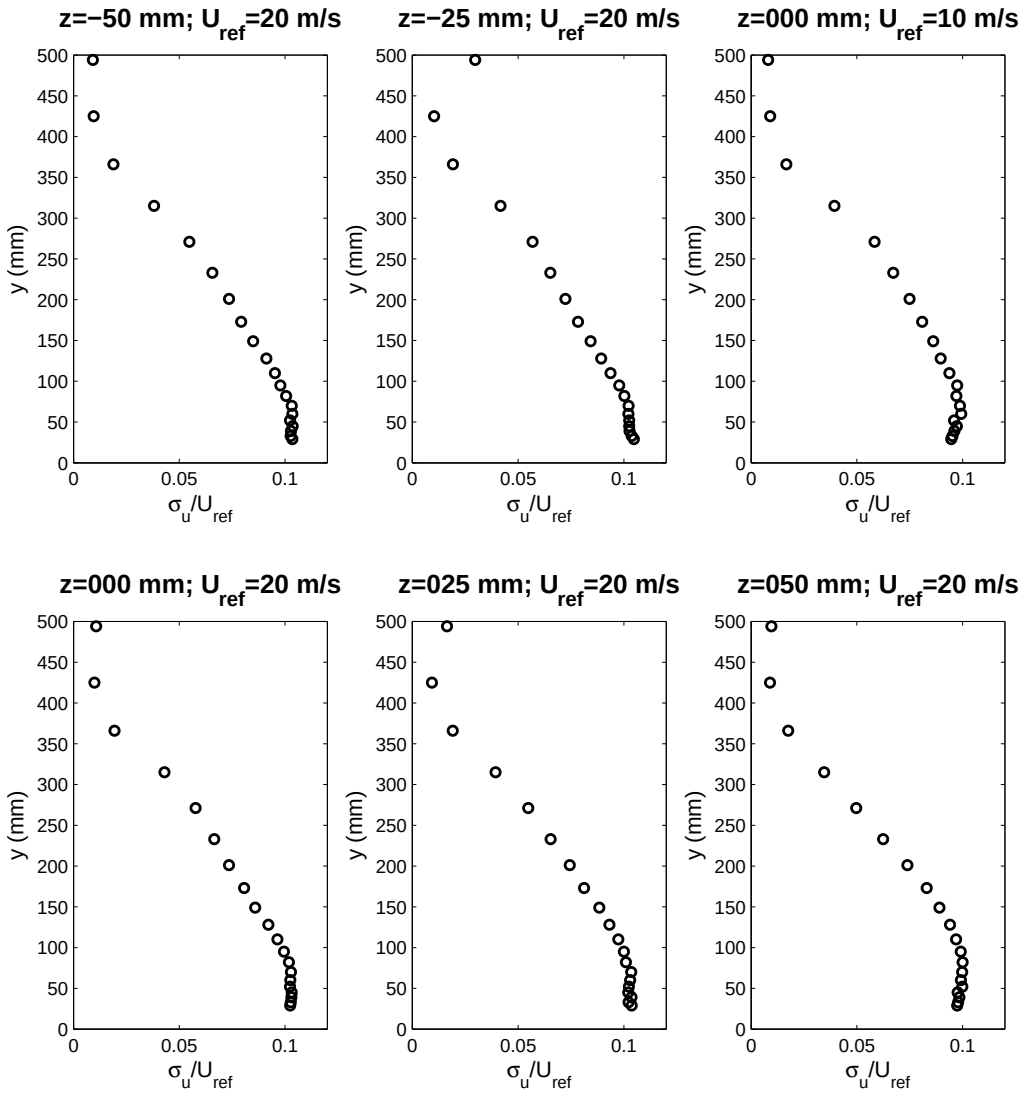

Figure 3.7: Standard deviations of streamline velocity for different lateral positions and velocity. For label see Figure 3.6.

The characterization of the boundary layer is now carried out by scaling velocity statistics using parameters pertaining to the log-law of the wall (equation 2.7). These are the friction velocity U_τ, the zero plane displacement d and the aerodynamic roughness length y_0, as shown in the equation below,

$$\frac{U}{U_\tau} = \frac{1}{\kappa} \ln\left(\frac{y-d}{y_0}\right).$$

3.2.4.2 Characterization of the boundary layers

Fitting the log-law in the inertial sub-layer means that, assuming the von Karman constant is universal (still a matter of debate in the literature), three unknowns have to be found (U_τ, d

and y_0) from one equation and hence the problem is ill-conditioned. Moreover, this fitting is also very sensitive to small experimental uncertainties in the acquired data.

This work proposes an alternative approach, which exploits the principle of outer-layer similarity. According to Townsend's outer layer similarity hypothesis (see section 2.1.3), there is evidence in the literature (see for example Castro, 2007, Flack et al., 2007, Schultz and Flack, 2005) that the variance of the fluctuating component of the velocity, $\overline{u^2}$, collapses to a profile that is the same regardless of the wall roughness if appropriately scaled with U_τ and δ. Imposing the profile of the measured $\overline{u^2}/U_\tau^2$ plotted versus $(y-d)/\delta$ to collapse with the profiles reported by Flack et al. (2007) it was possible to determine U_τ and d.

Before this procedure could be applied it was necessary to estimate the boundary layer thickness, δ. This is usually defined as that height at which the mean velocity reaches 99% of its freestream value. For these set of data, the ratio of U/U_{ref} did not always reach a value of 1 (the worst case was for $z = -50$ mm where its maximum value was 0.98). This can be considered as an estimation of the overall error in the measurements, due to the presence of turbulent fluctuations that could affect the Pitot reading in the freestream, or small temperature changes that could affect the hot-wire acquisitions and that have not been taken into account.

z (mm)	U_{ref} (m/s)	U_{max} (HW)	δ (mm)
−50	20.0	19.6	341
−25	20.2	20.0	356
0	10.2	10.2	352
0	20.0	20.0	374
25	20.2	20.1	357
50	20.0	19.7	370

Table 3.3: Boundary layers characterization.

Since the vertical locations will be scaled with δ in order to find U_τ, the value for δ was defined as the height were the velocity reaches the 99% of the maximum value measured with the hot wire for each profile (U_{max} HW). Obviously with this definition each profile had a different value for δ (ranging from ~ 340 mm to ~ 370 mm, see Table 3.3 for the exact values), and this affected the evaluation of d, U_τ and y_0 adding some uncertainty.

The data relative to a smooth wall, and to three different types of roughness were digitized from Flack et al. (2007). These data are represented in Figure 3.8 (red and black lines respectively) and a mean of the three different roughness curves was calculated and plotted as well (blue line). This curve was approximated with a sixth order polynomial curve.

A first attempt to fit this approximation with the outer measurements (from 0.3δ up to the end) was made with a non linear least square method. Knowing $\overline{u^2}$ from the experiments, and δ, the aim was to determine, for each profile, U_τ and d from the following equation:

$$\overline{u^2} = U_\tau^2 f\left(\frac{y-d}{\delta}\right), \tag{3.3}$$

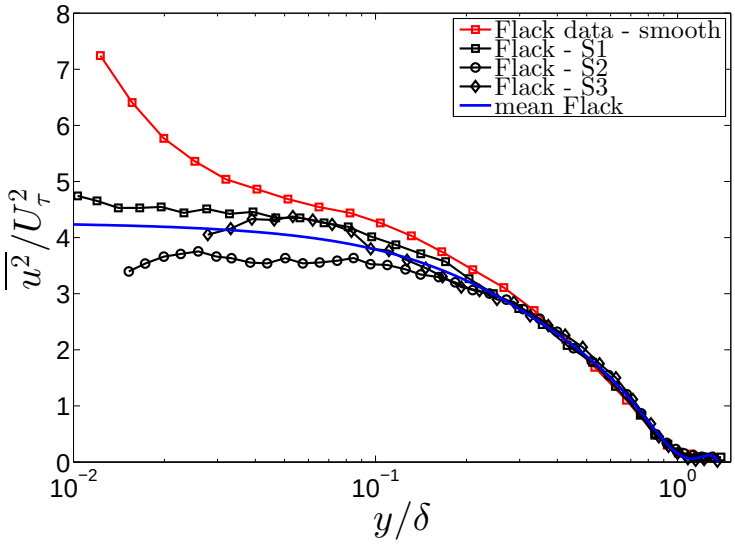

Figure 3.8: Variances of u plotted in outer layer scaling ($\overline{u^2}/U_\tau^2$): red line for a smooth wall, black lines for different sand grain roughness, blue line average of the three roughness (Flack et al., 2007).

imposing the fitting of the polynomial approximation of the mean of Flack data (i.e. $f((y - d)/\delta)$. The curves related to each fitting are shown in Figure 3.9, left.

With the data obtained from this procedure, a fitting of the log law was carried out for each profile (up to ~ 0.3δ) in order to determine y_0. In particular, the data were forced to fit with a non linear least square method, the following law:

$$U = \frac{U_\tau}{\kappa} ln\left(\frac{y-d}{y_0}\right), \tag{3.4}$$

where the only unknown is y_0. All the obtained values for each profile are listed in Table 3.4, together with a mean of the significant values.

z (mm)	U_{ref} (m/s)	d (mm)	e_d	U_τ (m/s)	e_{U_τ}	U_τ/U_{ref}	y_0 (mm)	e_{y_0}
−50	20.0	26	±25%	1.08	±2%	0.0542	0.193	±172%
−25	20.2	20	±76%	1.09	±4%	0.0539	0.279	±90%
0	10.2	24	±79%	0.54	±5%	0.0535	0.238	±64%
0	20.0	0	-	1.14	±16%	0.0569	0.658	±10%
25	20.2	7	±153%	1.15	±3%	0.0570	0.541	±34%
50	20.0	0	-	1.14	±2%	0.0569	0.785	±15%
average	-	13	-	-	-	0.0554	0.449	-

Table 3.4: First fitting attempt (considering $d \neq 0$) results. The errors are only related to the fitting procedure.

It can be noticed how the error obtained with the fitting of d is very high in all the cases (the cases without error are because the fitting was fixed with a lower limit of $d = 0$). It can also be noticed how the error related to y_0 decreases for the cases in which $d = 0$.

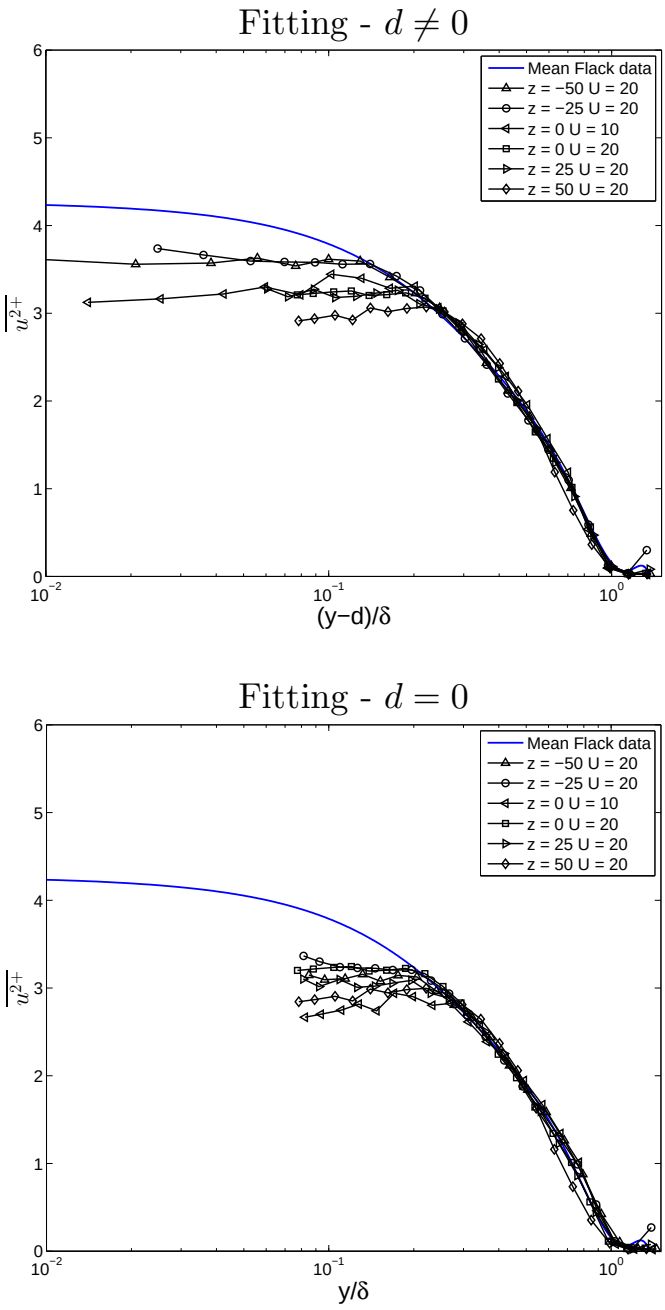

Figure 3.9: Plot of the variances scaled with d and U_τ found for two different fitting procedures: top, d was included in the fitting; bottom d was set to zero before the fitting.

Finally, the scaled profiles are plotted in Figure 3.10, left side. It is evident that this procedure does not lead to good collapse in the lower part of the boundary layers (logarithmic sub-layer), where the log law is supposed to hold.

For these reasons, a second fitting procedure was carried out. This second procedure is analogous to the first one, except for the fact that d was set to be equal to 0 from the beginning.

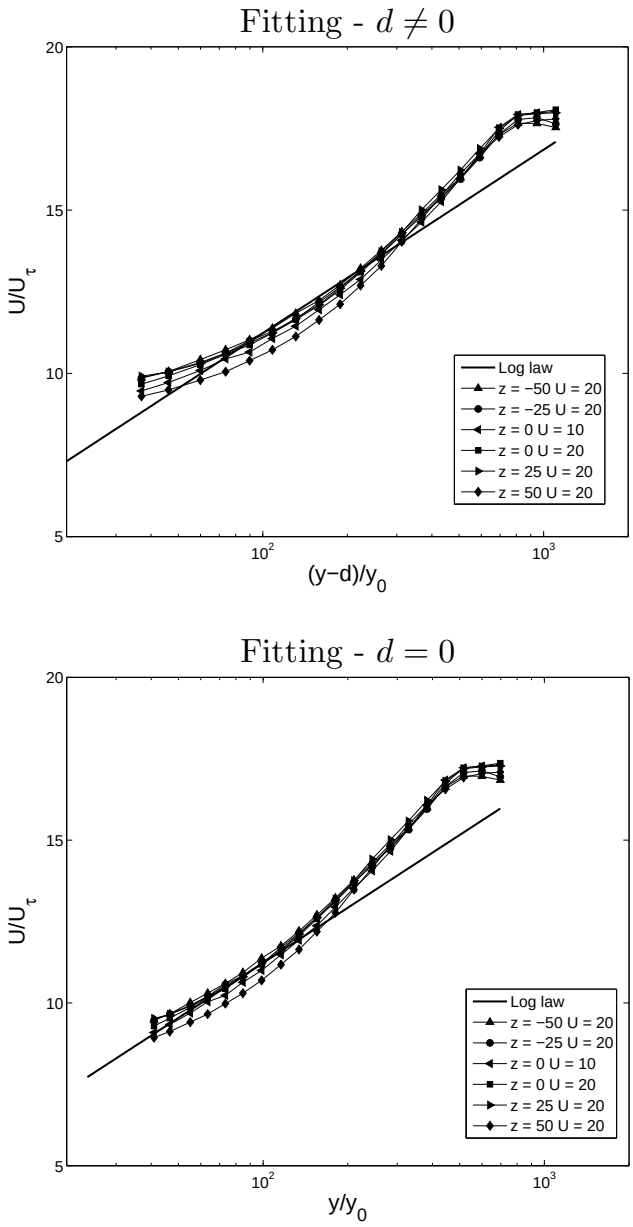

Figure 3.10: Plot of the boundary layers scaled with the values obtained from two different fitting procedure: top, all the boundary layers are scaled with $d = \overline{d} = 13$ mm, $U_\tau = \overline{(U_\tau/U_{ref})}U_{ref}$ and $y_0 = \overline{y_0} = 0.435$ mm (all the values from the first fitting procedure); bottom, each profile is scaled with $d = 0$, $U_\tau = \overline{(U_\tau/U_{ref})}U_{ref}$ and $y_0 = \overline{y_0} = 0.709$ mm (all the values from the second fitting procedure).

The expression $U/U_\tau = \kappa^{-1} ln(y/y_0)$ is commonly used in meteorological and wind engineering communities. The obtained results from this fitting are listed in Table 3.5. The fitting of the mean values from Flack et al. (2007) are shown in Figure 3.9, on the right and the scaled boundary layers are plotted in Figure 3.10.

It is evident from Figure 3.10 that this second procedure fits better over all the profiles.

z (mm)	U_{ref} (m/s)	U_τ (m/s)	e_{U_τ}	U_τ/U_{ref}	y_0 (mm)	e_{y_0}
−50	20.0	1.16	±4%	0.0581	0.664	±12%
−25	20.2	1.15	±3%	0.0568	0.631	±15%
0	10.2	0.59	±2%	0.0579	0.762	±6%
0	20.0	1.14	±2%	0.0570	0.658	±10%
25	20.2	1.18	±2%	0.0586	0.708	±19%
50	20.0	1.15	±2%	0.0576	0.814	±16%
average	-	-	-	0.0577	0.706	-

Table 3.5: Second fitting attempt (considering $d = 0$) results. The errors are only related to the fitting procedure.

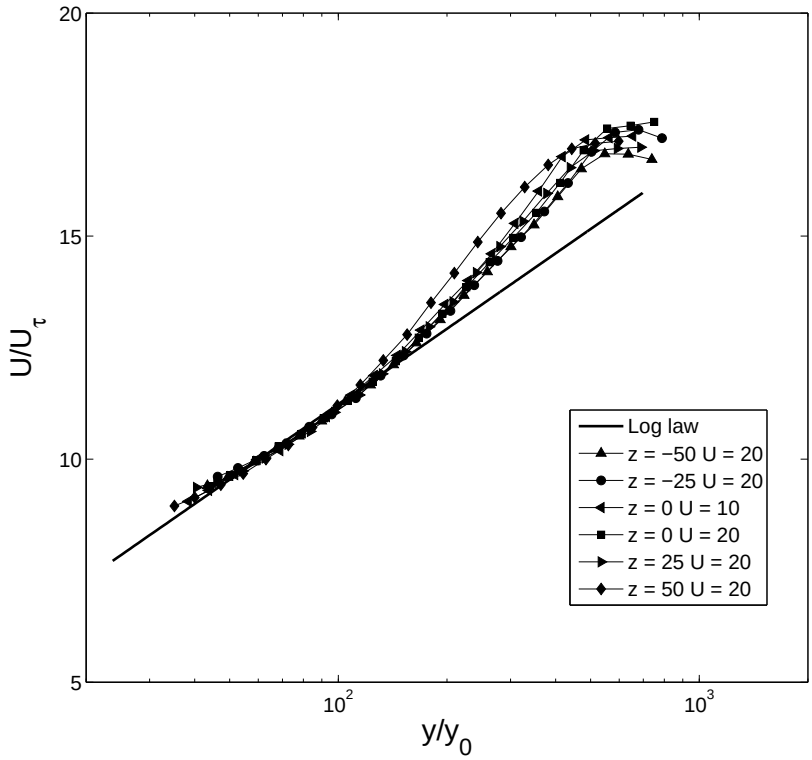

Figure 3.11: Plot of all the profiles scaled with their own parameters (see Table 3.5).

A plot of all the profiles scaled with their own parameters obtained with the second procedure is given in Figure 3.11. It is evident that the log law approximation is reasonable for all the profiles up to $y/y_0 \simeq 150$ that corresponds almost to 0.25δ.

The difficulties associated with the definition of the zero plane displacement, the friction velocity and the roughness length are partly due to the fact that there is not a uniform roughness, but rather different roughness with decreasing length, height and density. All the fitting procedures were carried out in order to estimate at least the order of magnitude of the parameters, and to have an idea of the main characteristics of the boundary layers generated with this flow conditioning. In particular it was important to have an overall estimation of the extension of the log layer.

Additional results and measurements in order to characterise the incoming boundary layer velocity profiles are reported in Appendix A.

3.2.5 Incoming boundary layer (without spires) results

3.2.5.1 Velocity profiles

The results for the same roughness distribution, but without the spires at the inlet, and for a freestream velocity of 20 m/s are shown herein.

The velocity profiles and the standard deviations of the longitudinal velocity at each point, non dimensionalised with the freestream velocity, U_{ref}, are presented in Figure 3.12.

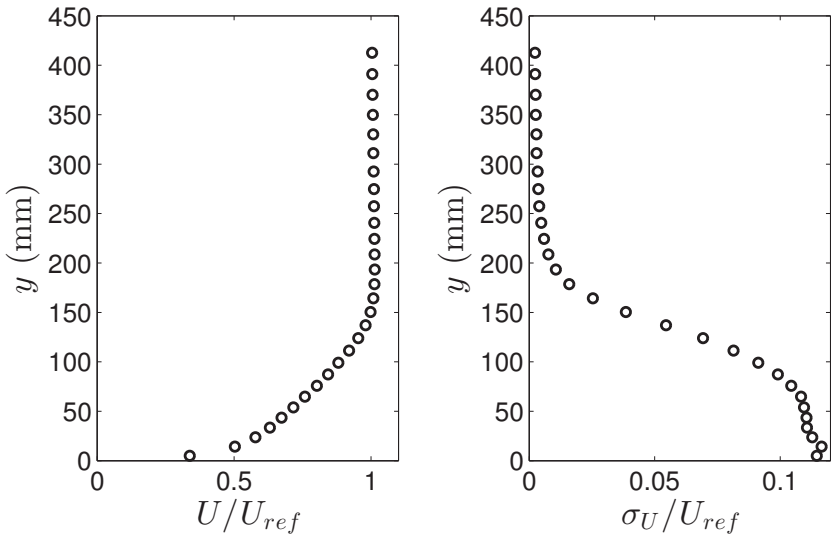

Figure 3.12: Velocity and standard deviation profiles for the flow conditioning without spires.

It is evident from these figures that the boundary layer thickness δ and the inertial sub layer extends for a shorter distance in this case. The velocity increases up to $y \simeq$150 mm, and σ_U is about constant up to $y \simeq$70 mm.

The boundary layer thickness δ is evaluated as the location at which the mean velocity reaches the 99% of the freestream velocity, and it is equal to 155 mm.

The flow without spires does not really exhibit a log region since the h/δ (where h is the height of the roughness elements) is high and therefore, the roughness elements occupy a large portion of the boundary layer. These measurements were taken in order to obtain data of large H/δ values of the patch. However, most of the results presented in the study is confined to the small H/δ values.

3.3 Model design and development

The model design is based on the work presented in Nicolle and Eames (2011). The ratio between the patch diameter D and the cylinders' diameter d proposed in their paper is equal to 21, with six different array densities ranging from 0.0159 with 7 cylinders and 0.3016 with 133 cylinders. For each patch the obstacles were arranged in concentric rings (with the most external coincident with the array circumference) and filling inwards, with an extra cylinder in the centre of the patch. The distance between two cylinders on the same ring, and the distance between two subsequent rings was set to be equal.

Starting with this design, the first thing that was set up was the ratio D/d equal to 20 for this project, and a major diameter D equal to 100 mm. The second step was to choose the heights H to test and 50, 75 and 100 mm were a suitable guess which results in an aspect ratio of the cylinders (i.e. H/d) ranges from 10 to 20, while the aspect ratio of the whole patch ranges between 0.5 and 1. One of the limitations to the heights derived from the fact that the main idea is to study patches with obstacles completely immersed in the inertial sub-layer of the incoming flow, the thickness of which therefore limits the maximum height achievable in the experiments presented herein. The second limitation derived from considerations about the blockage of the patch. In particular, with the chosen dimensions, the maximum blockage is 1.8%, which corresponds to a maximum overestimation of the drag of about 5% (ESDU 80024).

A first design with metal cylinders with a diameter of 5 mm and heights ranging from 50 to 100 mm was chosen to be the best solution for the obstacles. To hold them in place, a threaded end was a more secure and reliable choice, compared with gluing or fitting. Instead of buying customized rods with a threaded end (not easy to find with such a small diameter), the cylinders were obtained from DIN 912 bolts of different lengths, that were cut with a band saw, as shown in Figure 3.13.

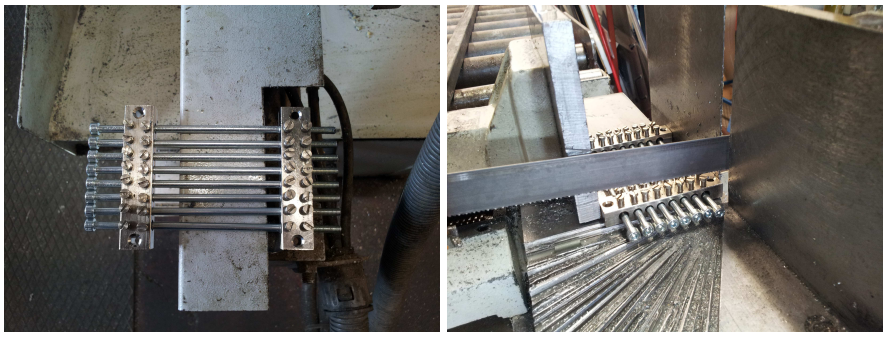

Figure 3.13: Cutting of the DIN 912 bolts to obtain the cylinders.

A 3D printed support was made as a base for the configurations with a number of cylinder raging from 7 to 95. The characteristics of each patch are tabulated in Table 3.6 where C_{N_C} is assigned to distinguish each configuration. The configuration with 133 cylinders was excluded, since the cylinders were too dense in this case to allow an easy and practical assembly of the model.

Case	C_7	C_{20}	C_{39}	C_{64}	C_{95}
N_C	7	20	39	64	95
ϕ	0.0175	0.05	0.0975	0.16	0.2375
$Rows$	1	2	3	4	5

Table 3.6: Characteristic of the patches.

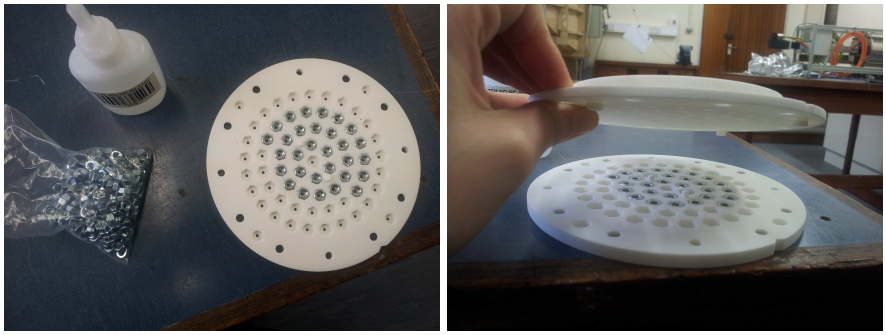

Figure 3.14: Second design of the base, configuration with 64 cylinders. View of the top side of the lower part, with the nuts allocations (left) and the two half of the base (right).

The base is split in two part along the biggest circumference (i.e. "sandwich configuration") to allocate the nuts that will keep the cylinders in place. The nuts were glued in hexagonal holes on the top side of the lower part (see Figure 3.14). The choice to keep the nuts inside the base, was to avoid the chance of a vertical shift of the nuts (and, consequently, the correspondent cylinder) along the vertical direction, in case the gluing was deteriorating. In this way the nuts are constrained inside the base, and no shift is allowed. All the densities are shown in Figure 3.15

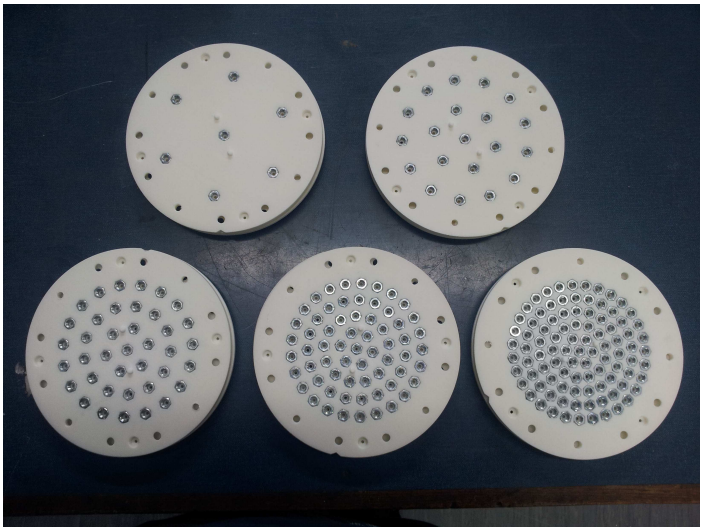

Figure 3.15: Top sides of the lower part of each patch.

The two parts are kept together with 8 screws along the sides, connected to nuts that are inserted in the lower side of the bottom part. The cylinders were then inserted from the top,

once the nuts were glued and the two parts connected (see Figure 3.16).

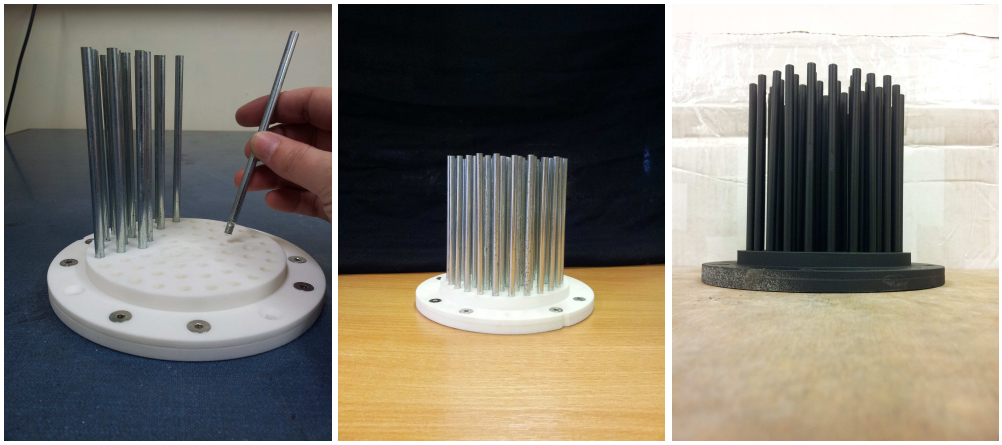

Figure 3.16: Building the patch (left), and final result (centre and right).

Finally, each model was painted with matt black spray paint, in order to minimize reflections when measuring with PIV and a wooden board with an appropriate location hole was made, in order to cover the patch and to make it flush with the surrounding plates.

Due to the fast spread ad developing of 3D printing technology, a second set of patches was realised by 3D printing the whole model in Acrylonitrile Butadiene Styrene (ABS) plastic, including the cylinders, as shown in Figure 3.17. The shape of the base and the cylinders distribution within the patch was kept the same.

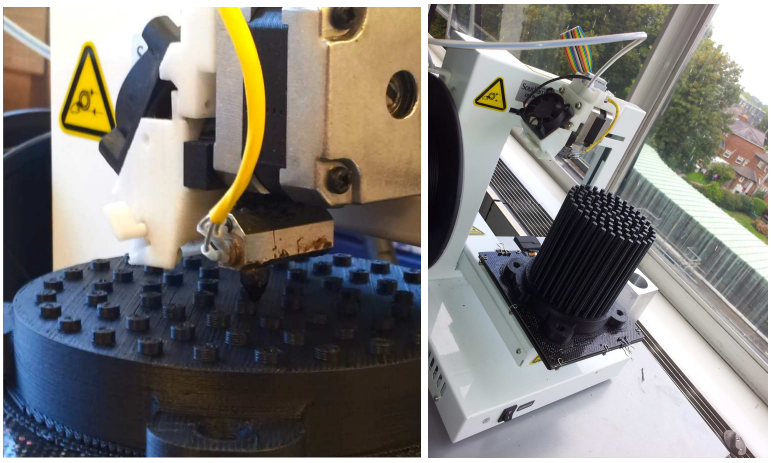

Figure 3.17: 3D printing of the C_{64} model (left) and C_{95} (right).

3.4 Horizontal PIV methodology

3.4.1 Horizontal PIV setup

A first set of PIV measurements was performed after characterizing the incoming flow. This first PIV experiment aimed to characterize the wake along a horizontal plane, in order to highlight the main differences from the 2D case due to the free end. Just one height of the obstacles was tested, i.e. 100 mm. The chosen plane is the plane located at the mid height of the patch, at 50 mm from the wind tunnel floor.

The main goal was to capture the wake development as far as possible from the obstacle. While the laser is shot from one side of the test section, the cameras had to be positioned on top. The biggest field of view that could be obtained without obstacles due to the constraints of the windowing of the ceiling was of the order of about 900 mm. In order to capture this large field of view, a combination of three cameras was used.

Each camera is an ImagerProLX CCD from LaVision with a resolution of 4872 pixel × 3248 pixel (e.g. 16 Mpixel), and was combined with a 50 mm Nikkor lens. The three cameras were positioned on top of the test section, and fixed to an aluminium frame using three supports that could rotate the cameras along the three main axes, to allow a finer alignment. The $f\#$ (aperture number) was set to 2.8. The field of view (FOV) of each camera with this configuration was about 30 cm × 40 cm, so the first camera (according to the flow direction) was positioned with the longest side aligned along x, while the second and the third camera were positioned with the short side aligned along x, in order to capture as much data as possible. A sketch of the resulting field of view is represented in Figure 3.18, and a picture of the cameras' setup is shown in 3.19(a). The details of the magnification and the exact dimensions of the field of view will be clear after the calibration procedure, described later. The patch position was almost in the centre of the short side of the first camera.

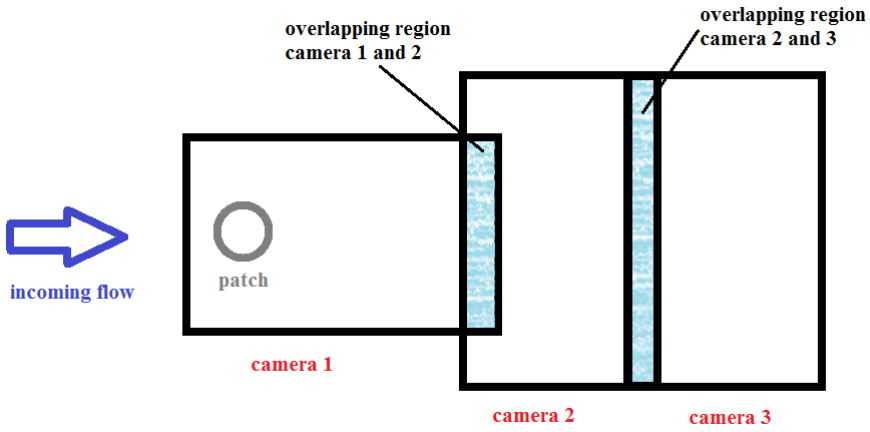

Figure 3.18: Sketch of the field of view (not in scale).

The laser sheet was generated combining two pulsed Nd:YAG lasers (Nano L200 15PIV, from Litron Lasers) with a wavelength of 523 nm, energy 200 mJ/pulse and repetition rate of 15 Hz. The lasers were mounted on a board, connected to an aluminium frame that allowed the vertical adjustment and positioning. To focus the lasers almost in the centre of the laser sheet, a combination of two cylindrical lenses were used for each laser, a plano-concave with focal length -50 mm and a bi-convex with focal length of 75 mm for the first laser and a bi-concave with a focal length of -50 mm and a plano-convex with a focal length of 75 mm for the second laser. Each pair of lenses was mounted on the frame and aligned with each beam, using optomechanical tools. The beams were then expanded into a light sheet using two cylindrical lenses, both with a focal length of -20 mm for the first laser, and a cylindrical lens with a focal length of -10 mm for the second laser. The lenses were then finely adjusted to align the two laser sheets. Finally, the thickness of the combined laser sheet was measured to be about 2 mm. A picture of the optics setup is shown in Figure 3.19(b).

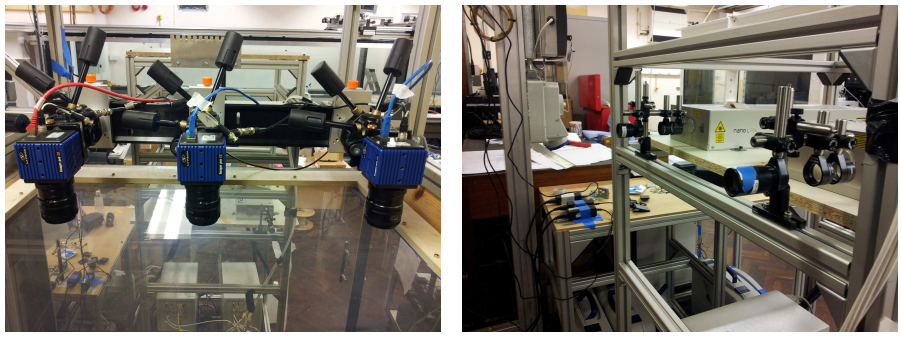

(a) Cameras setup (the flow is from right to left). (b) Laser optics setup: first laser lenses (right) and second laser lenses (left).

Figure 3.19: PIV setup.

The cameras and the lasers were then connected to a synchronization unit PTU 9 from LaVision and controlled using DaVis, an image acquisition and processing software from LaVision.

A smoke machine, loaded with a solution of glycols and de-mineralised water (Pro Smoke Super fluid from Martin) was used to seed the flow.

After all the lasers and the cameras were positioned, a calibration procedure was carried out. A calibration plate was positioned in correspondence to the horizontal pane at mid height and, as a first step, the cameras were focused on the calibration plate. Then the plate was removed from the test section, the flow was seeded and the cameras' focus was finely adjusted on the particles. Once all the cameras were focused properly, the calibration plate was positioned again, and calibration images were acquired. These images are shown in 3.20. The software provides the calibration conversion results by detecting the reference points of the calibration plate and then fitting all the frame with a 3rd order polynomial mapping function. The average deviation of the marked positions on the calibration plate and the ideal regular grid for each frame was less than 0.35 pixel for all the frame, which is considered almost an excellent precision, according to the software manual. From the calibration procedure the image magnification, intended as the

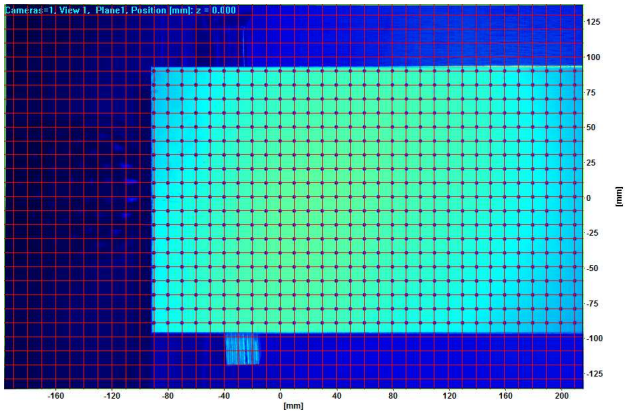

(a) Camera 1.

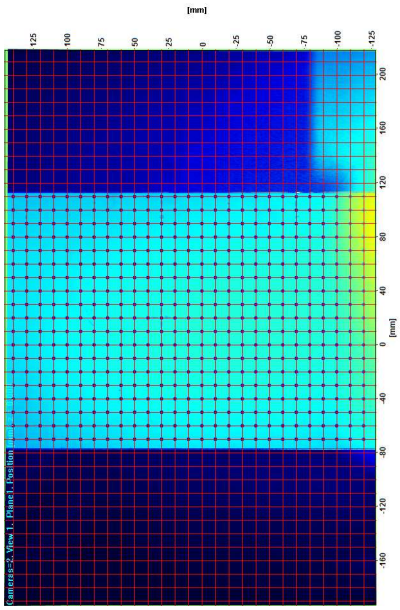

(b) Camera 2.

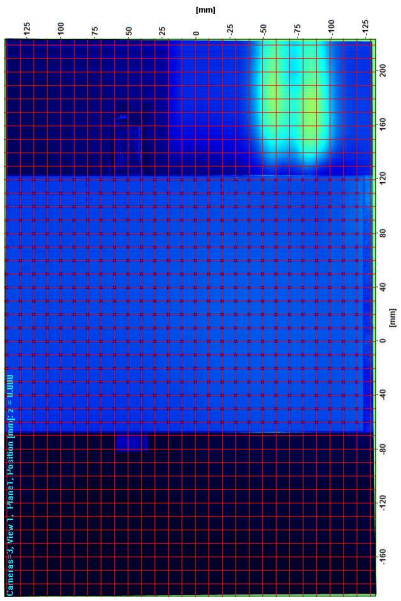

(c) Camera 3.

Figure 3.20: Calibration images.

ratio between the image distance and the object distance, was equal to 11.3, which corresponds to a conversion ratio of 12 px/mm that corresponds to a field of view of 406 mm × 270 mm for each camera. This leads to overlapping regions of almost 20 mm in both cases. The location of the patch with this configuration is almost centred in the short side of the first camera, and the field of view spans almost $1.3D$ from the centre of the patch along z on both sides and almost $8.7D$ from the centre of the patch along x.

3.4.2 Horizontal PIV measurements

Nine different configurations were tested during the PIV campaign, which are: the incoming flow with no model, the five different densities (models C_7, C_{20}, C_{39}, C_{64} and C_{95}), a solid finite cylinder with diameter equal to the diameter of the patch (i.e. 100 mm) and height equal

to the height of the obstacles (i.e. 100 mm), model C_S. The model with the lowest density was tested in 4 different orientations with respect to the incoming flow, rotating the model of 10° each time in order to see the effects of different blockages. Hereafter these cases will be referred to as C_7, $C_{7_{10}}$, $C_{7_{20}}$ and $C_{7_{30}}$, where C_7 is the configuration with three obstacles aligned with x.

The lasers were set to 172 mJ for laser A and 164 mJ for laser B for the first laser and 163 mJ for lasers A and B for the second laser. For the latter the attenuator was adjustable, and was set to 90% (which means that 90% of the light would go through).

The time interval between two subsequent frames was set to 100 μs, and the acquisition frequency was 0.375 Hz, due to the fact that the acquired data were stored in an external hard drive, and the acquisition speed was mainly constrained by the data transmission rate from the computer to the hard drive. The camera exposure was optimized by the software and equal to 610 μs. Different time intervals were tested and 100 μs was the one giving the best results, between time steps of 50, 100 and 200 μs.

For the incoming flow 500 pairs of images were taken, while for all the models a total of 3000 pairs were acquired for each configuration.

A Pitot-static tube was mounted above of the model location, at a hight of about 40 cm from the floor of the test section (almost the same location as the hot wire measurements) and connected to a Furness manometer to acquire the freestream velocity of the incoming boundary layer. All the measurements were taken for a velocity equal to 20 m/s. For each acquisition, the flow velocity, the ambient pressure and temperature were monitored from the manometer and a weather station respectively, and noted down every 15 minutes (each set of 1000 required 45 minutes to be acquired). The images were than post processed using DaVis software.

After the background subtraction, the PIV calculation was applied using the GPU card. A multi-pass iteration procedure was applied with windows of decreasing size: 2 passes with square windows of 64 × 64 with overlap 50% and 3 passes with square windows of 16 × 16 with overlap of 50%.

It was evident from the beginning that the first part of the field of view (i.e. where the patch was located) did not receive enough light to get a good quality PIV. An attempt was made to capture also the flow inside and around the patch, but the shadows due to the presence of the model did not allowed it for most of the densities. The problem due to insufficient light is evident looking at the mean and instantaneous flow without any model acquired with the first camera, in Figure 3.21.

A median filter was also applied to the final vector field: firstly, the vectors were deleted if their peak ratio was less than 1.2, then a filter to reject groups of spurious vectors was applied where vectors were removed if their residual was above twice the r.m.s. of the neighbours and alternate vectors were inserted if their residual was below three times the r.m.s. of the neighbours. Groups of wrong vectors with less than 5 vectors were removed automatically.

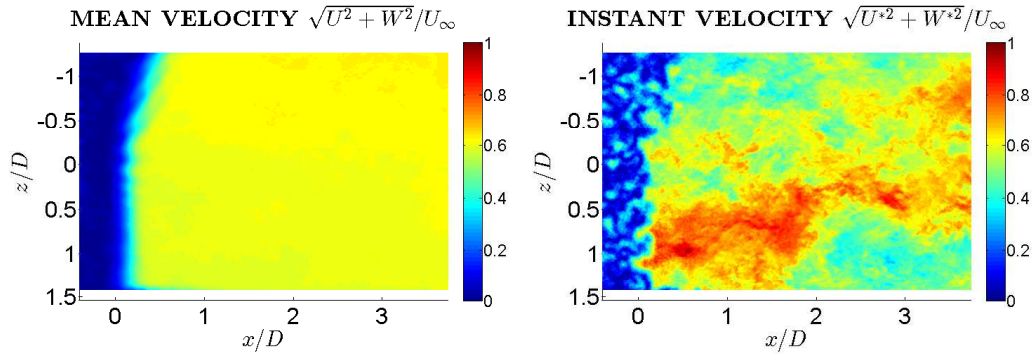

Figure 3.21: Mean and instantaneous incoming flow for camera 1 (flow from left to right).

The origin of the reference system corresponded approximately to the centre of the patch and the laser was shooting from positive z towards negative z: this is why the region with wrong results is more extended in the top part of the frame (up to $x \approx 0.7D$) than in the lower part (up to $x \approx 0.3D$), since the light intensity decreases further from the optics. The situation is enhanced for the solid cylinder: the region that has to be discarded is bigger than the previous case and extends to almost $x \approx D$, as can be seen in Figure 3.22. All these regions will not be

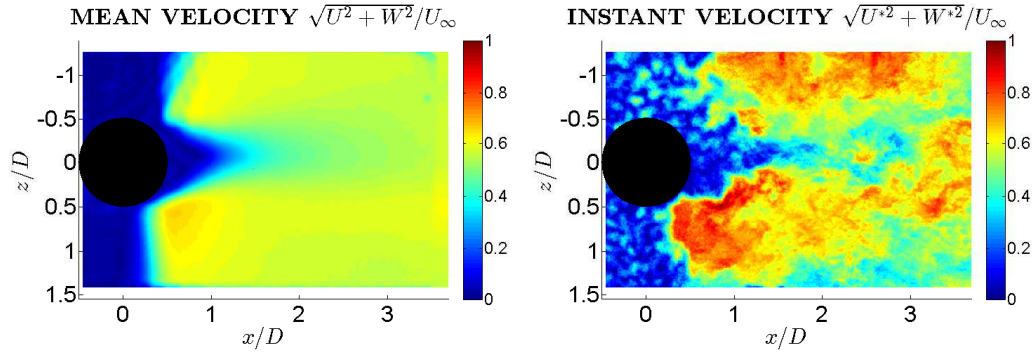

Figure 3.22: Mean and instantaneous flow for camera 1 for model C_S (flow from left to right).

considered and will be cut off from the field of view, checking for each case the limits where the flow is not affected anymore by this effect.

All the data were then exported in Matlab environment. In order to create one plot with the combination of the three frames, the following procedure was applied. Firstly, all the frames were cut at the edges, since after the calibration corrections, they showed some null value in correspondence of the borders. Secondly, the overlapping regions were stitched together: the field in this region was averaged using a customized weighting function. Two complementary surfaces, one for each camera, were linearly interpolated in Matlab with the function *griddata* for both the overlapping regions: the edges of these surfaces were set to 0 or 1, depending on the edge being the edge of the camera (0) or not (1). An example of how the limits were set is shown in Figure 3.23. At this point the coordinates of the whole field were linearly

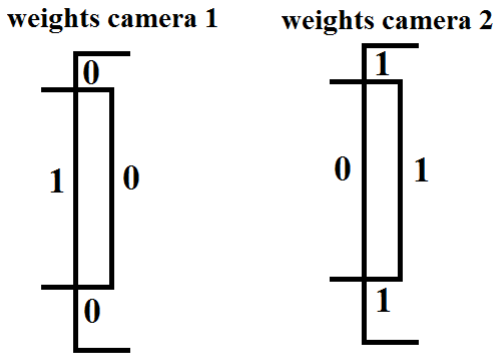

Figure 3.23: Limits of the weighting surface for the overlapping region between camera 1 and camera2 (not in scale).

interpolated across the whole region, as well as the velocity field, in order to have the same coordinate system and spacing for the entire plot.

3.5 Vertical PIV methodology

3.5.1 Vertical PIV setup

A second set of PIV measurements was performed. This second PIV experiment aimed to characterize the wake along a vertical plane, in order to highlight the development of the wake along the finite height of the obstacles. One height was tested for all the obstacles, i.e. 100 mm (AR = 1). The chosen plane is the plane located at the centreline of the patch ($x - y$ plane at z = 0).

The main goal was to capture the influence of the free end on the wake development. While the laser is shot from the top of the test section, the cameras had to be positioned on the side. The biggest field of view that could be obtained without obstacles due to the constraints of the windowing of the ceiling was of the order of about 700 mm. In order to capture this large field of view, a combination of three cameras was used.

Each camera is an ImagerProLX CCD from LaVision with a resolution of 4872 pixel × 3248 pixel (e.g. 16 Mpixel), and was combined with a 105 mm Nikkor lens. The three cameras were positioned on the side of the test section, and fixed to an aluminium frame using three supports that could rotate the cameras along the three main axes, to allow a finer alignment. The $f\#$ (aperture number) was set to 5.6 for the two external cameras and to 2.8 for the central camera, this difference due to the higher brightness of the lasers in this overlapping region. The field of view (FOV) of each camera with this configuration was about 30 cm × 20 cm, along x and y respectively. A sketch of the resulting field of view is represented in Figure 3.24. The details of

the magnification and the exact dimensions of the field of view will be clear after the calibration procedure, described later.

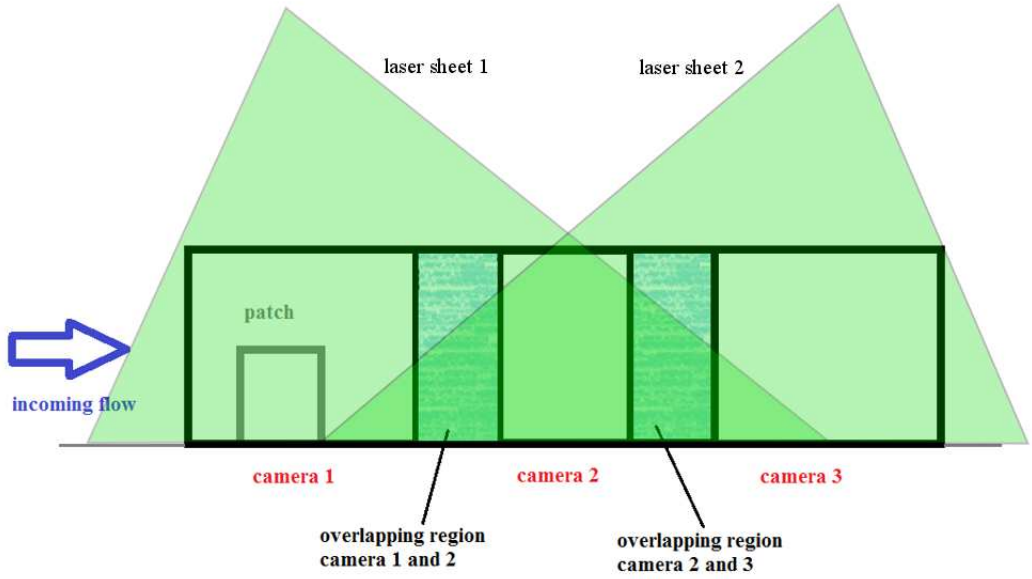

Figure 3.24: Sketch of the field of view (not in scale).

The laser sheet was generated combining two pulsed Nd:YAG lasers (Nano L200 15PIV, from Litron Lasers) with a wavelength of 523 nm, energy 200 mJ/pulse and repetition rate of 15 Hz. The lasers were mounted on an aluminuiom frame and positioned on the top of the test section. The frame was mounted on a second external frame, to keep the lasers detached from the wind tunnel, to avoid vibrations transmissions. The lasers were initially shot in the flow direction, deviated by two mirrors to direct them downwards into a beam converger to focus them. Finally, the beams were expanded into a light sheet using a cylindrical lens for each laser, with a focal length of −20 mm for the first laser (top positioned, laser sheet 2 in Figure 3.24), and a focal length of −15 mm for the second laser (low positioned, laser sheet 1 in Figure 3.24). All the optics were mounted on a frame and aligned with each beam, using optomechanical tools. The lenses were then finely adjusted to align the two laser sheets. Finally, the thickness of the combined laser sheet was measured to be about 2 mm. A picture of the lasers and optics setup is shown in Figure 3.25.

The cameras and the lasers were then connected to a synchronization unit PTU 9 from LaVision and controlled using DaVis, an image acquisition and processing software from LaVision.

A smoke machine, loaded with a solution of glycols and de-mineralised water (Pro Smoke Super fluid from Martin) was used to seed the flow.

After all the lasers and the cameras were positioned, a calibration procedure analogous to the horizontal measurements was carried out and the resulting calibration images are shown in

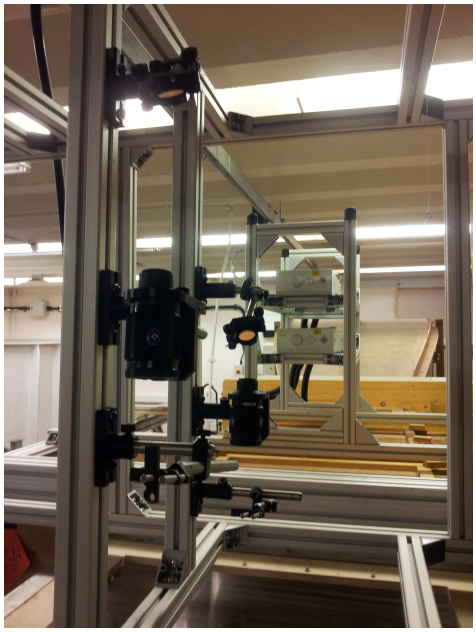

Figure 3.25: Lasers and optics setup.

3.26. Calibration was applied to the data with a Matlab code developed by Ronnie Hanson at the University of Southampton. The code provides the calibration conversion results by detecting the reference points of the calibration plate and then fitting all the frame with a 3rd order polynomial mapping function. The average deviation of the marked positions on the calibration plate and the ideal regular grid for each frame was less than 0.5% for all the frame, which is considered almost an excellent precision. From the calibration procedure the conversion ratio was of 17 px/mm that corresponds to a field of view of 280 mm × 170 mm for each camera. This leads to overlapping regions of almost 50 mm in both cases. The field of view spans from $1D$ upstream from the centre of the patch to almost $6D$ downstram from the centre of the patch along x and almost $2D$ from the wind tunnel floor along y.

3.5.2 Vertical PIV measurements

Nine different configurations were tested during the PIV campaign, which are: the incoming flow with no model, the five different densities (models C_7, C_{20}, C_{39}, C_{64} and C_{95}), a solid finite cylinder with diameter equal to the diameter of the patch (i.e. 100 mm) and height equal to the height of the obstacles (i.e. 100 mm), model C_S. The orientation of the obstacles with respect to the incoming flow was kept the same of the horizontal measurements.

The lasers were set to 175 mJ for laser A and 158 mJ for laser B for the first laser and 172 mJ for laser A and 164 mJ for laser B for the second laser.

The time interval between two subsequent frames was set to 50 μs, and the acquisition frequency was 0.375 Hz, due to the fact that the acquired data were stored in an external hard drive, and the acquisition speed was mainly constrained by the data transmission rate from

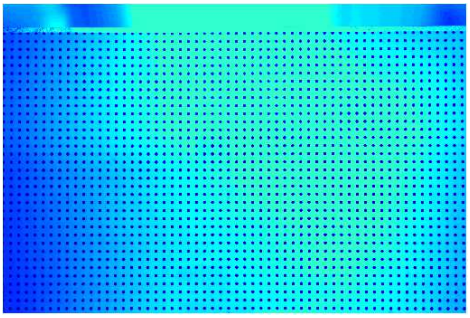

(a) Camera 1.

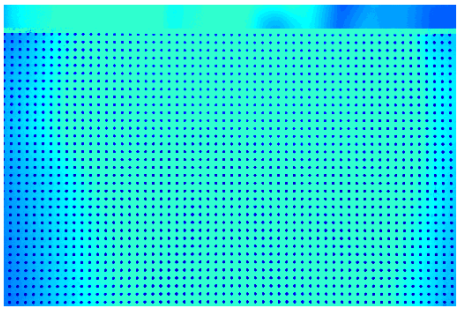

(b) Camera 2.

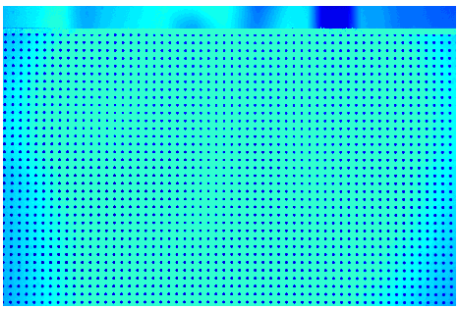

(c) Camera 3.

Figure 3.26: Calibration images.

the computer to the hard drive. The camera exposure was optimized by the software and equal to 610 μs. Different time intervals were tested and 50 μs was the one giving the best results, between time steps of 50, 100 and 200 μs.

For the incoming flow 500 pairs of images were taken, while for all the models a total of 3000 pairs were acquired for each configuration.

A Pitot-static tube was mounted above of the model location, at a hight of about 40 cm from the floor of the test section (almost the same location as the hot wire measurements) and connected to a Furness manometer to acquire the freestream velocity of the incoming boundary layer. All the measurements were taken for a velocity equal to 20 m/s. For each acquisition, the flow velocity, the ambient pressure and temperature were monitored from the manometer and a weather station respectively, and noted down every 15 minutes (each set of 1000 required 45 minutes to be acquired). The images were than post processed using DaVis software with the same settings described in 3.4.2.

Also in this case some regions of the filed of view were not properly illuminated, and proper cut-offs were applied.

All the data were then exported in Matlab environment. A code developed by Gregoire Fourrié and Eda Doğan at the University of Southampton was used to stitch the frames together where a linear interpolation with linear weighting along the horizontal direction is applied to the overlapping regions. Finally, the coordinates of the whole field were linearly interpolated across

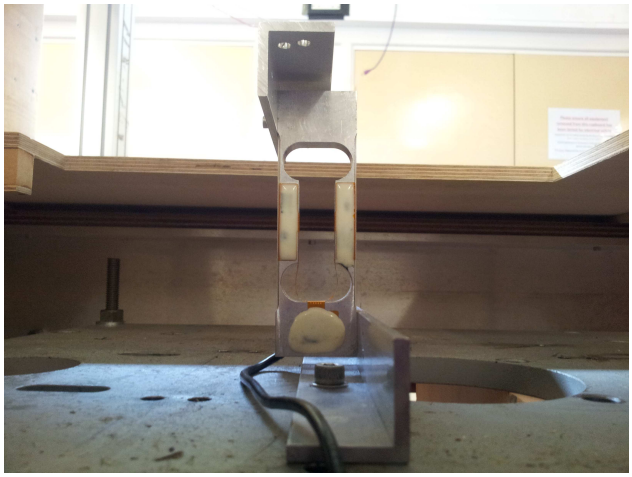

Figure 3.27: Picture of the load cell.

the whole region, as well as the velocity field, in order to have the same coordinate system and spacing for the entire plot.

3.6 Drag measurements methodology

3.6.1 Drag measurements setup

The mean drag force experienced by the patches was measured using a single point load cell (Vishay, model 1004, 600 g) positioned underneath them, and aligned with the flow. A picture of the load cell is shown in Figure 3.27. The patches were mounted on a plate, which was then connected to the load cell. The base of the patch was flush-mounted with the wind tunnel floor, leaving a clearance around the edges of about 2 mm. This gap allowed for patch movements required for drag measurements. Since the wind tunnel was a suction-type, care was taken to ensure that the whole system was sealed from the external environment, in order to prevent any airflow through the gaps. This was achieved by enclosing the whole drag-measurement system in a PVC box, sealed at the junction with the tunnel. A Pitot tube was mounted inside the box to monitor that the pressure inside the enclosure and in the test section were the same.

The load cell was connected to a signal amplifier and the signal was acquired at 20,000 Hz via a data acquisition board (NI USB-6212 BNC from National Instruments) driven by a Matlab code.

Before every experiment, a thorough calibration of the load cell was performed by loading the system with known calibration weights ranging from 10g to 200g using a pulley system connected to the model. A sketch of the load cell setup and the calibration system is shown in Figure 3.28(a). The calibration curve obtained from all the calibration-experiments is shown in Figure 3.28(b). The deviations from the fitting provide an indication of the measurements accuracy.

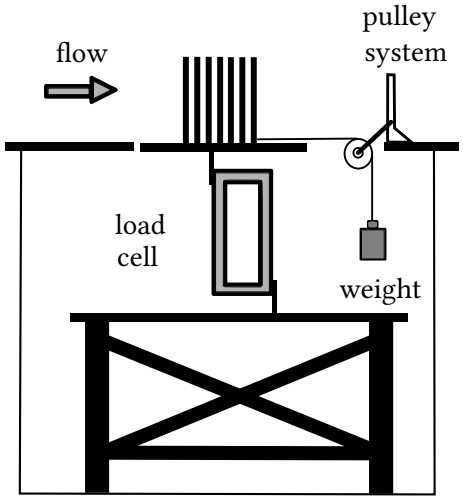

(a) Sketch of the load cell mounting setup and calibration system.

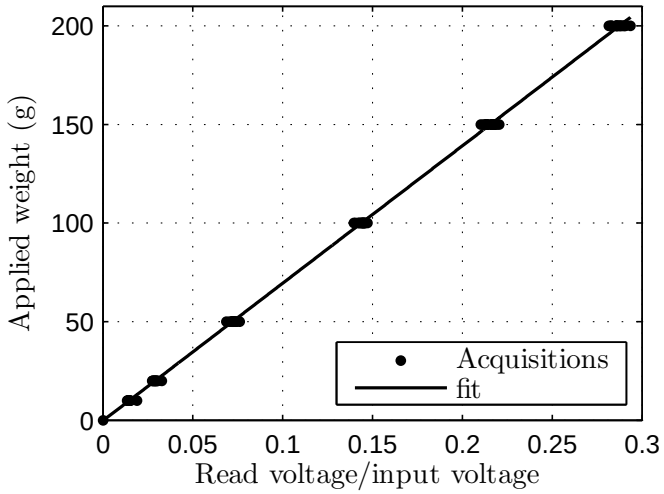

(b) Load cell calibration curve.

Figure 3.28: Load cell setup and calibration.

3.6.2 Drag measurements

Drag measurements were carried out in order to see how the drag of the patch is influenced by the density of the obstacles within it and by the ratio H/δ, where H is the height of the obstacles and δ is the oundary layer thickness. All the densities were tested with three different obstacles' heights (namely 100 mm, 75 mm and 50 mm, which correspond to $AR = 1, 0.75$ and 0.5, respectively). All the patches were also immersed in two different impinging boundary layers, one described in 3.2.1, and the second one obtained with the same roughness configuration without the spires.

For each patch, drag measurements were obtained at four different free-stream velocities (10, 15, 20, and 25 m/s) for three minutes at 20,000 Hz and each test was repeated three times to

ensure repeatability. The drag coefficient was then calculated as:

$$C_D = \frac{F_D}{1/2\rho U_\infty^2 DH}, \tag{3.5}$$

where F_D is the force measured with the load cell. The uncertainty on the drag-coefficient due to experimental errors associated with all the independent variables in equation 3.5 was evaluated using the standard error propagation theory as,

$$\frac{\epsilon_{C_D}}{C_D} = \sqrt{\left(\frac{\epsilon_{F_D}}{F_D}\right)^2 + \left(2\frac{\epsilon_{U_\infty}}{U_\infty}\right)^2}, \tag{3.6}$$

where ϵ_A represents the error on the generic quantity A. The uncertainty on F_D is given by the combination of rms error on the calibration, equal to ± 1.35 g, and considering the presence of an offset for each measurement due to electric interference of -2.51 ± 0.54 g. The uncertainty on U_∞ is given by the rms of the differences between the velocity on each run and the average velocity of the repetitions. The uncertainties on ρ, D and H (±0.25 mm for 100 mm) were neglected because they were much smaller than those of the variables included in equation 3.6. The total error on the drag coefficient was evaluated as

$$\epsilon_{C_{DTOT}} = \epsilon_{C_D} + \epsilon_{C_D rms}, \tag{3.7}$$

where $\epsilon_{C_D rms}$ accounts for the repetition error due to other unknown sources which are accounted for by repeating the measurements multiple times.

3.7 Wake hot wire velocity measurements methodology

3.7.1 Hot-wire setup for wakes characterisation

This set of measurements was carried out together with the drag measurements, in order to investigate the spectra of velocity fluctuations in the wakes of the patches. A single wire probe was used, with a resistance of 4.25Ω. The probe was mounted on the same traverse system used for the flow conditioning measurements and connected to a Dantec StreamLine Research CTA System. The output was connected to a data acquisition board (NI USB-6212 BNC from National Instruments) and the data was acquired using a Matlab code. The temperature of the test section was also acquired with the same board, and the ambient pressure was recorded manually, by mean of a weather station. For this setup, all the electrical equipment was connected to an UPS (Uninterrupted Power Supply), in order to reduce electrical noise.

The OHR was set equal to 1.8, while the sampling frequency was set again on 20 kHz. Gain and offset were set equal to 16 and -2.

The calibration was performed twice a day for 15 velocities ranging from 1.5 m/s to 30.8 m/s against a Pitot-static tube at a heigh of 400 mm from the wind tunnel floor. A linear interpolation of the two calibrations was carried out to take into account the temperature at the time of the measurements.

3.7.2 Hot-wire measurements for wakes characterisation

The probe was located behind the models at a distance of 480 mm downstream from the centre of the patch along x (4.8 D) due to physical constraints of the wind tunnel walls. From previous horizontal PIV measurements it was clear that at this distance, a peak in the streamline velocity fluctuations, $\sqrt{\overline{u^2}}$, was upstream of the probe for each patch: this peak coincides with the end of the recirculation zone and the start of vortex formation, when present (Castro, 1971). If any coherent vortex structures are shed from the model, they are detectable at this x location.

The lateral position was set to -60 mm along z (0.6 D) to ensure to be sufficiently out of the recirculation region (to avoid negative velocities). Similar location where chosen by Sakamoto and Arie (1983) and from previous results from the horizontal PIV data it was shown that at this z corresponds a peak in the vorticity ω_z shed from the sides of the patches.

The vertical position was set to half of the height of the tested patch. For each patch, hot-wire measurements were obtained at four different free-stream velocities (10, 15, 20, and 25 m/s) for three minutes at 20,000 Hz and each test was repeated three times to ensure repeatability.

The power spectral density was calculated using the Matlab function *pwelch* which estimates the PSD using Welch's method. According to this procedure, the signal is split up into overlapping segments which are then windowed in the time domain (Matlab uses by default a Hamming window). The periodogram of each segment is then calculated by a discrete Fourier transform (DFT) and these estimates are finally averaged to obtain the PSD. For this estimation of the PSD, each signal contained 3,600,000 samples (3 minutes at 20,000 Hz), the input for the *pwelch* function were chosen to be 20,000 for the length of the windows with 50% of overlap and 20,000 points to calculate the DFT. Before applying the *pwelch* computation, the data was treated with a *detrend* function, which allows to subtract the mean value from the data and calculate the spectra only for the fluctuations.

The obtained results for each repetition (i.e. velocity, statistics, spectra) were averaged between the three repetitions to obtain averaged values for each case. The resulting spectra for each case at 4 different velocities are reported in Appendix B. From these plots it is evident that the non dimensionalised premultiplied spectra vs fD/U_∞ is not dependent on the freestream velocity, and for this reason, only the data at 20 m/s will be considered, since they are consistent with PIV measurements. Similar considerations can be drawn for the spectra of the free flow (i.e. measurements without any patch) and the results are shown in Appendix B as well.

A smoothing procedure was carried out for the freestream flow spectra and for the averaged spectra of each case, in order to get a cleaner representation of the results. The procedure consists in applying a moving average on the data with a logarithmic spacing along the frequencies. Finally, the spectra of the free flow was subtracted by the spectra of the patches, in order to isolate the frequency content of the wakes, with the following equation:

$$\frac{PSDf}{U_{\infty}^2} = \frac{PSD_{patch}f}{U_{\infty,patch}^2} - \frac{PSD_{flow}f}{U_{\infty,flow}^2}. \tag{3.8}$$

Chapter 4

Characterisation of drag and wake properties

4.1 Introduction

This chapter presents a first description of the wake forming downstream of porous patches of obstacles with different densities, together with the wake of a solid cylinder with the same external dimension of the patch. Drag measurements are also presented and discussed, together with the mean PIV measurements along the vertical and horizontal plane, to characterise the main phenomena occurring in the wake of a porous obstacle.

4.2 Drag measurements

Figure 4.1 shows the variation of the drag coefficient, C_D as defined in equation 3.5, with Reynolds number, $Re_D = U_\infty D/\nu$, for all the patches. It can clearly be seen that the influence of Re on C_D is negligible, presumably because of the high level of turbulence characterising the incoming turbulent boundary layer. Therefore, in all subsequent results, we only present the data pertaining to U_∞ = 20 m/s ($Re_D \simeq 1.1 \times 10^5$) since the PIV measurements were carried out at this free-stream velocity.

Figure 4.2 shows the variation of C_D with density (see Table 4.1 for correspondence between ϕ and patch name and for the actual values). It can be seen that C_D increases with increasing ϕ and seems to converge to a value of about 0.37, that, however, does not correspond to the drag coefficient of the solid case, which is much lower. Surprisingly, the drag coefficient of the solid patch is rather comparable to the C_{20} case. Moreover, C_D does not exhibit any constant region as reported by Nicolle and Eames (2011) for the case of 2-D patches.

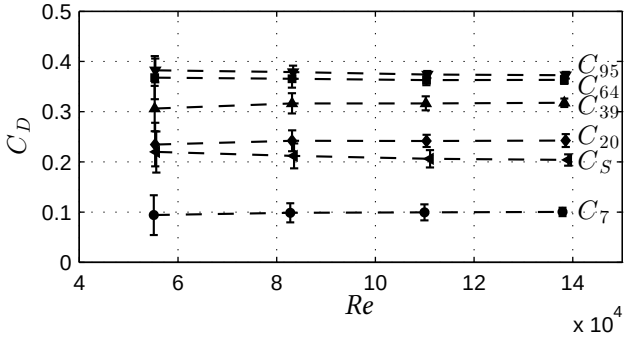

Figure 4.1: Drag coefficient variation with Reynolds number ($Re = U_\infty D/\nu$) for all the patches: • C_7, ◆ C_{20}, ▲ C_{39}, ■ C_{64}, ▼ C_{95}, ◀ C_S, as reported in Table 4.1.

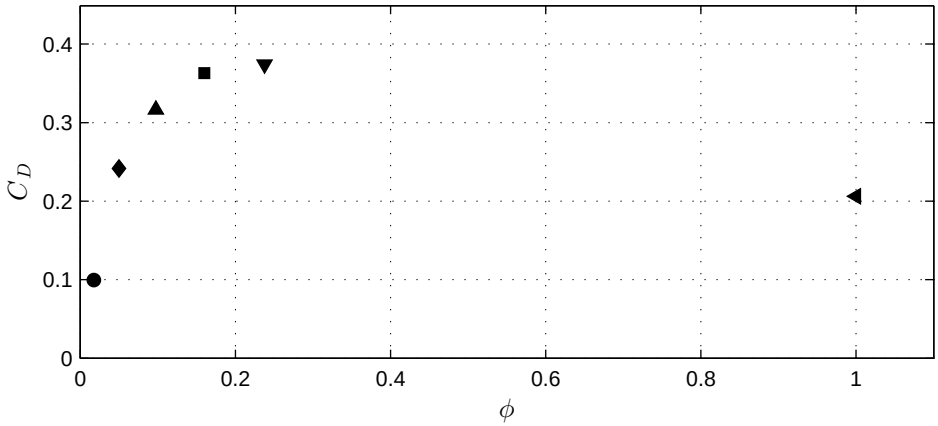

Figure 4.2: Drag coefficient variation with patches density. non-dimensionalised with U_∞ versus patches density.

It should be noted that Figure 4.2 shows a gap of data for densities within the range $0.24 < \phi < 1$ because, in the experiments presented herein, it was physically impossible to construct patches with $\phi > 0.24$ while maintaining a constant d/D ratio. Therefore, we do not intend to infer any conclusions on the behaviour of C_D vs density within this range as they would just be speculative.

The trend of C_D vs ϕ (for $0.018 < \phi < 0.24$) resemble those reported by Nicolle and Eames (2011) and Chang and Constantinescu (2015) at similar densities. However, the values of the drag coefficients in the present case are much lower. This is not surprising because: (a) it is well known that the drag of a finite-size obstacle is much lower than the drag of a 2-D obstacle with the same cross section (see for example Fox and West, 1993); (b) more importantly, the non-dimensionalising velocity chosen to calculate the C_D is U_∞, which in the present paper corresponds to the free-stream velocity of the boundary layer which is not fully representative of the actual flow impinging on the patches. If C_D is recalculated as

$$C_{Dbulk} = \frac{F_D}{1/2\rho U_{bulk}^2 DH}, \tag{4.1}$$

	C_7	C_{20}	C_{39}	C_{64}	C_{95}	C_S
N_c	7	20	39	64	95	1
ϕ	0.0175	0.0500	0.0975	0.1600	0.2375	1
Circles	1	2	3	4	5	NA
Symbol	●	◆	▲	■	▼	◀
C_D	0.10	0.24	0.32	0.36	0.37	0.21
C_{Dbulk}	0.29	0.69	0.91	1.04	1.08	0.59
L_r	3.7	> 8	> 8	7.7	7.3	3.1
U_∞ (m/s)	20.07	20.20	20.16	20.20	20.13	20.26
U_{bTE}/U_∞	–	0.46	0.33	0.19	0.16	–
V_{bTE}/U_∞	–	0.0074	0.0075	0.018	0.028	–
Recirculation bubble	NO	NO	NO	YES	YES	–
x_{rb}/D	–	–	–	2.0	1.5	–
$\omega_{zMAX}D/U_\infty$	–	-2.15	-2.79	-3.08	-3.24	-6.54
$y_{\omega_{zMAX}}$	–	0.97	1.04	1.08	1.15	1.01
$\omega_{yMAX}D/U_\infty$	–	1.07	1.62	2.32	2.74	3.38

Table 4.1: Patch characteristics: N_c, number of cylinders; ϕ density (d^2N_c/D^2, D diameter of the patch, d diameter of the individual cylinder). Measurements results for each patch: C_D, drag coefficient defined by equation 3.5 for U_∞ of 20 m/s; C_{Dbulk}, drag coefficient defined by equation 4.1; L_r, length of the recovery region along x non dimensionalised with D; U_∞, freestream velocity; U_{bTE}, mean streamwise bleeding velocity at the trailing edge ($x/D = 0.52$); V_{bTE}, mean vertical bleeding velocity at the trailing edge ($x/D = 0.52$); x_{rb}, streamwise coordinate of the centre of the recirculation bubble; $\omega_{zMAX}D/U_\infty$, minimum value of the top shear layer vorticity at $x/D = 0.75$ and its vertical coordinate $y_{\omega_{zMAX}}$; $\omega_{yMAX}D/U_\infty$, maximum value of the lateral shear layer vorticity at $x/D = 0.75$.

where U_{bulk} is the bulk velocity impinging on the patch ($U_{bulk} = 1/H \int_0^H U dy = 0.59U_\infty$), the values of C_{Dbulk} become much closer to those reported in Nicolle and Eames (2011) and Chang and Constantinescu (2015) although still significantly lower (Figure 4.3).

Finally, it should be noted that, in general, the C_D of an obstacle impinged by a turbulent flow can increase if turbulence levels are suppressed (Castro and Robins, 1977). Contrary to Nicolle and Eames (2011) and Chang and Constantinescu (2015) the patches investigated herein are impinged by a fully turbulent boundary layer (i.e. not a laminar flow) and hence this could explain the differences observed in C_D values. However, it will be shown that this contribution, at least for porous patches, is negligible and the differences in C_D between 2-D and 3-D patches are rather due to bleeding effects along the vertical axis. Bleeding flows and the general properties of the wakes generated by the patches are presented and discussed in the following section.

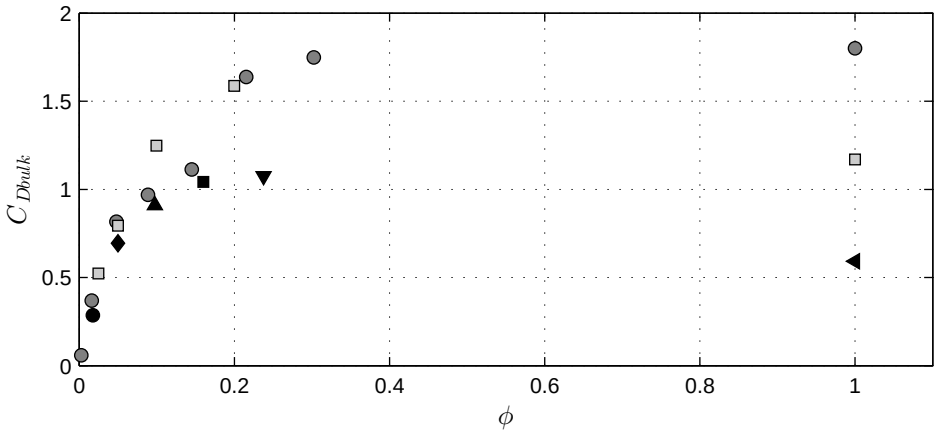

Figure 4.3: Drag coefficient computed using the bulk velocity impinging on the patch, $U_{bulk} = 1/H \int_0^H U dy = 0.59U_\infty$ versus patches density ϕ. Data are taken from Nicolle and Eames (2011) (dark grey dots), Chang and Constantinescu (2015) (light grey squares) and the present study (black symbols).

4.3 Velocity measurements

The differences in wake properties among the patches are now discussed in order to support and explain the drag coefficient behaviour reported in Figure 4.2. The first case to be discussed is the C_7 case ($\phi = 0.018$). Figure 4.4 shows the streamline velocity component non dimensionalised with the boundary layer velocity at the plane of the measurements (i.e. $U/U_{H/2}$) for all the C_7 patches. Unit velocity vectors (i.e., the magnitude of the vectors is always 1) are also shown to indicate the flow direction. In the C_7 cases the wake of the patch is made by individual cylinders wakes, which show no emergent group behaviour, i.e. the generation of wake turbulence at scales comparable to the patch diameter or height. Analogous results were reported for a similar patch-density by e.g. Nicolle and Eames (2011), Chen et al. (2012) and Chang and Constantinescu (2015) for 2-D flows.

The interactions between individual wakes of multiple obstacles, for different orientations and spacings were investigated in detail by Wang et al. (2013) and references therein, therefore the case C_7 is not further discussed in the present Chapter.

From this point on, the focus will be on the patch-densities that display a clear group behaviour. Figure 4.5 shows that for densities higher than C_{20}, the signatures of individual wakes on the mean longitudinal velocity disappears, hence suggesting the emergence of flow phenomena at the scale of the patch diameter. Within this range of patch-densities, the properties of the wakes change significantly with ϕ. The wake recovery length L_r (i.e. the distance downwind of the patch where the longitudinal mean velocities recover 90% of their original magnitude upwind of the patch) decreases with increasing ϕ for patch densities between C_{39} and C_S (Table 4.1). The field of view was not long enough to detect the recovery length for C_{20} and C_{39}, which is therefore larger than 8 patch diameters. However, from a qualitative analysis of Figure 4.5, it seems that the wake downwind of C_{39} recovers at a lower rate than C_{20} hence suggesting

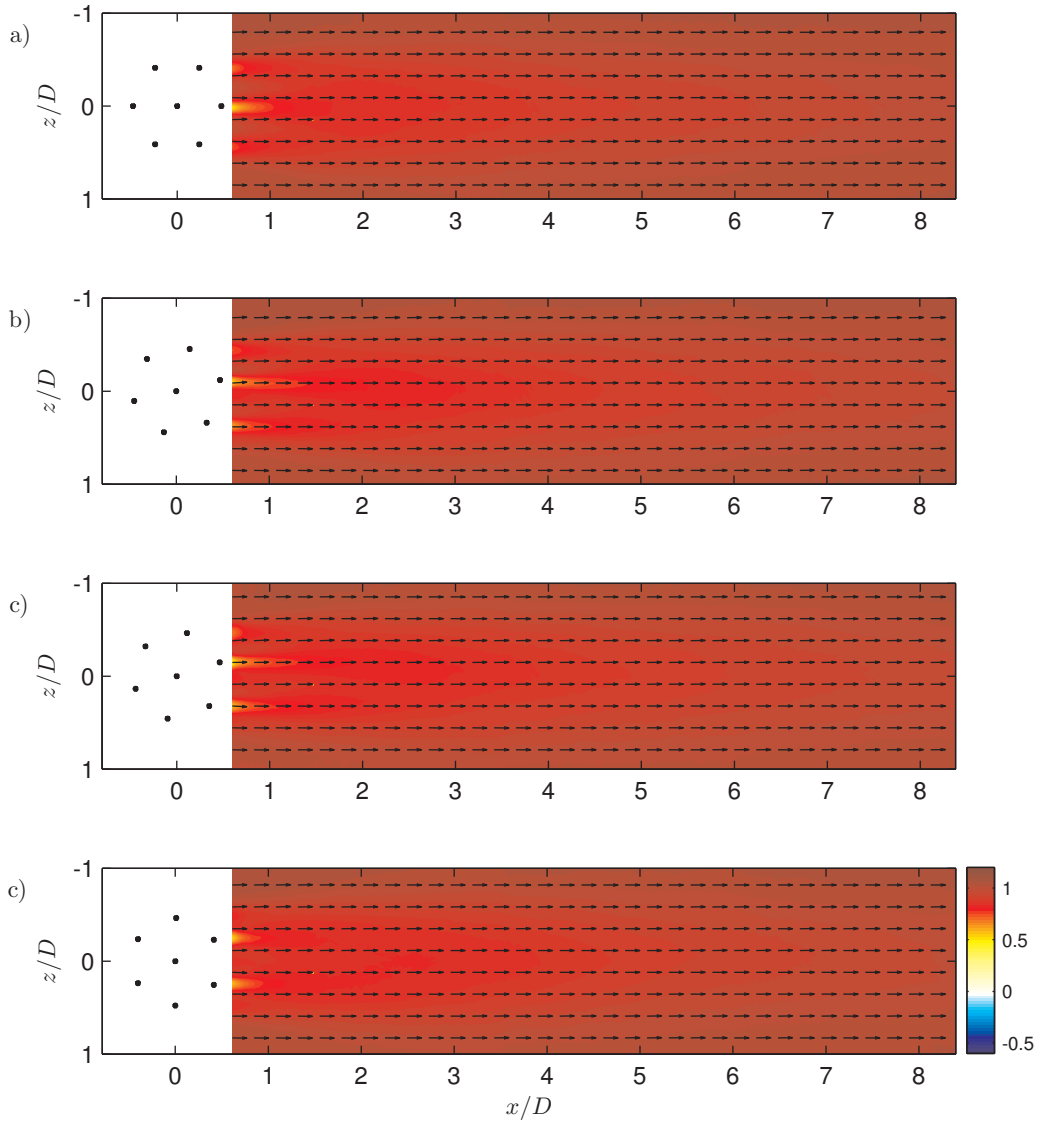

Figure 4.4: Plane view of the vector field and contours of streamline velocity $U/U_{H/2}$, where $U_{H/2}$ is the incoming velocity of the boundary layer at the plane of the measurements (y/D = 0.5). The vector field only indicates the flow direction, but not its intensity (the length of the vectors is not proportional to their intensity). Only one vector every 35 vectors is represented. Solid black line is the contour at where $U/U_{H/2}$ = 0. The cylinders are represented in their actual configuration. a) C_{7_0}, b) $C_{7_{10}}$, c) $C_{7_{20}}$ and d) $C_{7_{30}}$.

that L_r could be non-linearly related to ϕ. The wake recovery length for the solid case is much shorter than all the other cases, presumably because of the enhanced momentum transfer exerted by the shear layers forming around the solid surface of C_S. This aspect will be discussed further after introducing the mean vorticity plots in Figure 4.10. C_S is also characterised by the narrowest wake, which at $x/D = 1$ is bounded between $-0.3 < z/D < 0.3$. For all the other porous cases the lateral extents of the wake are contained within $-0.6 < z/D < 0.6$. The way the wake spreads laterally suggests that the flow separation along the sides of the porous patches takes place further upstream when compared to the solid cylinder. This could be due to the bleeding of fluid along the lateral direction which promotes early separation of the flow along the sides, fixing the separation point at the most external cylinder of the patch. This is consistent with the fact that, for the porous patches, the lateral extension of the wake at $x/D = 1$ is constant, i.e. it is not dependent on ϕ.

Figures 4.5 and 4.6 show that at the trailing edge of the porous patches, the mean longitudinal velocities are always positive and the denser is the patch the weaker is the bleeding, with C_S showing a recirculation bubble attached to its trailing edge. Interestingly, recirculation patterns are also observed for C_{64} and C_{95}, but, with respect to the solid case, these are located further downstream. Furthermore, Figures 4.5 and 4.6 show that the denser is the patch, the closer to the trailing edge the location of its recirculation bubble (the exact position of the recirculation bubble centre with respect to the patch is reported in Table 4.1 as x_{rb}). This makes sense as the shift of the bubble is caused by the trailing edge bleeding, which increases with decreasing ϕ. Similar shifts in the recirculation bubble downwind of porous objects are reported by Castro (1971) for porous plates and Chang and Constantinescu (2015) for 2-D canopy patches.

While a full 3-D characterisation of the wake downwind of the patches is not available, Figure 4.7 provides a combination of longitudinal velocity measurements carried out over the $x - y$ and $x - z$ planes, which, compared to Figures 4.5 and 4.6, gives a broader view of the wakes. Only three cases are shown because these cases contain all the flow phenomena discussed so far. In particular, this Figure gives a better perspective of the relative longitudinal and vertical size of the wakes for different densities. In particular the Figure shows that, with respect to the other two cases, the wake of C_{95} seems to "blown up", especially along the vertical direction. As it will be discussed later, this effect can be associated with vertical bleeding occurring at the free-end and at the trailing edge of porous patches, which increases with increasing ϕ.

Figure 4.7 also shows that for both C_{95} and C_S, the shape of the recirculation pattern is consistent with the so-called "arch-type" vortex forming at the junction between the wall and short-aspect-ratio solid cylinders, as observed in Sakamoto and Arie (1983) who firstly described them, or in Sumner (2013) and references therein. Similar structures were also found by Tanaka and Murata (1999) for long-aspect-ratio solid cylinders and are discussed in Wang and Zhou (2009). As it is pointed out in these last two references, it must be noted that the interpretation based on an arch-type vortex is only relevant to the mean flow and does not necessarily represent the flow structures shedding instantaneously from the patch. Analogously, in the present case, it is worth to point out that, while the recirculation patterns observed in

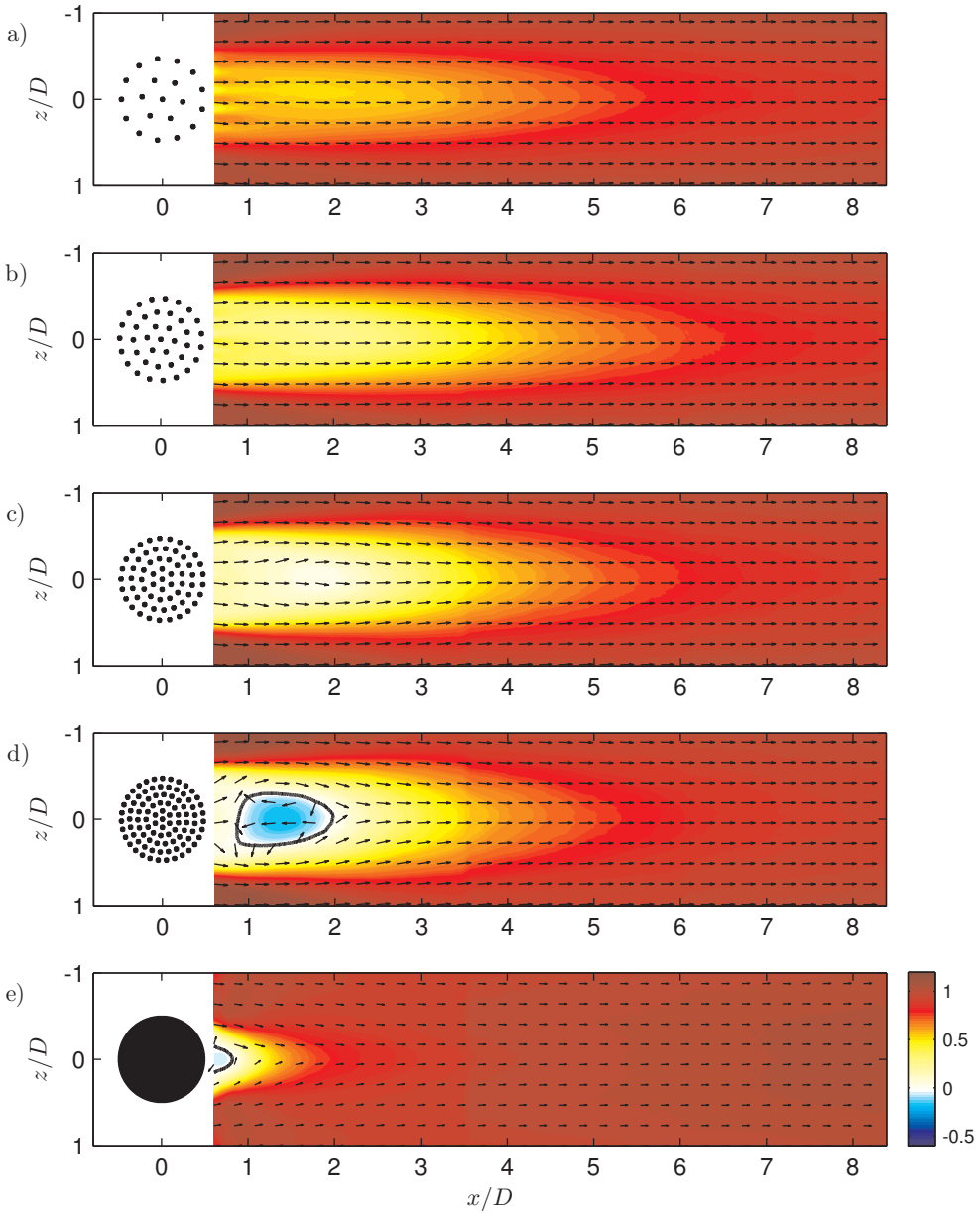

Figure 4.5: Plane view of the vector field and contours of streamline velocity $U/U_{H/2}$, where $U_{H/2}$ is the incoming velocity of the boundary layer at the plane of the measurements (y/D = 0.5). The vector field only indicates the flow direction, but not its intensity (the length of the vectors is not proportional to their intensity). Only one vector every 35 vectors is represented. Solid black line is the contour at where $U/U_{H/2}$ = 0. The cylinders are represented in their actual configuration. a) C_{20}, b) C_{39} c) C_{64}, d) C_{95} and e) C_S.

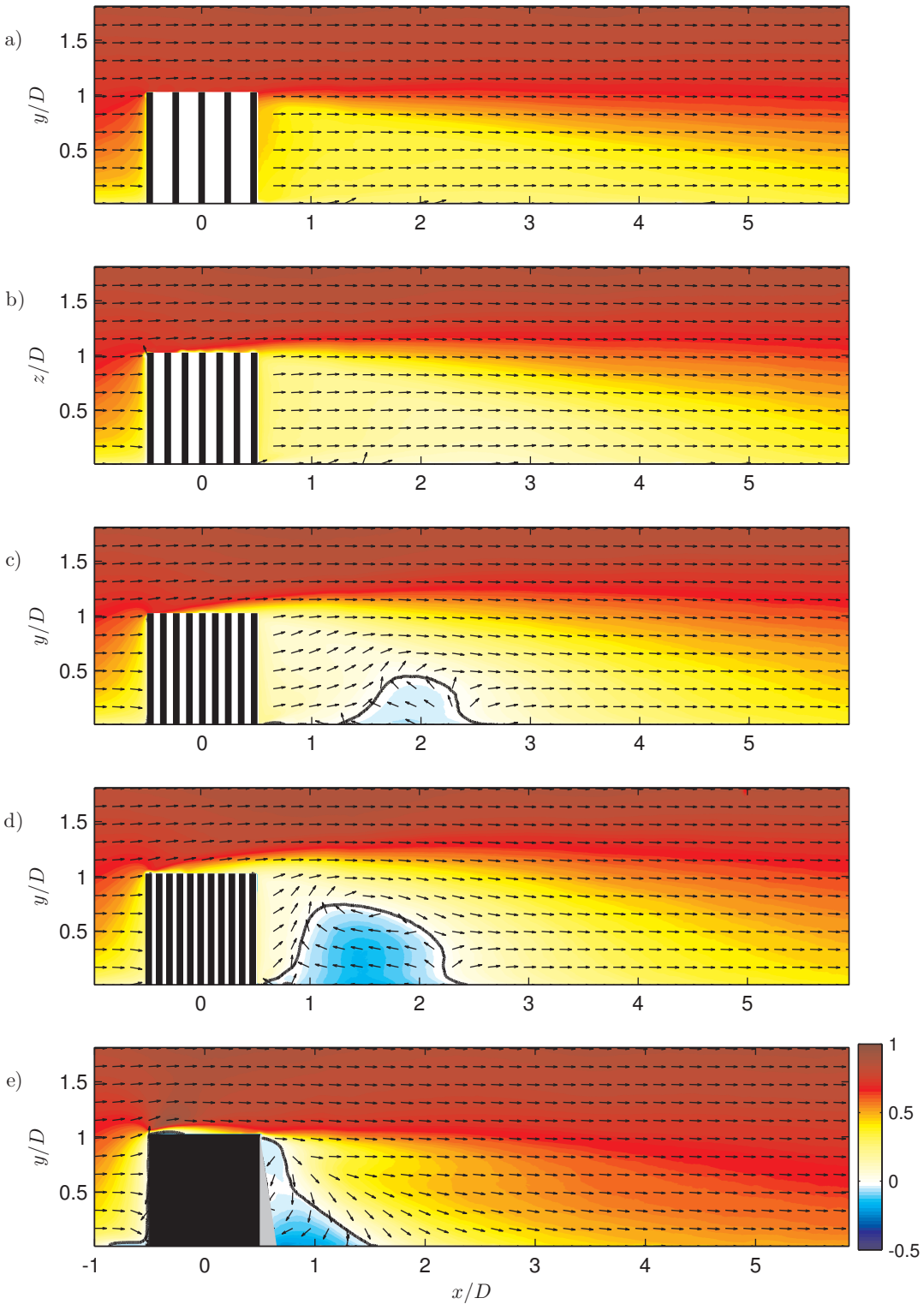

Figure 4.6: U/U_∞ in the vertical plane. The vector field only indicates the flow direction, but not its intensity (the length of the vectors is not proportional to their intensity). Only one vector every 35 vectors is represented. Solid black line is the contour at where $U/U_\infty = 0$. The cylinders are not drawn in their actual configuration, for the exact distribution of the cylinders at this plane, refer to Figure **??**. a) C_{20}, b) C_{39} c) C_{64}, d) C_{95} and e) C_S.

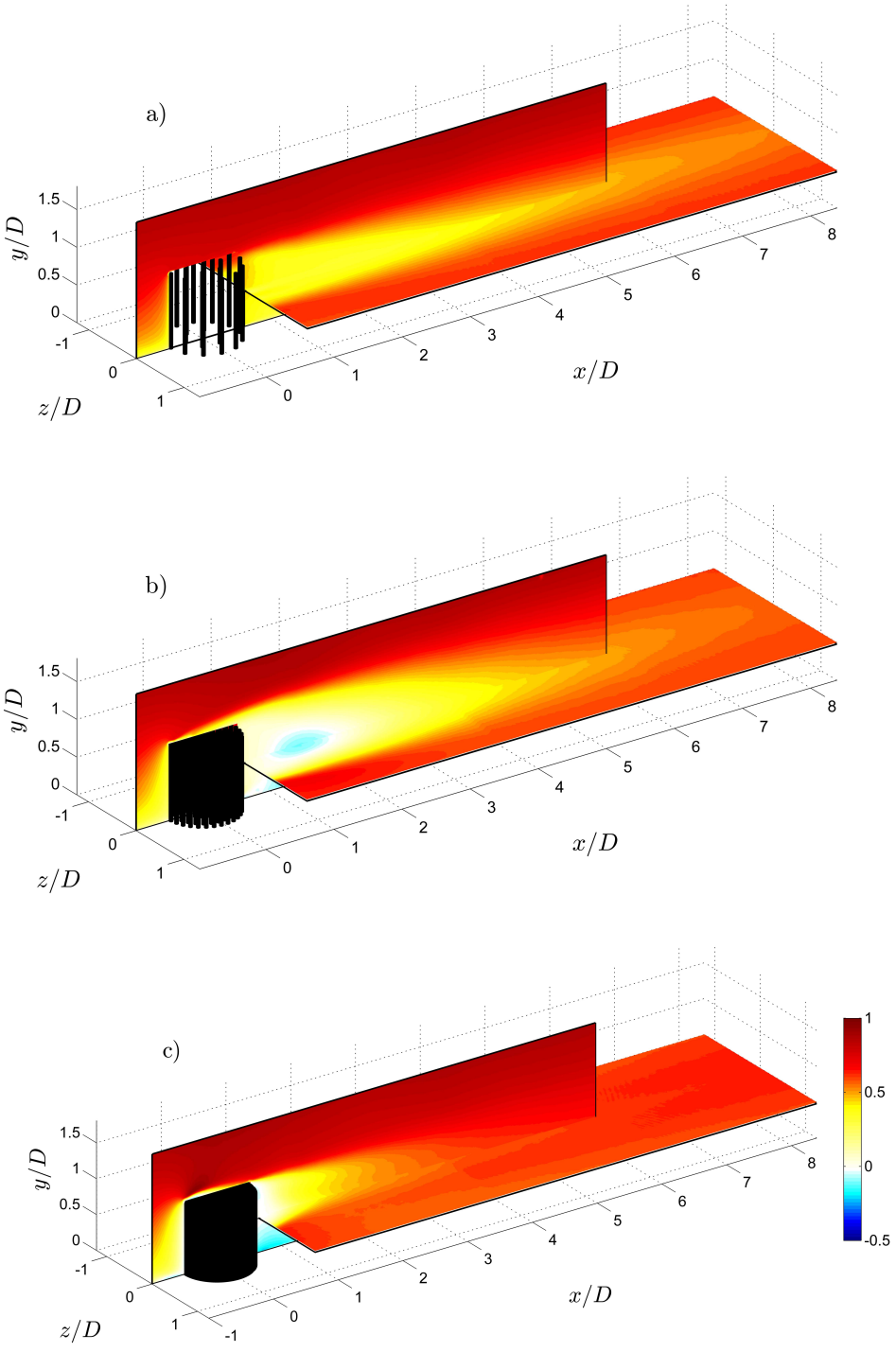

Figure 4.7: U/U_∞ along the plane $x-y$ for $z = 0$ and the plane $x-z$ for $y = D/2$. a) C_{20}, b) C_{95} and c) C_S. The cylinders are represented in their actual configuration.

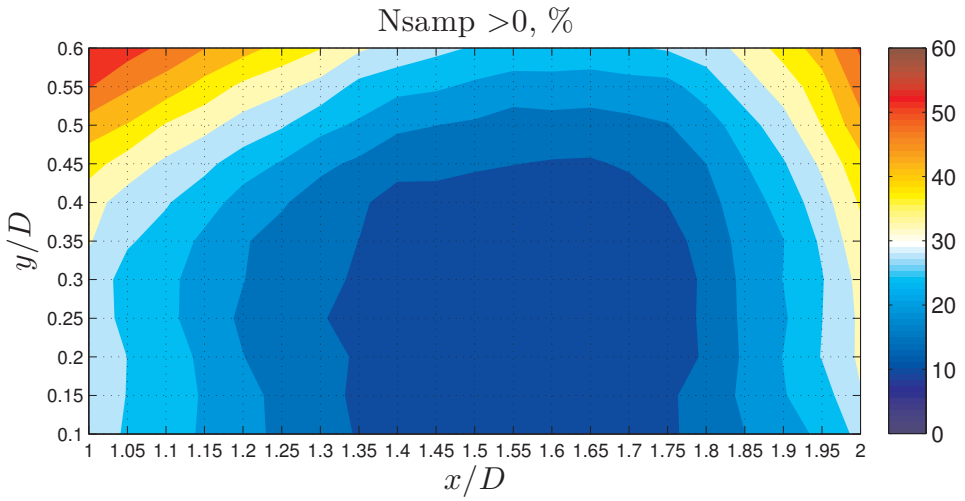

Figure 4.8: Contours of the percentage of positive samples within the recirculation bubble area. The contour steps correspond approximately to an increment of 5% and they have been evaluated for the points corresponding to the grid knots.

the mean flow of the porous patches are a strong signature of the instantaneous flow, they also show a level of intermittency, because recirculating features (i.e. a reverse flow region) were observed to disappear in some PIV snapshots.

Similar intermittent features of the recirculation region are reported by Cassiani et al. (2008), who conducted large eddy simulations to simulate the flow across forest edges and they found that the recirculation region forming downwind of a tall forested canopy is statistical and time intermittent. Similar results were found in the present case, for the C_{95} model. The 3000 statistically independent PIV snapshot were examined for 231 points within the recirculation bubble (equally spaced of 1 d, for $1 < x/D < 2$ and $0.1 < y < 0.6$) to determine the intermittent nature of the recirculation bubble. The number of samples (in terms of percentage of the total samples) that show reverse flow (i.e. $U < 0$) is computed for each point. Figure 4.8 shows this percentage for all the considered vectors. The contour level corresponds approximately to an increment of 5% in the number of positive samples, and it is clearly visible how this percentage increases as the distance from the centre of the bubble decreases. Cassiani et al. (2008) ascribe this intermittence to the superimposition of two different states, the "exit flow model" and the "back facing step model", and the existence of one state or another could occur with a relative frequency, depending of the patch density. It is not possible to study the time dependence of these conditions, since the present set of data is not time resolved, but it looks like this intermittency exists in the present study as well.

More insights on the wake of the patches are revealed by Figure 4.9, which shows the non-dimensional vertical velocity component V/U_∞ measured in the $x-y$ plane at $z = 0$. As in Figures 4.5 and 4.6, unit velocity vectors are also shown to indicate the flow direction. As surmised from Figure 4.6, Figure 4.9 confirms that, for the solid case, the flow separates at the leading edge of the cylinder, reattaches along the top and convects downwards immediately downstream of the model. In C_S the vertical velocity shows the largest spatial variations in

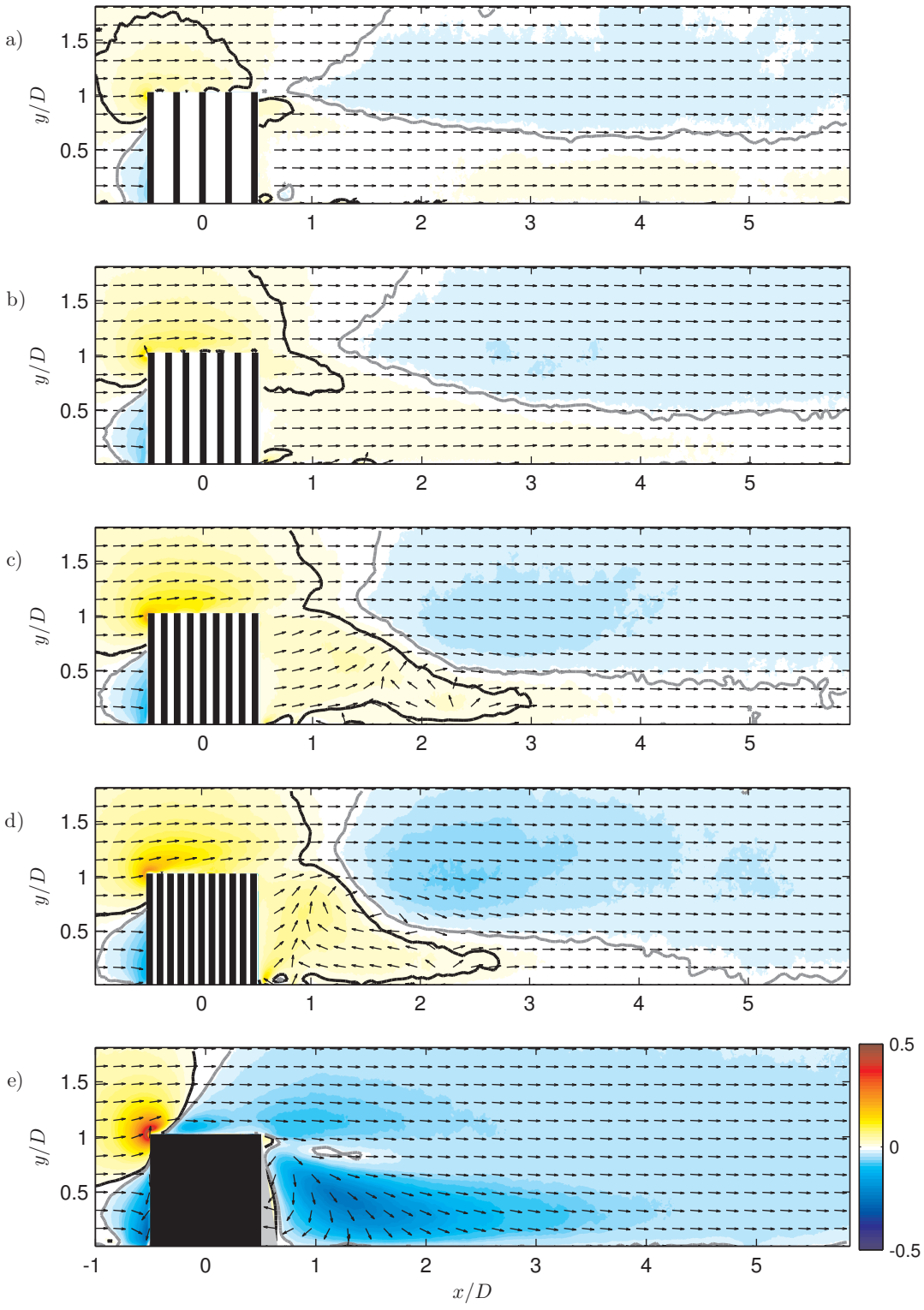

Figure 4.9: V/U_∞ in the vertical plane. The vector field only indicates the flow direction, but not its intensity (the length of the vectors is not proportional to their intensity). Only one vector every 35 vectors is represented. Solid black line is the contour at where $V/U_\infty = 0.01$ and the solid grey line is the contour at where $V/U_\infty = -0.01$. The contour is for a step of 10 data points along x and y. The cylinders are not drawn in their actual configuration, for the exact distribution of the cylinders at this plane, refer to Figure **??**. a) C_{20}, b) C_{39} c) C_{64}, d) C_{95} and e) C_S.

the flow field among all the investigated cases. Furthermore, V/U_∞ has a localized positive peak in proximity of the leading-edge top, but becomes negative immediately downwind and remains so for almost the entire field of view. Figures 4.6 and 4.9 show that for the solid case the longitudinal extension of the recirculating region is not uniform along y because it increases towards the wall. This could be interpreted as an effect of the shear layer at the free end, which contributes to strain the recirculation bubble by entraining momentum from the flow above the cylinder. The bubble enlarges towards the wall where free-end (i.e. top shear layer) effects are less intense.

Compared to the solid case the porous patches behave very differently. The peaks of V/U_∞ at the leading edge are lower in magnitude, presumably because of the permeability of the patches which allows for some fluid to go through their porous matrix rather then being all diverted upwards. For the same reason, the deceleration of the flow at the leading edge of the porous patches is less intense than for the solid case (see Figure 4.6). Consistently with this hypothesis, V/U_∞ at the top of the leading edge increases in magnitude with increasing ϕ (Figure 4.9) and also the mean longitudinal velocity U/U_∞ in front of the patch decreases with increasing ϕ (Figure 4.6). At the free-end of the porous patches, the flow does not separate and the mean vertical velocity V remains positive, indicating that the flow bleeds upward from the interior of the patch (Figure **??**). At an euristic level, this phenomenon can intuitively be ascribed to the pressure gradient generated by the difference in velocity between the faster flow that is immediately over the patch (that will result in lower pressure) and the slower flow within the patch (i.e. at higher pressure).

At the trailing edge of the porous patches both U and V are also positive. U_{bTE} and V_{bTE} are defined as the values of the mean longitudinal and vertical velocity components averaged over $0 < y/D < 1$ at the trailing edge, which are reported in Table 4.1. As observed from Figure 4.5, U_{bTE} decreases with increasing density whereas, analogously to the vertical bleeding, V_{bTE} increases. Therefore, with respect to the solid case, both the vertical and trailing edge bleeding are responsible for shifting upwards and further downwind the region of negative vertical velocity V/U_∞ and, as already discussed, the recirculation bubble that forms in C_{64} and C_{95}.

The vertical and trailing edge bleeding contribute to weaken the free-end effects on the wake development. Consistent with this, the longitudinal extension of the recirculation bubble observed for C_{64} and C_{95} is independent of y, and the region is much less strained than in C_S (Figures 4.6 and 4.7).

The contour plots of the mean vorticity along the spanwise ($\omega_z D/U_\infty$) and wall-normal ($\omega_y D/U_\infty$) directions are given in Figure 4.10. The chosen colour scale allows contours to saturate in some regions (i.e. at the top part of both C_S and C_{95}) in order to ensure that variations of vorticity at lower levels are visible. Furthermore, the contours of $\omega_z D/U_\infty = \pm 0.3$ and $\omega_y D/U_\infty = \pm 0.3$b are drawn to distinguish between positive and negative vorticity regions. The value of 0.3 was chosen to be as a reasonable threshold limit for vorticity to identify the boundaries of shear layers, which influence strongly wake entrainment and development. Figure 4.10 shows that

$\omega_z D/U_\infty$ over the top of the patches increases in intensity with increasing ϕ, especially in the top leading and trailing edges. In particular, the minimum $\omega_z D/U_\infty$ (i.e. the maximum in absolute value) at $x/D = 0.75$ at the top of the trailing edge, which presumably has the strongest influence on the wake development downstream of the patch, increases in magnitude and elevation from the bed (i.e. y/D) with increasing density (see Table 4.1). This indicates that the higher is the density of the patch, the more intense is the shear layer and the more this is shifted upwards. This upward shift is due to the vertical bleeding, which, as observed in Figure 4.9, also increases with increasing ϕ. The solid case is characterised by the strongest shear layers over both the top of the leading and trailing edge, although for the latter, due to the absence of vertical bleeding, the upwards shift cannot occur.

The contour plots of the mean vorticity measured along the horizontal plane show that for the C_{20} model, the wakes shed by individual cylinders are evident and detectable (see top right corner of Figure 4.10). However, two larger shear layers develop at the flanks of the patch, confirming also the presence of group behaviour.

At $x/D = 0.52$, which corresponds to the most upwind location for our fields of view, these patch-scale shear layers retain the same width regardless of patch density (Figure 4.10, right column). This is consistent with what observed from Figure 4.5 and the fact that the width of the wake is weakly influenced by ϕ because, as already discussed, the separation point along the flanks of the porous patches is fixed by the lateral bleeding effects. Further downwind, for all the patch densities, the inner contour of the lateral shear layers show essentially two regions: one where they converge towards the centre of the wake and another where they either diverge or grow uniformly. The first region shrinks in length with increasing ϕ. This is consistent with the fact that, with increasing density, the trailing edge bleeding diminishes and the intensity of both the lateral and top shear layer increases, hence leading to stronger wake entrainment. Ultimately, for the solid case, the first region disappears and the two shear layers collapse and then disappear at a very short distance from the cylinder.

Interestingly, the shear layers developing at the flanks and over the top of the patches (Figure 4.10 right and left panel, respectively) show a different behaviour with respect to ϕ. While they both increase in intensity with increasing density, the top shear layers show much larger variations with respect to ϕ, particularly between C_{95} and C_S. In particular, the maximum $\omega_y D/U_\infty$ at $x/D = 0.75$ at the flanks of the models, (see Table 4.1) increases by about 23% from C_{95} to C_S while $\omega_z D/U_\infty$ almost doubles at the same streamwise location for the same models. In other words the difference in the intensity of vorticity between C_{95} and C_S is larger for the shear layers at the top than at the flanks. This can be explained by the following argument: due to their packing and geometry, vertical cylinders within each patch form a porous medium characterised by an anisotropic permeability. In particular, the permeability along the vertical direction is much higher than the permeability along all directions lying on the $x - z$ plane. As shown by Manes et al. (2011a,b, 2012), enhanced permeability favours momentum transport at the interface between a turbulent flow and a permeable canopy, which weakens the velocity gradient at the canopy top and ultimately the intensity of the associated

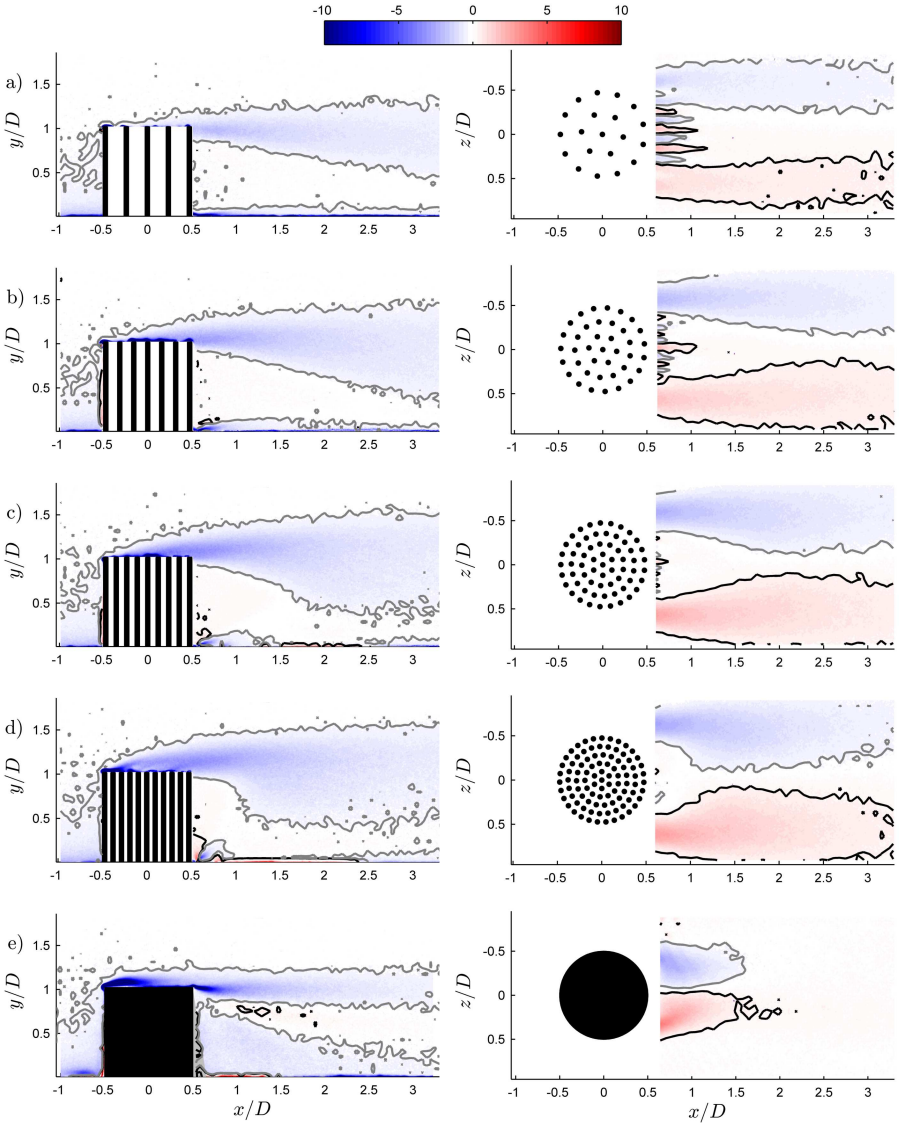

Figure 4.10: Mean vorticity contours along the two PIV planes: $\omega_z D/U_\infty$ (left) and $\omega_y D/U_\infty$ (right) for all the models a) C_{20}, b) C_{39} c) C_{64}, d) C_{95} and e) C_S. Solid black line is the contour at where $\omega D/U_\infty = 0.3$ and solid grey line is the contour at where $\omega_z D/U_\infty = -0.3$. These contours are for a step of 10 data points along x and y. The plot of ω_z is saturated at the top for some cases, but a different colour scale would not allow to see the contours in the other cases. For the plots in the vertical plane the cylinders are not drawn in their actual configuration, which is represented only for the horizontal plane.

shear layer. When switching from C_S to C_{95}, the permeability for the vertical component over the patch top increases much more than the permeability associated with lateral flow movements at the flanks. This explains why the differences in shear layer intensity between C_{95} and C_S are larger at the top than at the flanks of the patches.

4.4 Discussion

4.4.1 Bleeding effects in 3-D patches

From a momentum balance point of view, the drag coefficient of an obstacle is mainly influenced by the spread of its wake and the intensity of the velocity deficit in the wake itself. For porous patches, there are three main flow phenomena which affect the wake compared to a solid body: (i) the lateral bleeding, (ii) the vertical bleeding and (iii) the trailing edge bleeding.

The lateral bleeding prevents the reattachment of the flow along the sides of the patch and fixes the separation point at the most external cylinder. The effect of the vertical bleeding (always upwards for porous patches, as observed in Figure 4.6) is twofold: (i) it pushes upwards the shear layer forming at the patch-top hence enlarging the vertical size of the wake; and (ii) it weakens wake entrainment. This last effect is due to the positive vertical velocity generated immediately downwind of the trailing edge (i.e. V_{bTE}) which prevents the lower boundary of top shear layer to develop downwards and ultimately weakens the entrainment of fluid in the wake.

It can be concluded that both lateral and vertical edge bleeding contribute to either enlarge the size of the wake along z and y or to prevent wake entrainment. Both effects contribute to increase flow resistance, meaning that an increase in bleeding contribute to an increase of the patch drag coefficient C_D.

Conversely, the trailing edge bleeding has the opposite effect. In fact U_{bTE} contributes to diminish the velocity deficit in the wake and hence to lower C_D. Furthermore the trailing edge bleeding causes the recirculation region (if any) to move downstream, and decreases the intensity of the shear layers forming at the sides, which also contribute to lower C_D.

4.4.2 Interlinks between bleeding, patch-density and C_D

Bleeding effects help to explain the behaviour of C_D versus ϕ as depicted by Figure 4.2. The relation between the patch density ϕ and the intensity of the trailing edge bleeding U_{bTE} can be observed in Table 4.1; an increase in ϕ corresponds to a reduction of the bleeding at the trailing edge, which in turn corresponds to an increase in the velocity deficit and hence in C_D, consistently with Figure 4.2.

An increase in ϕ also results in an increase of bleeding along the vertical direction (Figure 4.6, Table 4.1) which, as discussed, contributes to increase C_D and this is also consistent with Figure 4.2.

The lateral extension of the wake does not seem to change much with ϕ (Figure 4.5) and therefore we conclude that the observed increase of C_D with increasing ϕ must be predominantly due to the increasing of vertical bleeding and the decrease of trailing edge bleeding with ϕ.

This last comment should not be misinterpreted. While lateral bleeding seems to have the only effect of fixing the lateral separation point around the patches and hence to have a minor role in explaining the dependence of C_D on ϕ, this does not mean that it does not have a role in dictating the absolute values of C_D for porous patches. This will be discussed more in detail in section 4.4.4.

4.4.3 2D vs 3D patches

Figure 4.3 shows that the C_{Dbulk} reported in the present paper for 3-D patches are lower than those reported in the literature for 2-D patches, and the difference increases for increasing densities. Presumably, this difference must be associated with top shear layer effects (i.e. the bleeding along y) and, perhaps, incoming turbulence, which was absent in the 2-D cases investigated in the literature. In fact, incoming turbulence can delay separation around bluff bodies and hence contribute to explain the observed discrepancies in C_D. However, in the case of a porous patch, this is unlikely to happen because the lateral bleeding fixes the separation point at the most external cylinder for all the patches, as described earlier. Even though the separation point around the most external cylinder may vary its location, such variations occur at very small scales (i.e. at the scale of d) and hence they cannot affect the overall lateral dimension of the wake at the patch-scale and ultimately its drag coefficient.

The top shear layer effects are dramatically evident in the case of a solid cylinder, where the drop in C_{Dbulk} is about 67% compared to Nicolle and Eames (2011) and 50% compared to Chang and Constantinescu (2015) (Figure 4.3). It has to be noted that, for the solid case, the incoming turbulence concurs to enlarge this difference by promoting entrainment on the top of the cylinder.

The discrepancy in C_{Dbulk} between 2-D and 3-D porous patches is much less intense compared to their solid counterpart and decreases with decreasing ϕ (up to 34% for the densest patch, less than 15% for the other cases). This is due to the fact that free-end (i.e. 3-dimensional) effects in the form of the top-shear layer intensity (i.e. $\omega_{zMAX}D/U_\infty$) and the vertical bleeding (i.e. V_{bTE}) decrease with decreasing ϕ (see Table 4.1).

4.4.4 Solid vs dense patches

So far the drag coefficient for porous patches and their dependence on the density ϕ have been predominantly discussed. However, the most striking and counter-intuitive result of the present Chapter emerges from the comparison between the drag coefficients of the porous and the solid cases. In particular, Figures 4.2 and 4.3 show that the drag coefficient of a solid cylinder is much lower than the C_D of a patch having the largest investigated density. Now that the mechanisms linking drag with bleeding have been clarified, this result can be easily explained. For the solid cylinder, the intense shear layers forming around its surface and the

absence of lateral and vertical bleeding promote strong wake entrainment, which contributes to narrow significantly the wake size along y and z and ultimately to lower the drag coefficient C_D. Clearly, the zero-bleeding at the trailing edge of the solid surface is not able to counteract all these effects and hence the C_D of the solid cylinder results much lower than the C_D of C_{95} where vertical and lateral bleeding effects are instead very strong. The end result is that the C_D of the solid cylinder is actually comparable to the case C_{20}, which was an unexpected result.

In order to see which of the bleeding processes is most responsible for the differences in drag between the solid and the dense patch, one more drag measurement was carried out. This was performed by gluing a circular wooden plate on top of the C_{95} model. This experiment was designed to weaken the effects of the vertical bleeding at the patch-top (model named C_{95T}) and to increase the intensity of the top shear layer. This experiment showed that the drag coefficient of the patch with a lid on top is close to the drag coefficient of the C_{95} model (namely C_D =0.371 for C_{95T}, vs C_D =0.374 for C_{95}). Hence this last experiment indicates that while the dependence of C_D on ϕ is strongly linked to top shear layer effects, the differences between the C_{95} and C_S seems to be more dictated by lateral bleeding effects. More in general, this experiment also suggests that, while differences in C_D for different ϕ are dictated mainly by vertical and trailing edge bleeding, lateral bleeding still plays an important role in drag generation, although this is weakly dependent on ϕ.

As a side note the results by Chang and Constantinescu (2015), who also observed a drop in C_D between a dense (where dense means with a density similar to our C_{95} case) and a solid 2-D patch are further discussed. Chang and Constantinescu (2015) observed that the pressure distribution around a solid and a dense 2-D patch is almost the same and hence they argued that this must lead to the build up of comparable pressure drag. However, with respect to the solid case, they also argued that a porous patch experiences some extra-drag due to the resistance offered to the flow by internal cylinders and this explains the drop in drag coefficient observed for solid patches. It has to be pointed out that, if the explanation given by Chang and Constantinescu (2015) holds, the same drop in C_D between the solid and the dense case should have also been detected by Nicolle and Eames (2011), but this is not the case. Therefore, this mechanism cannot explain the differences in drag between the solid and the dense porous patch. As already discussed, such differences must be rather associated with the more intense shear layers (see Figure 4.10 and Table 4.1) developing around solid patches, which promote wake entrainment and hence drag reduction. Such an entrainment is prevented in porous dense patches because of bleeding along directions perpendicular to the mean flow. The last question that remains to be answered is: why the drop in C_D for the solid cylinder was not reported also by Nicolle and Eames (2011)? It can be argued that the low Reynolds number of the simulations that these authors carried out allowed solid cylinders to be associated with higher values of C_D due to the earlier separation of the flow along the sides of the cylinders, which laterally enlarges the wake and increases the drag coefficient to a value which is comparable to the one of the densest patch.

4.5 H/δ influence on C_D

Drag measurements were taken for six different H/δ ratios, as described in Chapter 3. These ratios were obtained by using patches with the same D and three different heights combined with two different incoming boundary layers with two different δ. The values of the tested H and δ and the corresponding H/δ, $AR = H/D$ and D/δ are reported in table 4.2. The results presented in the previous sections of this Chapter correspond to $H/\delta = 0.28$.

H (mm)	δ (mm)	H/δ	$AR = H/D$	D/δ
100	154	0.65	1	0.65
75	154	0.48	0.75	0.65
50	154	0.32	0.5	0.65
100	358	0.28	1	0.28
75	358	0.21	0.75	0.28
50	358	0.14	0.5	0.28

Table 4.2: Tested H and δ and resulting H/δ, $AR = H/D$ and D/δ.

Figure 4.11 shows the obtained drag coefficient C_D for all the patches at the different H/δ. It can be seen how the trend of C_D against ϕ does not change with H/δ, but the general effect is that C_D reduces for increasing H/δ. It is evident already from this Figure that D/δ plays a role in the decreasing of C_D, since the drag coefficient for $H/\delta = 0.28$ is higher than that corresponding to $H/\delta = 0.32$.

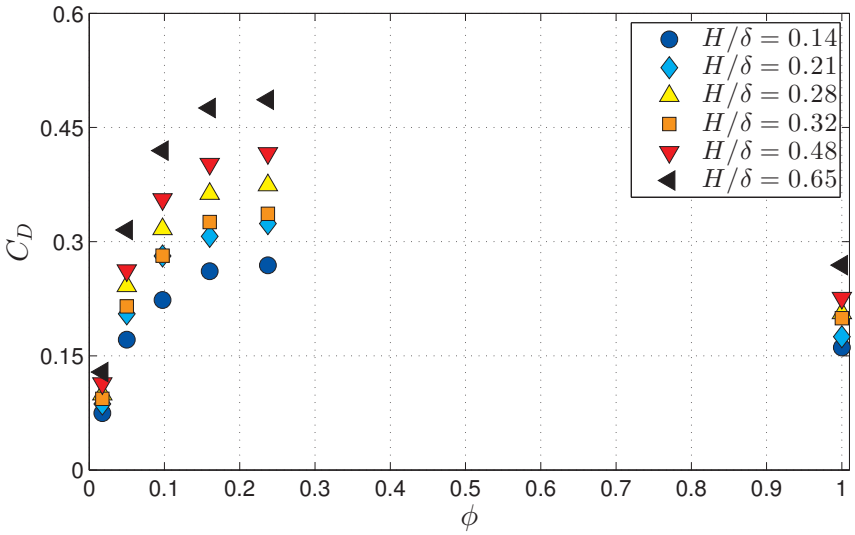

Figure 4.11: C_D vs ϕ for different H/δ.

By non dimensionalising each curve with the correspondent maximum drag coefficient (i.e. C_D of C_{95} model), all the curves collapse, as shown in Figure 4.12.

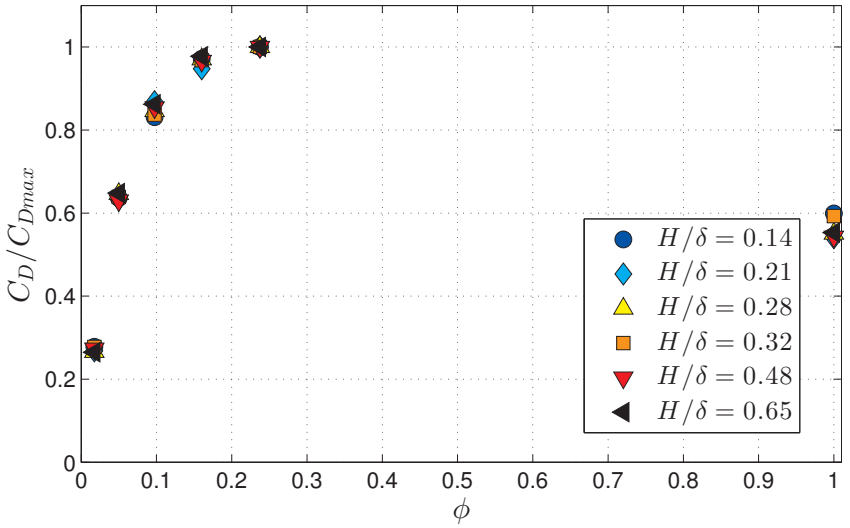

Figure 4.12: C_D/C_{Dmax} vs ϕ for different H/δ.

This means that the dependence of C_D on D, H and δ is ascribed to the maximum value of the drag coefficient C_{Dmax}, and is not dependent on the patch density:

$$C_D\left(\phi, \frac{H}{\delta}, \frac{D}{\delta}\right) = C_{Dmax}\left(\frac{H}{\delta}, \frac{D}{\delta}\right) f(\phi). \tag{4.2}$$

Figure 4.13 (left panel) shows the dependence of C_{Dmax} on H/δ, and D/δ. It seems that the trend of C_{Dmax} with H/δ is linear and that the only influence of D/δ is to shift the curves, but not to change the dependency on H/δ. However, three data points are far from being a robust set of data to fit any predictive law.

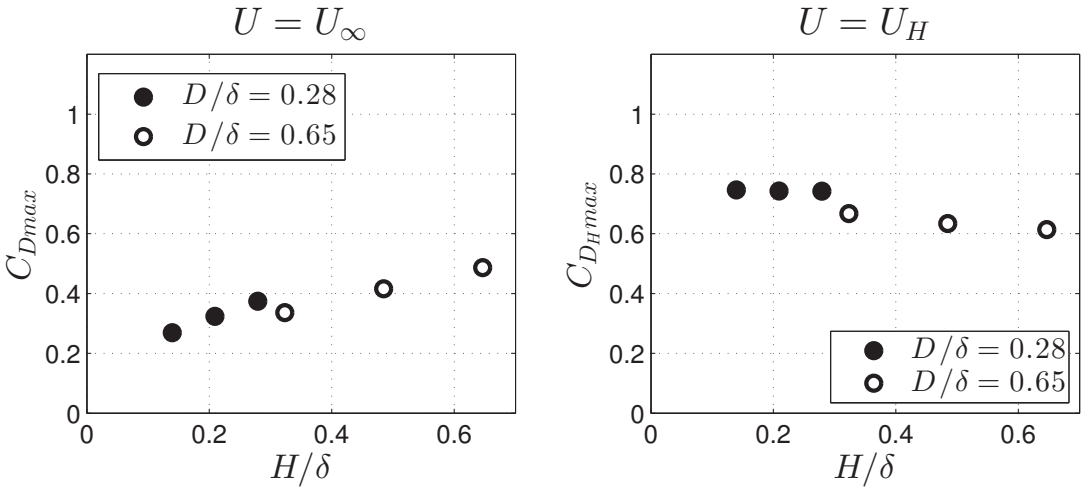

Figure 4.13: C_{Dmax} vs H/δ: left, C_{Dmax} defined with U_∞, right C_{Dmax} defined with U_H.

However, if C_D is defined as:

$$C_{D_H} = \frac{F_D}{1/2\rho U_H^2 DH}, \tag{4.3}$$

where U_H is the incoming boundary layer velocity at $y = H$, the trend of $C_{D_H max}$ is constant with H/δ, and, as a first approximation, the dependence on D/δ can be neglected, and this results in what is shown in Figure 4.14.

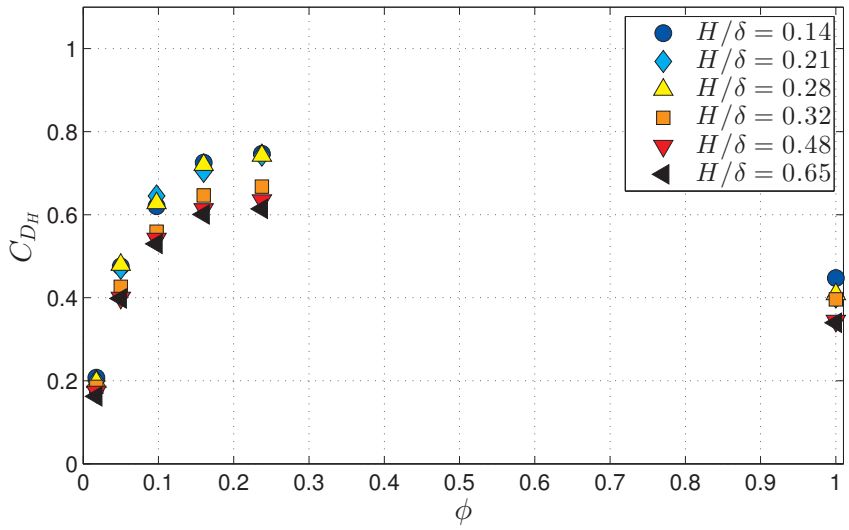

Figure 4.14: C_{D_H} vs ϕ for different H/δ.

It is evident from the Figure that this works reasonably as a first approximation scaling, but in order to define a more accurate scaling, more experiment with different H/δ and D/δ are needed.

4.6 Summary

The first results of this Chapter show that, within the range of ϕ investigated herein, the drag coefficient of porous patches increases with increasing ϕ. However, the coefficient of a solid case with the same external dimensions is almost half of the maximum value obtained for porous patches.

It was pointed out that the increase of the drag coefficient C_D with increasing ϕ is associated with an increase of vertical bleeding as well as a decrease in trailing edge bleeding. In particular, the increase in vertical bleeding promotes wake enlargement as well as working against wake entrainment. A decrease in trailing edge bleeding, instead, contributes towards developing more intense velocity deficits. Wake enlargement, strong velocity deficits and weaker wake entrainment all contribute towards the development of higher C_D.

Particular attention was paid to explain the counter-intuitive drop in C_D observed between the densest porous case and the solid case. The velocity measurements helped explaining that the drop in C_D is associated with the development of strong shear layers around the solid patch, which contribute to wake entrainment and hence to reduce C_D. The effect of these shear layers is weakened in the case of the densest porous patch, because of significant lateral and vertical

bleeding. In particular, it was argued that lateral bleeding could play a more important role than vertical bleeding in explaining the differences between the C_D of the dense and the solid patch.

It has to be pointed out that, due to experimental constraints, the C_D vs ϕ curves presented in Figure 4.2 and 4.3 show a big gap of data for $0.24 < \phi < 1$. This lack of data calls for more experiments to investigate, whether for $0.24 < \phi < 1$ the drag coefficient reaches a plateau and then abruptly decreases after a threshold value of density, or whether it shows a maximum and then smoothly decreases towards the solid case value.

Finally, the influence of H/δ and D/δ on the drag coefficient was studied, and it was found that, if C_D is defined by using U_H as the non dimensionalising velocity, these dependences can be neglected, in a first approximation.

4.7 Considerations on C_{Di}

Most of the literature pertaining patches of obstacles distinguish between patches behaviour by means of the non dimensional parameter $C_{Di}aD$, referred as the patch flow-blockage (where C_{Di} is the average drag coefficient of the cylinders within the patch, $a = nd$ is the frontal area per unit volume of the patch, being $n = N_c/(\pi D^2/4)$ the nuber of cylinders per unit area, d the diameter of each cylinder and D the external diameter of the patch), which was firstly introduced by Belcher et al. (2003).

The definition of C_{Di} given in Belcher et al. (2003) is "*the average sectional drag coefficient*", and is non dimensionalised using the spatially averaged time-mean wind at that height, i.e. $U(y)$ and the frontal width of the obstacles per unit floor area as the reference velocity and length, respectively. Nicolle and Eames (2011) define C_{Di} as "*the time averaged drag coefficient for an individual cylinder over a period of time*", and is non dimensionalised by U_∞ and the external diameter of the patch (i.e. D) as the reference velocity and length, respectively. Chen et al. (2012) define it as "*the cylinder drag coefficient*" and refer to Tanino and Nepf (2008) for its estimation, which, in turns, define it as "*a temporally and spatially averaged drag coefficient*" and it is non dimensionalised by "*the fluid velocity in the direction of the mean flow averaged over the pore space between stems*", which is the average flow velocity within the canopy (named U_p) and by the characteristic obstacle width (i.e. d)as the reference velocity and length, respectively. Zong and Nepf (2012), to introduce C_{Di}, refers to Rominger and Nepf (2011), which in turns, refers again to Tanino and Nepf (2008). Finally, Chang and Constantinescu (2015) define it as "*mean time-averaged solid cylinder streamwise drag parameter*" and non dimensionalise it by the free stream velocity and the cylinders diameter (i.e. d), as the reference velocity and length, respectively.

The choice of the velocity and length to non dimensionalise C_{Di} is crucial for its calculation. Using the free stream velocity, corresponds to average the drag coefficient of the patch within

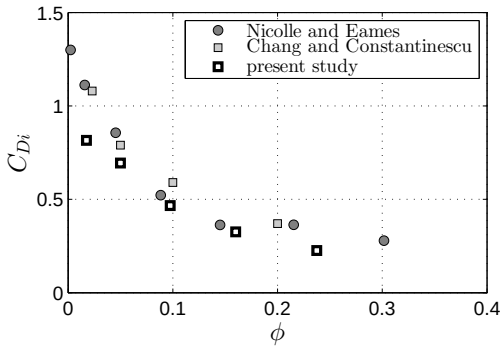

Figure 4.15: C_{Di} defined in equation 4.4 comparison with Nicolle and Eames (2011) and Chang and Constantinescu (2015) data defined in equation 4.5.

all the cylinders of the patch itself and this velocity is not dependent on the patch density. However, the mean streamline velocity of the flow within the patch U_p depends on ϕ itself and it is tricky to measure or to estimate. Moreover, it is meaningless to compare results within different studies if they do not provide the same scaling for C_{Di}.

A first comparison could be carried out with the data from Nicolle and Eames (2011), Chang and Constantinescu (2015) and the present study, defining C_{Di} as:

$$C_{Di} = \frac{F_D}{1/2\rho U_{bulk}^2 dH N_c}, \tag{4.4}$$

for the present case and as:

$$C_{Di} = \frac{F_D}{1/2\rho U_{\infty}^2 dN_c}, \tag{4.5}$$

for Nicolle and Eames (2011) and Chang and Constantinescu (2015).

Figure 4.15 shows a comparison of the obtained values of C_{Di} for the three cases. The differences in C_{Di} are more evident for lower values of density, while for C_D the differences between the two studies were increasing for increasing density. However, a collapse cannot be reached, because the total drag coefficient C_{Dbulk} of the present case is lower for higher densities, but the differences in the drag exerted on each cylinder is much reduced between 2D and 3D if the number of cylinders is sufficiently high. C_{Di} decreases with increasing density, which make sense looking at equations 4.4 and 4.5 and considering that the increase in F_D are lower compared to the increase in N_c.

This definition of C_{Di} allows a good comparison with analogous 2D cases, however, Chen et al. (2012) studied extensively the wake properties depending on $C_{Di}aD$, with a different definition of C_{Di}.

Figure 4.16 shows the plot of C_{Di} vs ϕ for Chen et al. (2012) data. It seems that the trend is linear with ϕ. Even though they state they calculated C_{Di} with the model described by Tanino and Nepf (2008), these results are not in a close agreement with the model itself. Specifically, Tanino and Nepf (2008) estimate $C_{Di} = 2(\alpha_0/Re_p + \alpha_1)$, where α_0 depends linearly on ϕ and α_1

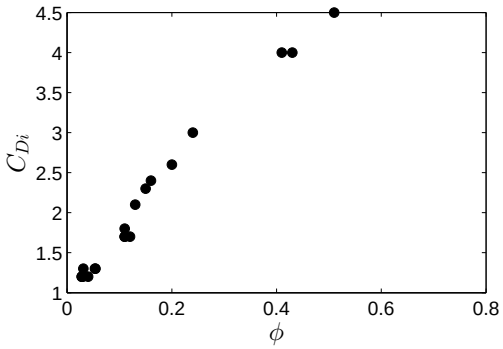

Figure 4.16: C_{Di} vs ϕ for Chen et al. (2012) data.

is a constant: C_{Di} depends linearly on ϕ and inversely on stem Reynolds number $Re_p = U_p d/\nu$, which in turns, should depend on ϕ itself so a linear dependence of C_{Di} on ϕ is not possible. Moreover, Nepf (2011) reports that, at low Reynolds number, the main contribution to C_{Di} is from viscous stresses, which increases for increasing density, while at high Reynolds number ($Re_p > 1000$), the main contribution to C_{Di} is from pressure drag which should decrease for increasing density, as reported in Nepf (1999) which again is in contrast with the prediction model of Tanino and Nepf (2008).

In the present study there are no available information about the velocity within the patch U_p, and the first step in order to provide a comparison between the present data and Chen et al. (2012) was to evaluate U_p for at least three of their cases, where the densities were close to the densities in Tanino and Nepf (2008). However, the model is too sensitive on small changes in values of C_{Di} (a change of C_{Di} of 4% leads to a change in U_p of 62%), and the obtained results were meaningless. The second attempt was to find a suitable way to evaluate U_p from the velocity measurements around the patch provided by the vertical PIV results. Different attempts were made, but none of them exhibited the C_{Di} vs ϕ trend that is similar to the one shown in Figure 4.16.

Nonetheless, an interesting result observed while carrying out this analysis was that if U_p is defined as:

$$U_p = (1 - \phi)U_{in} + \phi U_{out}, \tag{4.6}$$

where U_{in} and U_{out} are the average velocity immediately upstream and downstream of the patch, respectively (i.e. $U_{in} = 1/(H - 2d)\int_d^{H-d} U(x/D = -0.55)dy$ and $U_{out} = 1/(H - 2d)\int_d^{H-d} U(x/D = 0.55)dy$). The two velocities are calculated along the height of the patches starting from a distance d from the wall, up to a distance $H - d$, in order to neglect the wall and free end effects, which could mislead the values; the x coordinates to evaluate U_{in} and U_{out} are $x/D = -0.55$ and $x/D = 0.55$, respectively, which is one d upstream and downstream of the patch in order to reduce the effects of the distribution of the cylinders within the patch which could or could not be inline with the measurements plane. The values of U_{in} and U_{out} are reported in Table **??** and their trend with ϕ are represented in Figure 4.17.

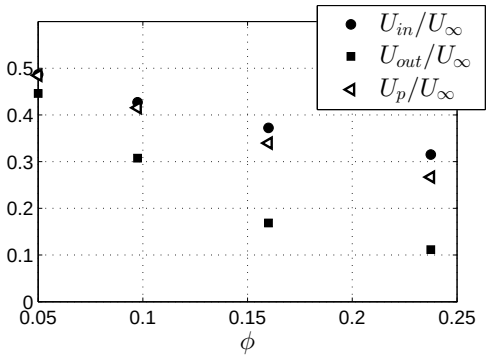

Figure 4.17: U_{in}, U_{out} and U_p, non dimensionalised with U_∞ vs ϕ.

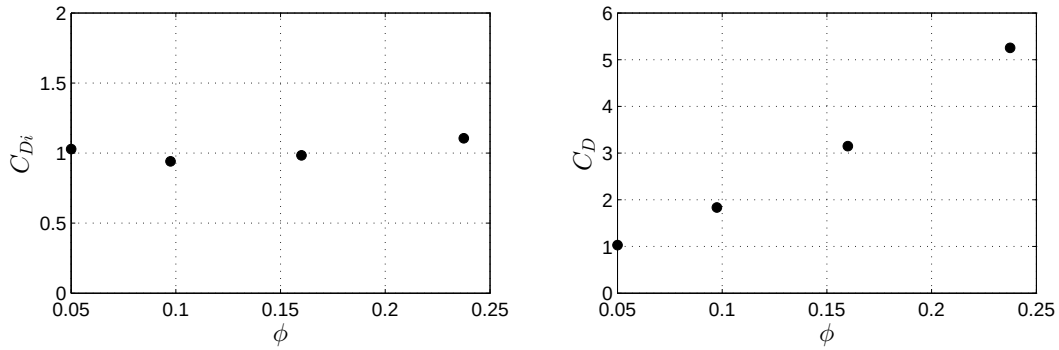

Figure 4.18: C_{Di} vs ϕ, with $C_{Di} = F_D/(1/2\rho U_p^2 H d N_c)$, where U_p is defined in 4.6 and C_D vs ϕ with C_D=$C_{Di} N_c d/D = F_D/(1/2\rho U_p^2 H D)$.

With this definition of U_p, C_{Di} vs ϕ is approximately a constant and equal to 1, and the trend of C_D is linear with ϕ, as shown in Figure 4.18, left and right respectively.

Unfortunately, it is not possible to determine the values of U_{in} for the set of experiments in Chen et al. (2012) to make a comparison. They provide values for U_{out}, which are affected by a huge uncertainty, and furthermore, for the range of D/d comparable for the present one, most of them are for very low densities (i.e. $\phi < 0.05$) which are not in the range of the models studied herein (from C_{20} to C_{95}).

To summarise, trying to fit a suitable law to predict U_p knowing the density is not possible but, provided that U_{in} and U_{out} are known, if C_{Di} is defined as $C_{Di} = F_D/(1/2\rho U_p^2 H d N_c)$, then for a three dimensional patch, it is about 1, and the correspondent drag coefficient of the whole patch varies linearly with ϕ.

Due to the difficulties in evaluating C_{Di} either with direct or indirect procedures, it is not possible to verify whether the results of Chen et al. (2012) are still valid for 3D patches of obstacles. However, a different analysis of the wake characteristic lenghtscales is carried out in Chapter 6 and 5, and good collapses are found, regardless of the range of C_{Di} (presumably, C_{95} model should belong to the range of flow blockage grater than 20, which is the "solid body" range).

Chapter 5

Wake velocity profiles at the vertical plane

5.1 Introduction

This Chapter presents a description of how the wake velocity profiles develops along the symmetry plane. Two distinct regions are found: the very near wake, where the wake properties are constant along the height of the model, as a first approximation, and the near wake, where the velocity profiles for different patches collapse. Scaling laws and parameters for the velocity profiles are introduced. Subsequently, an analysis of the trend of these parameters with ϕ and y is carried out and, where possible, a predictive law is evaluated.

5.2 Vertical profiles

The vertical profiles of the mean longitudinal velocity component non dimensionalised with the freestream velocity U/U_∞ are presented and discussed in this section. The incoming velocity profiles are represented as well in Figure 5.1, as a reference (dashed line).

At $x/D = 1$, all the patches display a constant region for U/U_∞ for almost their entire height (up to $y/D = 0.8$ for C_{20} and $y/D = 0.98$ for all the other patches), and then the velocity increases to recover the freestream value. As we move at $x/D = 2$, the plateau region shrinks downward, and its reduction is more intense for the denser models C_{64} and C_{95}, whose curves almost overlap from this length onwards. Further downstream the differences between the curves of different patches reduces, and at $x/D = 5.5$, they almost overlap, and are indistinguishable from each other.

At the furthest length showed here (and this is evident also from the contour plots in Figure 4.6), the wake of all the patches has not recovered up to a value close to the incoming velocity,

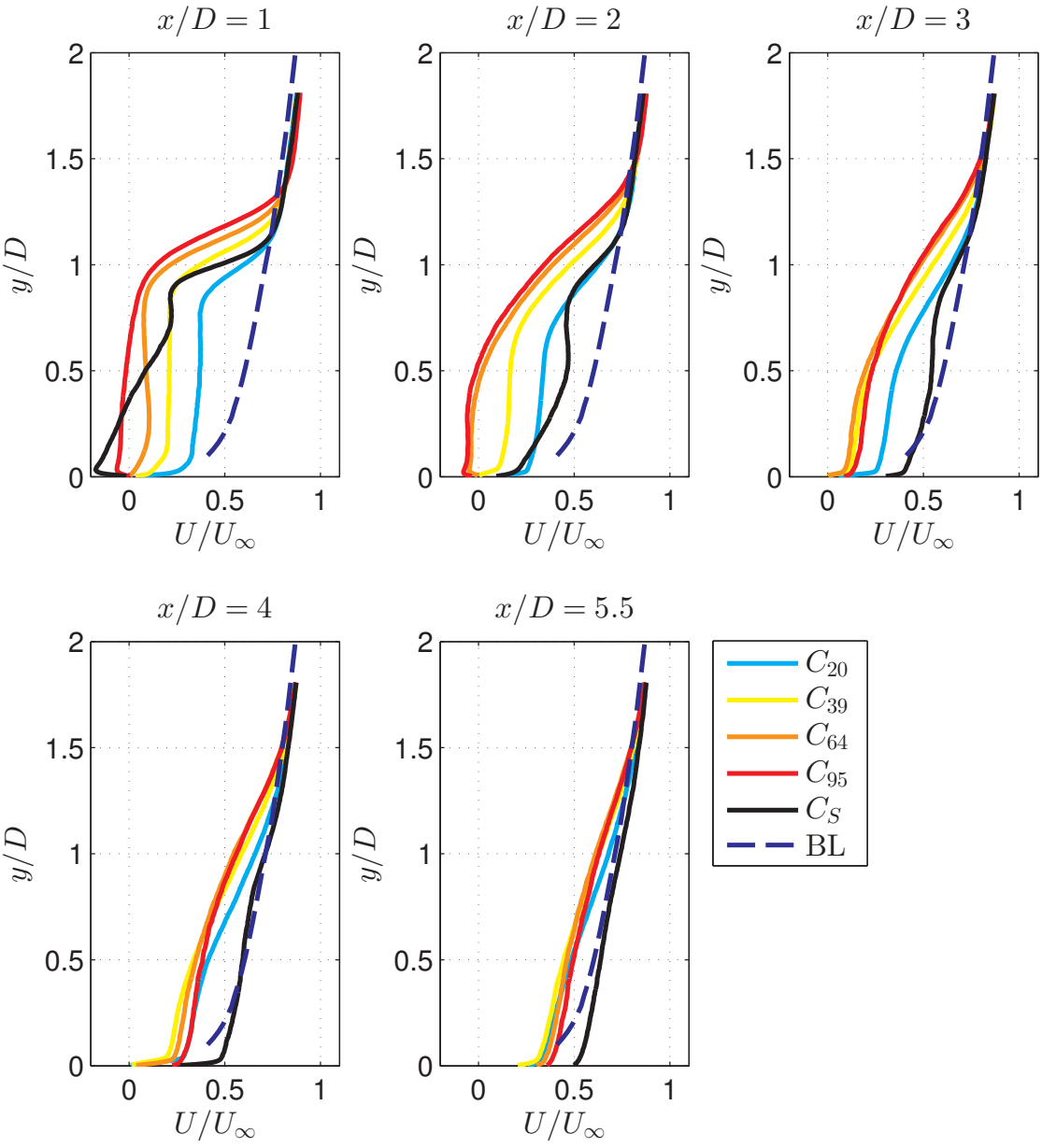

Figure 5.1: U/U_∞ along y at five different streamwise locations for all the patches. The dashed blue line is the incoming boundary layer profile.

while this happens much upstream for the solid cylinder case, and the differences are more pronounced the more we go closer to the wall. Comparing these plots with the contours of the shear layers in Figure 4.10, it is evident that it is the top shear layer that drives the wake development along the $x-y$ plane. As soon as the top shear layer reaches a certain height from the wall, the velocity profiles overlap, while if the shear layer has not reached a certain height, the velocity is constant all along the height. A detailed analysis of the shear layers growth is carried out in Chapter 7.

It is evident that for $x/D > 4$ it is almost impossible to distinguish the wakes of different patches. This suggests that beyond a certain streamwise location, the patches tend to similar characteristics,which is remarkable and counter-intuitive, considering the differences in drag coefficient shown in Chapter 4. From a momentum balance point of view, this can be ascribed to an interplay between the drag generated by the patch and the friction generated at the wall (which both corresponds to a loss in momentum). For less dense patches, the bleeding velocity is higher, resulting in a higher loss in momentum at the wall, while this effect is reduced for denser patch, which in turn is related to a higher momentum loss in the flow due to their higher drag coefficient. Therefore, a compensation between the loss of momentum due to the drag of the patch and the loss of momentum due to the friction at the wall must take place in the near wake, leading to a collapse of all the wakes velocity profiles. This can happen because the top shear layer effects are confined in the upper region of the wake and this allows the formation of an internal boundary layer at the wall. This does not happen for the solid case.

In the very near wake, for a significant portion of the height, the velocity profiles are constant along y, which indicates that the patch behaves as a 2-D obstacle. The effects of the top shear layer are gradually detected at the top part of the wake, but they do not seem to influence the lower half of the wake, where, as a first approximation, the wake properties and characteristics seem constant along the height.

5.3 Characteristic lengthscales analysis

In the following, a discussion on characteristic lengthscales and velocity scales of the flow and their variation along the height of the patches is carried out.

5.3.1 Vortex formation length L_w

L_w, "vortex formation length" or "wake formation length", is the x coordinate where the peak in the turbulence intensity σ_W is located and corresponds to the approximate position of the vortex formation, if any vortex street is generated behind the patch. This length is an indicator of the near wake, where the near wake is considered to be the streamwise distance that is required for immediate wake recovery.

Figure 5.2 shows how L_w was evaluated for each patch. The thin lines at each height are the measurements of σ_W from PIV, non dimensionalised by $U_{y\infty}$. These lines were fitted with a 6^{th} degree polynomial function (thick line in the figure), in order to obtain smoother trends, and hence better identify the location of maxima, which in turn identifies L_w. Figure 5.2 shows that the maximum in L_w are easily identifiable for C_{64}, C_{95} and C_S. For C_{39}, the values of L_w at very low heights (i.e. $y/D \leq 0.2$) are probably underestimated, because it is well known that the polynomial fittings are not reliable at the tails. This procedure works satisfactorily for intermediate densities but it is completely off for C_{20}. This is attributable to a lack of well

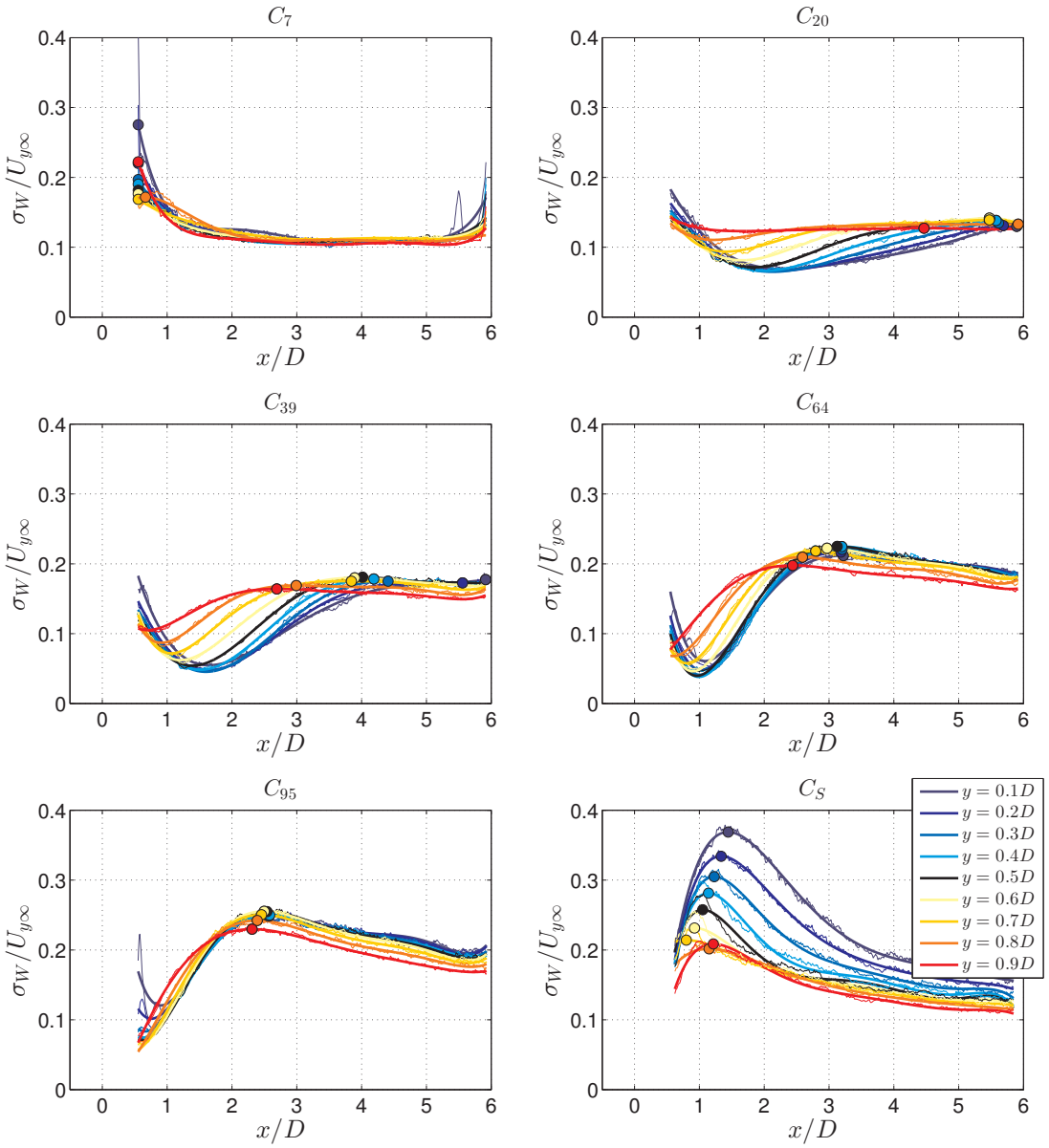

Figure 5.2: $\sigma_W/U_{y\infty}$ vs x/D at different vertical locations for all the patches. Thin line, measurements; thick line, fit; dots, location of L_w.

defined maxima in the longitudinal profiles of σ_W and hence the difficulty in defining L_w (see Figure 5.2).

Figure 5.3 shows L_w/D against y/D for all the models. As it was already discussed, the values for the model C_{20} are not reliable, and the values for the model C_7 are meaningless in this context since the patch show no group behaviour. However, the results for C_{39}, C_{64} and C_{95} show interesting trends.

For the C_{39} case, L_w decreases all along the height. For low heights (i.e. $y/D < 0.26$), the plots of σ_W in Figure 5.2 show similar problems of the case C_{20}, where the maximum in the fluctuations is not easily detectable, therefore in this region the results presented in Figure

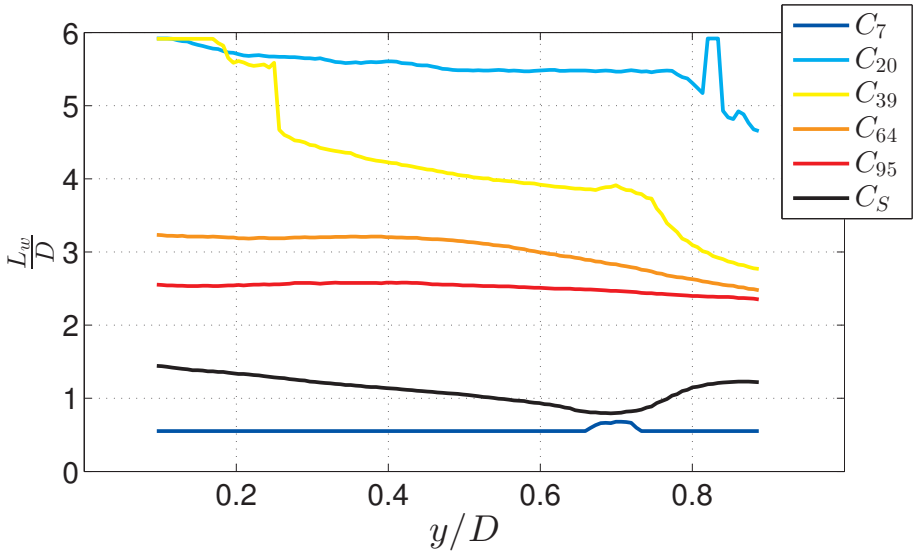

Figure 5.3: L_w/D along the height for all the models.

5.3 for C_{39} must be taken with care. Nonetheless, for the heights greater than $0.26D$, the decreasing in L_w is about linear (except for a small bump around $y/D = 0.7$).

For higher density, (i.e. for case C_{64}), the vortex formation length is constant up to $y/D = 0.5$, and then decreases. The region where it is constant corresponds to the location of the recirculation bubble. Outside of the recirculation bubble, L_w decreases again with the height. C_{95} shows a very similar behaviour although the linear decay is much slower than in C_{64} and the vertical profile looks even more constant. In particular, L_w for these two last models, marks the end of the recirculation region along x. This can be interpreted as after the recirculation region (i.e. for $x > L_w$) the wakes have the same behaviour along y at the same x location, regardless of the incoming velocity profiles and the free end effects are somehow cancelled by the upward spread of the bubble.

These considerations demonstrate that the formation of a recirculation bubble reduces the free end effects on the wake, and the denser the patch, the longer the extension of the recirculation bubble along y, and the vortex formation length is constant along the height, despite the short aspect ratio of the patch.

In general, these results show that if a vortex formation length can be evaluated, it is always lower then $x/D = 5$ for all the heights, which means that the threshold for all the densities between very near/near wake can be considered to be $x/D = 5$. For shorter distances from the patch, the velocity profiles are constant for the majority of the patch height, while for greater distances they all collapse to the same curve.

5.3.2 Maximum velocity deficit location L_{min}

L_{min} is the x location of the minimum velocity value U_{min} along the centreline. It can be considered as a virtual origin of the wake, which shifts downstream the start of the velocity recovery. L_{min} is a representative lengthscale for the very near wake characteristics, since it corresponds to the length where the velocity in the wake starts to adjust.

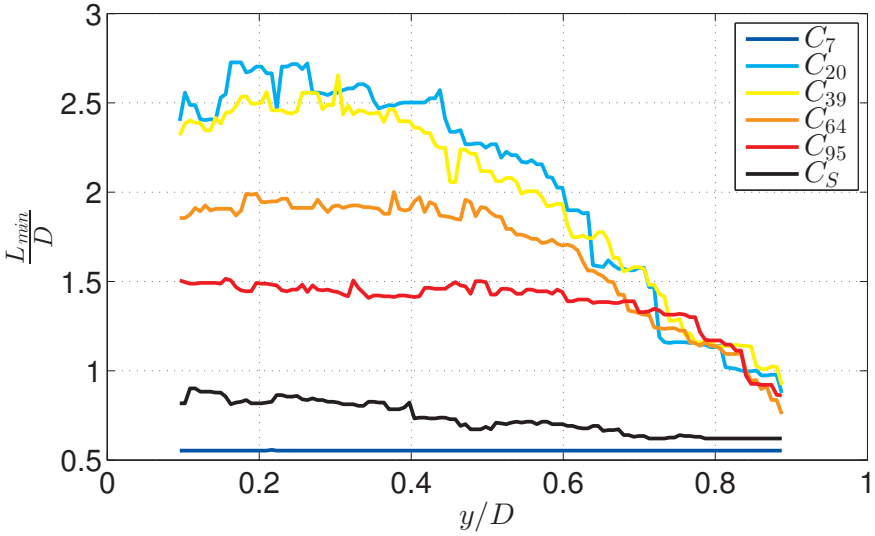

Figure 5.4: L_{min}/D along the height for all the models.

Figure 5.4 shows the trend of L_{min}/D vs y/D for all the patches. The curves for C_{20} and C_{39} are comparable and show that the location of U_{min} along x is about constant up to $y/D = 0.4$ and equal to about $2.7D$ and $2.5D$ (not considering some wall proximity effects which promote a reduction in L_{min} close to the wall), respectively, then it starts to decrease with increasing y/D. The curves for C_{64} and C_{95} show a plateau in correspondence of the recirculation bubble extension (i.e. up to $y/D = 0.5$ and $y/D = 0.75$, respectively). All these curves show a reasonable collapse in their final part, meaning that the position of L_{min} outside of the recirculation bubble, or in the higher part of the wake, is independent of the density of the patch (in fact, curves for C_{20} and C_{39} collapse with the scaling in Figure 5.4). This is consistent with the observation that in the very near wake, the wake characteristics are constant for a great portion of the height of the patch.

Excluding the models C_7 and C_S, a multilinear fitting for each patch has been carried out in order to find the two lines that best-fit the curves in Figure 5.4, by varying the threshold limit y_* along y. The two fitting lines for each patch are represented in Figure 5.5.

The fitting procedure consists in applying the following equations:

$$\begin{cases} \dfrac{L_{min}}{D} = k & \text{for } \dfrac{y}{D} < y_*, \\ \dfrac{L_{min}}{D} = m\dfrac{y}{D} + q & \text{for } \dfrac{y}{D} > y_*. \end{cases} \tag{5.1}$$

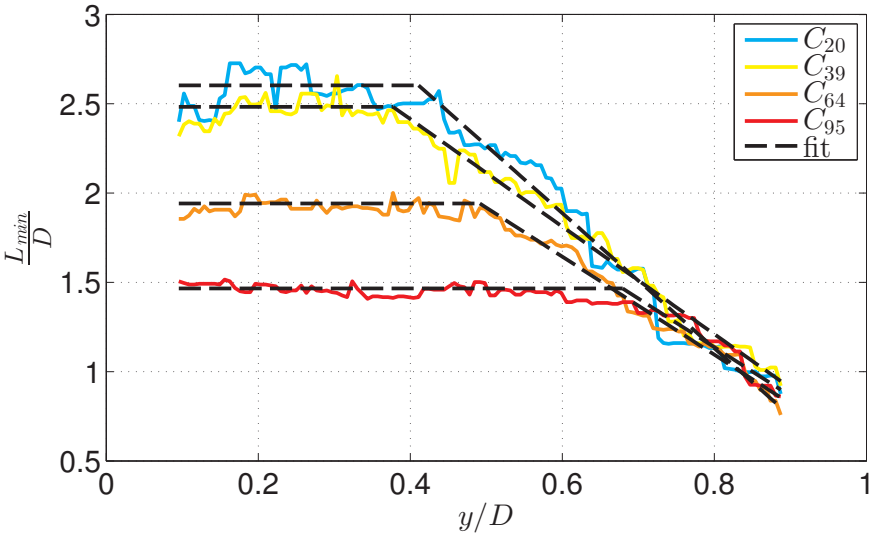

Figure 5.5: L_{min}/D along the height for all the models.

	C_{20}	C_{39}	C_{64}	C_{95}	average
m	−3.78	−3.01	−2.74	−2.73	−3.06
q	4.16	3.62	3.29	3.32	3, 60
y_*	0.41	0.38	0.49	0.68	0.49
k	2.60	2.48	1.94	1.47	2.12

Table 5.1: Multilinear fitting results for L_{min}.

By varying the location of y_* along y, the parameters m and q were obtained by fitting L_{min}/D in the range $y/D > y_*$ with a non linear least square method. For the obtained values of m and q at each vertical location, the correspondent k has been evaluated by applying the constraint that

$$k = my_* + q, \tag{5.2}$$

obtaining the fitted curve for the range of data $y/D < y_*$. The sum of the squared residual calculated between the fitted lines and the original data was then minimized, in order to find, for each patch, the best values for m, q and k. The curves which correspond to these values are represented in Figure 5.5 and the correspondent values of m, q, k and y_* are reported in table 5.1, while their trend with ϕ is represented in Figure 5.6.

From Figure 5.6 it is evident that each of the parameters shows a dependence on ϕ. Nonetheless, as a first approximation, the curves in Figures 5.4 and 5.5 seem to reasonably collapse along their linear part. By representing L_{min}/k against $y/D - y*$ (Figure 5.7) it can be seen how this collapse is still reasonable among the different patches, so a first level of approximation of the linear region, neglecting the dependence on ϕ of the fitted parameter (also represented in the Figure as dashed line) can be obtained by averaging m/k over all the patches since, in this

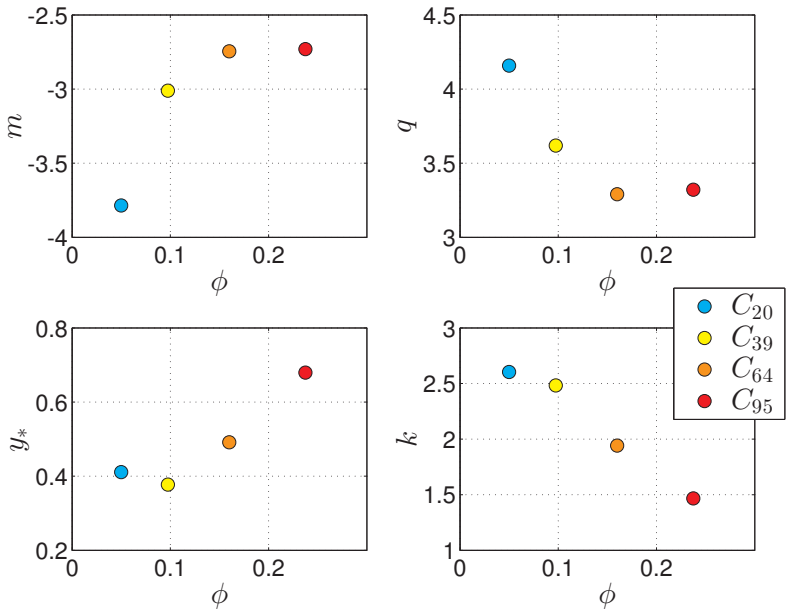

Figure 5.6: Trends of the multilinear fitting parameter with ϕ.

scaling, the average line corresponds to

$$\frac{L_{min}}{k} \sim \frac{\overline{m}}{\overline{k}}\left(\frac{y}{D} - y_*\right) + 1, \tag{5.3}$$

where the overbar corresponds to the averaged quantity. It is worth to notice that the plots of the actual data L_{min}/k and $y/D - y_*$ are done for the exact value of k and y_* for each patch, while the linear fitting result has been obtained with the averaged quantities.

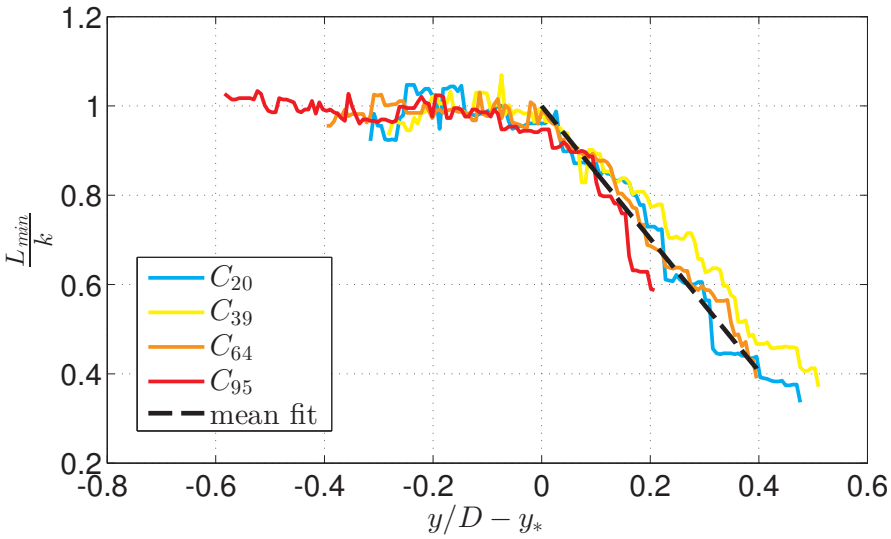

Figure 5.7: L_{min}/k vs $y/D - y_*$ for all the patches and averaged fitting result from equation 5.3.

As it shown in Figure 5.8 m/k and my_*/k still show a dependence on ϕ, so the result of equation 5.3 and 5.7 are for a first level of approximation and can predict L_{min} only if the scaling quantities k and y_* are known, therefore more data are needed to define a suitable scaling of m, k and y_* with ϕ.

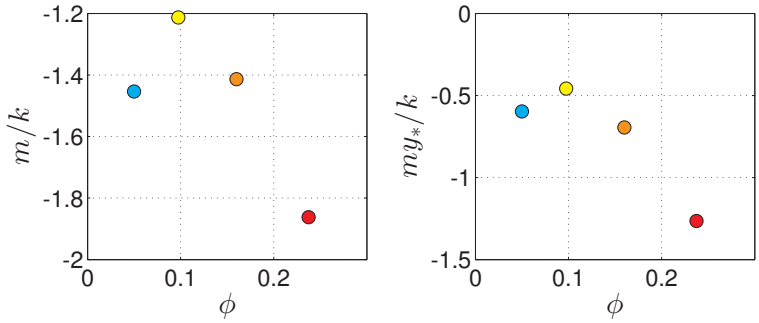

Figure 5.8: Trends of the multilinear fitting parameter with ϕ.

This suggests that by applying suitable scaling parameters, also the very near wakes of patches with different densities might be collapsed.

5.4 Vertical wake profiles scaling

Figure 5.9 and 5.10 shows the "global" and the "local" longitudinal velocity deficit ($\Delta U_{bulk}/U_{bulk}$, left, and $\Delta U_y/U_{y\infty}$, right, respectively) along x at different vertical locations for all the models. The "global" velocity deficit was evaluated as $\Delta U_{bulk} = U_{bulk} - U_y$, while the "local" velocity deficit is defined as $\Delta U_y = U_{y\infty} - U_y$ where U_y is the longitudinal velocity component at the considered y location, U_{bulk} is the bulk velocity of the incoming flow (defined in Chapter 4) and $U_{y\infty}$ is the velocity of the incoming flow at the considered y location.

Looking at the plots for C_{20}, the maximum $\Delta U_{bulk}/U_{bulk}$ decreases with increasing height and moves upstream. The maximum local velocity deficit $\Delta U_y/U_{y\infty}$ seems to be constant along y and moves upstream with increasing height. This indicates that local variables provide a better scaling than bulk variables. Such scaling is less satisfactory when approaching either the patch top or the wall. Furthermore, the steady velocity region (i.e. the plateau in the longitudinal development of mean velocities) increases in length with decreasing distance from the wall. This makes sense, because towards the patch top, free end effects disturb the trailing edge bleeding by entraining momentum from the overlying flow regions, hence decreasing the velocity deficit.

The velocity deficit for C_{39} seems to be less affected by the proximity to the wall: only the profile at $y/D = 0.1$ diverges from the trend after $x/D > 4$. Velocity deficit profiles for C_{64} and C_{95} diverge from the previous cases since neither local nor bulk variables provide a satisfactory collapse neither of the maxima, nor the rest of the profiles. The steady velocity region is also shrunk significantly and only occurring in C_{64} for $y/D > 0.6$. This is probably due to

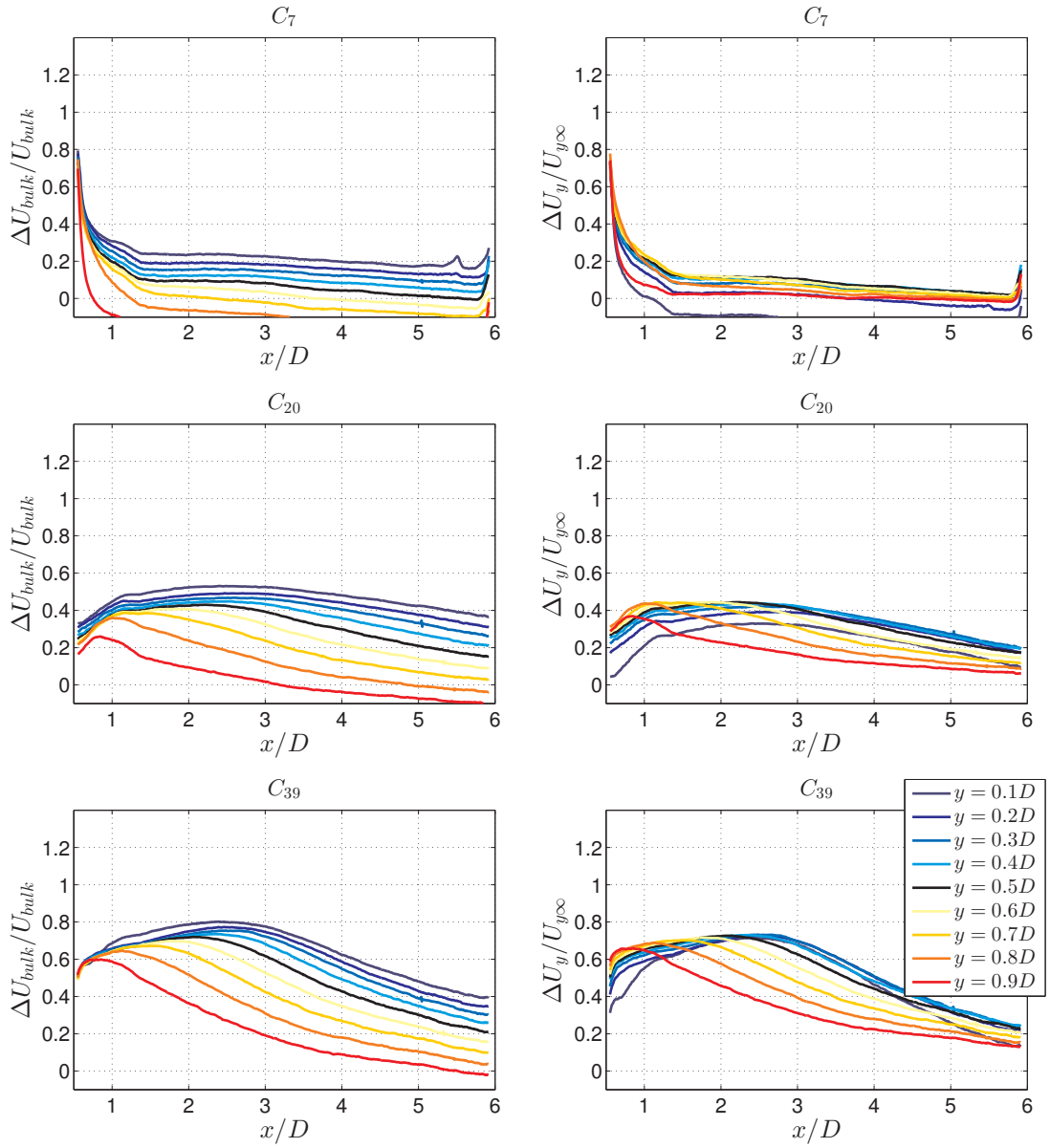

Figure 5.9: $\Delta U_{bulk}/U_{bulk}$, left, and $\Delta U_y/U_{y\infty}$, right, at different vertical locations for the patches C_{7_0}, C_{20} and C_{39}.

the presence of the recirculating region. This generates heterogeneity in the wake, with the lower portion of it being subject to recirculation and the upper portion of it not. Such vertical heterogeneity hampers to find a unique scaling parameter.

For all the patches, Figure 5.9 and 5.10 show that the local velocity deficit $\Delta U_y/U_y$ for $y/D < 0.5$ collapses reasonably well onto each other after $x/D \simeq 3$. This means that the lowest half of the wake at the symmetry plane scales with local velocities of the incoming turbulent boundary layer. Only the curves at $y/D = 0.1$ diverge from this trend for some of the patches, probably because of wall proximity effects. This is obviously consistent with the fact that the lower part of the wake is more affected by the development of the lateral shear layer, while the upper part of the model is more affected by the free end effects.

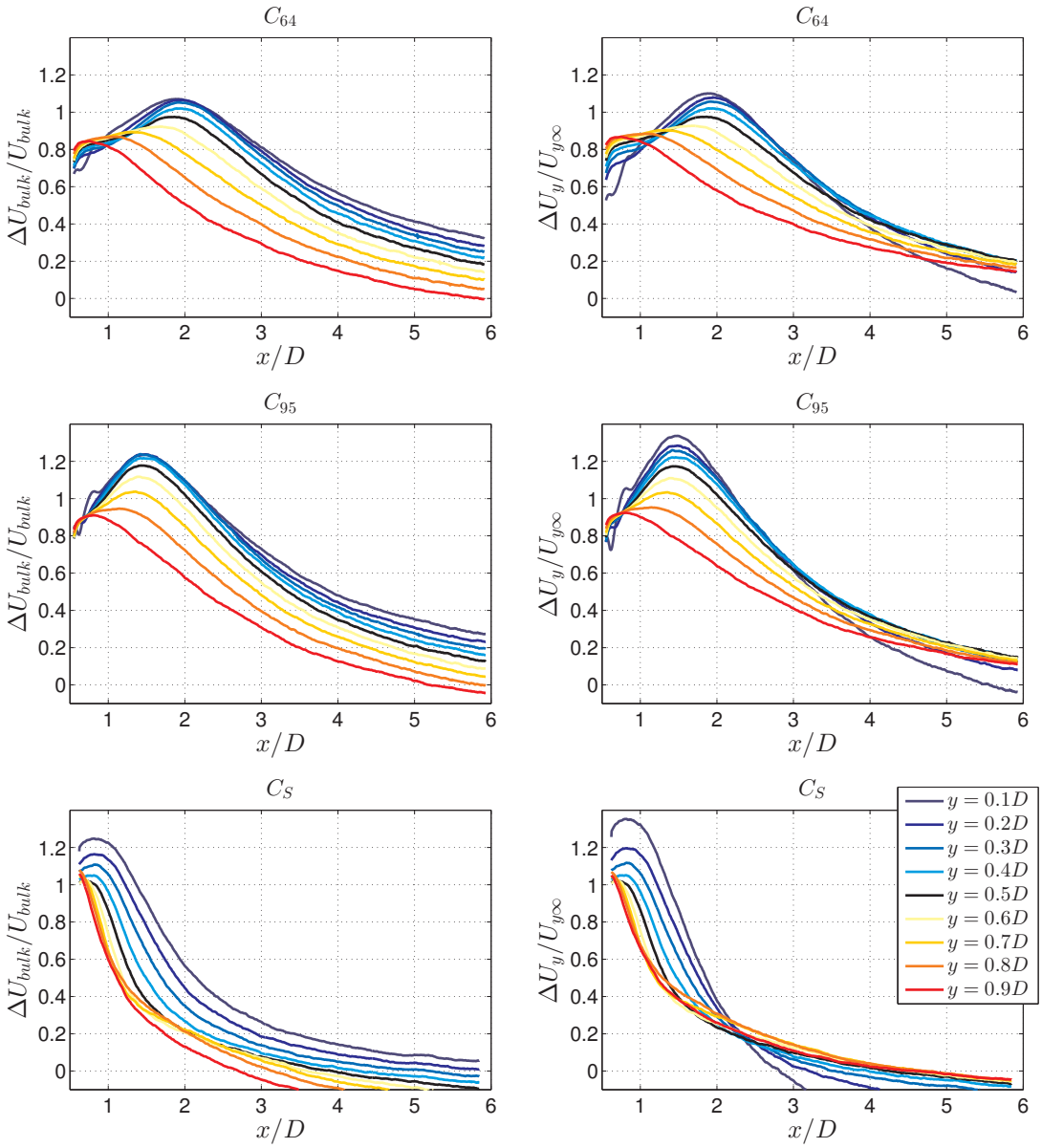

Figure 5.10: $\Delta U_{bulk}/U_{bulk}$, left, and $\Delta U_y/U_{y\infty}$, right, at different vertical locations for the patches C_{64}, C_{95} and C_S.

An attempt to scale the velocity deficit along the height was made, by shifting the origin of the wake by L_{min} and non-dimensionalising the longitudinal direction with L_w. Figure 5.11 shows the global velocity deficit non dimensionalised with its maximum value, at different height. The values of L_{min} and L_w are evaluated for each height and reported in Table 5.2 and 5.3 respectively.

This scaling works satisfactorily for intermediate densities but it is completely off for C_{20}. This might be due to the difficulties in defining L_w for this patch.

Despite this issues, the proposed scaling works satisfactorily for C_{39}. For the cases C_{64} and C_{95} the proposed scaling also provides a satisfactory collapse, although velocity curves at $y/D <$

	C_7	C_{20}	C_{39}	C_{64}	C_{95}	C_S
$y = 0.1D$	0.5527	2.4085	2.3885	1.9117	1.4873	0.8173
$y = 0.2D$	0.5527	2.4693	2.4586	1.9491	1.4826	0.8173
$y = 0.3D$	0.5574	2.5815	2.4867	1.9211	1.4172	0.8267
$y = 0.4D$	0.5527	2.5254	2.3324	1.8883	1.4639	0.8080
$y = 0.5D$	0.6603	2.2262	2.0613	1.8603	1.4265	0.6864
$y = 0.6D$	0.5527	1.8803	1.7481	1.6733	1.3985	0.6958
$y = 0.7D$	0.5527	1.1885	1.4817	1.2433	1.3517	0.6350
$y = 0.8D$	0.5527	1.0109	1.1404	1.0937	1.1461	0.6210
$y = 0.9D$	0.5527	0.8519	0.8553	0.7524	0.8095	0.6210

Table 5.2: L_{min}/D values for all the patches at different y locations.

	C_7	C_{20}	C_{39}	C_{64}	C_{95}	C_S
$y = 0.1D$	0.5527	5.8957	5.9131	3.2206	2.5438	1.4437
$y = 0.2D$	0.5527	5.6901	5.5578	3.1832	2.5484	1.3362
$y = 0.3D$	0.5527	5.6153	4.4079	3.2019	2.5718	1.2287
$y = 0.4D$	0.5527	5.5779	4.1882	3.1972	2.5811	1.1399
$y = 0.5D$	0.5527	5.4797	4.0153	3.1271	2.5391	1.0510
$y = 0.6D$	0.5527	5.4750	3.8937	2.9682	2.4970	0.9248
$y = 0.7D$	0.5527	5.4750	3.8423	2.7952	2.4549	0.7986
$y = 0.8D$	0.6649	5.9191	2.9915	2.5895	2.3895	1.1492
$y = 0.9D$	0.5527	4.4653	2.6924	2.4399	2.3100	1.2147

Table 5.3: L_w/D values for all the patches at different y locations.

0.5 seem to peel off the main trend for $(x - L_{min}/L_w > 1)$. This effect is induced by the presence of the recirculation region which "locks" the values of L_w (see Figure 5.2 and Table 5.3). It was already shown that the appropriate scaling for this region is $\Delta U_y/U_{y\infty}$ vs x/D. This confirms that L_w is the threshold length to distinguish between vary near and near wake. For the cases where a recirculation bubble is present, this definition is straightforward (before/after the recirculation region), while for lower values of density, the loss of momentum due to the friction at the wall stabilise this threshold to $x/D \sim 5$.

Given the richness of flow features characterising the wakes, it is extremely difficult to find a set of scaling parameters that collapse the velocity defect curves along the vertical direction where top-end and wall effects spread throughout the flow region of interest. This contributes to create a wake characterised by many length and velocity scales, whose effect is difficult to lump in few scaling parameters. As a first approximation, the scaling found herein might work properly along the height of the patches as well, provided that the values of L_w are evaluated correctly and that there is no recirculation region downstream of the model. Further experiments are needed to confirm this hypothesis, in order to have a better evaluation of L_w.

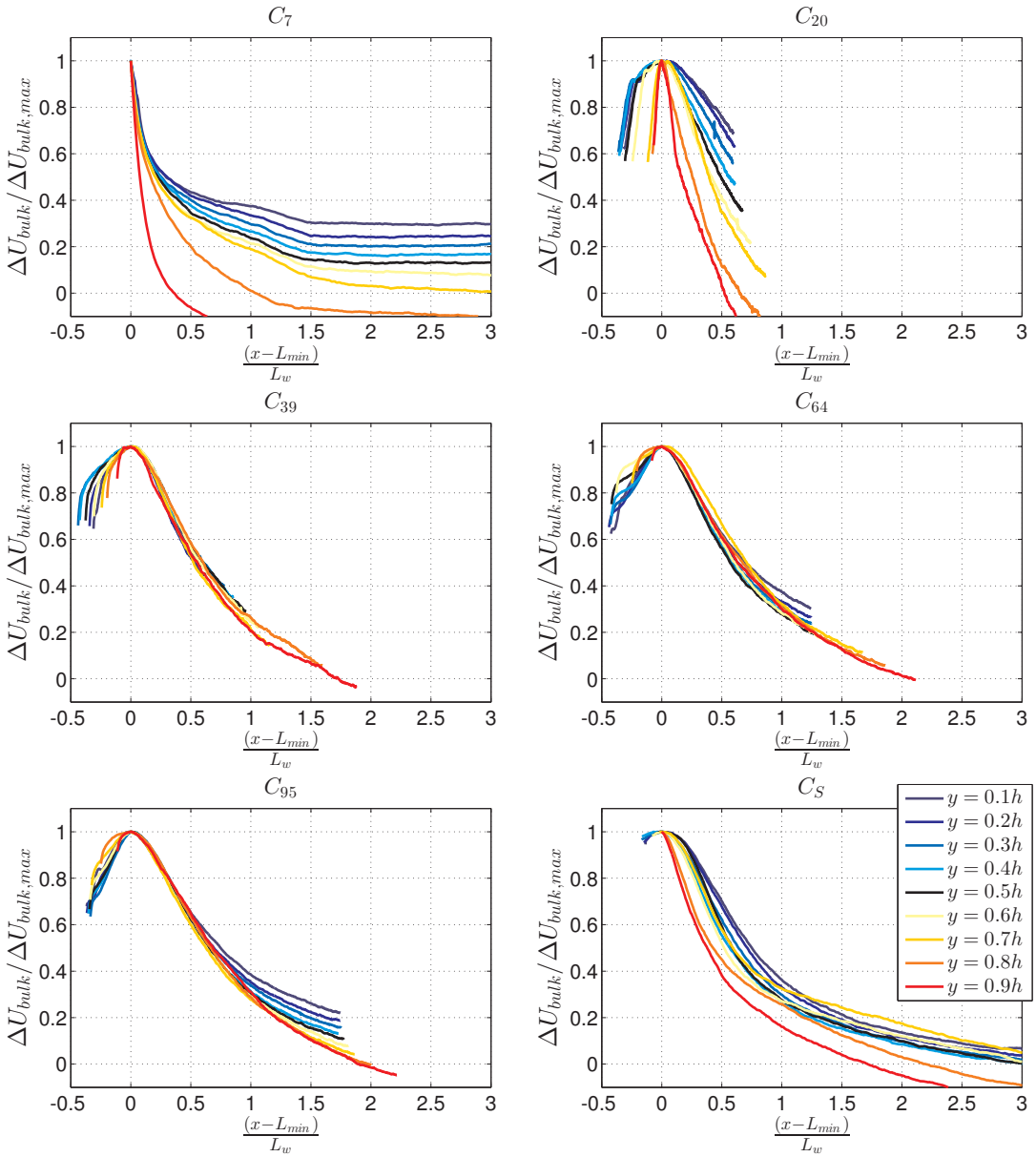

Figure 5.11: $\Delta U_{bulk}/\Delta U_{bulk,max}$ vs $(x - L_{min})/L_w$ at different vertical locations for all the patches.

5.4.1 Maximum velocity deficit ΔU_{max}

Figures 5.12 and 5.13 show the trend of the maximum global and local velocity deficit along the height of the patches. The curves for C_{20} and C_{39} decrease with increasing y/D in the global case, but are constant in the local plots. This means that for low values of density (i.e. the absence of a recirculation bubble), the maximum velocity deficit within the wake scales better with local variables and hence is dictated by the incoming velocity profile.

If a recirculation bubble is present (i.e. cases C_{64} and C_{95}) the maximum velocity deficit, both in the global and the local cases, occurs at the centre of the bubble itself. In particular, the global velocity deficit is constant for the inner region of the bubble, and start to decrease at

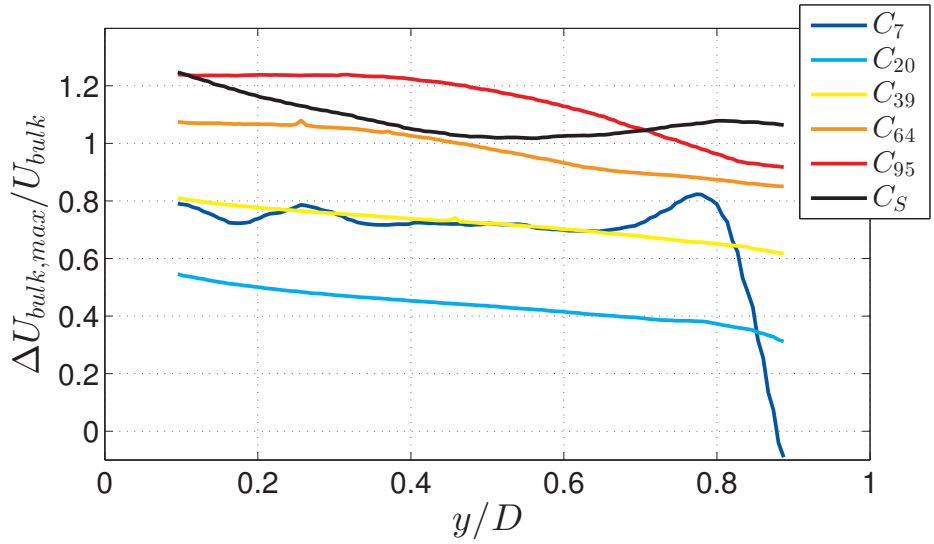

Figure 5.12: $\Delta U_{bulk,max}/U_{bulk}$ along the height for all the models.

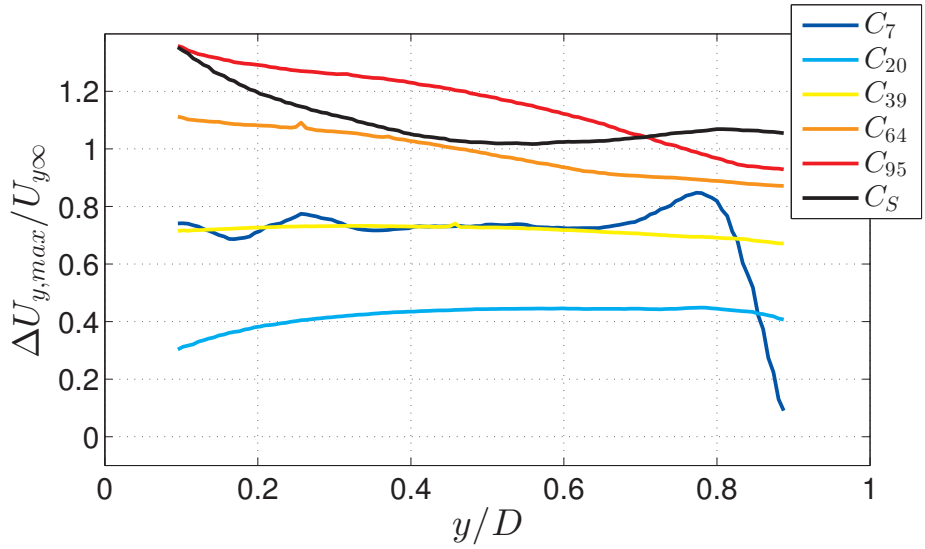

Figure 5.13: $\Delta U_{y,max}/U_{y\infty}$ along the height for all the models.

its top towards a region where the local velocity deficit is constant. This last region shrinks in size for increasing density and is limited to the top of the patch, where the effects of the free end are still present. This means that the presence of a recirculation bubble reduces the effects of the incoming velocity profile in setting U_{min} in the wake along the height of the patch.

In order to analyse the effects of the patch density on the maximum velocity deficit, we can split the problem in two parts, where the deficit does not depends on the height of the patch: (i) $\Delta U_{bulk,max}/U_{bulk}$ vs ϕ within the recirculation bubble; (ii) $\Delta U_{y,max}/U_{y\infty}$ when no recirculation bubble is present. However, in the present study, only two cases are present for each part (i.e. C_{64} and C_{95} for (i) and C_{20} and C_{39} for (ii)), which makes it impossible to conduct a deeper analysis and further experiments are needed.

5.5 Summary

From the analysis of the development of the velocity profiles along the height downstream of the patch, it was shown that two distinct region can be distinguished in the wake: a very near wake region, where the velocity is about constant for a major portion of the height of the patch, and a near wake region, where all the patches displays the same velocity profiles regardless of their density. The presence of a recirculation bubble marks these two region in a clear way, by confining the effects of the top shear layer at the top part of the wake. For the models where no recirculation bubble is present, the development of a boundary layer at the wall contrasts the development o f the top shear layer, so that an equilibrium is reached further downstream, leading to a collapse of all the wake profiles after $x/D \simeq 5$.

Two different behaviours were found for L_w, ΔU_{max} and L_{min} in the presence or absence of a recirculation region. In all the cases it was shown that, if a recirculation bubble is present, all the characteristic lengthscales and velocity scales lock to a constant value within the recirculation bubble, for all its vertical extension. In this region the wake is not affected by free end effects and characteristic velocity and length scales are independent of y/D. As a first approximation, this consideration can be extended even to those model which do not show a recirculation bubble, meaning that in the very near wake the wake properties are constant for a major portion of its height.

Chapter 6

Wake velocity profiles at the mid-height plane

6.1 Introduction

The main objective of this section is to find a scaling law for the velocity profiles in the wake of the patches, along the longitudinal direction for the near wake. The focus will be only at the mid height plane (which means only at the centreline for the vertical PIV data) since it was shown that the wake properties can be considered constant along the height of the patches in the near wake (as a first approximation). Firstly, the appropriate scaling parameters for the velocity profiles are found, both for the profiles in the $x-z$ plane and in the $x-y$ plane. Subsequently, a fit of the trend of these parameter with ϕ is carried out to find a predictive law, starting from the values of density. Finally, a comparison of the velocity profiles with data taken in 2-D patch experiments will be shown.

6.2 Lateral wake profiles scaling

Figure 6.1 shows the velocity profiles of the mean longitudinal velocity component non- dimensionalised with $U_{H/2}$ (i.e. incoming flow velocity at the plane of the measurements) on the horizontal plane, for six different longitudinal locations for all the models.

The first thing to notice is how the wake of a solid cylinder with the same external height and diameter is completely different from the porous patches. The velocity profiles are narrower and the velocity recovery occurs further upstream compared to the porous cases.

From the plots in Figure 6.1, it is evident that, after $x/D > 4$, it becomes almost impossible to distinguish between the wake profiles from different patches, provide we exclude C_7 and C_S cases. This confirms what was found in Chapter 5, that the far wakes of the patches collapse,

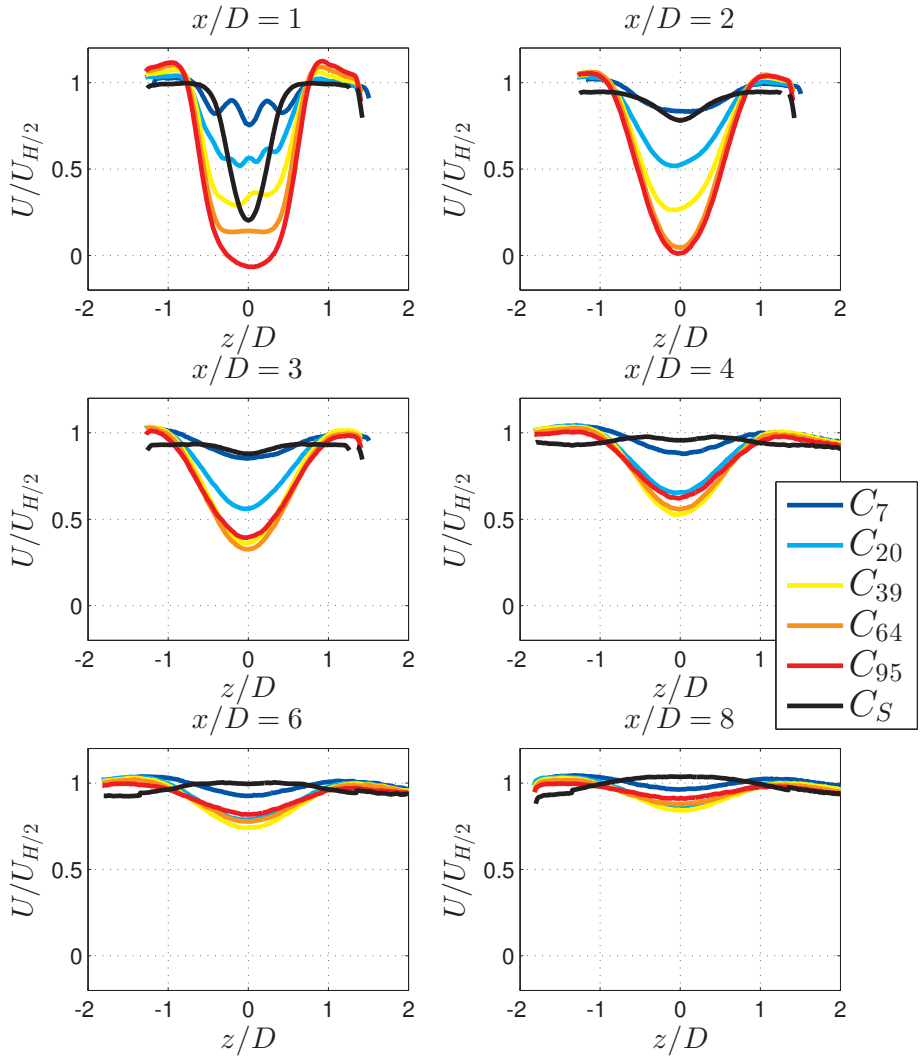

Figure 6.1: $U/U_{H/2}$ along z at six different longitudinal locations for all the patches.

regardless of the patch density. As observed in Chapter 4, the patch wakes have all the same lateral extension (i.e. $\pm D$), regardless of the patch density, and this is consistent with the occurrence of a fixed separation point at the flanks of the patches.

A more common way to represent velocity profiles in the wake, is by means of the velocity deficit $\Delta U = U_{H/2} - U$, as shown in Figure 6.2.

For wake generators, (Pope, 2011, Wygnanski et al., 1986), usually a self-preserving state is achieved, and the mean flow can be described by means of a characteristic velocity deficit (i.e. the maximum velocity deficit $\Delta U_0 = U_{H/2} - U_0$, where U_0 is the minimum U along the profile, in correspondence of $z/D = 0$) and a characteristic lenghtscale (i.e. the wake half width $z_{1/2}$, which is the z location where the velocity deficit is half of its maximum value). If

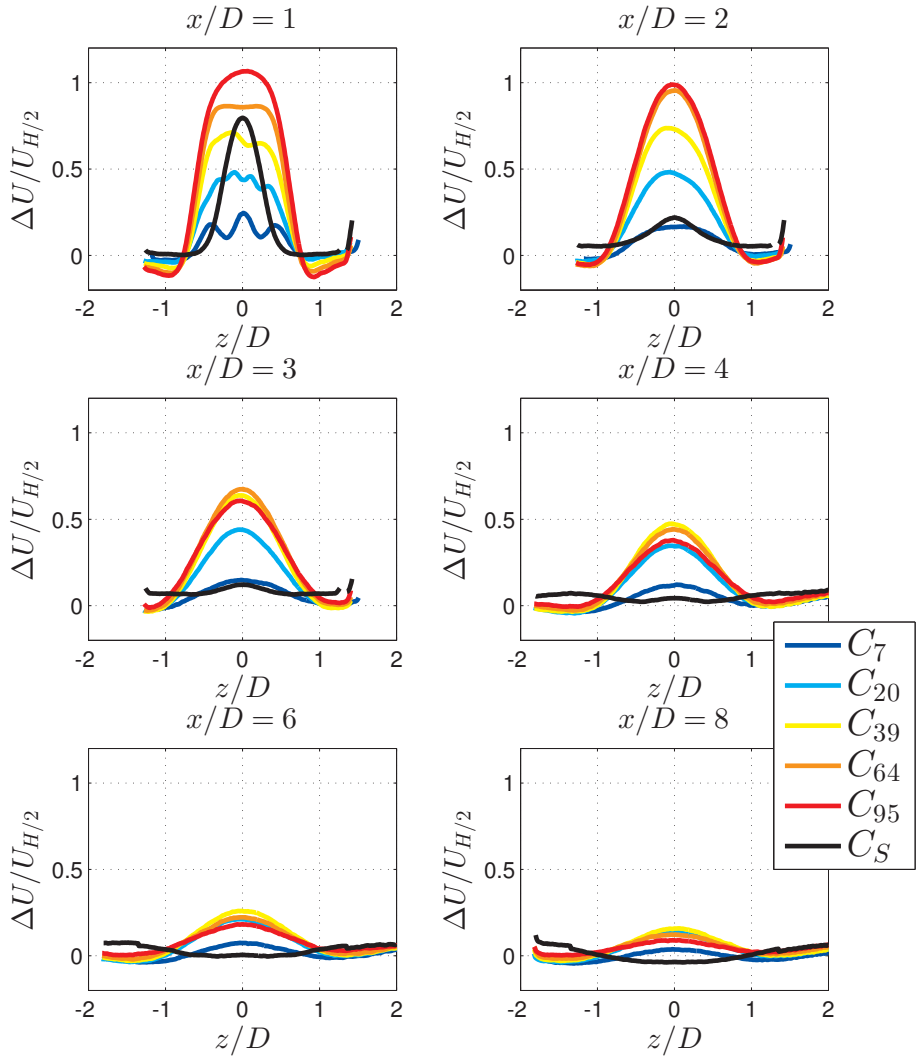

Figure 6.2: $(U_{H/2} - U)/U_{H/2}$ along z at six different longitudinal locations for all the patches.

a self-similarity holds, the mean velocity deficit profiles for the patches can be described as

$$\Delta U(x, z, \phi) = \Delta U_0(x, \phi) f(z/z_{1/2}(x, \phi)), \tag{6.1}$$

where the characteristic lenghtscale and velocity scale depend only on the longitudinal coordinate x and the patch density ϕ. This allows to predict the wake development downstream of the model just by knowing the characteristic functions which are independent from each other, and to predict the wake growth and length just by knowing the patch density.

Figure 6.3 shows the velocity deficit profiles normalised with the characteristic velocity scale against the lateral coordinate normalised by the characteristic lenghtscale of the wake at six different longitudinal locations.

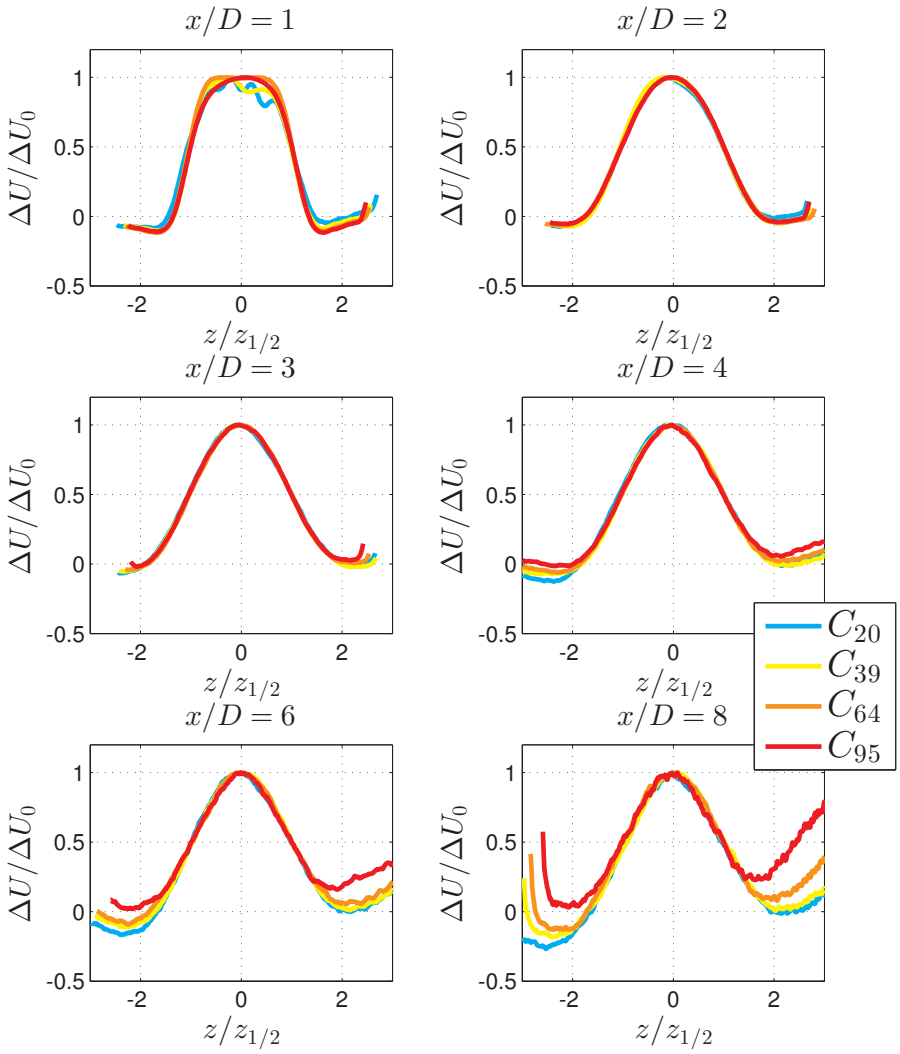

Figure 6.3: Normalised velocity deficit $\Delta U/\Delta U_0$ vs normalised lateral coordinate $z/z_{1/2}$ at six different longitudinal locations for all the patches.

A superimposition of all these profiles is shown in Figure 6.4. From this Figure and Figure 6.3 it is evident that the tails are not self similar for all the profiles, however the collapse is reasonable in the central part of the wake, for $x/D > 1$. This is in agreement with wakes self-similarity theory, according to which self-similarity holds only after a certain distance downstream of the obstacles. Moreover, the wakes of all the patches excluding C_7 and C_S (not represented) are self-similar, regardless of the patch density ϕ. This self similarity only holds at the mid height plane, but as it was notice in Chapter 5, the near wakes of the patches are about constant along the height of the obstacles, so, as a first approximation, this self similarity can be considered to hold for a major portion of the height of the wake.

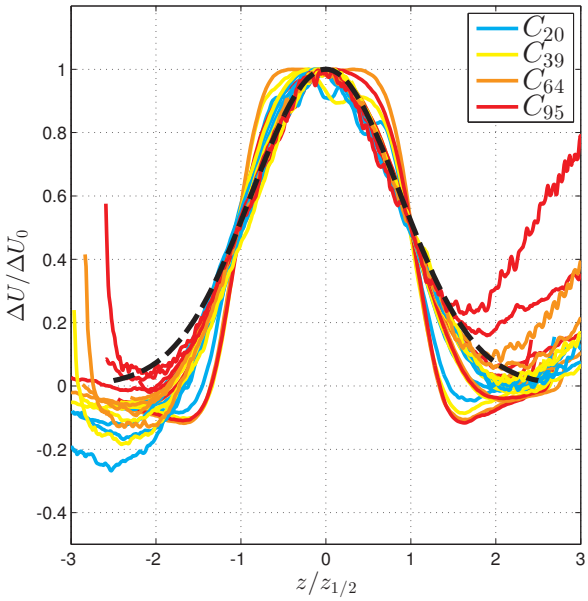

Figure 6.4: Superimposition of the normalised velocity deficit $\Delta U/\Delta U_0$ vs normalised lateral coordinate $z/z_{1/2}$ at six different longitudinal locations for all the patches. Dashed line, fitting of all the curves.

For self preserving wakes, the function $f(z/z_{1/2})$ in equation 6.1 should scale as

$$f(z/z_{1/2}) = exp\left(-\alpha\left(\frac{z}{z_{1/2}}\right)^2\right), \tag{6.2}$$

where α is equal to 0.693 for plane wakes of 2D obstacles (Pope, 2011). The exponential function was fitted to all the scaled profiles along x for all the patches with a non-linear least square method for $-2 < z/z_{1/2} < 2$. The fitting resulted in $\alpha = 0.756 \pm 0.001$ for the present data, with R-square equal to 0.97. The fitted curve is represented in Figure 6.4 as a dashed line. The value of α reduces to 0.714 ± 0.001 for $-1.5 < z/z_{1/2} < 1.5$ and to 0.653 ± 0.001 for $-1 < z/z_{1/2} < 1$, which means that the central part of the wake has the same scaled form as a 2D circular cylinder, while the tails differ from that case.

According to wake theory (see e.g. Wygnanski et al., 1986), the normalising lengthscale $z_{1/2}$ should vary as:

$$\frac{z_{1/2}}{D} \sim \left(C_D \frac{x - x_0}{D}\right)^{0.5}, \tag{6.3}$$

where x_0 is a virtual origin, which, in this thesis, was chosen to be equal to L_{min}, which is the x location of U_{min} along the centreline (U_{min} is the minimum U_0 along x). Figure 6.5 shows the two terms of equation 6.3, and a linear fit which was carried out for the positive values of $C_D(x - x_0)/D$, which confirms the linear trend of the equation. In particular, the fitting coefficients are $z_{1/2}/D = (0.135 \pm 0.002)(C_D(x - x_0)/D)^{0.5} + (0.461 \pm 0.002)$ with R-square equal to 0.81, and the fitting was carried out only for $(C_D(x - x_0)/D)^{0.5} > 0.4$, where the data

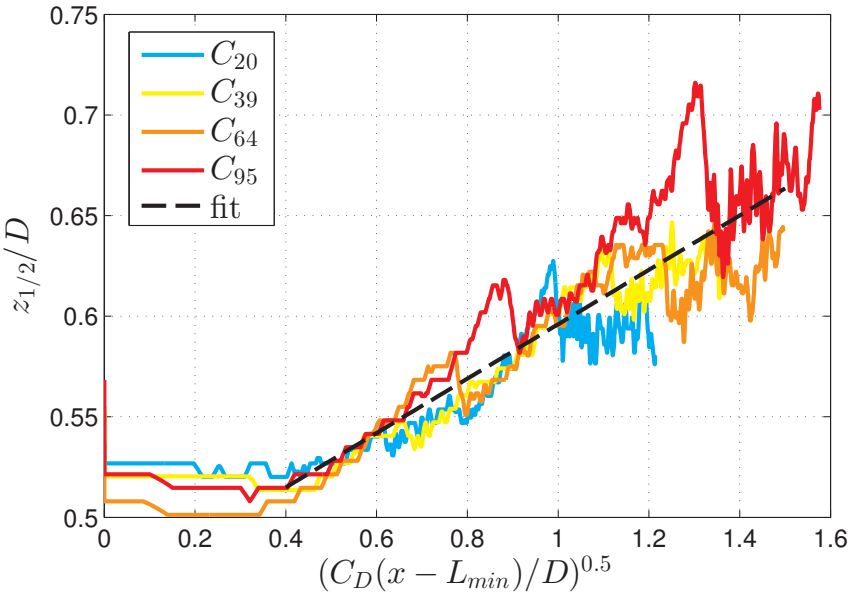

Figure 6.5: Self-similarity trend of the characteristic lengthscale $z_{1/2}$ vs $(C_D(x - x_0)/D)^{0.5}$ for different patches and linear fit.

is actually increasing. This is consistent with the fact that self-similarity in wakes only holds for some distances downstream, and not necessarily for near wakes. Furthermore, with this scaling of the abscissa, $z_{1/2}$ is independent of the patch density ϕ.

In the following section, an estimate for the maximum velocity deficit as a function of the density (ϕ) and the longitudinal coordinate (x) is empirically derived.

6.3 Velocity profiles along the centreline

A first check on the results obtained with the horizontal and the vertical PIV for the longitudinal velocity along the centreline was carried out and it is shown in Figure 6.6. The results seem comparable for all cases, and slight differences are present for the C_7 and C_{20} (where the velocity is slightly higher in the vertical PIV resuts), and for C_S which shows a faster recovery. A comparison of the fluctuating quantities, e.g. σ_U of the two sets of measurements and σ_W with σ_V (to compare the trends) are reported in Appendix E.

A first significant consideration on these plots is that, for 3D patches, there is no evident steady velocity region in the wake. According to Nicolle and Eames (2011), Zong and Nepf (2012), Chen et al. (2012) and Chang and Constantinescu (2015), a region of constant velocity forms downstream of the patch, where the velocity at the centreline of the models is constant and equal to the minimum velocity value in the wake. The extension of this region reduces with increasing density, and the wake behind the patches becomes similar to the wake behind the corresponding 2D solid cylinder with the same external diameter. In the present case it has already been shown in Chapter 4 that the wake behind a very dense patch does not correspond

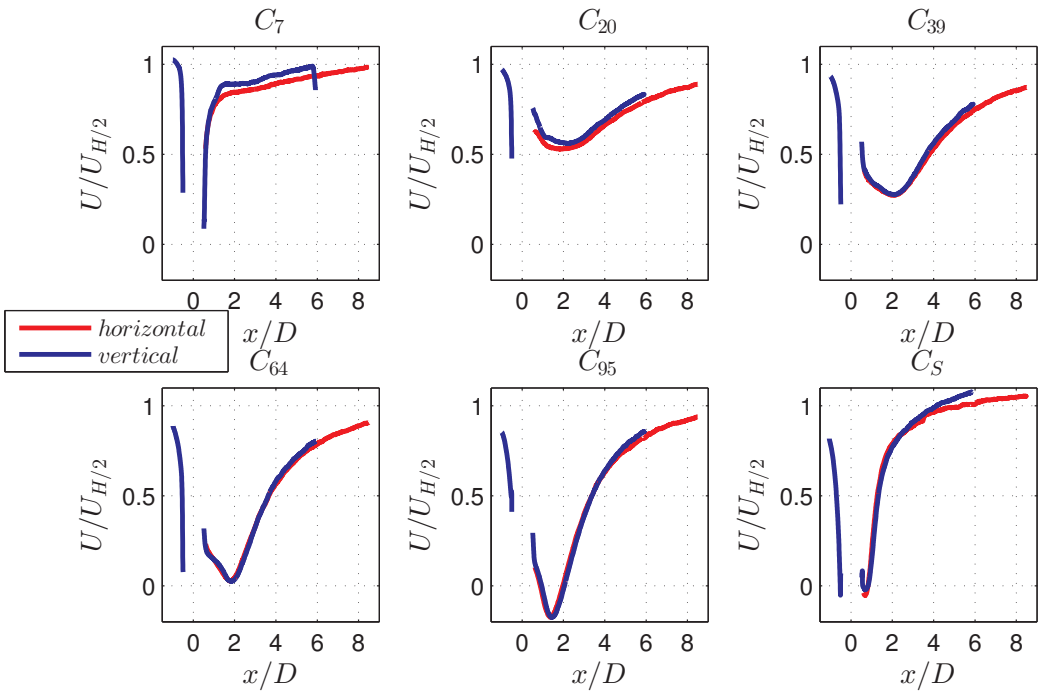

Figure 6.6: $U/U_{H/2}$ along x for all the patches: comparison between horizontal PIV results (red) and vertical PIV results (blue).

to the wake behind the correspondent solid case in 3D conditions. Furthermore, from Figure 6.6, it is also evident that in three dimensional patches, the presence of a steady velocity region is not as evident as in two dimensional cases. For the models C_{20} and C_{39} a short plateau of U_{min} can be detected, but it is much shorter compared to their two dimensional counterparts. This can be ascribed as an effect of the free end. Figure 4.10 in Chapter 4 shows the vorticity contours both in the vertical and in the horizontal mid-planes. The horizontal shear layers developing at the flanks of the patches resemble those of two dimensional patches. In particular, from the C_{20} plots it looks like these shear layers are far from merging at x/D = 3. For this case, at the same longitudinal location, the wake appears to have already recovered at the centreline. This means that the velocity recovery for 3D patches is mainly driven by the entrainment of fluid from the freestream over the wake (which has a higher velocity compared to the mid plane) than from the sides. This could be the reason why three dimensional patches show much shorter steady velocity regions for low densities, and do not show these regions at all for higher densities. This is in agreement with the fact that the drag coefficients for three dimensional patches are lower compared with the drag coefficient of two dimensional patches with comparable density (i.e. smaller wakes correspond to lower drag). A broader comparison with 2D results will be carried out in Section 6.6.

Before discussing the dependence of ΔU_0 on x, a scaling procedure for the velocity deficit profiles along the centreline for all the patches was carried out. Figure 6.7 (left) shows the non-dimensional velocity deficit $\Delta U/U_{H/2}$ along x at the centreline of the mid-height plane (i.e. $y/D = H/2$, $z/D = 0$) for all the patches. These velocity profiles correspond to the values

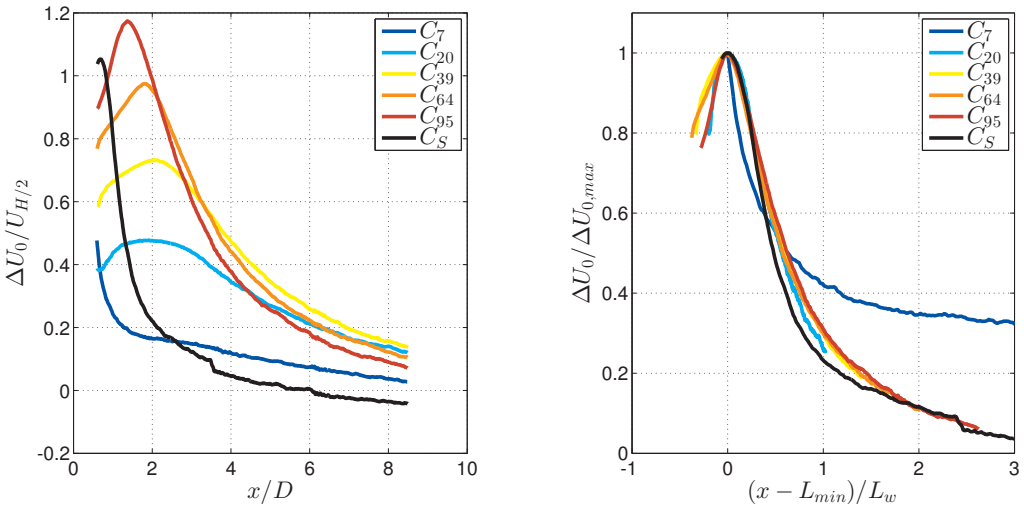

Figure 6.7: Left: $\Delta U_0/U_{H/2}$ along x at the mid-height plane (i.e. $y/D = H/2$) for all the patches. Right: scaled velocity deficit profiles vs the scaling length $(x - L_{min})/L_w$, where L_{min} is the x location of U_{min} and L_w ("vortex formation length") is the x coordinate of the peak in the turbulence intensity.

of ΔU_0 at the horizontal plane for all the x locations, therefore their development along x represent the self-similarity scaling function $\Delta U_0(x, \phi)$. It can be seen that the x location of the maximum shifts downstream with decreasing ϕ, while after $x/D = 4$ the curves seem to converge, as was previously shown for the horizontal measurements.

Figure 6.7 (right) shows appropriately scaled (and shifted using the virtual origin) streamwise development profiles of the wake recovery. The virtual origin, L_{min}, shifts the location of the maximum at the same coordinate. The second lengthscale, L_w, collapses all the curves; L_w is usually referred as "vortex formation length" or "wake formation length", and is the x coordinate where the peak in the turbulence intensity σ_W is located. The profiles of the turbulent fluctuations along the centreline (i.e. σ_U, σ_V and σ_W) are shown in Appendix E, and they show that the three standard deviations peaks are located at the same longitudinal coordinate. This length is referred to also in previous study (see e.g. Chen et al., 2012), and Castro (1971) states that this location corresponds to the approximate position of the vortex formation, if any vortex street is generated behind the patch. Both of these lengths are evaluated from the centre of the patch, differently from previous studies which evaluated it from the end of the patch. The values of these lengths for both the horizontal and vertical measurements are reported in Table 6.1, together with the density and the drag coefficients of each patch.

The streamwise translation of L_{min} is due to the fact that the bleeding at the trailing edge is different for different densities, and this causes the minimum to be translated further downstream for lower densities. This change in L_{min} essentially moves the origin for wake recovery, i.e. the location where wake recovery begins. Once, the origin is fixed, the near-field recovery of the wake appears to be well captured by L_w. This wake length scale captures the behaviour of the patch and does not account for the individual cylinders within the patch.

	C_7	C_{20}	C_{39}	C_{64}	C_{95}	C_S
ϕ	0.0175	0.05	0.0975	0.16	0.2375	1
C_D	0.10	0.24	0.32	0.36	0.37	0.21
L_{min}/D hor	0.59	1.91	2.12	1.84	1.37	0.68
L_{min}/D ver	0.66	2.23	2.06	1.86	1.43	0.69
L_w/D hor	0.68	6.41	4.53	3.29	2.71	1.17
L_w/D ver	0.55	5.48	4.02	3.13	2.54	1.05
$\Delta U_{0,max}/U_{H/2}$ hor	0.48	0.48	0.73	0.97	1.17	1.05
$\Delta U_{0,max}/U_{H/2}$ ver	0.73	0.45	0.73	0.98	1.17	1.02
U_{bTE}/U_∞	–	0.46	0.33	0.19	0.16	–
U_e/U_∞ hor	0.52	0.61	0.42	0.23	0.10	−0.04
U_e/U_∞ ver	0.48	0.72	0.42	0.21	0.14	−0.01

Table 6.1: ϕ is the patch density, C_D is the patch drag coefficient ($C_D = F_D/(1/2\rho U_\infty^2 HD)$). Measurements results for each patch from horizontal (hor) and vertical (ver) PIV measurements: L_{min}, is the x location of U_{min} (U_{min} is the minimum U along the centreline), L_w is the x coordinate where the peak in the turbulence intensity is located, $\Delta U_{0,max} = U_{H/2} - U_{min}$, U_{bTE}, mean longitudinal bleeding velocity at the trailing edge ($x/D = 0.52$), U_e bleeding velocity at mid-height at $x/D = 0.6$.

According to the self-similarity theory (see e.g. Wygnanski et al., 1986), the normalised velocity deficit at the centreline should vary as:

$$\frac{\Delta U_0}{U_{H/2}} \sim \left(\frac{x - x_0}{C_D D}\right)^{-0.5}. \tag{6.4}$$

The two terms of equation 6.4 are plotted against each other in Figure 6.8. It has to be noticed that the horizontal axis of this plot refers to x at the power -0.5, which means that the far wake of the patches is related to small values of the horizontal axis, while the near wake is related to higher values (i.e. the downstream direction is from right to left, for decreasing values of the abscissa).

It can be seen that, for the initial part of the curves (i.e. for the far wake), the trend of $\Delta U_0/U_{H/2}$ against $((x - L_{min})/C_D D)^{-0.5}$ is linear for all the patches, as expected from self-similarity equations. Furthermore, if ΔU_0 is non-dimensionalised with $\Delta U_{0,max}$ and $C_D D$ is substituted by L_w, all the curves collapse, as shown in Figure 6.9.

A linear fit was carried out and it resulted in $\Delta U_0/\Delta U_{0,max} = (0.597 \pm 0.02)((x - L_{min})/L_w)^{-0.5} - (0.301 \pm 0.02)$, with R-square equal to 0.99.

This result, together with the $z_{1/2}$ results, show that the wakes downstream of porous patches of obstacles are self similar, and can be scaled as shown in equation 6.1, provided that

$$f(z/z_{1/2}) = exp\left(-0.76\left(\frac{z}{z_{1/2}}\right)^2\right), \tag{6.5}$$

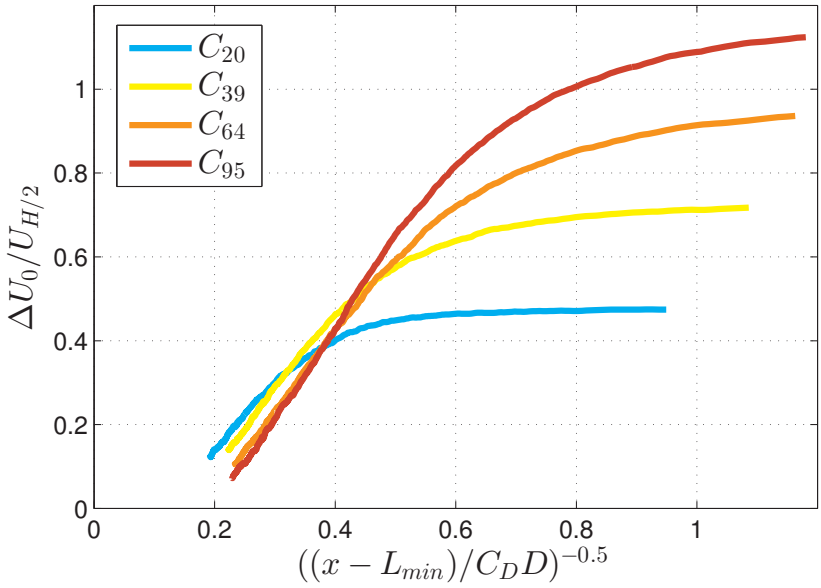

Figure 6.8: Self-similarity trend of the characteristic velocity scale $\Delta U_0/U_{H/2}$ vs $((x - L_{min})/C_D D)^{-0.5}$ for different patches and linear fit.

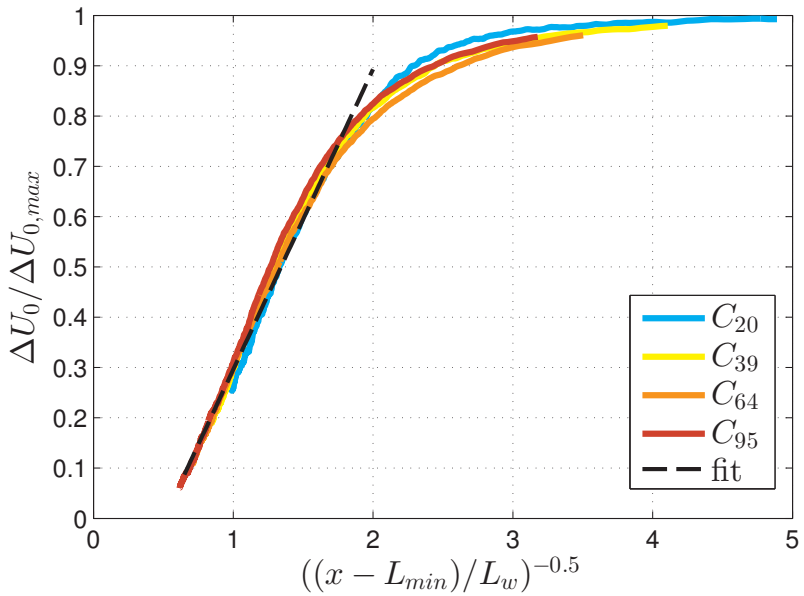

Figure 6.9: Self-similarity trend of the characteristic velocity scale $\Delta U_0/\Delta U_{0,max}$ vs $((x - L_{min})/L_w)^{-0.5}$ for different patches and linear fit.

$$\frac{\Delta U_0(x,\phi)}{\Delta U_{0,max}(\phi)} = 0.6\left(\frac{x - L_{min}(\phi)}{L_w(\phi)}\right)^{-0.5} - 0.3, \tag{6.6}$$

$$\frac{z_{1/2}(x,\phi)}{D} = 0.13\left[C_D(\phi)\frac{x - L_{min}(\phi)}{D}\right]^{0.5} + 0.5. \tag{6.7}$$

The coefficients evaluated from the fittings carried out so far are not exact, but give the order

of magnitude of the proportionality which holds between the terms of equations 6.1, 6.3 and 6.4, which are the equations for self-similarity in wakes. The dependence on the patch density ϕ is related only to L_{min}, $\Delta U_{0,max}$, L_w and C_D and will be studied in the following sections.

6.4 Dependence on ϕ of the scaling parameters

This section provides predictive models for the trends of L_w, L_{min}, C_D and $\Delta U_{0,max}$ with changing in ϕ. Except for C_D, all the other parameter changes with changes in height, as it was shown in Chapter 5. However, as a first approximation, the scaling laws that will be found in this section, can be considered to be constant in the near wake for a major portion of the height of the model.

6.4.1 Vortex formation length L_w

L_w, "vortex formation length" or "wake formation length", is the x coordinate where the peak in the turbulence intensity σ_W is located and corresponds to the approximate position of the vortex formation, if any vortex street is generated behind the patch.

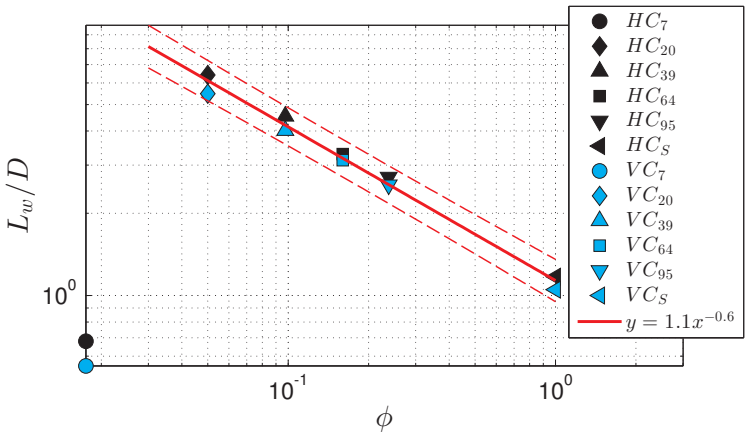

Figure 6.10: L_w/D vs ϕ for all the patches, for the horizontal (black) and vertical (blue) PIV measurements, and a power law fitting (red) evaluated for C_{20}, C_{39}, C_{64}, C_{95} and C_S with confidence interval (dashed line).

Figures 6.11 shows the trend of L_w/D against ϕ, for both the horizontal measurements (black) and the vertical measurements (blue). The vortex formation length decreases with increasing density, which is in agreement with the fact that the downstream shifting of the wake due to the trailing edge bleeding is reduced for increasing density, and this is confirmed by the fact that, for C_{64} and C_{95} the recirculation bubble was shifted more upstream for the denser model. Due to the less intense bleeding velocity, the shear layers develop faster and thei interaction location (which corresponds to L_w) is moved upstream, i.e. reduces.

It is evident that L_w shows a power trend with respect to ϕ, excluding C_7 but including C_S. A linear fit with a non-linear least square method was carried out in the log-log space. This is represented in the Figure by the red line and expresses the following function:

$$\frac{L_w}{D} = (1.1 \pm 0.15)\phi^{(-0.60\pm0.05)}, \tag{6.8}$$

with R-square of the fitting equal to 0.98.

6.4.2 Drag coefficient C_D

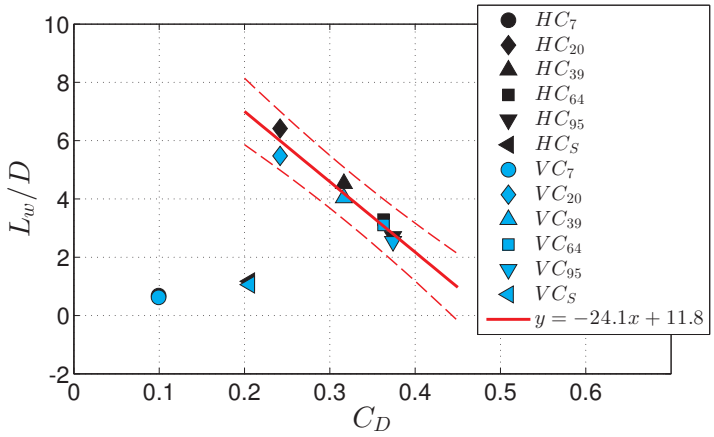

Figure 6.11: L_w/D vs C_D for all the patches, for the horizontal (black) and vertical (blue) PIV measurements, and a linear fitting (red) evaluated for C_{20}, C_{39}, C_{64} and C_{95} with confidence interval (dashed line), evaluated as the prediction bounds of the fitting.

From Figure 6.11, L_w shows a linear trend with respect to C_D, at least for all the patches excluding C_7. A linear fit to the data results in:

$$\frac{L_w}{D} = (-24.1 \pm 5.7)C_D + (11.8 \pm 1.9), \tag{6.9}$$

with R-square = 0.96. The fact that L_w shows a linear trend with C_D means that this length is proportionally related to the drag coefficient of the patch. This confirms that this length is the appropriate lengthscale to scale the velocity profiles among different patches because it is representative of the patch drag, which in turn is related to the velocity deficit and extension of the wake. This is also consistent with the fact that by substituting $C_D D$ with L_w in equation 6.4, the results still scale appropriately.

By substituting equation 6.8 in equation 6.9, a prediction law for C_D with ϕ can be found as:

$$C_D = \frac{11.8 - 1.1\phi^{-0.6}}{24.1} = (0.5 \pm 0.2) - (0.05 \pm 0.02)\phi^{(-0.60\pm0.05)}, \tag{6.10}$$

where the errorbars are evaluated considering the bounds of the two fittings, and this result is shown in Figure 6.12, red line. The red bounds for this prediction were evaluated by means of the error propagation theory, considering the bounds of each coefficient of the predictions as the absolute error on each quantity.

A direct linear fitting for $C_D - \phi$ in the log-log space was carried out, but the prediction bounds of the fitting were huge, and the accuracy of the curve was worse than the predictive law in equation 6.10. This is normal, considering that we were trying the fitting procedure over 5 data points which are not a robust set of data. The fitting carried out for L_w is for a greater number of data points (i.e. 8 points for the first fitting and 10 points for the second) and this makes the prediction law in equation 6.10 more robust. For all these reasons, equation 6.10 will be used hereafter.

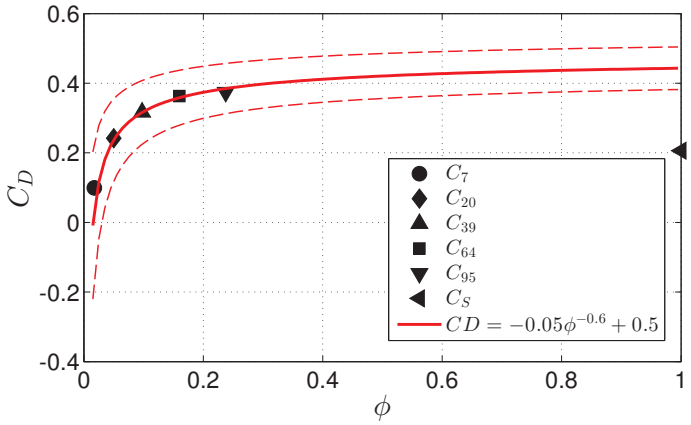

Figure 6.12: C_D vs ϕ for all the patches and predicting law evaluated in equation 6.10 with confidence interval (dashed line). The confidence intervals were evaluated as the error propagation values for the predictive law.

From this figure it looks like that, despite the fact that C_7 was always excluded from the fitting, this prediction law fits the C_D value of this patch as well. According to this model, the trend of C_D for $0.35 < \phi < 1$ is always increasing, and the gap of data in this range makes it hard to predict whether there is a threshold density value to which corresponds an abrupt drop of C_D, or whether C_D reaches a peak and then decreases up to the value of the solid case. Despite the fact that it is not clear up to which density this law holds, it can be said that it works properly for the range of densities investigated herein.

6.4.3 Maximum velocity deficit $\Delta U_{0,max}$

Figure 6.13 shows how the maximum velocity deficit $\Delta U_{0,max}/U_{H/2}$ varies with the drag coefficient C_D for both the horizontal measurements (black) and the vertical measurements (blue), respectively. As expected, the maximum velocity deficit along the centreline increases with increasing drag, since the momentum loss is higher for higher $\Delta U_{0,max}$.

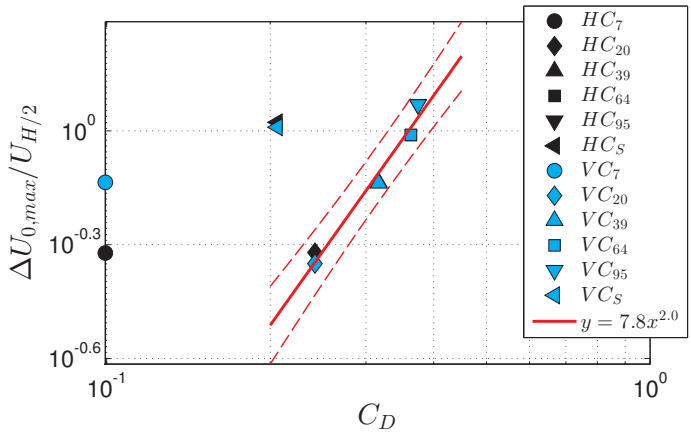

Figure 6.13: $\Delta U_{0,max}/U_{H/2}$ vs C_D for all the patches, and the predicting law evaluated in equation 6.11 with confidence interval (dashed line) evaluated as the prediction bounds of the fitting.

$\Delta U_{0,max}/U_{H/2}$ shows a power law trend with respect to C_D, at least for all the patches excluding C_7. A power law fit with a non-linear least square method is represented in Figure 6.13 (red), and results in:

$$\frac{\Delta U_{0,max}}{U_{H/2}} = 7.8(5.3 \div 11.6)C_D^{2.0\pm0.3}, \tag{6.11}$$

with the R-square of the fitting equal to 0.97. By substituting equation 6.10 in equation 6.11 we obtain a predictive law for $\Delta U_{0,max}/U_{H/2}$ as a function of C_D.

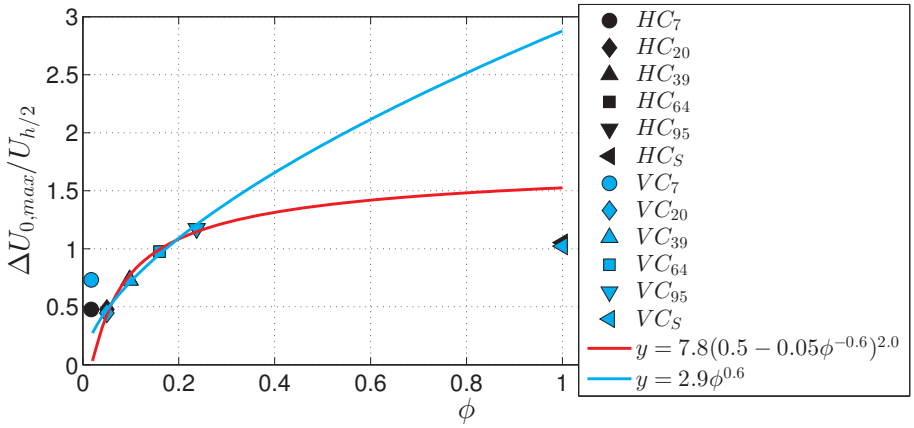

Figure 6.14: $\Delta U_{0,max}/U_{H/2}$ vs ϕ for all the patches from horizontal PIV (black) and vertical PIV (blue), and the predicting law evaluated by substituting equation 6.10 in equation 6.11 (red). Direct fit of the data (blue line).

The trend of $\Delta U_{0,max}/U_{H/2}$ vs ϕ is shown in Figure 6.14, together with the predictive law (red), which shows that the relation between C_D and ϕ fits well the velocity deficit. The bounds for this prediction law are quite high, due to the effects of propagation error within the three different fit, so they are not reported in Figure 6.14. A direct fit of $\Delta U_{0,max}/U_{H/2}$ vs ϕ with a power law was carried out as well, and it is shown in Figure 6.14. It is evident how this fit is in

agreement with the predictive law for the ranges of ϕ studied herein, but it strongly diverges for higher values of density. Physically, the fact that the maximum velocity deficit converges towards a "constant" value is more meaningful, since the drag coefficient converges (or seems to converge for the data showed herein) and the wake dimension is fixed, which means that higher densities are expected to have similar wakes, at least for densities slightly higher than 0.25 and this is not the case for the direct fit law.

6.4.4 Minimum velocity location L_{min}

L_{min} is the x location of U_{min} along the centreline (U_{min} is the minimum U_0 along x), and corresponds to the location of $\Delta U_{0,max}$.

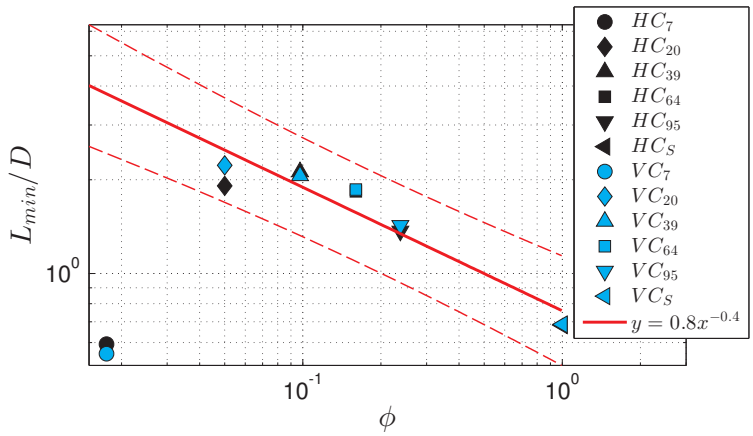

Figure 6.15: L_{min}/D vs ϕ for all the patches, for the horizontal (black) and vertical (blue) PIV measurements, and a linear fitting (red) evaluated for C_{20}, C_{39}, C_{64}, C_{95} and C_S with confidence interval (dashed line).

Figures 6.15 shows the trend of L_{min}/D vs ϕ, for both the horizontal measurements (black) and the vertical measurements (blue). As expected, L_{min} decreases with increasing ϕ, due to the decreasing of the bleeding velocity, which reduces the wake downstream shifting, and to the faster development of the shear layers, which fastens the velocity recovery.

L_{min} shows a power-law trend with respect to ϕ, at least for all the models excluding C_7. A power law fit with a non-linear least square method was carried out, it is represented in the Figure as well (red) and it results in:

$$\frac{L_{min}}{D} = (0.8 \pm 0.2)\phi^{(-0.4\pm0.1)}, \tag{6.12}$$

with R-square= 0.90. It is evident from the bounds of the coefficient that this fitting is not ideal. Excluding the results from the patch C_7, which are of course unrealistic in this scenario (i.e. the minimum velocity for this patch corresponds to the wake of the single cylinder inline with the centreline, therefore it is not representative of the patch behaviour), from Figure 6.15 it appears that L_{min} for C_{20} and C_{39} are very similar. The vertical and horizontal values of C_{20}

are not in good agreement, and while the vertical measurements shows an increase compared to C_{39}, the horizontal value is actually lower. The uncertainty in defining the location of the minimum for the C_{20} model is mainly due to the presence of the plateau (see Figure 6.6), so it is not straightforward to understand whether the location of the minimum in velocity is constant below a certain density, or whether it keeps on increasing with decreasing density. More cases of patches with density in the range between 0.05 and 0.1 could help to better understand the trend of L_{min} in this range of ϕ.

6.5 Bleeding longitudinal velocity U_e

The location of the minimum in longitudinal velocity along the centreline could be related to the bleeding longitudinal velocity downstream of the patch. The average longitudinal bleeding velocity U_{bTE} was defined in Chapter 4, and is reported again in table 6.1. This bleeding velocity is evaluated from the vertical PIV data averaging the bleeding along the trailing edge of the patch. A second characteristic bleeding velocity U_e was evaluated from both horizontal and vertical data as the longitudinal velocity component at x/D = 0.6 and is reported in table 6.1. Both U_{bTE} and U_e are related to U_{out} discussed in section 4.7, which is evaluated in between the x location of the previous two. Figure 6.16 shows that the two characteristic

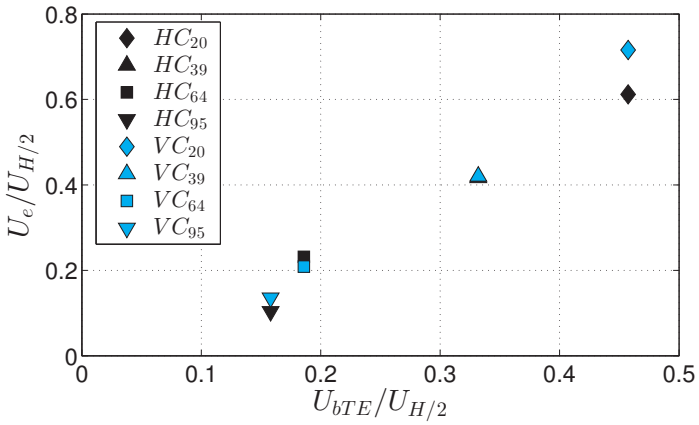

Figure 6.16: $Ue/U_{H/2}$ vs $UbTE/U_{H/2}$, for the horizontal (black) and vertical (blue) PIV measurements.

bleeding velocities (and therefore U_{out}) are linearly related. U_e was evaluated at x/D = 0.6 in order to have a value for both the vertical and the horizontal measurements, while U_{bTE} and U_{out} are evaluated at x/D = 0.52 and x/D = 0.55 (respectively) and are available only for the vertical measurements. Chen et al. (2012) state that the velocity downstream of the patch has a linear decrease from the value at the exit point, down to the steady velocity value, and this is confirmed also from Figure 6.6, therefore, U_e can be used as a reference value for the bleeding velocity even though it is not the exact bleeding velocity at the trailing edge at the mid-height plane, but it is linearly related to it, and to the average bleeding velocity.

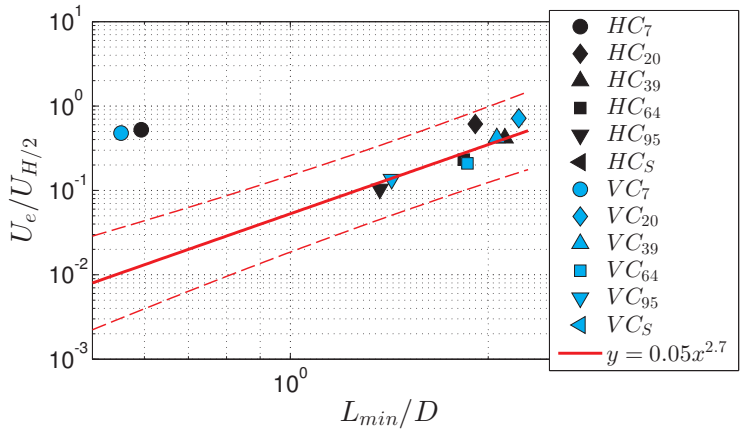

Figure 6.17: L_{min}/D vs $Ue/U_{H/2}$, for the horizontal (black) and vertical (blue) PIV measurements, and a power law fitting (red) evaluated for C_{20} (ver), C_{39}, C_{64}, C_{95} and C_S with confidence interval (dashed line).

Figures 6.17 shows the trend of $Ue/U_{H/2}$ vs L_{min}/D for both the horizontal measurements (black) and the vertical measurements (blue). $Ue/U_{H/2}$ shows a power-law trend with respect to L_{min}/D, at least for all the models excluding C_7 and the horizontal value for C_{20}. A power law fit with a non-linear least square method was carried out, it is represented in the Figure as well (red) and it results in:

$$\frac{Ue}{U_{H/2}} = (0.05 \pm 0.03)\left(\frac{L_{min}}{D}\right)^{(2.7\pm0.7)}, \tag{6.13}$$

where the R-square of the fitting is 0.92. It is evident from the bounds of the coefficient that this fitting is not very accurate, but still, some considerations on the average results, regardless of the bounds, can be drawn. Excluding the horizontal value of C_{20} the trend makes perfect sense: as the bleeding longitudinal velocity increases (i.e. lower ϕ), the location of the minimum moves downstream with a law expressed in equation 6.13.

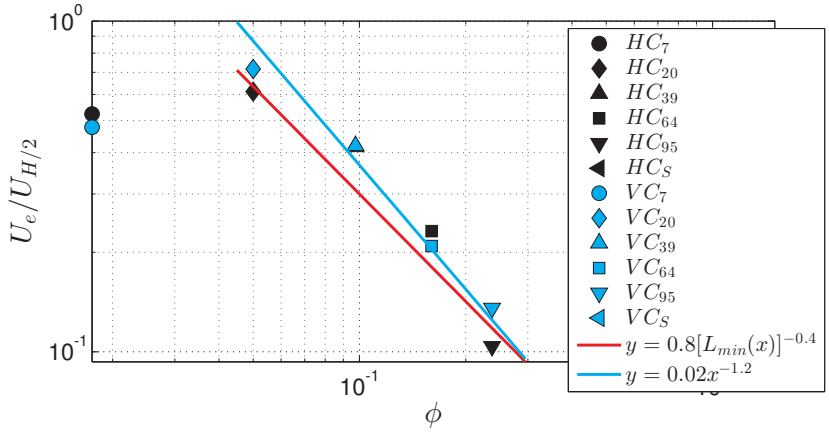

Figure 6.18: $Ue/U_{H/2}$ vs ϕ, for the horizontal (black) and vertical (blue) PIV measurements, and the predictive law

By substituting equation 6.12 in equation 6.13, we obtain a predictive law for $U_e/U_{H/2}$ as a function of ϕ. The trend of $U_e/U_{H/2}$ vs ϕ is shown in Figure 6.18, together with the predictive law (red), which shows that the relation between L_{min} and ϕ does not fit too well the bleeding velocity trend. The bounds for this prediction law are quite high, due to the effects of propagation error within the three different fit, so they are not reported in Figure 6.18. A direct fit of $U_e/U_{H/2}$ vs ϕ with a power law was carried out as well, an it is shown in Figure 6.18, blue line. It results in

$$\frac{Ue}{U_{H/2}} = (0.02 \pm 0.01)\phi^{-1.2\pm0.3}, \tag{6.14}$$

with R-square equal to 0.94. The coefficient bounds are quite broad for this fitting as well, but it is evident how this fit fits better the experimental data. This is probably due to the fact that the fitting of L_{min}/D vs ϕ is not really accurate (R-square 0.90), and in this case there are enough data points to neglect the dependence of the fitting on the starting point.

6.6 Comparison with 2D data

The first comparison with 2D results is carried out for the velocity deficit data. Both from Figure 6.13 and 6.14 it is evident that the patches C_7 and C_{20} have a comparable $\Delta U_{0,max}/U_{H/2}$, despite having different drag coefficient. The values of $\Delta U_{0,max}/U_{ref}$ from Chen et al. (2012) for low densities (i.e. $\phi < 0.05$) are all included around 0.45 ± 0.4 except case 5, which are in close agreement with the values found in the present work, regardless of the values of $C_{Di}aD$ or of the ratio D/d. The values of $\Delta U_{0,max}/U_{ref}$ from Chen et al. (2012) are plotted in Figure 6.19 and 6.20.

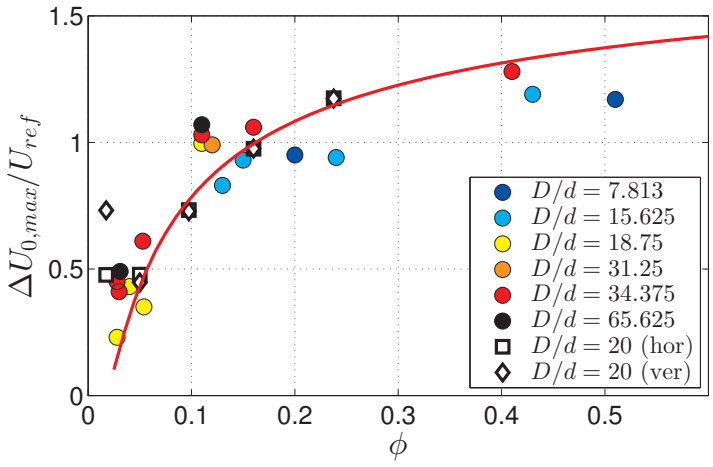

Figure 6.19: $\Delta U_{0,max}/U_{ref}$ vs ϕ from Chen et al. (2012) highlighting the different D/d. Hollow symbols are for the present study, and the red line is the prediction law found in section 6.4.3.

From Figure 6.19, for higher densities, this agreement becomes less consistent for highest values of densities, and it seems that the ratio D/d affects the discrepancies with the prediction

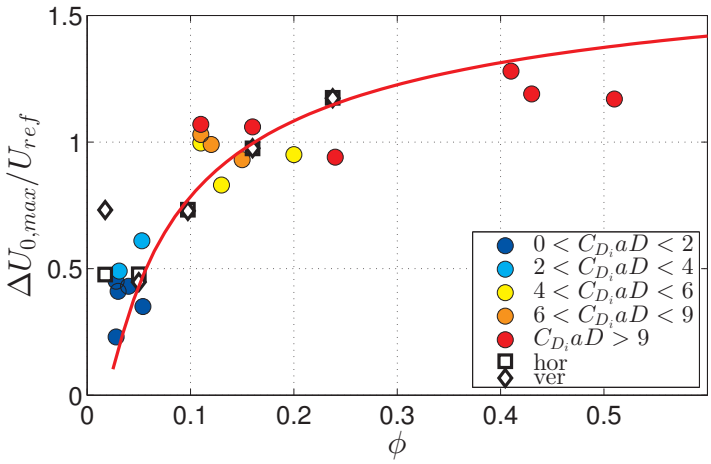

Figure 6.20: $\Delta U_{0,max}/U_{ref}$ vs ϕ from Chen et al. (2012) highlighting the different $C_{Di}aD$. Hollow symbols are for the present study, and the red line is the prediction law found in section 6.4.3.

law and the data from Chen et al. (2012). In particular, it seems that for lower values of D/d, $\Delta U_{0,max}/U_{ref}$ is lower than expected and vice versa. The worst agreement for $\phi > 0.05$ is found for the extreme values of D/d, while it reduces for intermediate values. Figure 6.20 also shows the same plot distinguishing among different $C_{Di}aD$. In this case the effect of $C_{Di}aD$ are not straightforward as they were for D/d. It seems that similar $C_{Di}aD$ have comparable values of $\Delta U_{0,max}/U_{ref}$, as it is stated in Chen et al. (2012).

It has to be noticed that Figure 6.19 and Figure 6.20 are a comparison between 2D and 3D data, and it is surprising to find such a good agreement. It can be suggested that the three dimensionality of the patch influences mainly the far wake development, while the maximum velocity deficit in the wake at the mid plane mainly depends on the two dimensional sectional characteristics of the patch. In particular, the top shear layer drives the characteristic lengthscales of the wake, while the characteristic velocity scales are set by the 2-D sectional properties of the patches, regardless of the free end effects.

A deeper comparison for the velocity profiles for similar values of densities with different D/d is reported in Appendix D.

6.7 Summary

This Chapter presents the scaling and self-similarity of wakes downwind of porous patches, which, as a first approximation, holds for most of the patch height, at least in the near wake.

Firstly the profiles were represented with the usual velocity deficit ΔU, and it was observed to scale with $\Delta U_{0,max}$ and $z_{1/2}$. This shows that the wakes of porous patches are self similar if scaled with the appropriate velocity and length scales.

By fitting empirical relations, consistent with self-similarity hypothesis, the trend of $z_{1/2}(x, \phi)$ against x was found and it is independent on the patches density. Furthermore, the non-dimensional velocity deficit curve (i.e. $f(z/z_{1/2})$) which defines the shape of $\Delta U/\Delta U_0$ profiles (see equation 6.1) was fitted along the wake and ws found to be consistent with 2D studies. Similar considerations were drawn for $\Delta U_0(x, \phi)$, and appropriate scaling laws were found to collapse the data.

The relation between the location of the minimum velocity in the wake and the bleeding longitudinal velocity U_e was finally investigated, in order to find an appropriate scaling for U_{out} used in the previous Chapter to non-dimensionalise the average drag coefficient of each cylinder C_{Di}.

The longitudinal velocity profiles along the centreline for different patches were analysed, and it is evident that for 3D cases the general length of the wake is shorter, and that the steady velocity region is much shorter compared to 2D cases, or even not present. This is ascribed to the effects of the free end, which hastens the velocity recovery and reduces the wake extension (and the drag). The comparison of the trend of the non-dimensionalised maximum velocity deficit $\Delta U_{0,max}/U_{H/2}$ with ϕ between 2-D and 3-D cases shows a dependence on D/d, but there is a good agreement within the 2D and 3D data which suggests that the three dimensionality has an influence on the far wake development, while the near wake characteristics depend only on the sectional properties (i.e. 2D) of the patch.

Chapter 7

Wake fluctuations analysis

7.1 Introduction

This Chapter presents a description of the fluctuating quantities along the horizontal and vertical plane. The results for the C_7 cases, both along the horizontal and vertical directions, are reported in Appendix C, since they do not exhibit any emergent group behaviour. Appendix C also shows the contours of the Reynolds stresses along the horizontal plane ($\overline{uw}/U^2_{H/2}$) and along the vertical plane ($\overline{uv}/U^2_{H/2}$) for completeness but are not strictly necessary to discuss the results presented in this Chapter. The results confirm what was already found in previous Chapters in terms of very near wake and near wake. Furthermore, they suggest presence of an alternate vortex street behind all the patches.

7.2 Fluctuations at the vertical symmetry plane

Figures 7.1 and 7.2 shows the dimensionless standard deviation of the longitudinal velocity component, $\sigma_U/U_{H/2}$ and the dimensionless standard deviation of the vertical velocity component $\sigma_V/U_{H/2}$, along the vertical plane for all the patches. $U_{H/2}$ was chosen as the non dimensionalising velocity in order to be consistent with the following section, which shows second order statistics at the mid-height plane.

From Figure 7.1 it is evident that σ_U increases in correspondence of the top shear layer (see Figure 4.10), which means that the bulk of the longitudinal fluctuations is ascribed to the top shear layer growth. From Figure 7.2, it can be seen that the bulk of the vertical fluctuations happens in correspondence of the end of the recirculation bubble (if present), where the free flow starts to be entrained in the wake. For the models C_{20} and C_{39}, for which no recirculation bubble is present, the wake entrainment starts gradually following the top shear layer growth. The intensity of σ_U and σ_V increases with increasing density. This is consistent with the findings of previous Chapters, confirming that the higher the density, the more intense the top

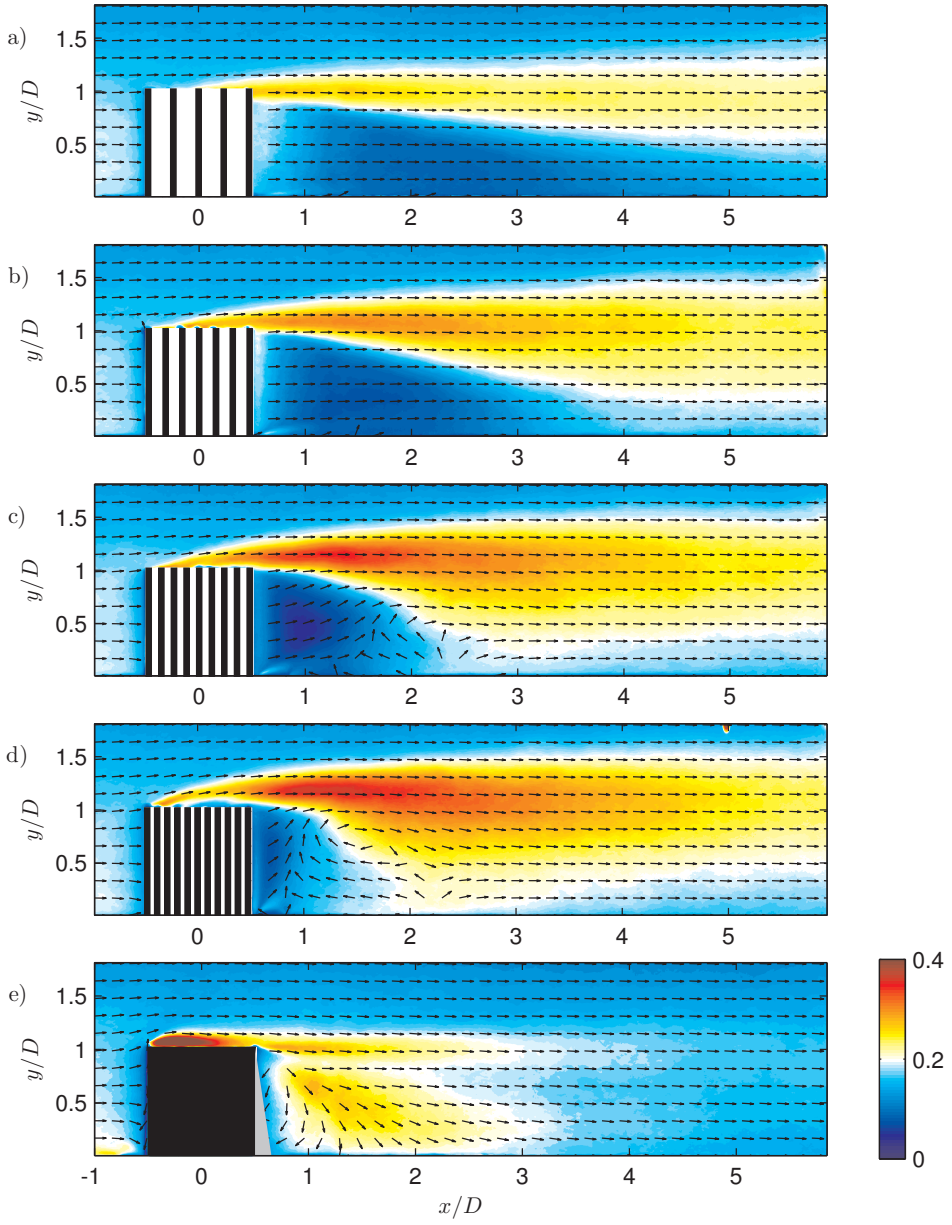

Figure 7.1: Plots of $\sigma_U/U_{H/2}$, where $U_{H/2}$ is the incoming velocity of the boundary layer at mid height (y/D = 0.5). The vector field only indicates the flow direction, but not its intensity (the length of the vectors is not proportional to their intensity). Only one vector every 35 vectors is represented. (a) C_{20}, (b) C_{39}, (c) C_{64}, (d) C_{95} and (e) C_S.

shear layer, and therefore, the more intense is the wake entrainment and momentum transfer induced in the wake.

Figures 7.3 and 7.4 show the profiles of $\sigma_U/U_{H/2}$ and $\sigma_V/U_{H/2}$ along y, respectively, at five different streamwise locations. Both Figures show that there is a region downwind of the

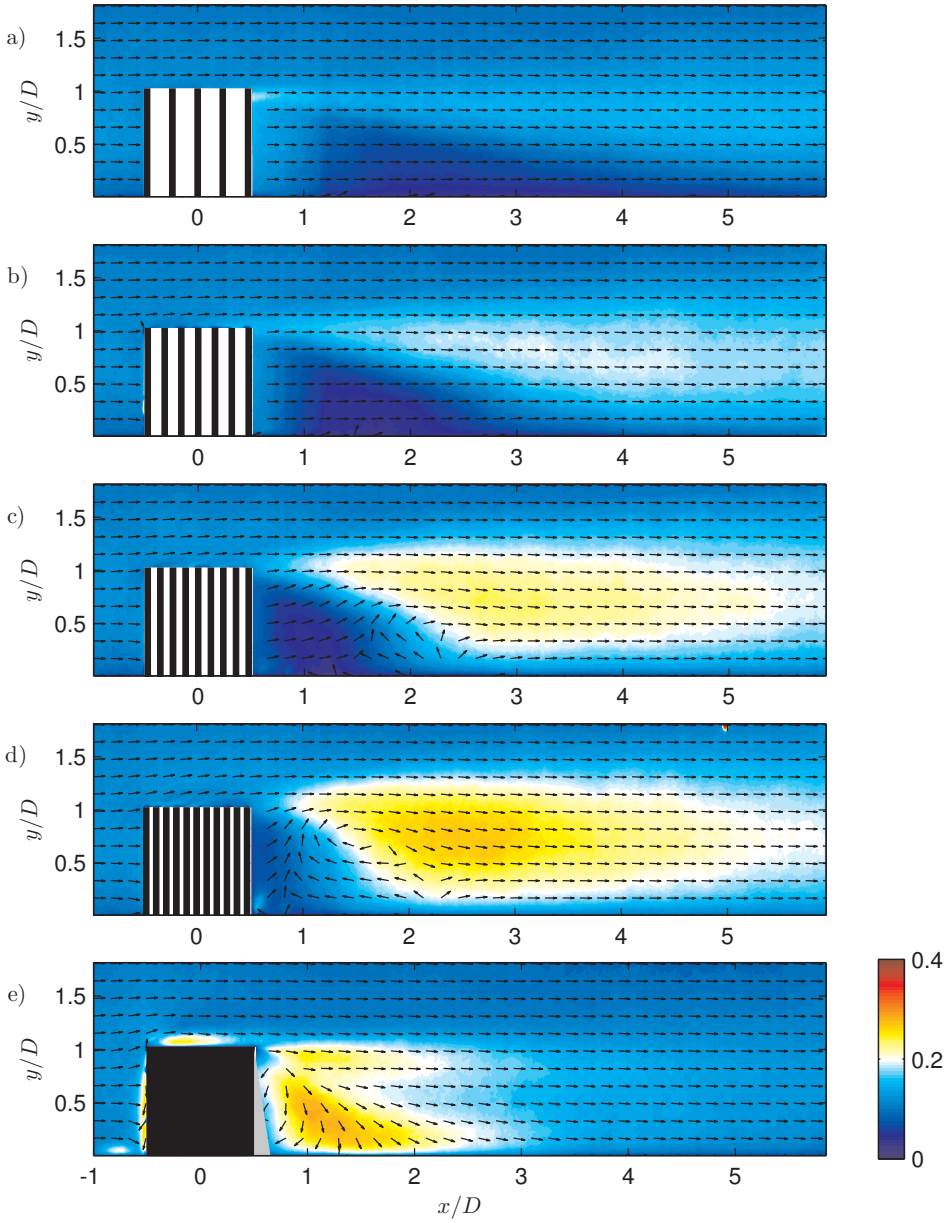

Figure 7.2: Plots of $\sigma_V/U_{H/2}$, where $U_{H/2}$ is the incoming velocity of the boundary layer at mid height (y/D = 0.5). The vector field only indicates the flow direction, but not its intensity (the length of the vectors is not proportional to their intensity). Only one vector every 35 vectors is represented. (a) C_{20}, (b) C_{39}, (c) C_{64}, (d) C_{95} and (e) C_S.

patches where this second order statistics are constant (very near wake), and this region shrinks in height moving downstream. At x/D = 5.5 a good collapse among the curves is obtained both for σ_U and σ_V. In this case the collapse is less satisfactory than what was found for the mean velocities, especially for the C_{20} case. However, the trends of the profiles for the C_{20} case suggest that a better collapse could be obtained further downstream and the field of view was

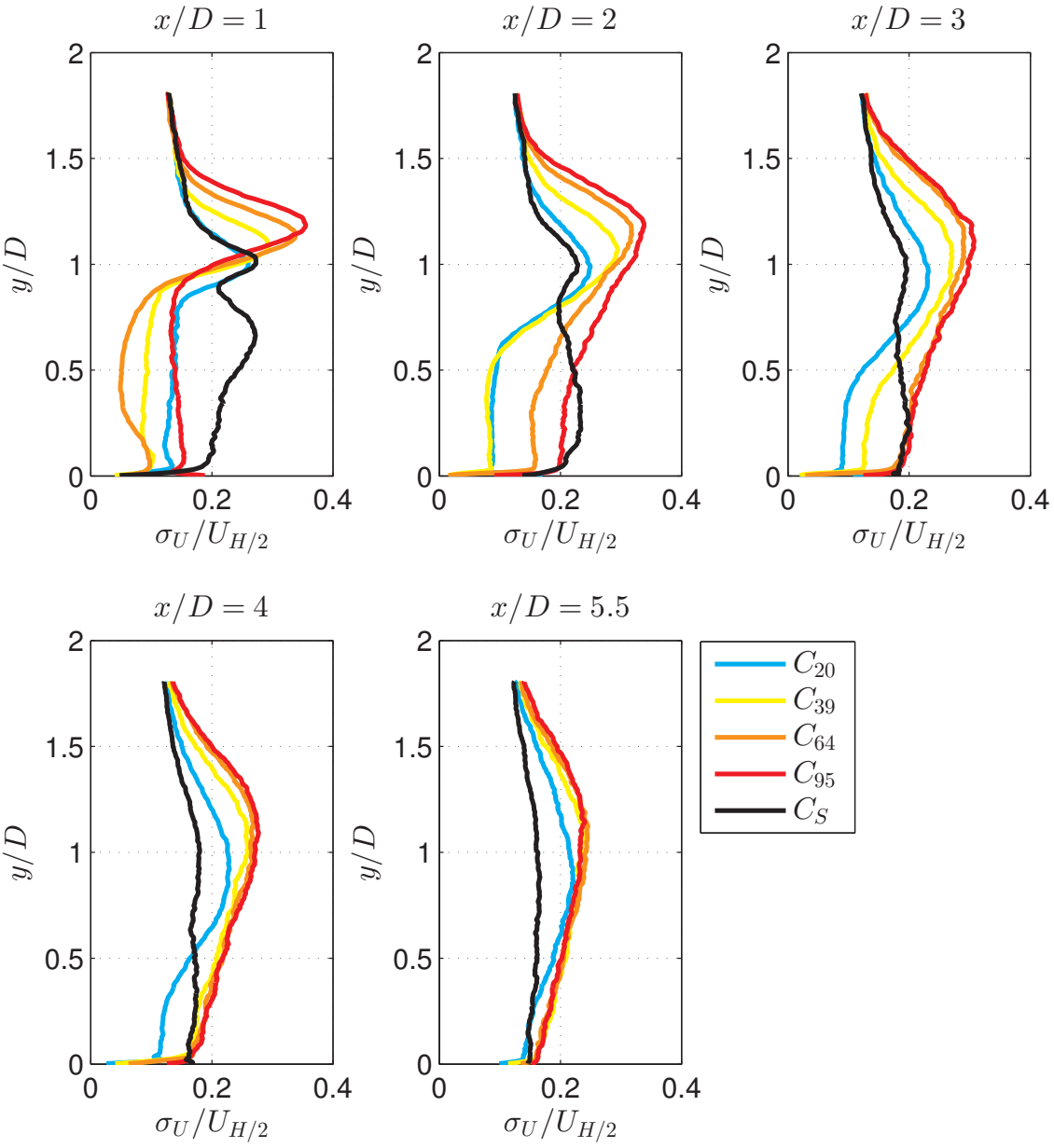

Figure 7.3: $\sigma_U/U_{H/2}$ along y at five different streamwise locations for all the patches.

not long enough to capture it. The far wake downstream of $x/D = 5.5$ needs to be investigated more in detail because the collapse of second order statistics may occur more far away from the patches.

At $x/D = 1$ for all the patches σ_U (Figure 7.3) exhibits a constant region for almost the whole height of the patch. For C_{20} and C_{95} the intensity of σ_U in this region is comparable, while it diminishes for C_{39} and for C_{64}. This could be due to two different reasons. For the C_{20} case, this high level of σ_U can be ascribed to the recirculation regions forming behind each obstacle within the patch. For the C_{95} case, the high level of σ_U can be ascribed to the patch-scale

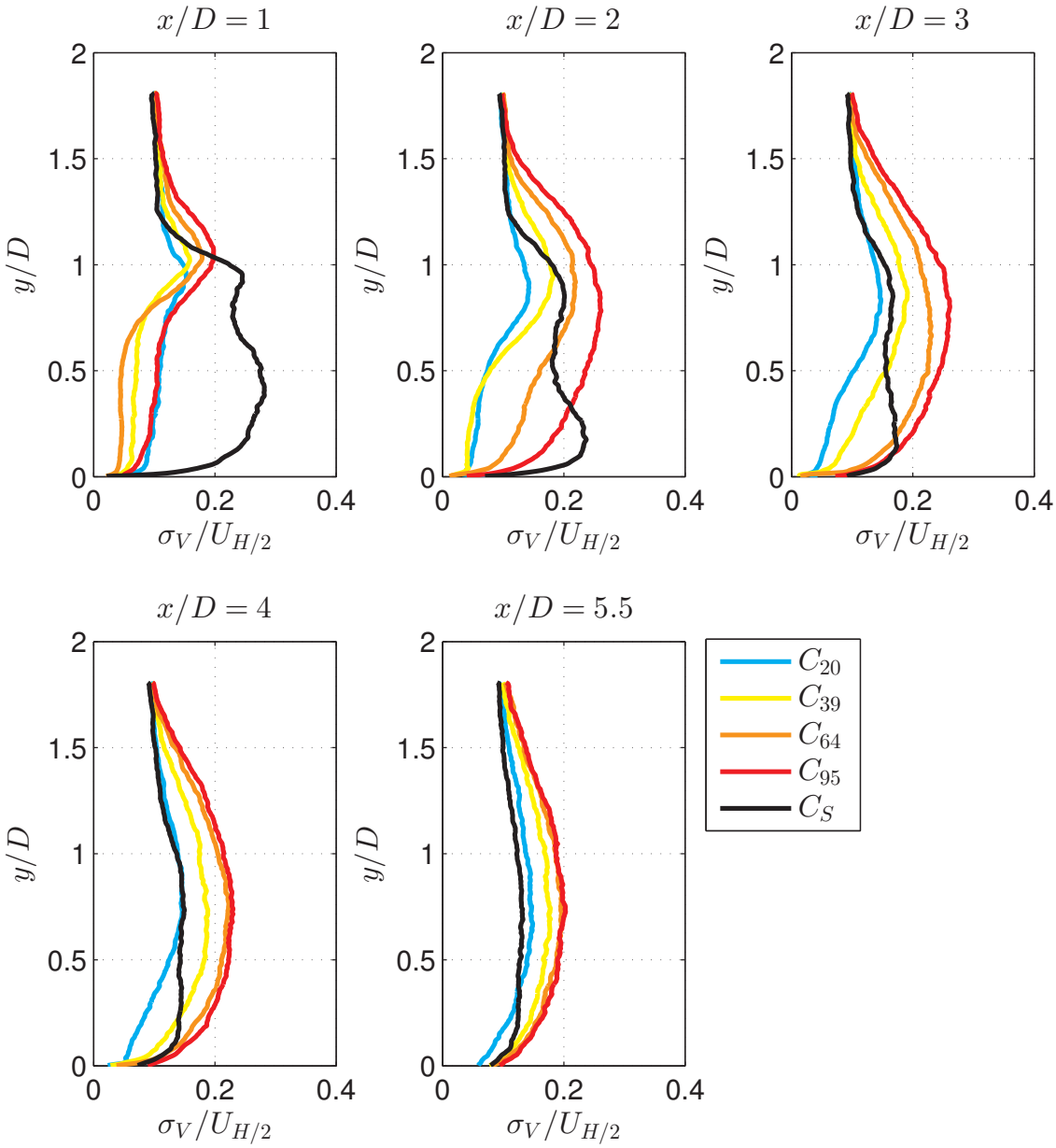

Figure 7.4: $\sigma_U/U_{H/2}$ along y at five different streamwise locations for all the patches.

recirculation region. In fact, with increasing density the influence of the individual cylinder wakes is reduced along x, due to the loss in U_{bTE}, and the patch-scale dynamics start to take over. The characteristic lengthscales associated to the high values of turbulence intensity will be further investigated in section 7.4.

7.3 Fluctuations at the mid-height plane

Figures 7.5 shows the mean non dimensionalised longitudinal velocity fluctuations, $\sigma_U/U_{H/2}$ along the horizontal plane, where $U_{H/2}$ is the incoming velocity of the boundary layer at the plane of the measurements (y/D = 0.5).

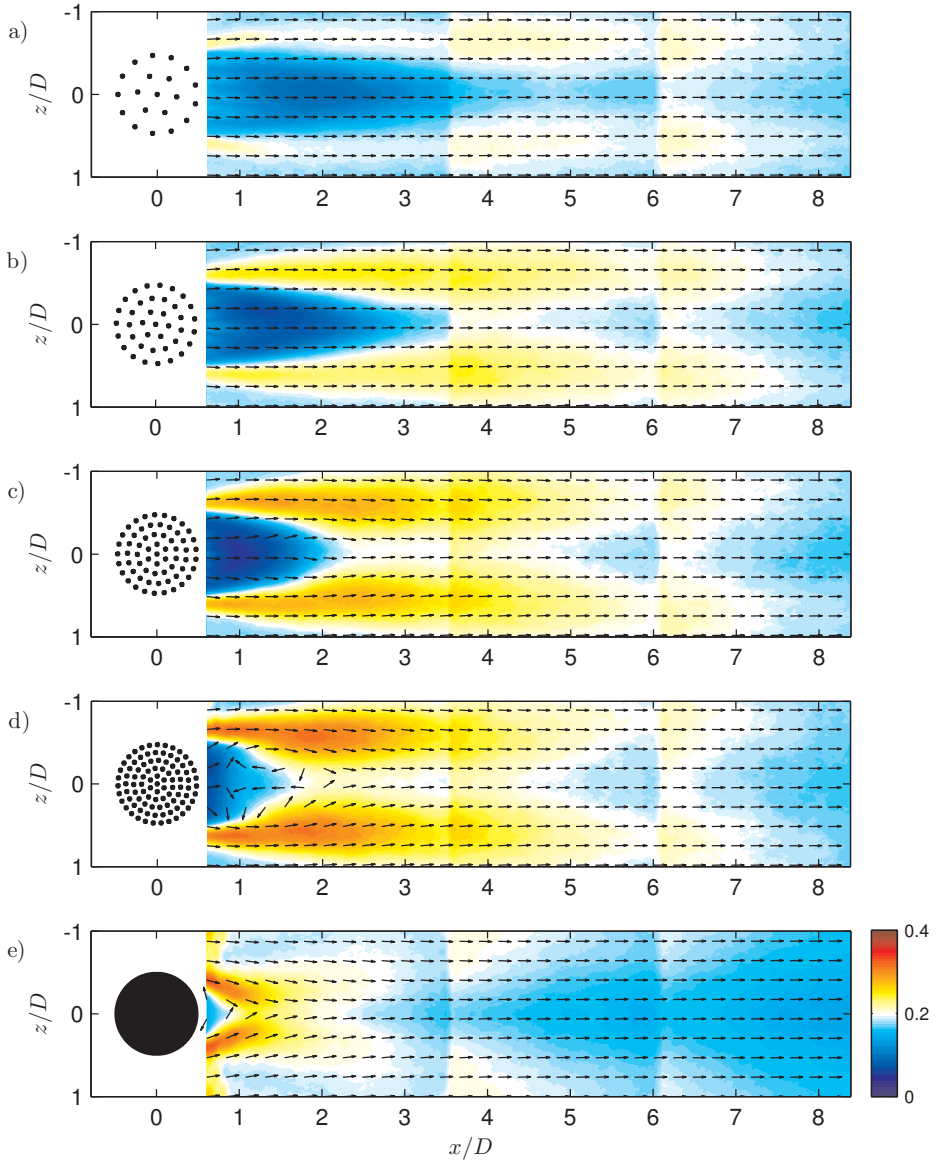

Figure 7.5: Plots of $\sigma_U/U_{H/2}$, where $U_{H/2}$ is the incoming velocity of the boundary layer at the plane of the measurements (y/D = 0.5). The vector field only indicates the flow direction, but not its intensity (the length of the vectors is not proportional to their intensity). Only one vector every 35 vectors is represented. (a) C_{20}, (b) C_{39}, (c) C_{64}, (d) C_{95} and (e) C_S.

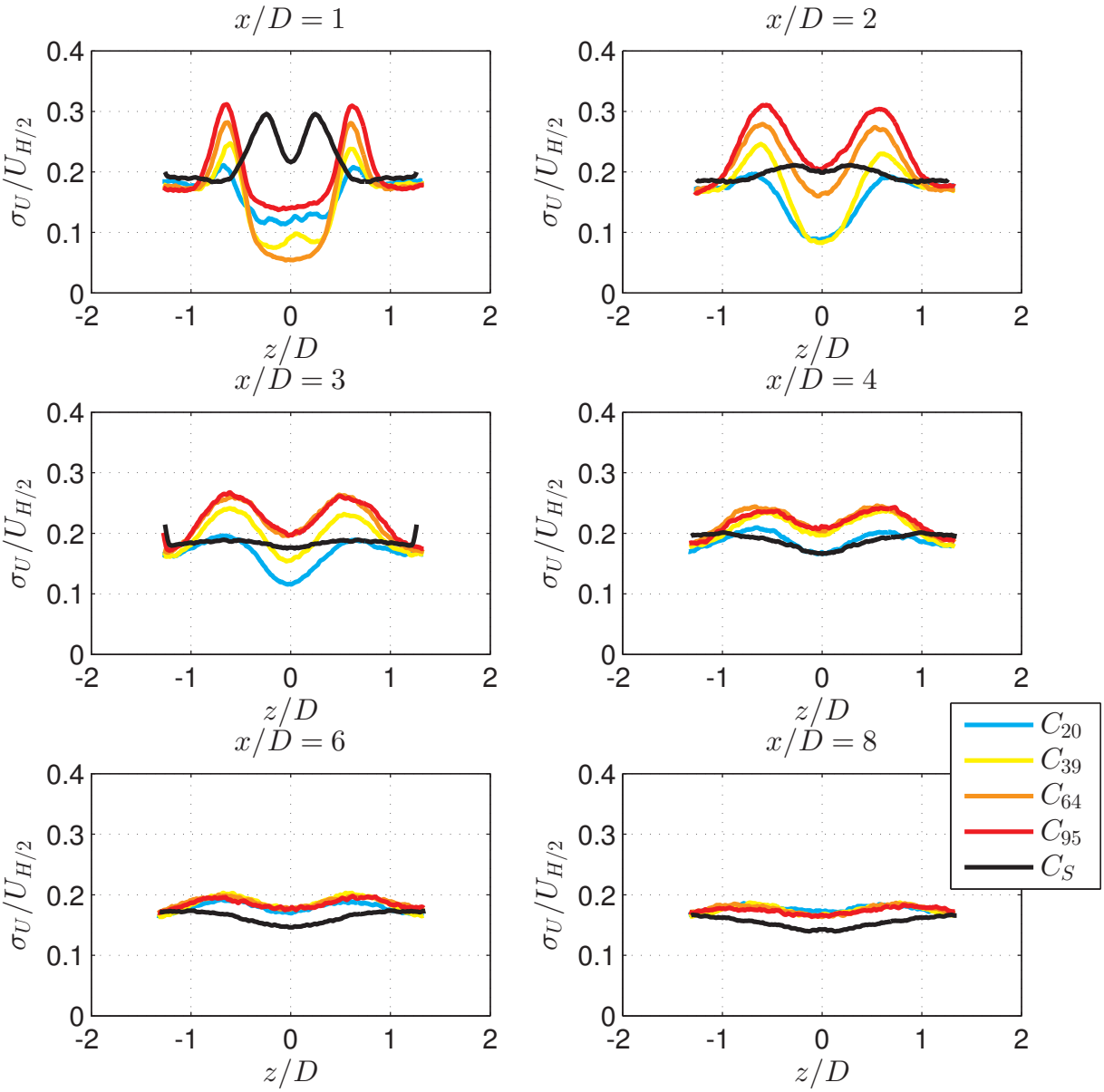

Figure 7.6: $\sigma_U/U_{H/2}$ along z at six different streamwise locations for all the patches.

It can be seen that all the cases have different levels for each camera. A comparison with the vertical PIV results (see Appendix E) shows that there is a drop in $\sigma_U/U_{H/2}$ along the longitudinal direction for each camera, which could probably be due to either a slight misalignment of the cameras or to pixel locking issues. However, the trend of the $\sigma_U/U_{H/2}$ is not affected, but just shifted from one camera to another. A corrective procedure was not carried out since the comparison with the vertical PIV data shows how to interpret this set of data, therefore a qualitative analysis of these results can be carried out, regardless of the problems. Quantitative analysis was not necessary for the purposes of this thesis, therefore it was decided not

to invest time in adjusting these results because they already provide an insight in the wake characteristics.

Analogous to the plots along the vertical plane, the contours of σ_U follow those reported for ω_y (see Figure 4.10), indicating that the bulk of longitudinal fluctuations happens in correspondence of the region where the lateral shear layers form and develop.

The profiles of $\sigma_U/U_{H/2}$ along z are shown in Figure 7.6 at six different streamwise locations. This Figure shows that the peaks of σ_U appearing in correspondence of the lateral shear layers have a consistent behaviour for all the patches. This is consistent with previous Chapters, confirming that the lateral spread of the wake is the same for all patches. The peaks decrease in intensity and broaden with increasing x/D. The solid case displays the same behaviour but its peaks seem to decrease much more quickly than for the porous patches. This is consistent with the fact that the wake of porous patches is much more persistent that the wake of the solid case.

The location of the peak in σ_U was evaluated fitting a 10^{th} degree polynomial curve to the data contained in the range $-1.25 < z/D < 0$ in order to smooth the data. The peak location was then identified as the maximum of each fitted curve. The resulting trend of the peak position (z_{peak}/D) is shown in Figure 7.7, which was obtained applying a smoothing average with a span of $\pm 0.1 x/D$, to reduce the noise.

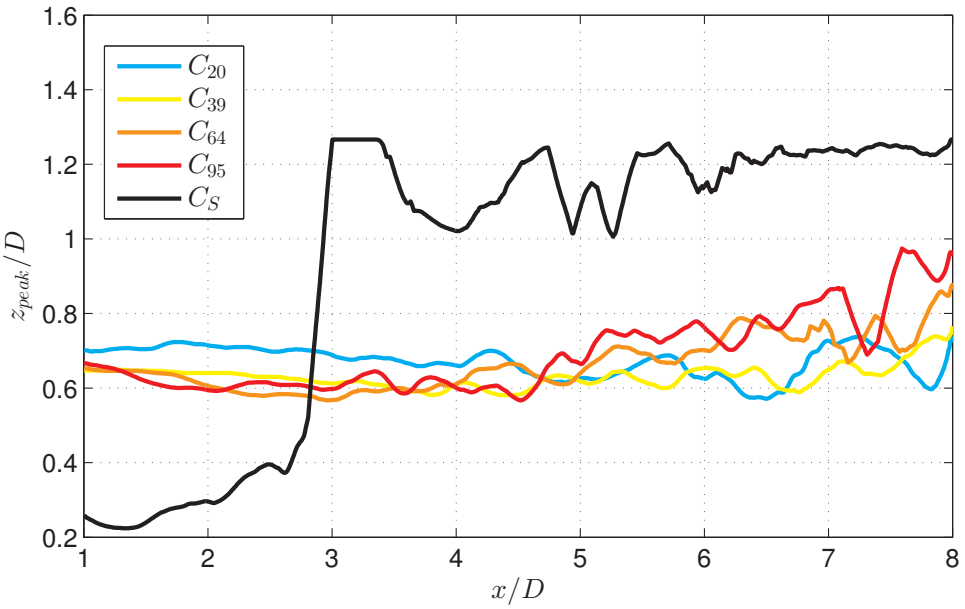

Figure 7.7: Location of the peak in $\sigma_U/U_{H/2}$ along x/D.

From Figure 7.7 it can be seen that z_{peak}/D oscillates around a constant value for C_{20} and C_{39} for all the length of the field of view, while it tends to increase after $x/D = 5$ for C_{64} and C_{95}. These results are comparable with those of a 2D square cylinder, (see e.g. Wang et al., 2006), which is consistent with the fact that the separation point at the flanks of porous patches is

fixed at the most external cylinder. Furthermore, from a deeper comparison with Wang et al. (2006), it can be seen the position of the peak in the present case is more similar to the position of the peak behind a 2D square cylinder (z_{peak} = ±0.6 at x/D = 1.5) than to the case of 3D square cylinder (z_{peak} = ±1 at x/D = 1.5), which confirms the fact that free end effects on wake development are not as strong for porous patches as they are for solid obstacles.

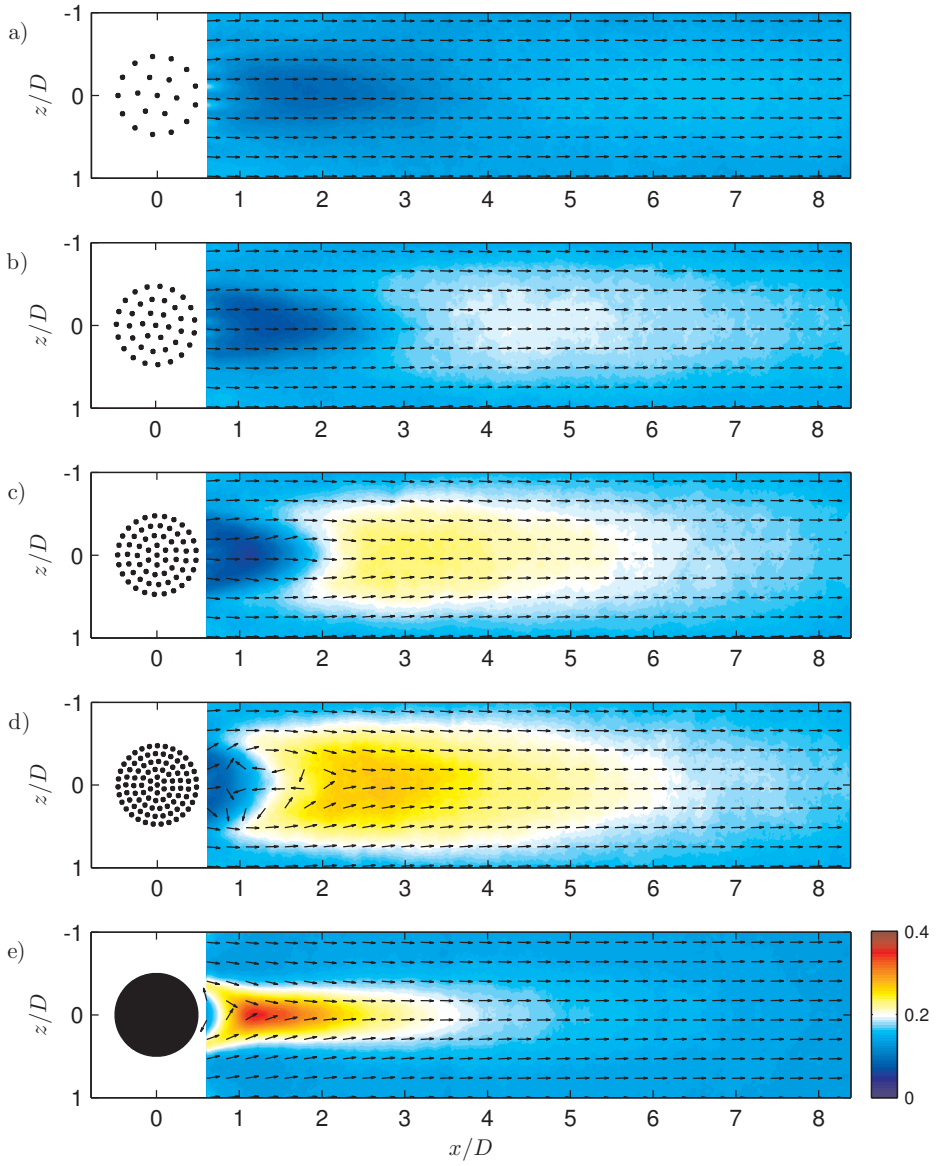

Figure 7.8: Plots of $\sigma_W/U_{H/2}$, where $U_{H/2}$ is the incoming velocity of the boundary layer at the plane of the measurements (y/D = 0.5). The vector field only indicates the flow direction, but not its intensity (the length of the vectors is not proportional to their intensity). Only one vector every 35 vectors is represented. (a) C_{20}, (b) C_{39}, (c) C_{64}, (d) C_{95} and (e) C_S.

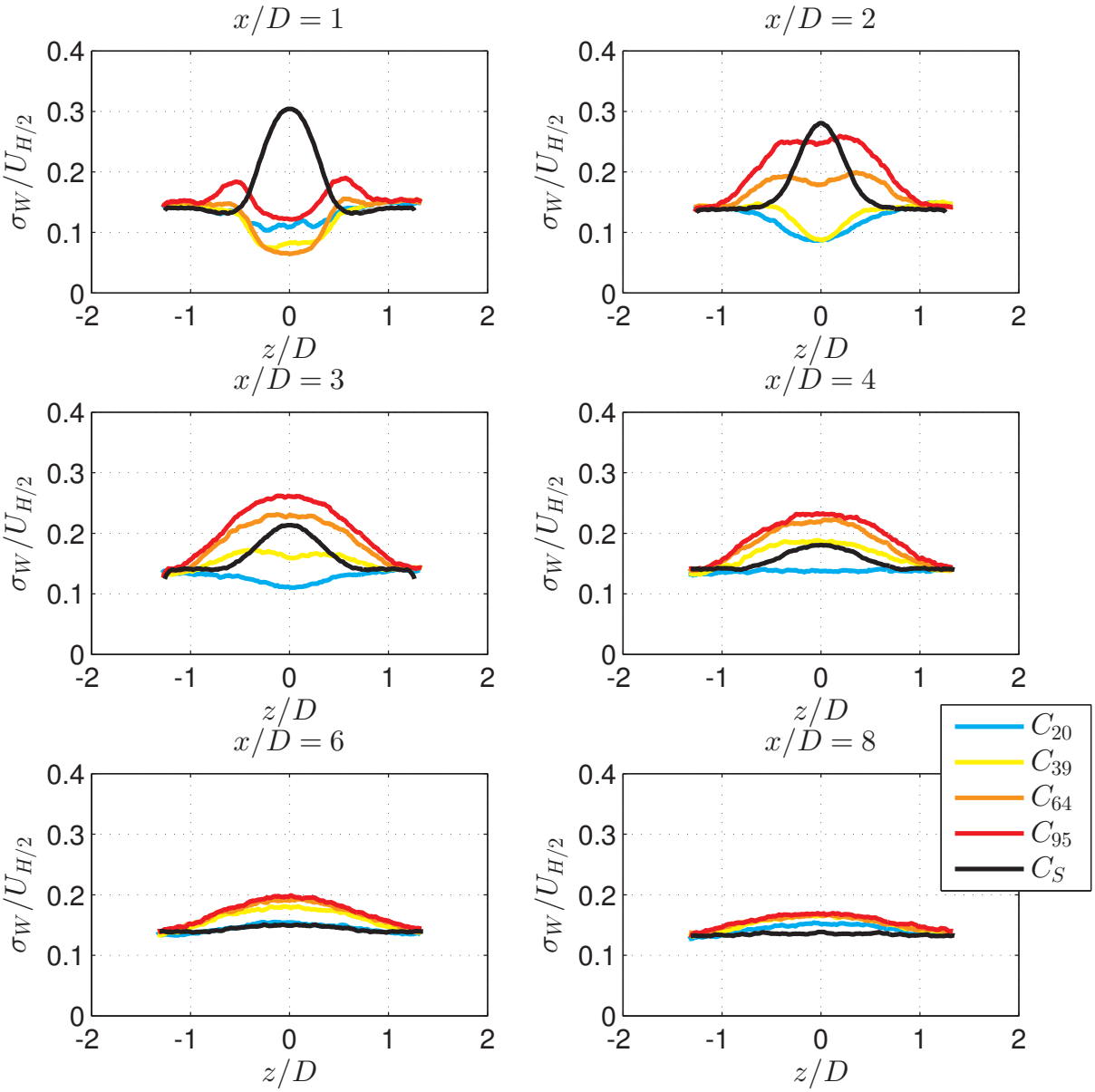

Figure 7.9: $\sigma_U/U_{H/2}$ along z at six different streamwise locations for all the patches.

Figures 7.8 and 7.9 shows the mean non dimensionalised lateral velocity fluctuations, $\sigma_W/U_{H/2}$ and the profiles of $\sigma_W/U_{H/2}$ along z at six different streamwise locations, respectively. From these Figures it can be seen that significant lateral fluctuations in the wake start in correspondence of the interaction of the two lateral shear layers, after the recirculation bubble, when present. This region corresponds to lateral flow entrainment in the wake.

Also in the case of σ_W, the profiles tend to the same curve for different densities, after a certain distance downstream. At $x/D = 8$ all the profiles collapse, except for C_{20}. As it was observed for the vertical plane, it takes longer for the second than for the first order statistics to adjust,

but the trend seems to suggest that a collapse of all the profiles may happen further downstream for σ_W as well.

7.4 Spectral analysis

As it was described in Chapter 3, a hot-wire probe was positioned behind the patch at the coordinates $x = 4.8D$, $y = H/2$ and $z = -0.6D$ during the drag measurements, in order to verify if there are any dominant frequencies in the wake fluctuations.

In this context, Sakamoto and Arie (1983) carried out an extensive study on the dependence of Strouhal number of circular cylinders with different aspect ratios immersed in different boundary layers giving multiple H/δ. In particular, they found two different trends of St with the aspect ratio of the cylinders, depending on the vortex type shedding from the finite-length cylinder. For $H/D < 2.5$ they conclude that an arch-type vortex is shed behind the obstacle (symmetrical configuration), while for higher aspect ratio, the von Karman type vortex (anti-symmetrical configuration) forms and this results in a change of the trend of St with H/D. The two vortex-types are shown in Figure 7.10. Wang and Zhou (2009) suggest that the occurrence of one of the two configurations is the instantaneous switch af an arch-type vortex structure shedding from the model (see Chapter 2) whose "legs" tend to assume an anti-symmetrical configuration for high AR and to assume a symmetrical configuration for low AR.

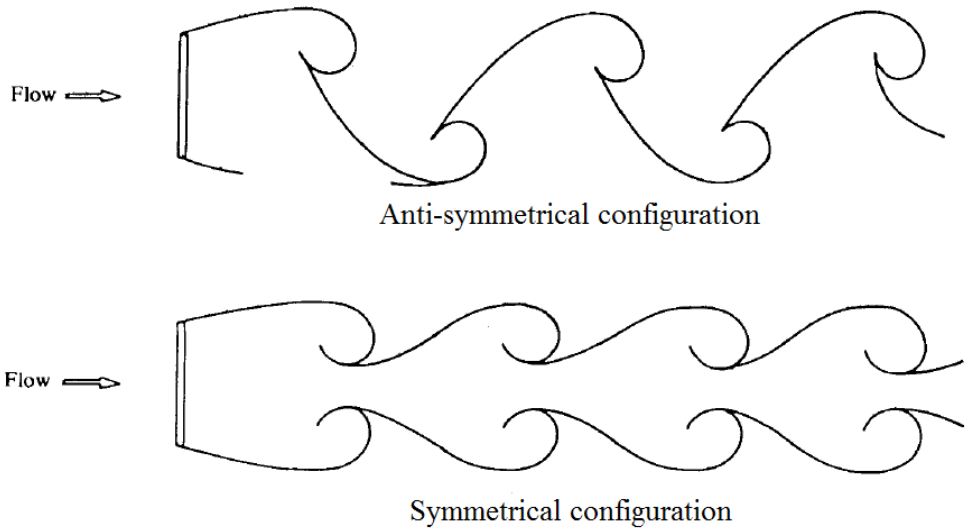

Figure 7.10: Sketch of the two different shedding configurations behind a solid finite obstacle, from Sakamoto and Arie (1983).

Castro (1971) measured St for porous plates at different porosity values and observed that a peak in the Strouhal number is also present when no vortex street is formed (i.e. for sufficiently low values of density), and this is ascribed to a meandering of the wake at a preferred frequency. For these cases, Castro (1971) reports that, compared to the case of wakes with

a vortex street, the energy spectrum is broader and the peak is less defined. The broadening of the spectrum increases with increasing porosity until it becomes impossible to define any dominant frequency. With increasing porosity, Castro (1971) also reports a sudden drop in C_D occurring at porosities corresponding to the crossover between vortex street and meandering wakes. For the case of circular patches Nicolle and Eames (2011) show that an alternate vortex street forms even for low values of density and in absence of a recirculation region. Nicolle and Eames (2011) report no sudden drop in C_D and this could be a confirmation that for porous patches a vortex street forms when the two lateral shear layer interacts downstream of the patch. Similar results were found also by Zong and Nepf (2012) and Chang and Constantinescu (2015).

Figure 7.11 shows the premultiplied non dimensonalised power spectral density ($PSDf$) of the hot-wire data, against the non dimensionalised frequency. The spectra were obtained by the subtraction of the premultiplied non dimensionalised spectra of the flow with the patch and the premultiplied non dimensionalised spectra of the free flow without the patch, at the same location, as described by equation 3.8 in Chapter 3.

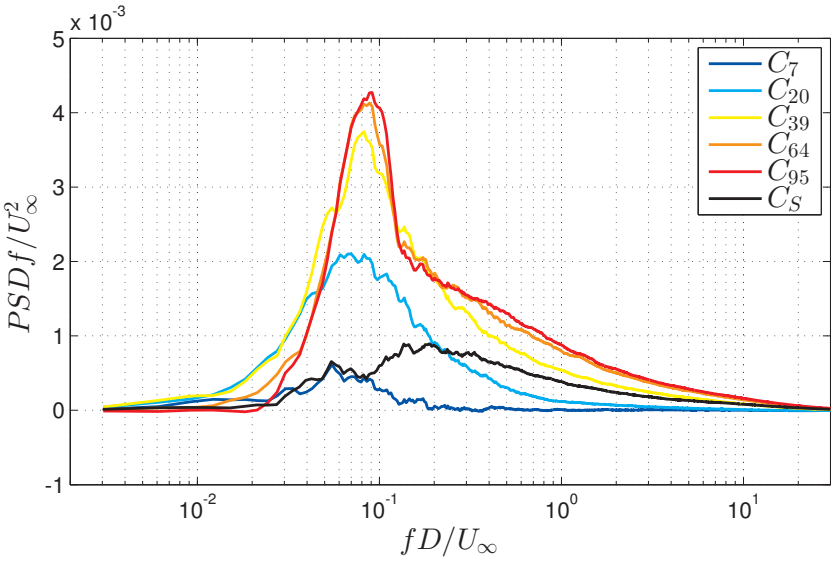

Figure 7.11: Premultiplied non dimensionalised power spectral density (PSD) for all the patches: f is the frequency value, D is the diameter of the patch, U_∞ is the freestream velocity (H/δ = 0.28).

From this Figure, it is evident that the power spectral density narrows for higher values of density (i.e. for C_{39}, C_{64} and C_{95}) and a clear peak in the spectra is visible for these patches suggesting the presence of coherent vortex structures shedding from the patch. In order to identify the non dimensional frequency of the peak, a Gaussian function was fitted to the PSD data around the point of the maximum values, over three different frequency spans in log coordinates. The peak obtained from each Gaussian fit were averaged to obtain the Strouhal number (St) value for each patch. These values are represented in Figure 7.12 and the errorbar in the plot corresponds to the rms of the average between the three ranges of fitting.

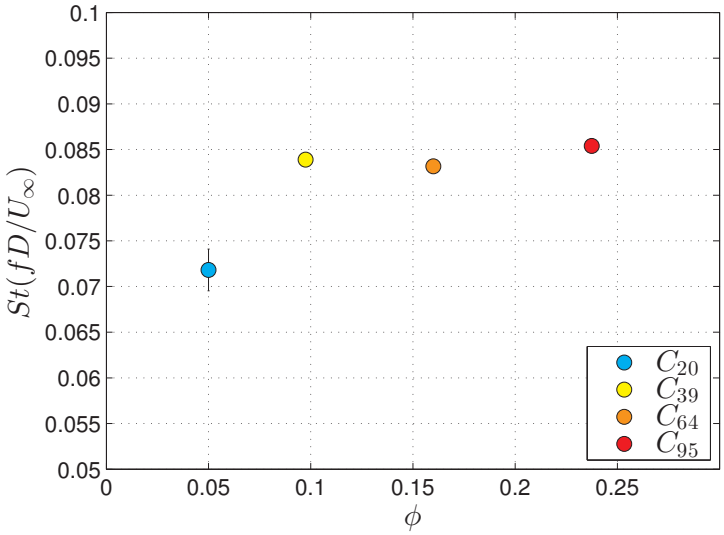

Figure 7.12: Strouhal number of the peak for each patch.

From the Figure it looks like that for all the patches except of C_{20}, the Strouhal number is about 0.085. From Figure 7.11 it can be seen that the energy content of the spectra at this frequency is about the same for C_{64} and C_{95} and slightly lower for C_{39}. However, for the model C_{39} the bleeding downstream of the patch is strong enough to prevent the formation of a recirculation region, therefore, this peak in the spectrum cannot correspond to the "canonical" vortex shedding, but it is rather more consistent with an alternate vortex street of the far wake as it was shown in Nicolle and Eames (2011) for lower values of ϕ.

For the other two cases (i.e. C_{64} and C_{95}), the Strouhal number of the patch is lower with respect to those reported by Sakamoto and Arie (1983) for circular cylinders. The value of 0.085 is instead comparable with the values they found for square prisms either for much higher H/δ ratios and same AR of the porous patch, or for similar H/δ and much higher AR. In both cases this would correspond to a solid obstacle with a greater H, which confirms that porous patches have a wake which resembles the wake generating behind a long AR *square* cylinder. The influence of H/δ on the results presented so far will be discussed in Section 7.4.1. The fact that the St number is closer to the one of a square cylinder is consistent with the observation that the separation point of the flow along the sides of the patches is fixed by the lateral bleeding at the most external cylinder. This is the condition of a square prism, where the lateral separation point is fixed at the sharp corner. This condition may not be satisfied for a square cylinder, in the case of strong incoming turbulence levels that can promote flow reattachment along the sides (see e.g. Castro and Robins, 1977), but from the flow visualisation in Sakamoto and Arie (1983) it is evident that this is not their case.

Furthermore, the fact that the lower part of the wake is not affected by free-end effects and behaves like part of a 2D obstacle means that the shedding type configuration has to be predominantly an alternate vortex shedding, instead of a symmetric vortex shedding. This is also confirmed by the fact that the mean velocities profiles and the second order statistics profiles

are comparable in shape and intensity, with those behind long AR square prisms, as shown in Wang et al. (2006) (see Figures 6.1, 7.5 7.8). Furthermore, if any rows of vortices is forming behind the patches, their intensity and coherence increases in the very near wake (i.e. for $x/D < 6$) with increasing density, but converges in the near wake (i.e. for $x/D > 6$), regardless of the patch density.

The interesting result is that for the model C_{39}, the trailing edge bleeding is strong enough to prevent the formation of the recirculation region behind the patch, however the peak in the spectrum is comparable in size and energy to the denser cases. Despite its lower density, also the C_{20} model shows a peak in the spectra, although this is characterised by a lower intensity and St. This means that a vortex street is present also for lower values of density, even if the energy content of the spectrum in this case is lower and the peak is broader compared to higher ϕ values. This is in agreement of the results in Nicolle and Eames (2011).

H (mm)	δ (mm)	H/δ	$AR = H/D$	D/δ
100	154	0.65	1	0.65
75	154	0.48	0.75	0.65
50	154	0.32	0.5	0.65
100	358	0.28	1	0.28
75	358	0.21	0.75	0.28
50	358	0.14	0.5	0.28

Table 7.1: Tested H and δ and resulting H/δ, $AR = H/D$ and D/δ.

7.4.1 H/δ influence on the spectra

Hot wire measurements were taken for six different H/δ ratios, as described in Chapter 3. These ratios were obtained by using patches with the same D and three different heights combined with two different incoming boundary layers with two different δ. The values of the tested H and δ and the corresponding H/δ, $AR = H/D$ and D/δ are reported again in table 7.1. For each case, the hot wire probe was positioned at the same x and z coordinate of the previous section, and its height was positioned at mid height (i.e. at $y = H/2$) accordingly to the height of the patch. The results presented in the previous sections of this Chapter correspond to $H/\delta = 0.28$.

Figure 7.13 shows the premultiplied non dimensonalised power spectral density of the hot-wire data, against the non dimensionalised frequency. The spectra were obtained with the same procedure described previously. It can be seen that both the aspect ratio of the patch and the ratio between the patch height and the boundary layer thickness, play a role in changing the power spectral density distribution. By increasing the AR of the patch (i.e. same D/δ), the peaks become narrower and more intense, which is consistent with the fact that any structure shedding from the patch is more coherent for higher aspect ratio, i.e. the free end effects affect a smaller portion of the height. For smaller δ (i.e. greater H/δ) and same AR, the intensity of

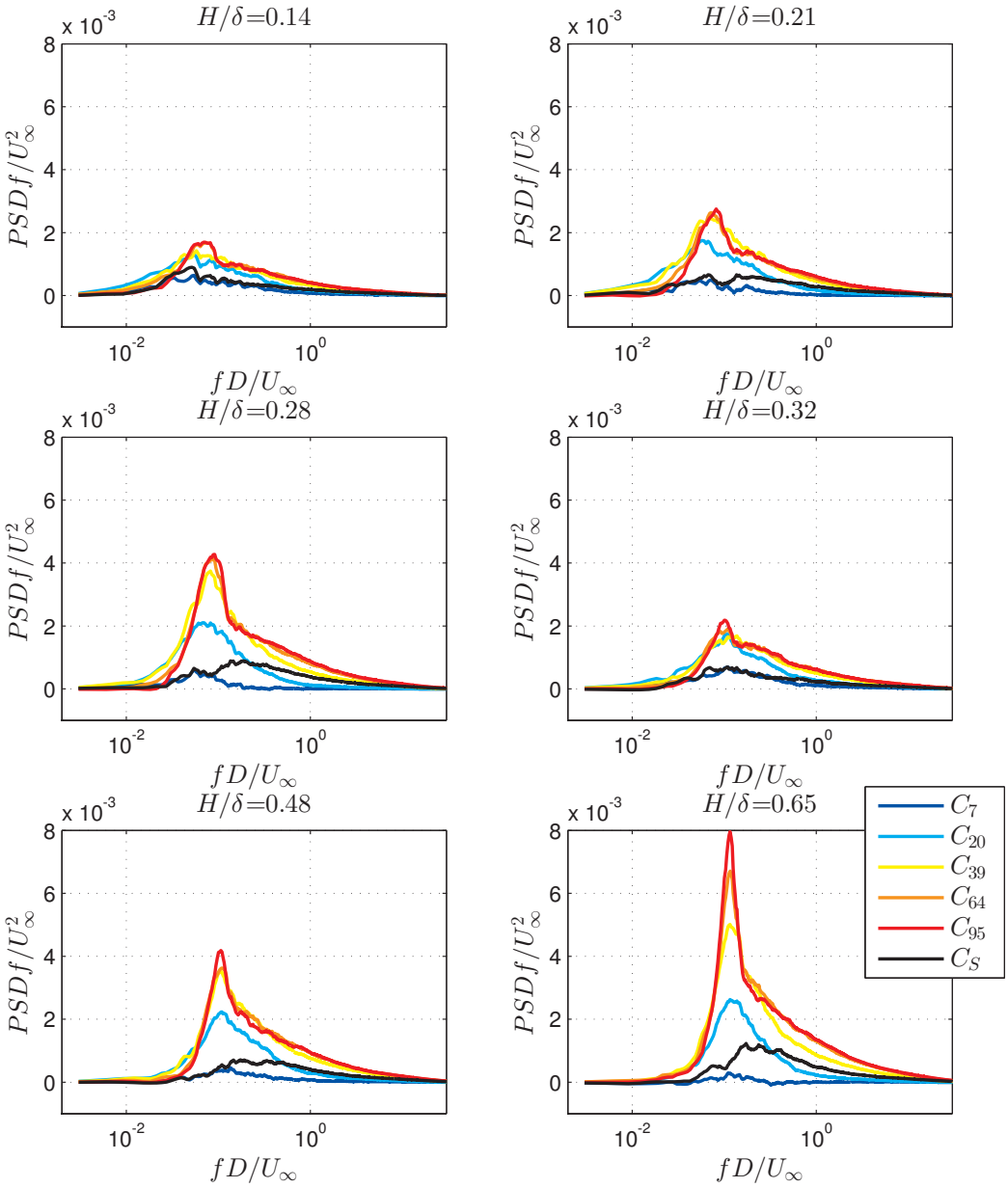

Figure 7.13: Premultiplied non dimensionalised power spectral density (PSD) for all the patches, for six different H/δ: f is the frequency value, D is the diameter of the patch, U_∞ is the freestream velocity (for $H/\delta < 0.3$, $D/\delta = 0.28$, for $H/\delta > 0.3$, $D/\delta = 0.65$).

the peak is higher compared to the lower δ, which makes sense considering that the gradient of the mean velocity profile along the height of the patch is smaller, which corresponds to more coherent structures shed in the wake (see e.g. Kappler et al., 2005, Tavoularis et al., 1987). The intensities of the peak for each patch against H/δ is represented in Figure 7.14.

Figure 7.15 shows how the Strouhal number of the peak is affected by changing in H/δ. Two

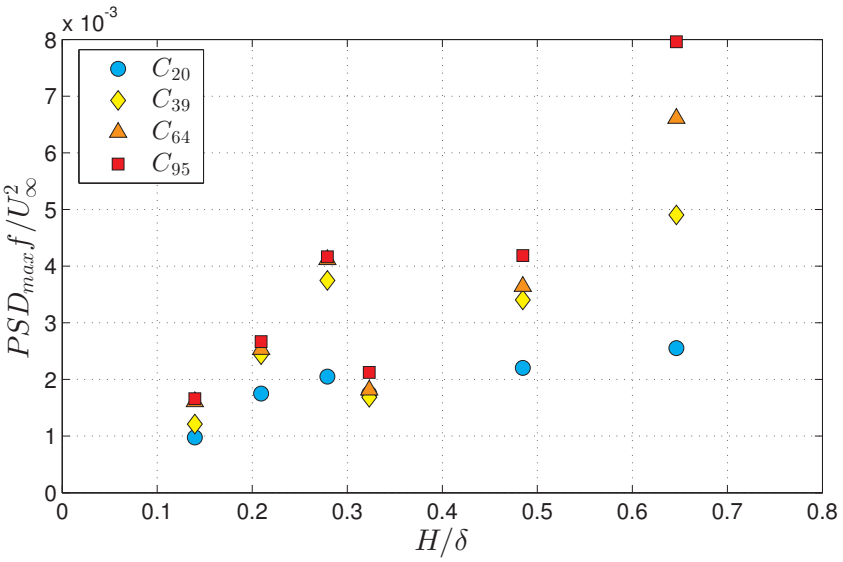

Figure 7.14: Peak intensity for all the patches vs H/δ (for $H/\delta < 0.3$, $D/\delta = 0.28$, for $H/\delta > 0.3$, $D/\delta = 0.65$).

different trends are distinguishable for each D/δ. Similar results were found by Sakamoto and Arie (1983), and they ascribed the change in trend to the switch from the symmetrical shedding configuration to the alternate configuration. It is hard to guess whether the same conclusion can be drawn in the present case, or if the change in trend is due to the influence of D/δ. It is interesting to point out that St is not influenced by the patch density, except for C_{20} at the higher δ (which might be due to the fact that the peaks are broader for these cases, as shown in Figure 7.13), and one value for the C_{39} model at $H/\delta = 0.32$ (for which an exact peak is not clearly detectable, despite the smoothing applied to the spectra).

However, by defining $St = fD/U_H$, where U_H is the incoming boundary layer velocity at $y = H$ the dependence on H/δ of the Strouhal number of the peak can be neglected, as a first approximation, as shown in Figure 7.16. As it can be seen from the Figure, St is about constant for $H/\delta < 0.3$ (which corresponds to $D/\delta = 0.28$) and for $H/\delta > 0.3$ (which corresponds to $D/\delta = 0.65$). Only a dependence on D/δ is left, except for the case C_{20} for $H/\delta < 0.3$, for which some discrepancies are present. Similar conclusions were found for C_D in section 4.5.

7.5 Shear layers analysis

A last analysis related to fluctuating quantities and second order statistics concerns the shear layers development both along the horizontal and vertical planes. Following the analysis of Zong and Nepf (2012) and Chen et al. (2012), the inner edge of the shear layers was evaluated as the point where the Reynolds stress $\overline{uv}$ and $\overline{uw}$ reach zero at each longitudinal location (along the vertical and horizontal plane, respectively). The characteristic width of the shear layer δ_{sl} is then defined as the distance from the sides of the patch (i.e. from $z/D = 0.5$) and

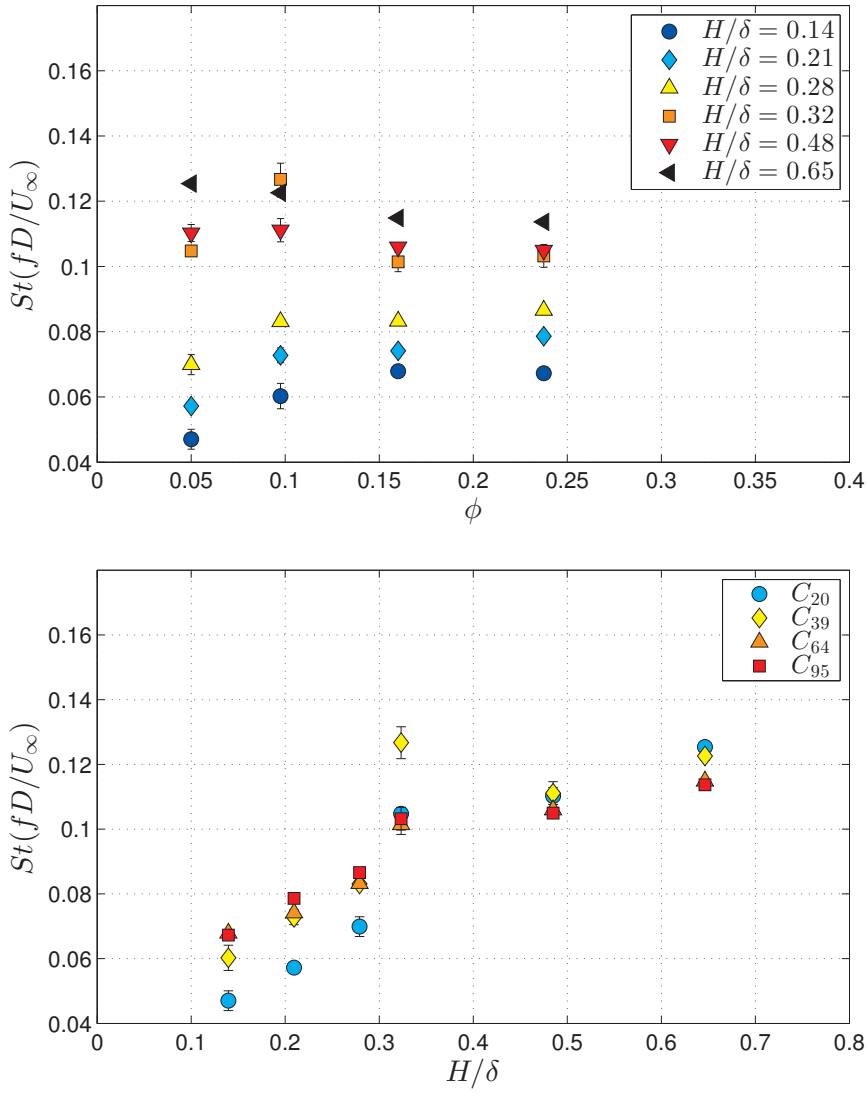

Figure 7.15: Strouhal number of the peak for each patch (fD/U_∞) vs density at different H/δ (top), and vs H/δ for different densities (bottom); for $H/\delta < 0.3$, $D/\delta = 0.28$, for $H/\delta > 0.3$, $D/\delta = 0.65$.

the top of the patch (i.e. from $y/D = 1$) of the zero-Reynolds-stress point, for the lateral and top shear layer respectively.

Figure 7.17 shows the variation of the width of the shear layers along x for both the top and the lateral shear layers. It can be seen that the three shear layers meet at the centreline of the mid-height plane, since they both reached a characteristic width of 0.5 at the same x/D location. For the models where no recirculation bubble is present (i.e. C_{20} and C_{39}), the shear layers, both lateral and vertical, grow with a linear trend, as shown in Zong and Nepf (2012) and Chen et al. (2012). For the model C_{20} the lateral shear layer does not grow for $x/D < 1.3$ and this is due to the presence of the wakes of the individual cylinders within the patch (see Figure **??**), which prevent the lateral shear layer to develop within the wake. These wakes are shorter for higher densities, and the lateral shear layer development starts further upstream for denser

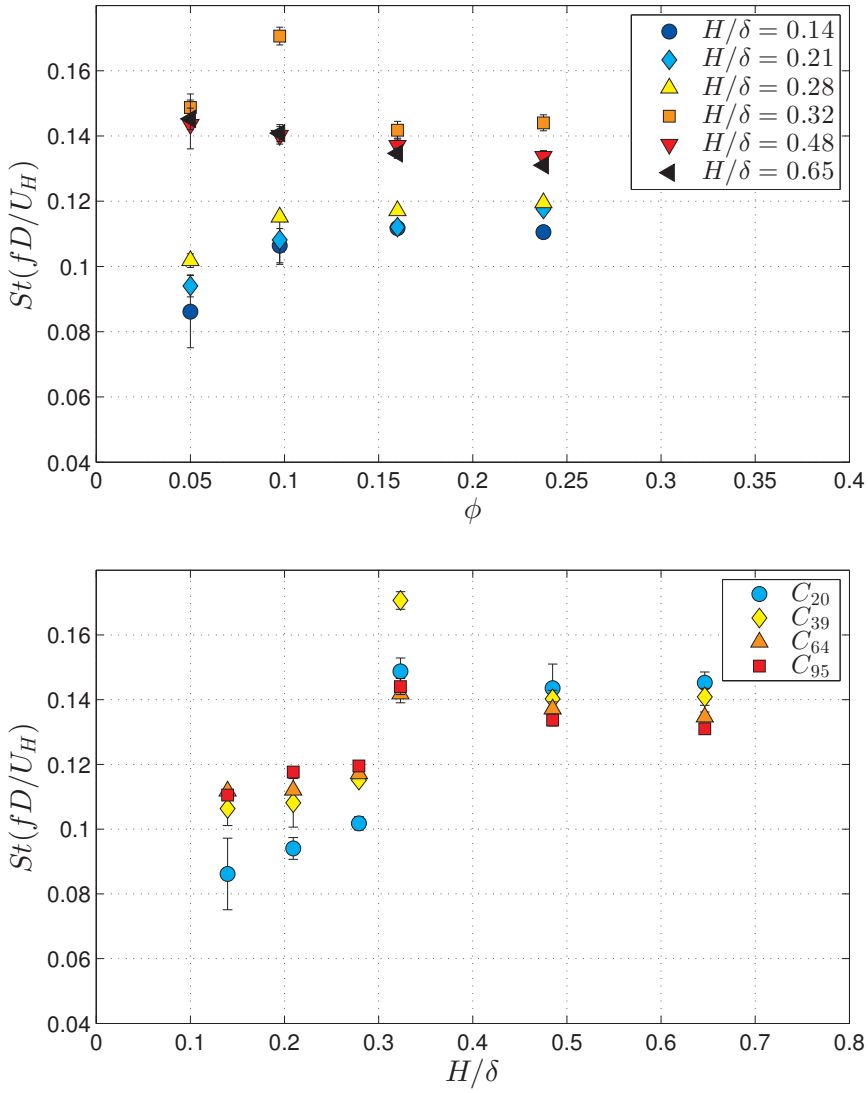

Figure 7.16: Strouhal number of the peak for each patch (fD/U_H) vs density at different H/δ (top), and vs H/δ for different densities (bottom); for $H/\delta < 0.3$, $D/\delta = 0.28$, for $H/\delta > 0.3$, $D/\delta = 0.65$.

patches. Furthermore, for higher values of density (i.e. for C_{64} and C_{95}), the development of both the lateral and top shear layer is is strained by the presence of the recirculation bubble and this is why its growth is not linear along x, but curved (i.e. it follows the topology of the bubble).

In literature, for 2D patches of obstacles, the distance downstream of the patch where the lateral shear layers meet, corresponds to the length of the steady velocity region L_1 and to the onset of the von Karman vortex street. A predictive model for this length is given by assuming a linear growth of the shear layers both in Zong and Nepf (2012) and Chen et al. (2012), as shown in section 2.2.2. For the present case it is evident that this assumption only holds only for the less dense cases.

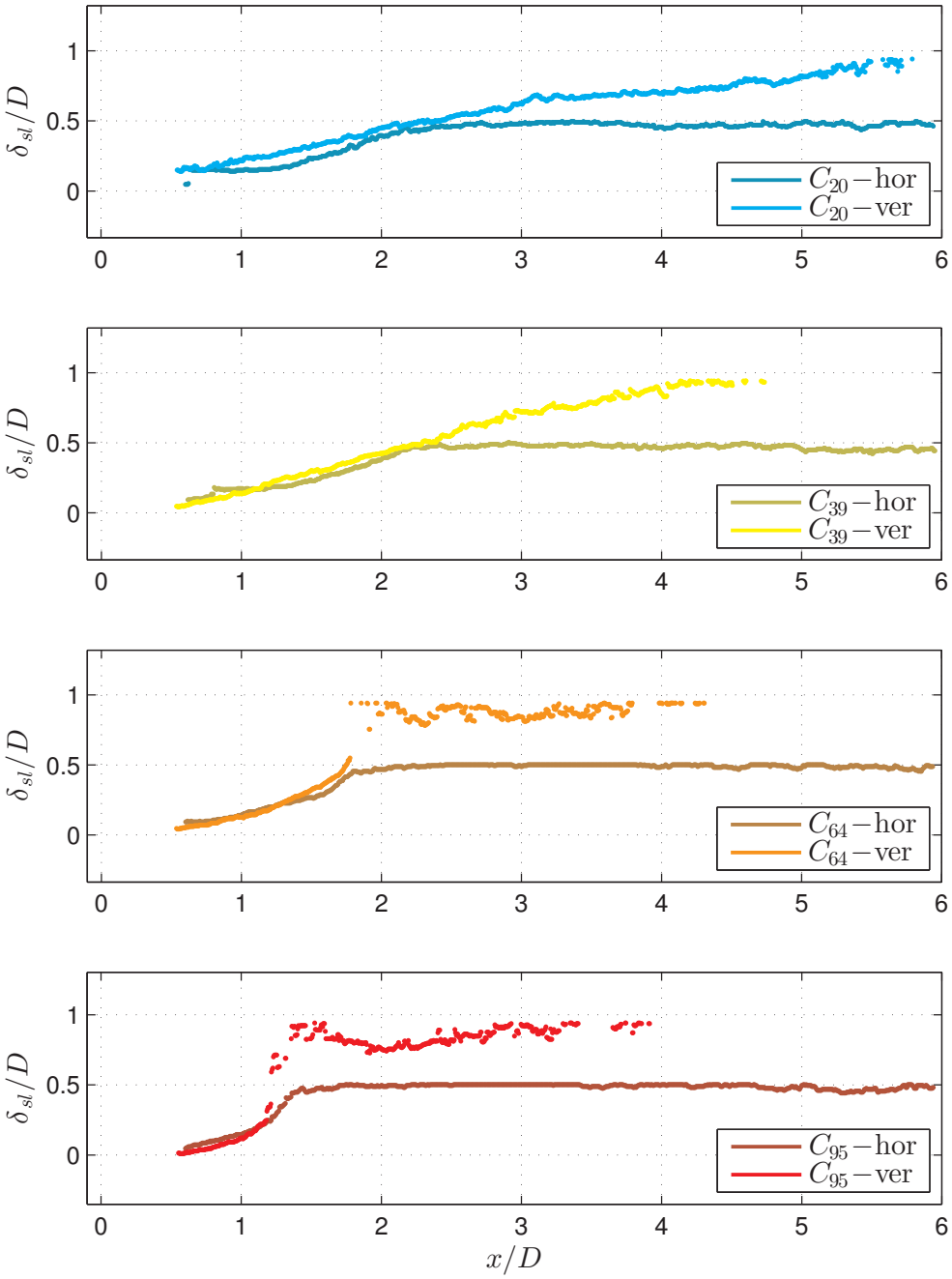

Figure 7.17: Characteristic width of the lateral and top shear layers δ_{sl} for all the models along x.

7.6 Summary

The analysis of the second order statistics confirms that the wake behind porous patches can be divided in two regions (i.e. the very near wake and the near wake). In the first region, the second order statistics are constant for most of the height of the obstacle, while in the second region they seem to adjust towards a similar profile, regardless of the patch density as it was observed for the mean velocities in the previous Chapters. However, the limited field of view downwind of the patch hampers to draw anything conclusive in this respect.

Spectral analysis indicates the presence of an alternate vortex street is present behind the patches, whose coherence and intensity increase with increasing density. The Strouhal number corresponding to this shedding is comparable to the Strouhal number of a square prism with long AR, which again confirms that the top shear layer effects (which contributes to decorrelate the wake) for porous patches are much less effective compared to a solid cylinder with the same external dimensions. The Strouhal number of the patch was found to be independent on H/δ when St is non-dimensionalised by U_H.

The analysis of the shear layer development showed that the hypothesis of a linear growth only holds for lower values of densities. For higher values of ϕ, the vertical bleeding at the trailing edge starts to play a major role on the top shear layer development, resulting in a non-linear trend of its width when a recirculation bubble is formed downwind of the patch.

Chapter 8

Conclusions and future work

8.1 Summary

The aim of this thesis is to investigate the drag and wake properties of arrays of obstacles fully immersed within a turbulent boundary layer.

A literature review on the topic was presented in Chapter 2, based on which it was concluded that there is a need to carry out a systematic study to examine drag and wake characteristics behind a group of obstacles. Towards this end, a detailed experimental campaign was undertaken and the results from these measurements have been presented in this thesis.

Chapter 3 and methods including a description of the procedures used to simulate a fithickfi boundary layer as well the techniques (hot-wire, PIV and force sensor) used to carry out the measurements.

Chapter 4 presented an analysis on the drag coefficient of patches of obstacles with different obstacle densities, and the relations between C_D and wake properties.

The development of the wake along a vertical plane at the centreline of the patches was given in Chapter 5, while self similar properties of the wakes of patches with different densities was given in Chapter 6. Characteristic velocity and length scales and their dependence on patch density were analysed in detail.

Finally, Chapter 7 presented an analysis of fluctuating quantities and on possible dynamical behaviour of the wakes.

8.2 Conclusions

In this section, the major findings of this thesis are summarised and are mapped to the critical objectives of this work raised in 1.

8.2.1 Drag coefficient

It was shown in Chapter 4 that the drag coefficient C_D of porous patches immersed in a turbulent boundary layer is independent of the Reynolds number $Re_D = U_\infty D/\nu$ (D is the patch diameter). Furthermore, it was observed that the drag coefficient of porous patches increases with increasing ϕ, at least within the range of ϕ investigated herein. The trend of C_D with ϕ results similar to the trend found in literature for two-dimensional patches of obstacles (as in the case of e.g. patches of aquatic vegetation piercing the free surface of a river). However, the most counter-intuitive outcome was that the drag coefficient of a solid cylinder with the same external dimensions of the patches is almost half of the maximum value obtained for the densest porous patch. This was explained as the effect of strong shear layers developing around the solid patch, which contribute to wake entrainment and hence to reduce C_D. The effect of these shear layers is weakened in the case of the densest porous patch, because of significant lateral and vertical bleeding, therefore very dense patches have a higher drag coefficient.

8.2.2 Main phenomena in the wake

The main phenomena which affect the wake development in porous patches were identified to be (i) lateral bleeding, (ii) vertical bleeding and (iii) trailing edge bleeding. The lateral bleeding prevents the reattachment of the flow along the sides of the patch and fixes the separation point at the most external cylinder. The vertical bleeding (always upwards for porous patches) pushes the shear layer forming at the patch-top upwards, hence enlarging the vertical size of the wake. It also weakens wake entrainment preventing the lower boundary of top shear layer from downward motion towards reattachment. The trailing edge bleeding diminishes the velocity deficit in the wake, causes the recirculation region (if any) to move downstream, and decreases the intensity of the shear layers forming at the sides. These phenomena are affected by the patch density: lateral and trailing edge bleeding decrease for increasing ϕ, while vertical bleeding increases for higher ϕ.

From a momentum balance point of view, the drag coefficient of an obstacle is mainly influenced by the spread of its wake and the intensity of the velocity deficit in the wake itself. The drag coefficient trend with ϕ was explained as the combination of these three different phenomena, which contribute to the wake dimensions and velocities.

8.2.3 Characteristic velocity and length scales

From the analysis of the development of the velocity profiles along the wall-normal direction downstream of the patch, it was shown that two distinct regions appear in the wake: a very near wake region, where the velocity is constant for a major portion of the height of the patch, and a near wake region, where velocity profiles in classical scaling collapse, regardless of patch density. The presence of a recirculation bubble marks these two regions in a clear way by

confining the effects of the top shear layer at the top part of the wake. For the models where no recirculation bubble is present, the development of a boundary layer at the wall contrasts the development of the top shear layer, so that an equilibrium is reached further downstream, leading to a collapse of all the wake profiles after $x/D \simeq 5$.

The characteristic length and velocity scales were identified as L_w, L_{min} and $\Delta U_{0,max}$, respectively. L_w, "vortex formation length" or "wake formation length", is the streamwise location where the peak in the turbulence intensity σ_W is located and corresponds to the approximate position of the vortex formation, if any vortex street is generated behind the patch. This length is an indicator of the near wake, where the near wake is considered to be the streamwise distance that is required for immediate wake recovery. L_{min} is the x location of the minimum velocity value U_{min} along the centreline. It can be considered as a virtual origin of the wake, which shifts the start of the velocity recovery downstream. L_{min} is a representative lengthscale for the very near wake characteristics, since it corresponds to the length where the velocity in the wake starts to adjust.$\Delta U_{0,max}$ is the maximum velocity deficit at the centreline and is an indicator of the momentum loss in the wake.

If a recirculation bubble is present, all the characteristic lengthscales and velocity scales lock to a constant value within the recirculation bubble, for all its vertical extension. In this region the wake is not influenced by free-end effects and characteristic velocity and length scales are independent of y/D. As a first approximation, this consideration can be extended even to those patches that do not show a recirculation bubble, meaning that in the very near wake the wake properties are constant for a major portion of the patch-height.

Along the horizontal plane at mid height, the wake of the patches were found to be self similar if scaled with the appropriate velocity and length scales. An extensive study of the dependence on ϕ of these characteristic lengths and velocity was carried out, and predictive models were obtained.

8.2.4 Drag forces parametrisation

A predictive law to estimate the drag coefficient of a three dimensional patch C_D by knowing the patch density ϕ was evaluated. This was obtained by fitting the data of L_w against C_D with a linear fitting and the data of L_w against ϕ with a power law function. By combining the resulting laws it was possible to determine a relation between C_D and ϕ. A direct fitting for $C_D - \phi$ lead to worst results, since the prediction bounds of the fitting were huge, and the accuracy of the curve was worse than the predictive law.

8.2.5 Velocity fluctuations analysis

The analysis of the second order statistics confirmed that the wake behind porous patches can be divided in very near wake and near wake, even though it takes longer for the statistics to adjust with respect to mean velocities.

Spectra results showed the presence of an alternate vortex street, whose coherence and intensity increase with increasing patch density. The Strouhal number of this shedding was comparable to the Strouhal number of a square prism with long AR, which again confirms that the top shear layer effects for porous patches are much less effective compared to a solid cylinder with the same external dimensions.

The analysis of the shear layer development showed that the hypothesis of a linear growth only holds for lower values of densities. For higher values of ϕ, the vertical bleeding at the trailing edge starts to play a major role on the top shear layer development, resulting in a non-linear trend of its width when a recirculation bubble is formed downwind of the patch.

8.2.6 H/δ influences

The influence of H/δ and D/δ on the drag coefficient was studied, and it was found that, if C_D is defined by using U_H as the non dimensionalising velocity, these dependences can be neglected, to a first approximation. Similar conclusions were drawn for the Strouhal number of the patch, which was found to be independent on H/δ by using U_H as the non dimensionalising velocity.

8.3 Future work

Areas of further research that complement or extend the work presented in this thesis are herein suggested.

Dimensional analysis showed that the wake characteristics and drag forces mainly depend on the following set of parameters (see section 2.3):

$$\frac{U_\tau}{U}, \frac{H}{D}, \frac{H}{\delta}, \frac{(\rho U D)}{\mu}, \frac{d}{D}, \phi. \tag{8.1}$$

Within this context the experiments were carried out to investigate and isolate the effects of ϕ, $(\rho U \delta)/\mu$ and H/δ while U_τ/U, D/δ and d/δ were kept as fixed parameters for most of the experiments. While U/U_τ is likely to vary little in real applications (environmental flows generally occur in the fully rough regime), d/δ and D/δ can vary extensively (e.g. a vegetation patch and a cluster of buildings are associated with completely different values of d/D or H/D, which in turn correspond to different values of d/δ and D/δ). Therefore a comprehensive study

of the influence of these parameters on the drag coefficient and the characteristic lengths and velocity scales is necessary.

Furthermore, the densities that have been investigated show a big gap of data for $0.24 < \phi < 1$. This lack of data calls for more experiments to investigate, whether for $0.24 < \phi < 1$ the drag coefficient reaches a plateau and then abruptly decreases after a threshold value of density, or whether it shows a maximum and then smoothly decreases towards the solid case value.

More experiments for values of densities in the same range investigated herein would be useful in order to confirm the prediction laws evaluated in this work, and to analyse more deeply the behaviour of L_w, L_{min} and $\Delta U_{0,max}$ along the height of the patches. The more interesting question that still remains is to find the threshold density value for which a recirculation bubble forms behind a porous patch, and how it is affected by increasing ϕ.

Experiments for the far wake would be interesting in order to evaluate L_w for low values of density, and consequently, in order to verify if the scaling proposed for the very near wake in Chapter 5 holds for lower ϕ. These experiments would also confirm whether the second order statistics adjust to the same profile in the far wake, as it happens for mean velocities.

Appendix A

Incoming boundary layer - additional results

A.1 Incoming boundary layer (with spires): single wire measurements, additional results

A.1.1 Modified Clauser method

Perry and Li (1990) propose a method to determine U_τ in rough wall boundary layers. Assuming a wake strength parameter Π equal to 0.55, the mean velocity in the inertial sub-layer can be written as:

$$\frac{U(y)}{U_\infty} = 1 + \frac{1}{\kappa}\frac{U_\tau}{U_\infty} ln \frac{y}{\delta_*} + \frac{1}{\kappa}\frac{U_\tau}{U_\infty} ln \frac{U_\tau}{U_\infty} + 0.493\frac{U_\tau}{U_\infty}, \tag{A.1}$$

where δ^* is the displacement thickness of the boundary layer. This method has been used by Flack et al. (2005) and Flack et al. (2007) among others to determine the friction velocity, together with a total stress method and the results from the two procedures differ by less than 3%. In their approach, the vertical coordinate should be considered measured from the top of the roughness, and a wall datum offset was also fitted from the equation. In the present case, the vertical position is measured from the floor of the test section, so it has firstly been tried to carry out a fitting including the zero-plane displacement d, but also in this case, all the obtained values were negative, which has no physical meaning. Again, a second fitting with a non linear least square method has been carried out, imposing $d = 0$ from the beginning, and the obtained results are reported in Table A.1. The data that have been fitted this time are up to $y = 100$ mm which correspond almost to 0.3δ, since looking at Figure 3.11 it seems that the logarithmic region extends almost up to that height.

The error reported in Table A.1 is just the standard error of the regression fit, and does not take into account other sources of uncertainty.

z (mm)	U_{ref} (m/s)	δ^* (mm)	U_τ (m/s)	e_{U_τ}	U_τ/U_{ref}
−50	20.0	61.71	1.093	±0.47%	0.0546
−25	20.2	61.60	1.119	±0.66%	0.0554
0	10.2	61.13	0.599	±0.61%	0.0590
0	20.0	59.59	1.150	±0.54%	0.0576
25	20.2	57.78	1.163	±0.90%	0.0575
50	20.0	65.06	1.210	±0.97%	0.0604
average	-	61.15	-	-	0.0574

Table A.1: Modified Clauser method fitting results.

The obtained mean value for U_τ/U_{ref} is in close agreement with the one found with the previous procedure. Both of the methods have their limitations, but this perfect agreement provides confidence on the reliability of the method developed in the previous section.

A test on the sensitivity of the method on δ^* showed that a reduction of 10% of δ^* corresponds to an increase in U_τ/U_{ref} of about 6%, and vice versa an increase in δ^* of 10% corresponds to a reduction in the evaluated U_τ/U_{ref} of about 5%. In the present case δ^* is probably underestimated, due to the limited y locations and the algorithm for calculating it which computes an approximation of the integral via the trapezoidal method (*trapz* function in Matlab) and this has to be considered in the total uncertainty of this method's results.

A.1.2 Spectral characterization

Finally, a spectral characterization of the data has also been carried out. The power spectral density (PSD, E in the picture) normalized by the variance is plotted in Figure A.1 for three different wall-normal location for all the boundary layers. These locations are y = 29, 52 and 233 mm that are, respectively, about 2%, 15% and 60% of the boundary layer thickness. The "Kolomogorov" slope of $-5/3$ is also represented by a solid black line in each picture. A plot of the premultiplied power spectral density is given Figure A.2.

The power spectral density was calculated using the Matlab function *pwelch* which estimates the PSD using Welch's method. According to this procedure, the signal is split up into overlapping segments which are then windowed in the time domain (Matlab uses by default a Hamming window). The periodogram of each segment is then calculated by a discrete Fourier transform (DFT) and these estimates are finally averaged to obtain the PSD. For this estimation of the PSD, each signal contained 2,400,000 samples (2 minutes at 20,000 Hz), the input for the *pwelch* function were chosen to be 20,000 for the length of the windows with 50% of overlap and 20,000 points to calculate the DFT.

It is evident that the frequency content of these measurements is what is expected for a turbulent boundary layer. All the spectra follow the $-5/3$ slope in the inertial region and show an exponential cut-off in the dissipative region. It should be pointed out that it is impossible to reproduce in a wind tunnel environment a complete, for example, atmospheric spectrum (important for some of the applications of the proposed research project) since, in this last case, the

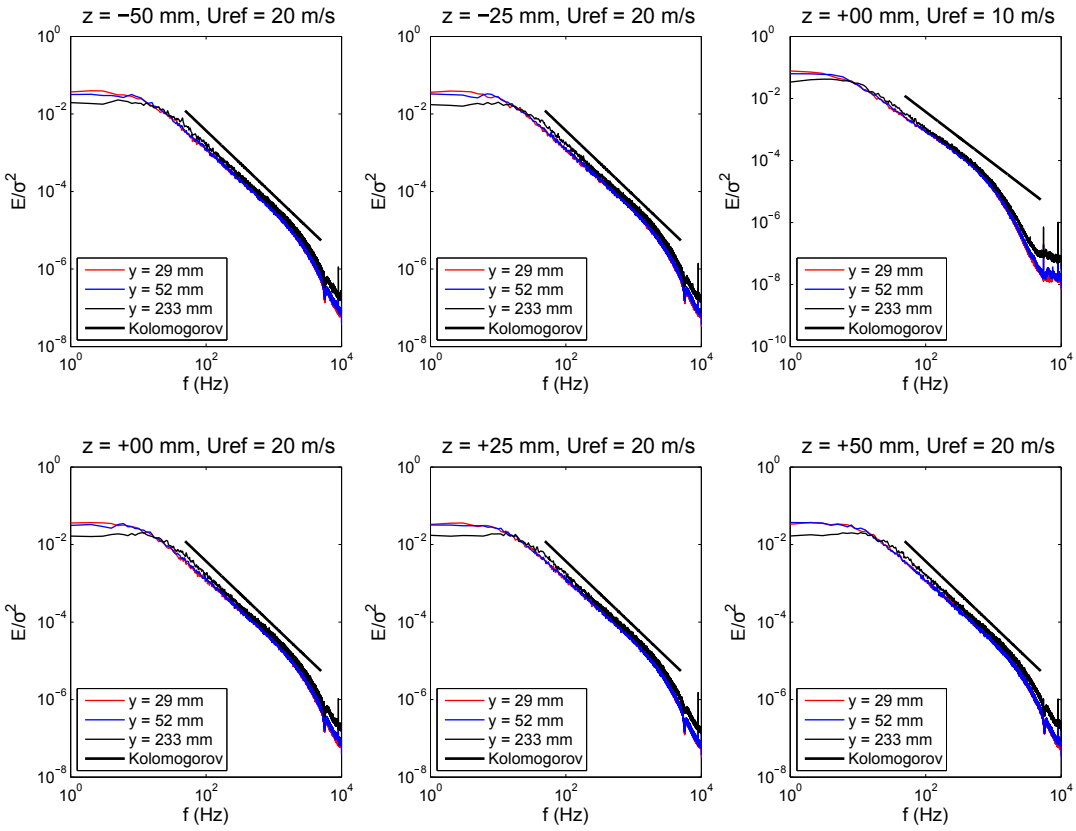

Figure A.1: Power spectral density (E) normalized by the variance at three different y location. Solid line, Kolmogorov slope at $-5/3$.

low frequencies are influenced by the presence of scales of motion which are not reproducible in a wind tunnel. For an atmospheric spectrum, the low frequency energy content should be higher (see, for example Lim et al., 2007), nevertheless the behaviour of the spectra at higher frequencies is consistent.

The spike at around 6000 Hz has been found to be related to electrical noise, and it has no physical meaning. For the next measurements an isolation of the instrumentation using an UPS (Uninterrupted Power Supply) is planned, in order to reduce this noise as much as possible.

A.2 Hot-wire additional setup for flow conditioning

An additional set of experiments was carried out using two singles and an x-wire probes, to characterize the spanwise homogeneity of the flow. The three probes were aligned along the z direction in a configuration like "single-x-single" at a distance of 2 cm apart, with the x-wire positioned 4 mm higher than the two singles with respect to the wind tunnel floor. This system was mounted on a rotating arm, connected to the traverse system described above. The rotating arm was necessary to perform the calibration of the x-wire. The configuration of

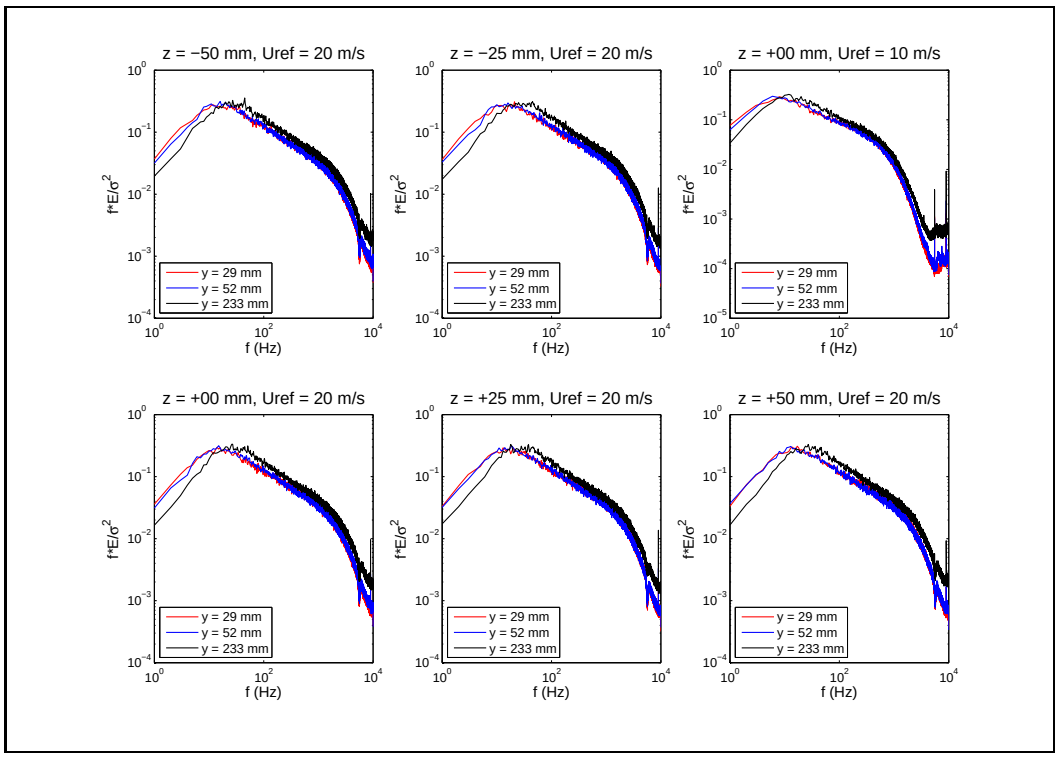

Figure A.2: Premultiplied power spectral density for three different y locations.

the whole structure is shown in Figure A.3. In the picture, just one single wire is present and it is connected to the inclined probe holder, while the x-wire is connected to the horizontal probe holder. In the configuration used for this project, an additional single wire was added on the other side of the x-probe, symmetrically disposed with respect to the single shown in the picture.

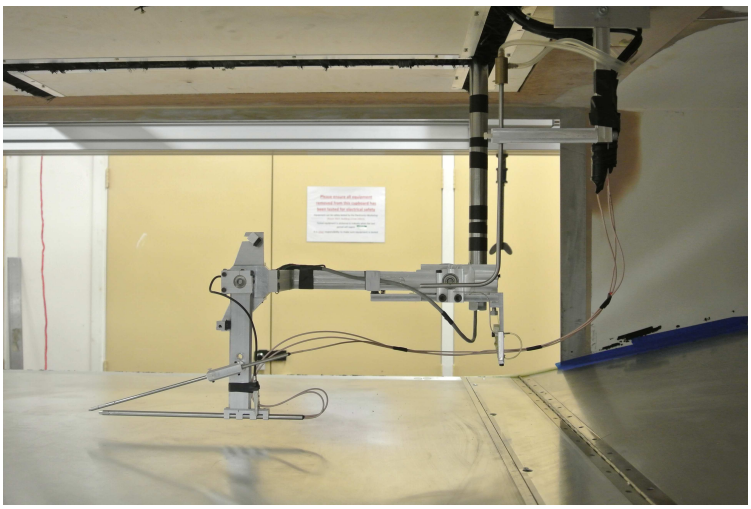

Figure A.3: Probe holders, rotating arm and traverse connection of the hot-wire system (Photo by Ronnie Hanson).

The two single wires were connected to the Newcastle hot-wire system, while the two wires of the x-probe were connected to a Dantec StreamLine Research CTA System. The output

was connected to a data acquisition board (NI USB-6212 BNC from National Instruments) and the data was acquired using a Matlab code written using Matlab Data Acquisition Toolbox functions provided to acquire analogue signals. The temperature of the test section was also acquired with the same board, while the pressure of the laboratory was recorded manually, by mean of a weather station. For this second setup, all the electrical equipment was connected to an UPS (Uninterrupted Power Supply), in order to reduce electrical noise.

The OHR was set equal to 1.8 for the two single wire, and 1.75 for the two wires of the x-probe, while the sampling frequency was set again on 20 kHz for all the wires. For the Dantec streamline system, it was possible to set gain and offset, which were equal to 16 and -2 for both the wires.

The calibration was performed once a day for 10 velocities ranging from 1.4 m/s to 14.1 m/s the first day and from 1.2 m/s to 24.7 m/s the second day and for 9 yaw angles ranging in both occasions from -30°to $+30$°, with respect to the x axis. A view of three steps of the calibration procedure is shown in Figure A.4.

Figure A.4: Three calibration steps (Photo by Ronnie Hanson).

To convert the output voltages of the x-wire, both the procedures described in Bruun et al. (1990) and in Tropea et al. (2007) have been implemented in a Matlab routine. The results showed no difference between the methods, so the one from Tropea et al. (2007) was chosen to be used to evaluate the final results. According to this method, each pair of (E_1 E_2) corresponds to one pair of (U^* γ), where U^* is the flow velocity intensity γ is its angle with the x axis, that are known from the calibration, so a look-up table can be built, fitting two surfaces corresponding to $U*$ and γ respectively, and then applying this fitting to the output voltages. In this way, no assumptions on the wire geometry or response are made. The data have been fitted using the Matlab function *griddata*, choosing a linear method of interpolation. The fitted surfaces for the second calibration (e.g. U^* ranging from 1.2 m/s to 24.7 m/s) are shown in Figure A.5.

A.3 Hot-wire additional measurements for flow conditioning

The second set of experiments aimed to characterize the spanwise velocity profile (i.e. along z). Each profile has been characterized by 28 points equally spaced along the z direction. The profiles were acquired for 3 different locations along the y direction, namely 30, 100 and 200

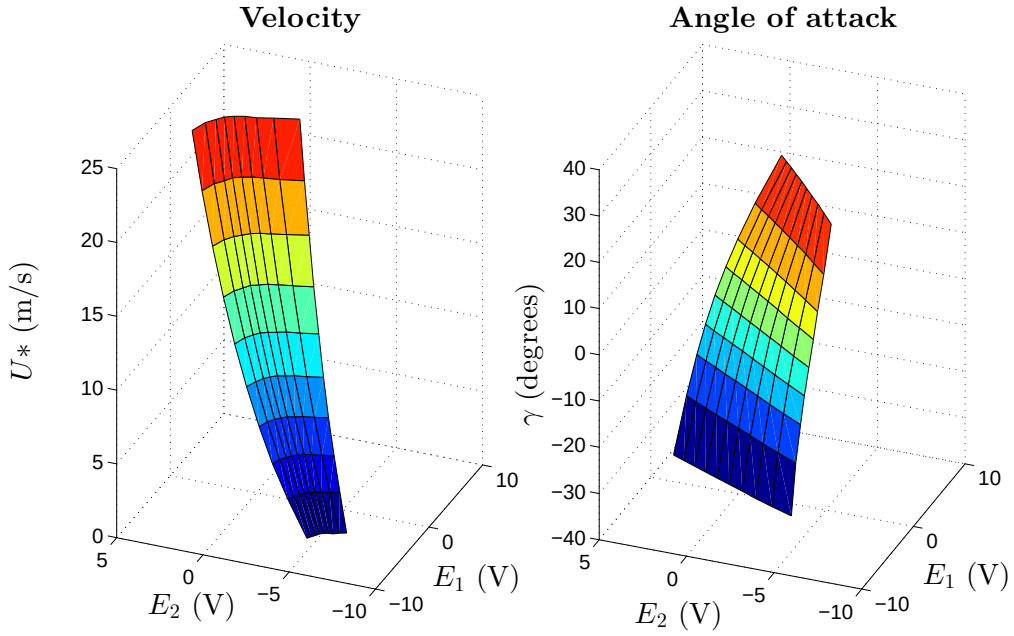

Figure A.5: Fitted surfaces for U^* and γ.

mm from the tunnel floor. The profile along the centreline was acquired for one value of the freestream velocity, namely 11 m/s.

Each acquisition was taken for 2 minutes, at $20,000$ Hz, and acquired simultaneously. The ambient temperature was acquired using a temperature sensor located at the ceiling of the test section, while the ambient pressure was manually noted, using a weather station as a reference.

The reference velocity was not acquired via the Pitot tube. In order to obtain a value for the reference velocity, the mean data obtained from the spanwise profiles from the three probes were averaged, and the reference velocity has been extrapolated from the vertical mean profiles obtained with the first set of experiments.

A.4 Incoming boundary layer (with spires): single-X-single wires measurements

The velocity profiles for 10 m/s and 20 m/s, non-dimensionalised with the reference velocities, are shown in Figure A.6, and the corresponding statistics in Figure A.7.

Due to physical constraints, the arm supporting and moving the probes could not reach a height higher than 300 mm (i.e. $\sim 0.83\delta$). Nonetheless, the mean profiles collapse onto each other, if nondimensionalised with the reference velocity U_{ref}, reaching almost 95% of U_{ref} at y =300 mm. The streamline fluctuations are reasonably similar to the ones shown in Figure 3.7, with a constant value of 0.1 up to almost 100 mm, reducing moving far from the wall.

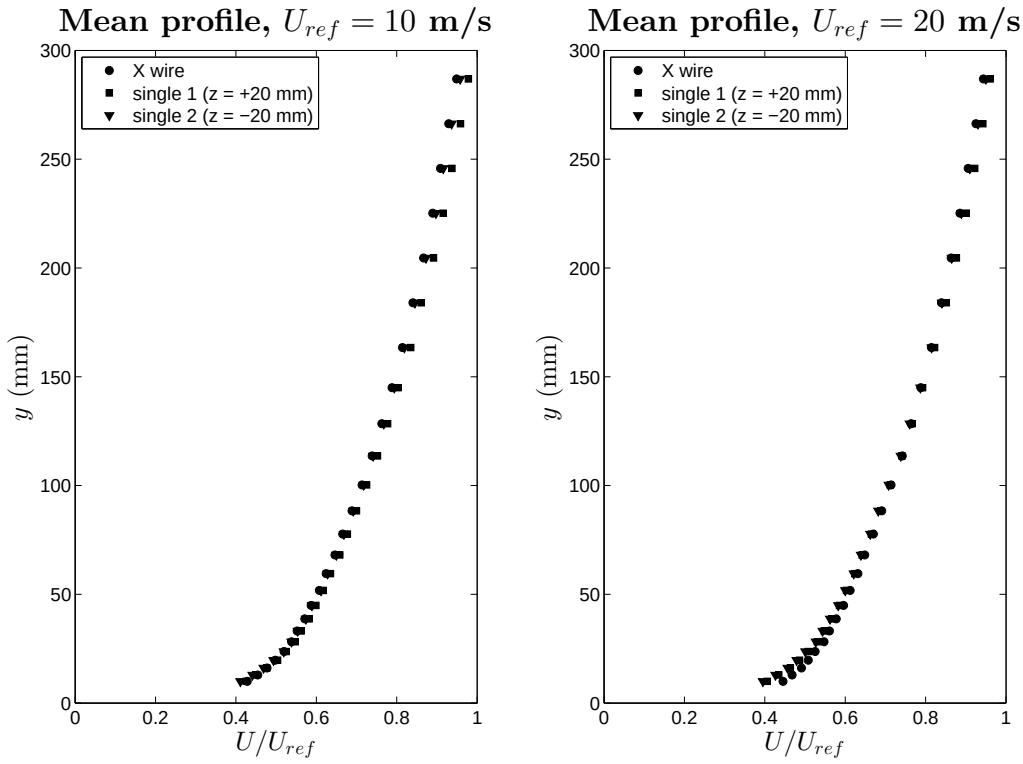

Figure A.6: Mean velocity profiles measured with the configuration single-X-single wires for a freestream velocity U_{ref} of 10 m/s and 20 m/s. The locations of the single wires are specified in the legend.

The profile of the lateral velocity fluctuations, is not constant as expected inside the inertial sub-layer, but it shows a plateau between 40 mm and 100 mm at a value of about 0.06. The profiles of the Reynolds stresses $-\overline{uv}/U_\tau^2$ show a plateau in the same region of σ_v/U_τ, at a value of about 0.045. A similar trend is reported also in Raupach et al. (1991) and it is mainly ascribed to measurement errors of X-wire probes, due to their limitation of $\pm 45°$ acceptance angle. It was shown that when measuring with omnidirectional sonic anemometers, the shear stress $-\overline{uv}$ is constant above the roughness element height, which for those authors corresponded to 6 mm. The other interpretation that can be given to this behaviour is that for the flow conditioning used in the present work, the roughness sub-layer could be of the order of 40 mm (which is 1.33 times the highest obstacle height). In order to clarify which one of the two hypothesis is correct, further investigation will be carried out with other methodology (e.g. PIV), to verify if it's a problem due to the X-wire limitation, or if the roughness sub-layer extends for such a large region.

A common way to evaluate U_τ is to approximate it by the viscous contribution to the stress, since the Reynolds number is sufficiently high. With this approximation the value of U_τ is considerably lower than the one found with the previous procedure (that was 0.057), which is another indicator that the X-wire measurements for vertical fluctuations and shear stresses may not be correct. This will be further investigated.

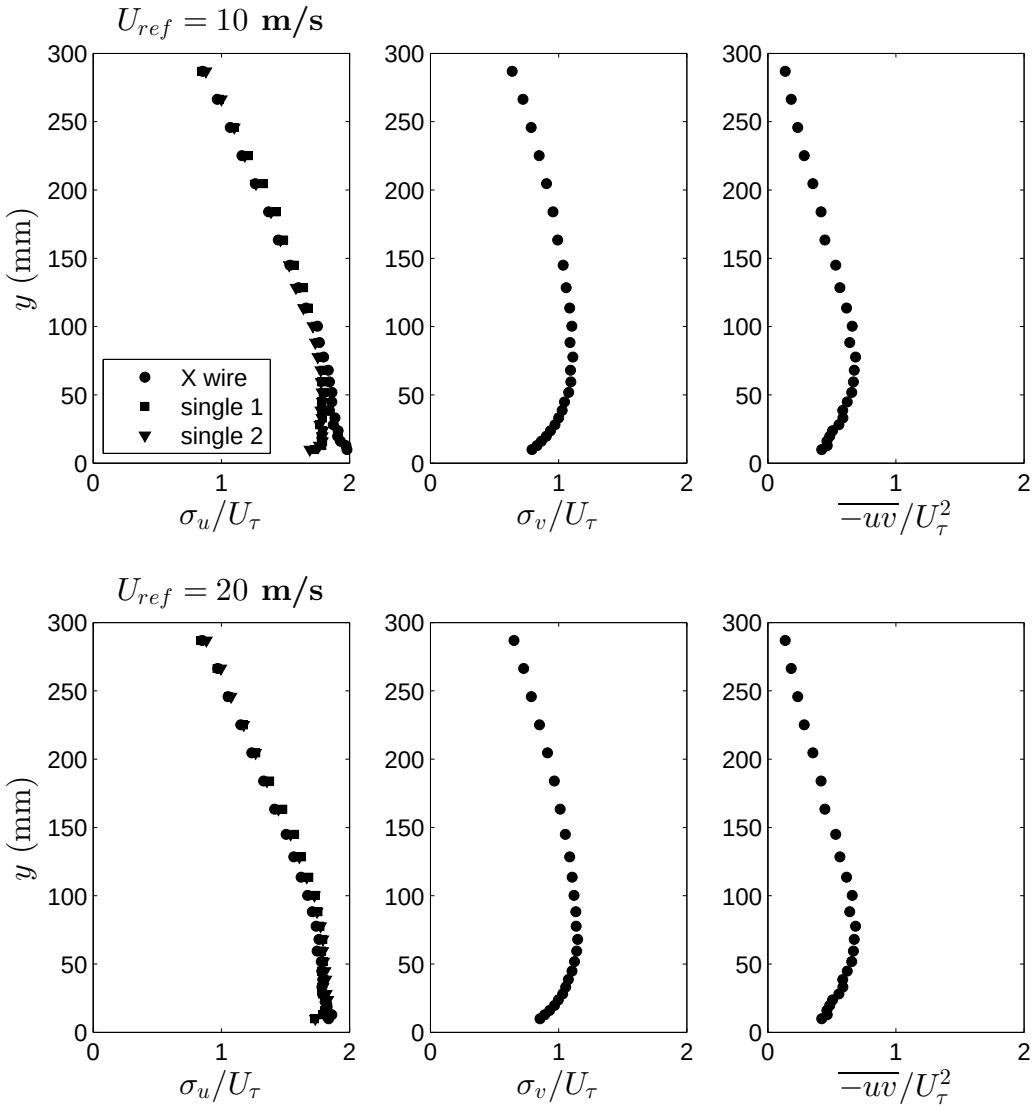

Figure A.7: Statistics measured with the configuration single-X-single wires for a freestream velocity U_{ref} of 10 m/s (first row) and 20 m/s (second row). The locations of the single wires are the same as in Figure A.6.

A.5 Incoming boundary layer (with spires): horizontal PIV

The mean velocity obtained with the PIV measurements and non dimensionalised with the velocity obtained from the Pitot is shown in Figure A.8.

The mean velocity along x (U) and its standard deviation (σ_u) have been evaluated for eight different x locations (i.e. from $x/D = 1$ to $x/D = 8$ with steps of 1) and are represented in Figure A.9(a). The variations from the mean value (obtained by a spatial average of the whole field) are represented in Figure A.9(b). For what concerns the mean velocity, the spanwise deviations from the mean value at all the y locations are less than 5% in all the cases, except

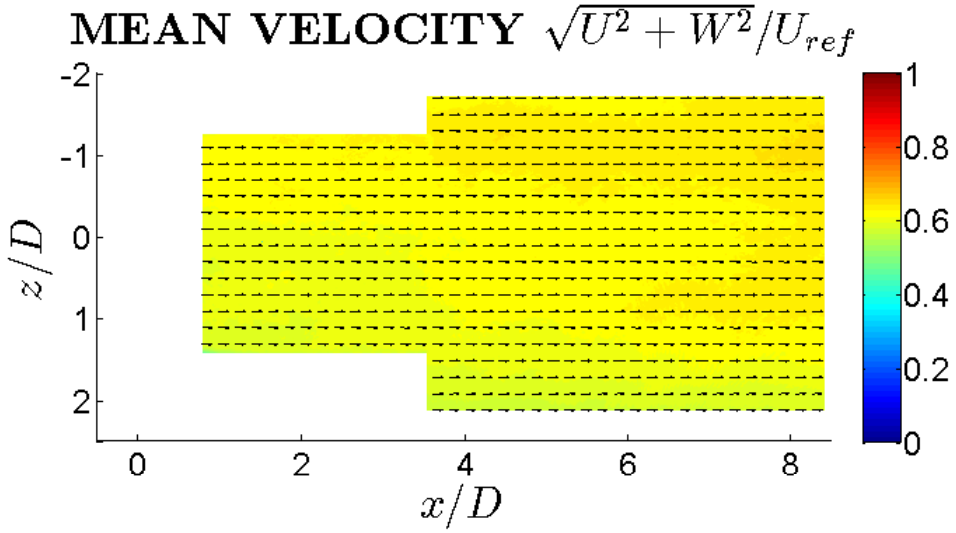

Figure A.8: Mean incoming flow.

for $z > 1.5$ which is far from the area of interest in this project. The variations of σ_u seem to have a high percentage value with respect to the mean velocity, but for all the cases, they are lower than 10% the mean value at that location (higher percentage value if the average value along the whole field is considered as a reference) for almost all the span. These results are comparable with what has been obtained with the X-wire measurements, which is that the velocity is always between $\pm 5\%$ of its averaged value. The standard deviation profiles in this case are similar to what was measured with the hot wires, spanning a range of values between $\pm 10\%$.

A.6 Hot-wire spanwise profiles

One of the goals of the second set of hot wire measurements of the incoming flow was to characterize the spanwise homogeneity of the incoming flow. The main results for three different y locations (namely 30 mm, 100 mm and 200 mm which correspond to almost 0.08δ, 0.28δ and 0.56δ, respectively) are shown in Figure A.10. The single wires are positioned 4 mm lower with respect to the X-wire, as mentioned before in §3.2.2. The spanwise locations are non dimensionalised by the patch diameter D equal to 100 mm. The patch will be located in correspondence of $z = \pm 0.5D$.

The differences with respect to the average are shown in Figure A.11. The curves for U and σ_u are obtained averaging the value of the three wires at that location (and neglecting the 4 mm difference in the vertical positioning).

For what concerns the mean velocity, the spanwise deviations from the mean value at all the y locations are less than 5% in all the cases, except for $z > 1.5$ which is far from the area of interest in this project. The variations of σ_u and σ_v seem to have a high percentage value

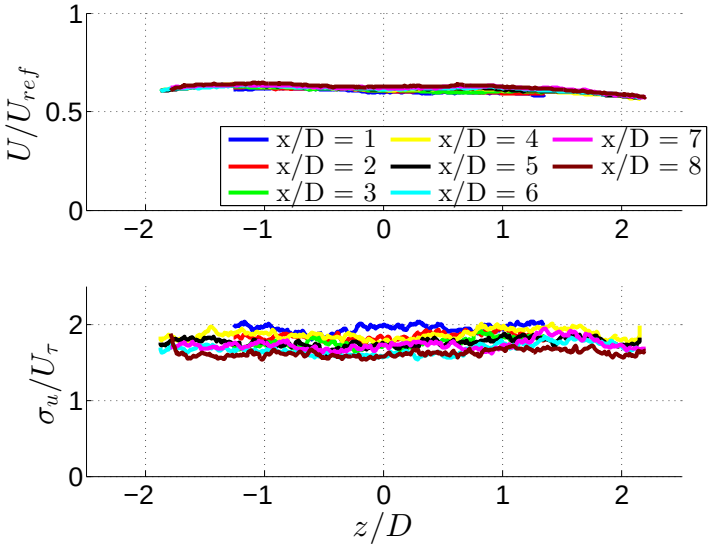

(a) Spanwise profiles.

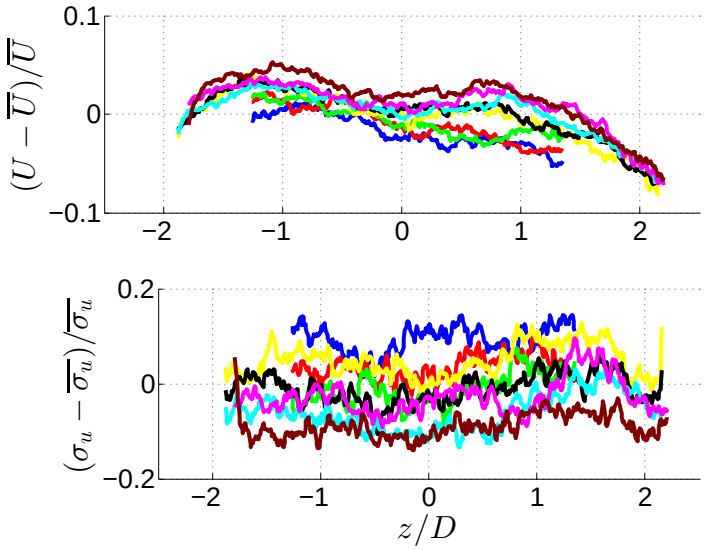

(b) Spanwise variations.

Figure A.9: Spanwise profiles (a) and variations from the mean (b) of U and σ_u along z for eight different x/D.

with respect to the mean velocity, but in any case, they are lower than 10% for almost all the span. Finally, the variations related to $-\overline{uv}$ tend to be higher in percentage tor higher locations (namely for y = 30 mm and y = 100 mm). This could be due to the fact that the mean value of $-\overline{uv}$ is much smaller than the mean of σ_u and σ_v, so small fluctuations results in a bigger percentage value. In any case thay are less than 20%.

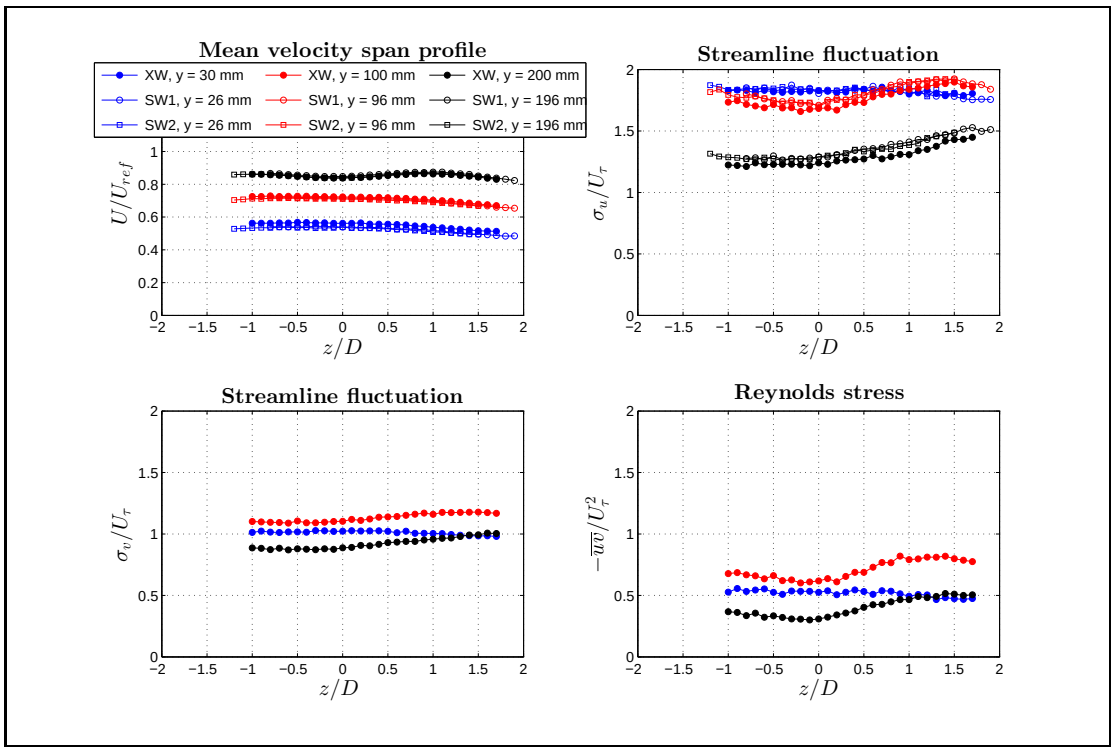

Figure A.10: Spanwise profiles of mean velocities and fluctuations. The colours identify three different vertical locations (black corresponds to y =200 mm, red to y = 100 mm and blue to y =30 mm from the tunnel floor for the X-wire). XW corresponds to the X wire measurements, SW1 to the first single wire (located at +20 mm along z with respect to the X wire), and SW2 to the second single wire (located at −20 mm along z with respect to the X wire).

A.7 Incoming boundary layer (with spires): vertical PIV

The mean velocity obtained with the PIV measurements and non dimensionalised with the velocity obtained from the Pitot, the standard deviation of U and V, σ_U and σ_V non dimensionalised with U_τ and the Reynolds stress non dimensionalised with U_τ^2 are shown in Figure A.12.

From the figures it is evident that the flow is still developing at the patch location and that the number of images taken to characterise the flow does not give a smooth result for the time-averaged statistics. In order to have a better comparison, a spatial average along x has been taken and the three profiles are shown in Figure A.13, together with the how wire results described in A.4 for 20 m/s, up to y = 200 mm, which is about the maximum height of the PIV measurements.

From the averages, it is evident that the hot wire underestimated all the fluctuations. Despite the module, the trends of the statistics measured by the hot wire and by PIV seem to be the same for all the quantities. The plateau in σ_U/U_τ is more pronounced for the PIV data and it extends up to y = 100 mm, confirming what was previously found in this chapter. The trend of the lateral velocity fluctuations σ_V/U_τ and Reynolds stress $-\overline{uv}/U_\tau^2$ decreasing below $y \simeq 40$

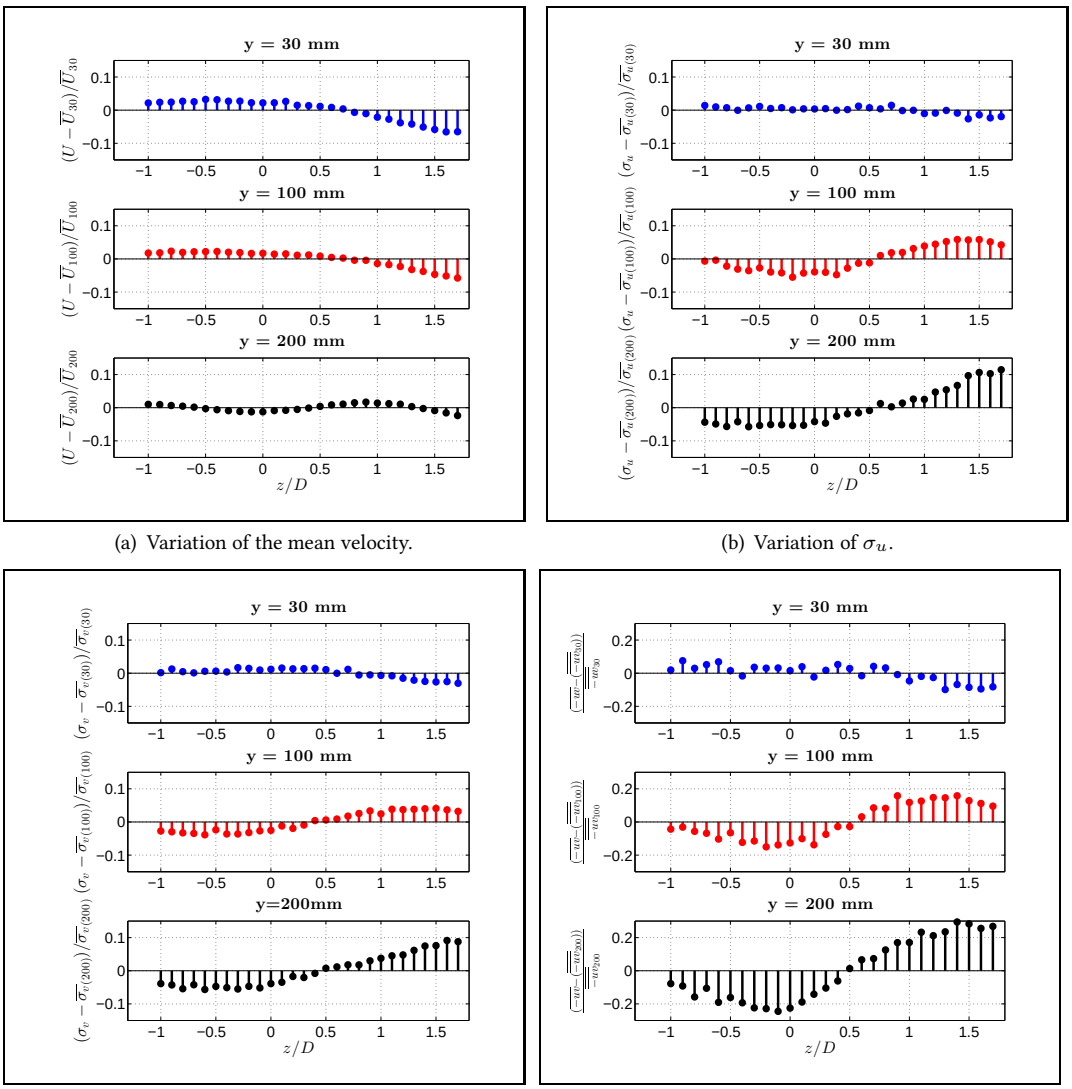

(a) Variation of the mean velocity.

(b) Variation of σ_u.

(c) Variation of σ_v.

(d) Variations of $-\overline{uv}$.

Figure A.11: Average spanwise variations over the three HW for the mean velocity and statistics at different y locations.

mm is confirmed as well from the PIV results, which suggests that for the flow conditioning used in the present work, the height of roughness sub-layer is of the order of this length.

The evaluation of the friction velocity by the viscous contribution to the stress gives a value of U_τ/U_{ref} ≃0.055, which is closer to what was found in 3.2.4. This value is within 5% of the previous value, which is considered a very good agreement with the previous results.

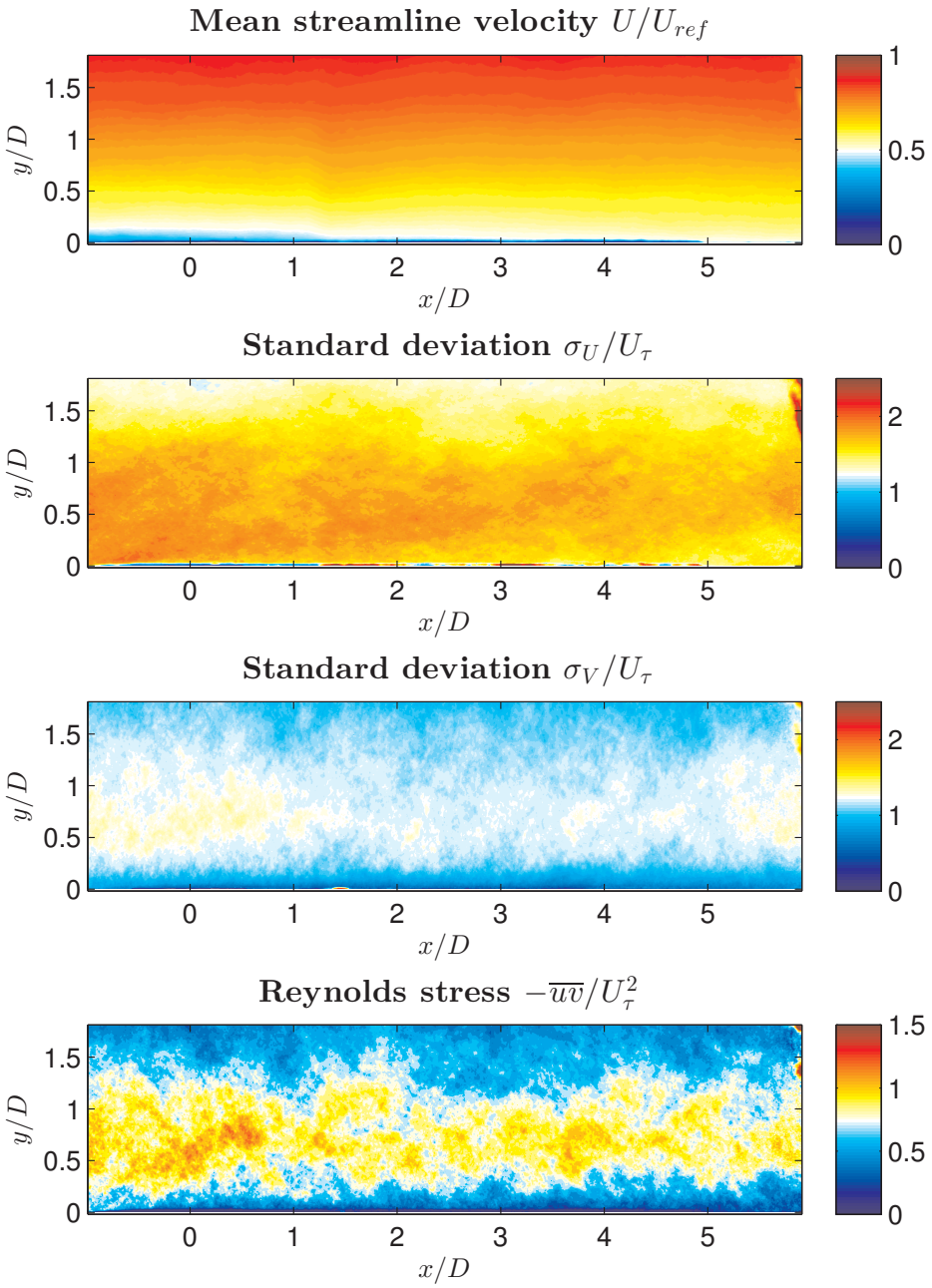

Figure A.12: Vertical PIV, incoming flow results.

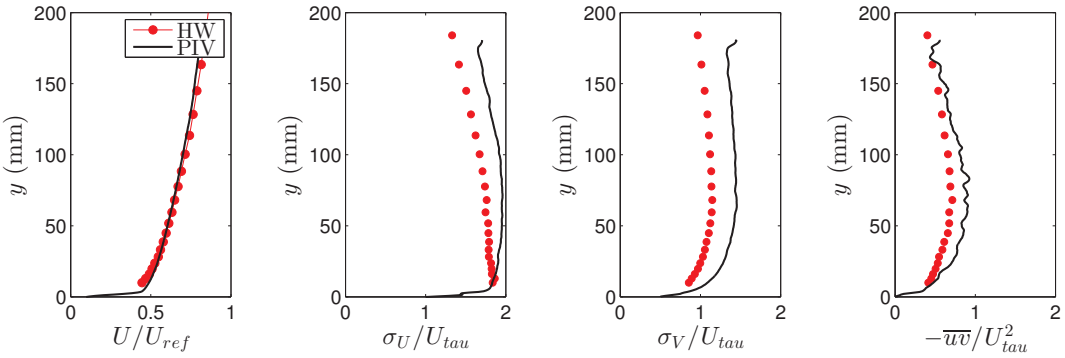

Figure A.13: Spatial average of mean quantities from vertical PIV experiment.

Appendix B

Spectra from hot-wire measurements in the wake

All the following plots are the plane view of the vector field and contours of various quantities. $U_{h/2}$ is the incoming velocity of the boundary layer at the plane of the measurements (y/D = 0.5). The vector field only indicates the flow direction, but not its intensity (the length of the vectors is not proportional to their intensity). Only one vector every 35 vectors is represented. The cylinders are represented in their actual configuration. XXXXXXXXXXX

B.1 All spectra at different velocities

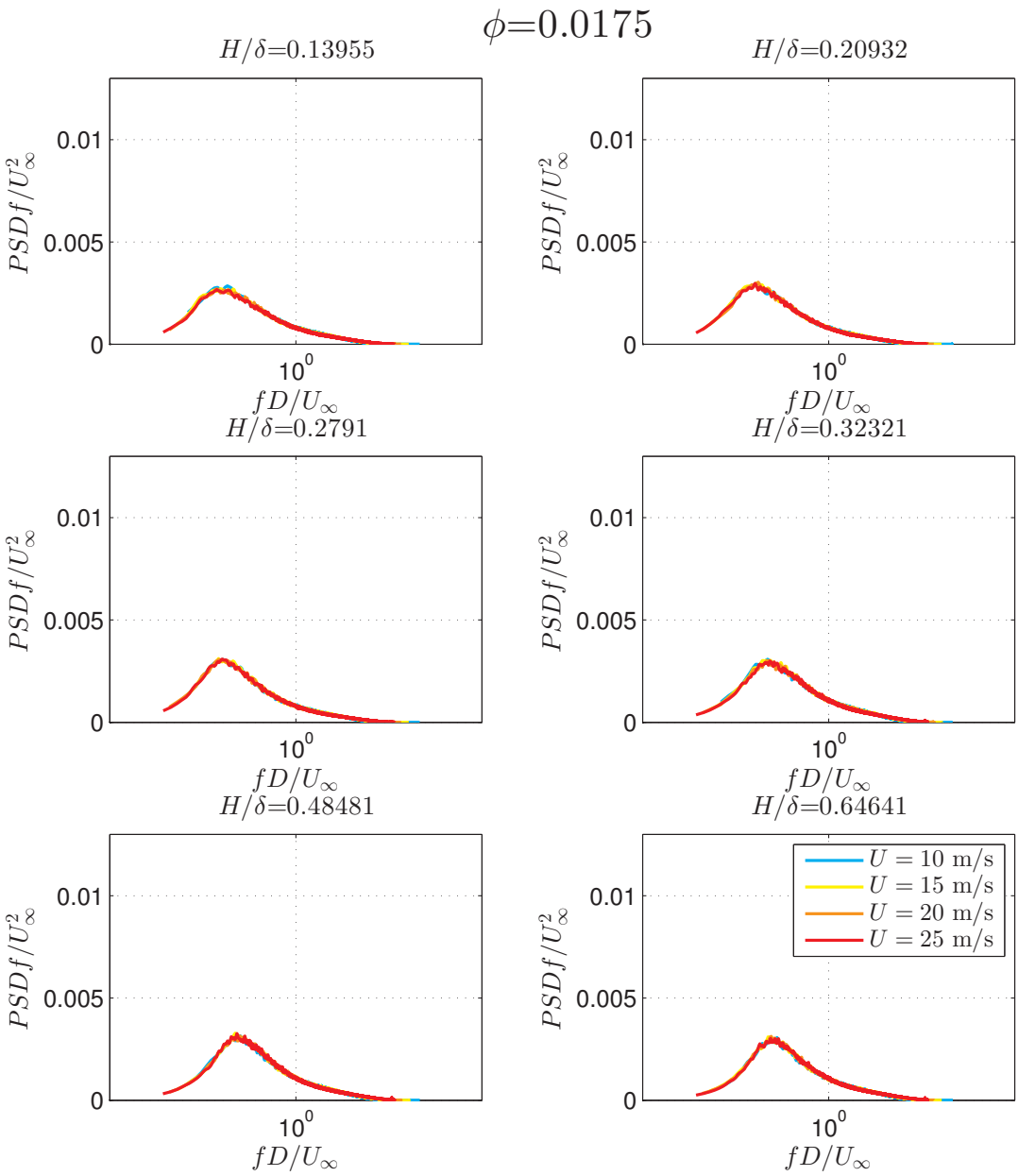

Figure B.1: Plots of premultiplied spectra for ϕ = 0.0175 (i.e. C_7) at different H/δ for four different freestream velocities.

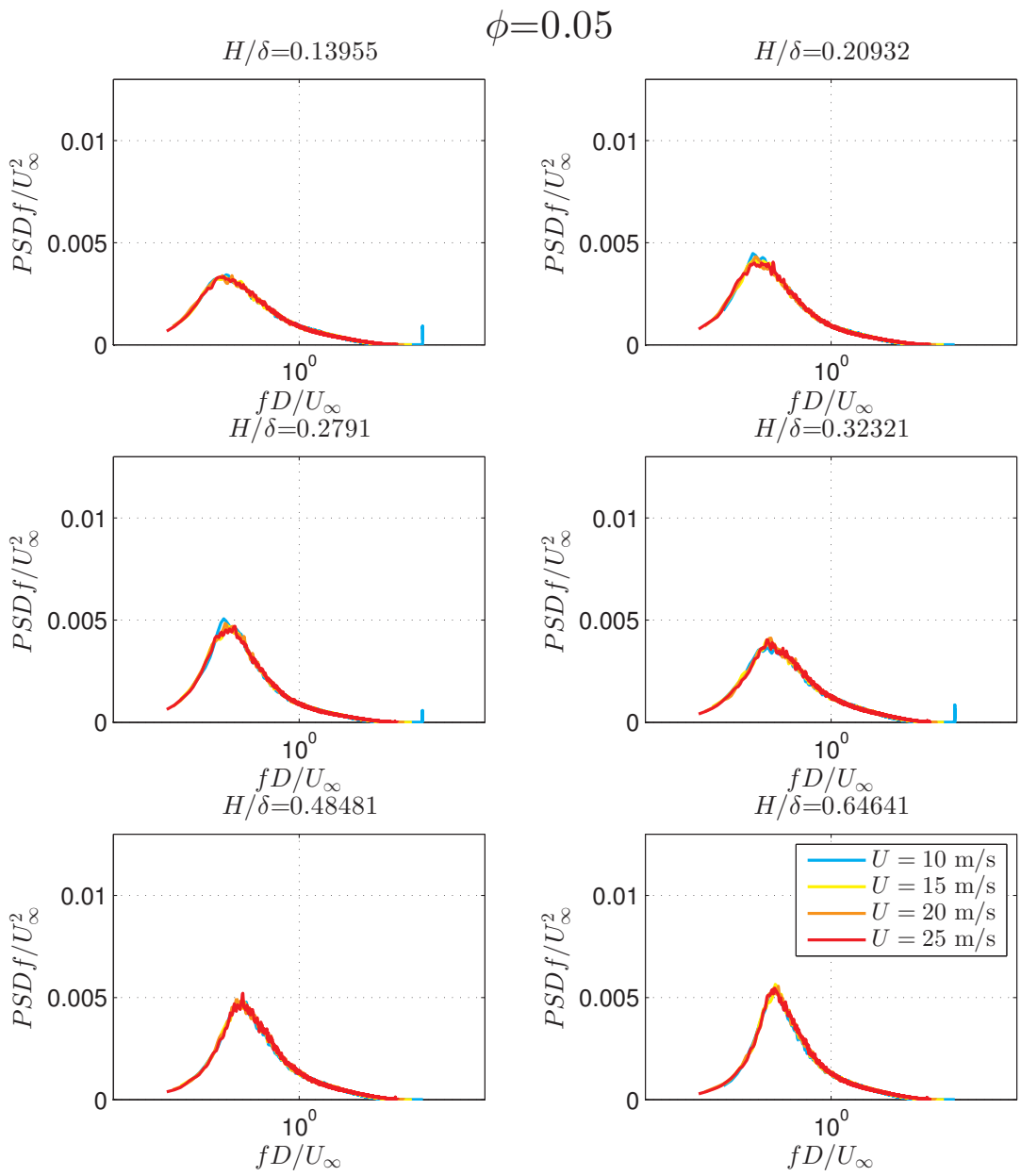

Figure B.2: Plots of premultiplied spectra for ϕ = 0.05 (i.e. C_{20}) at different H/δ for four different freestream velocities.

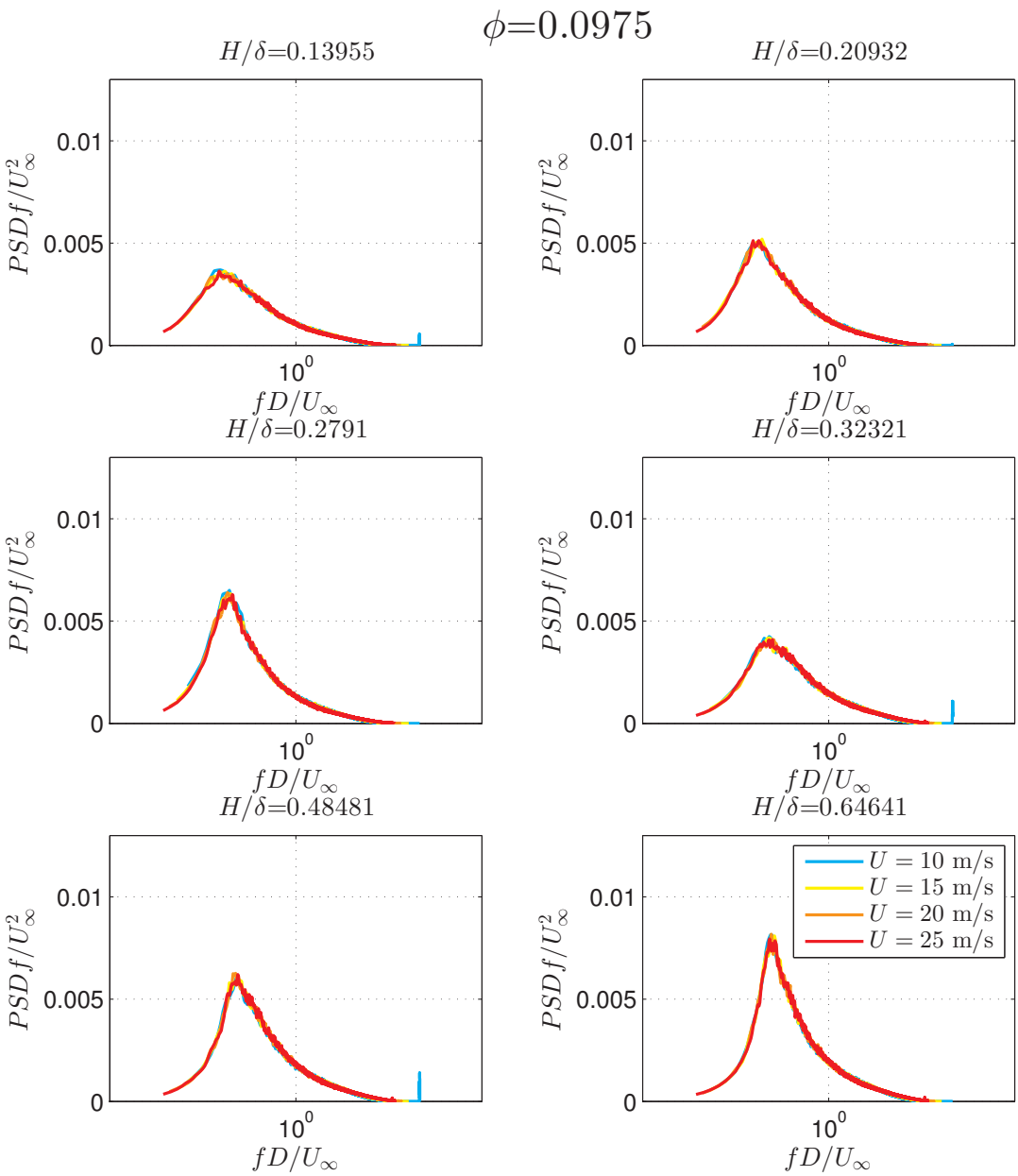

Figure B.3: Plots of premultiplied spectra for ϕ = 0.0975 (i.e. C_{39}) at different H/δ for four different freestream velocities.

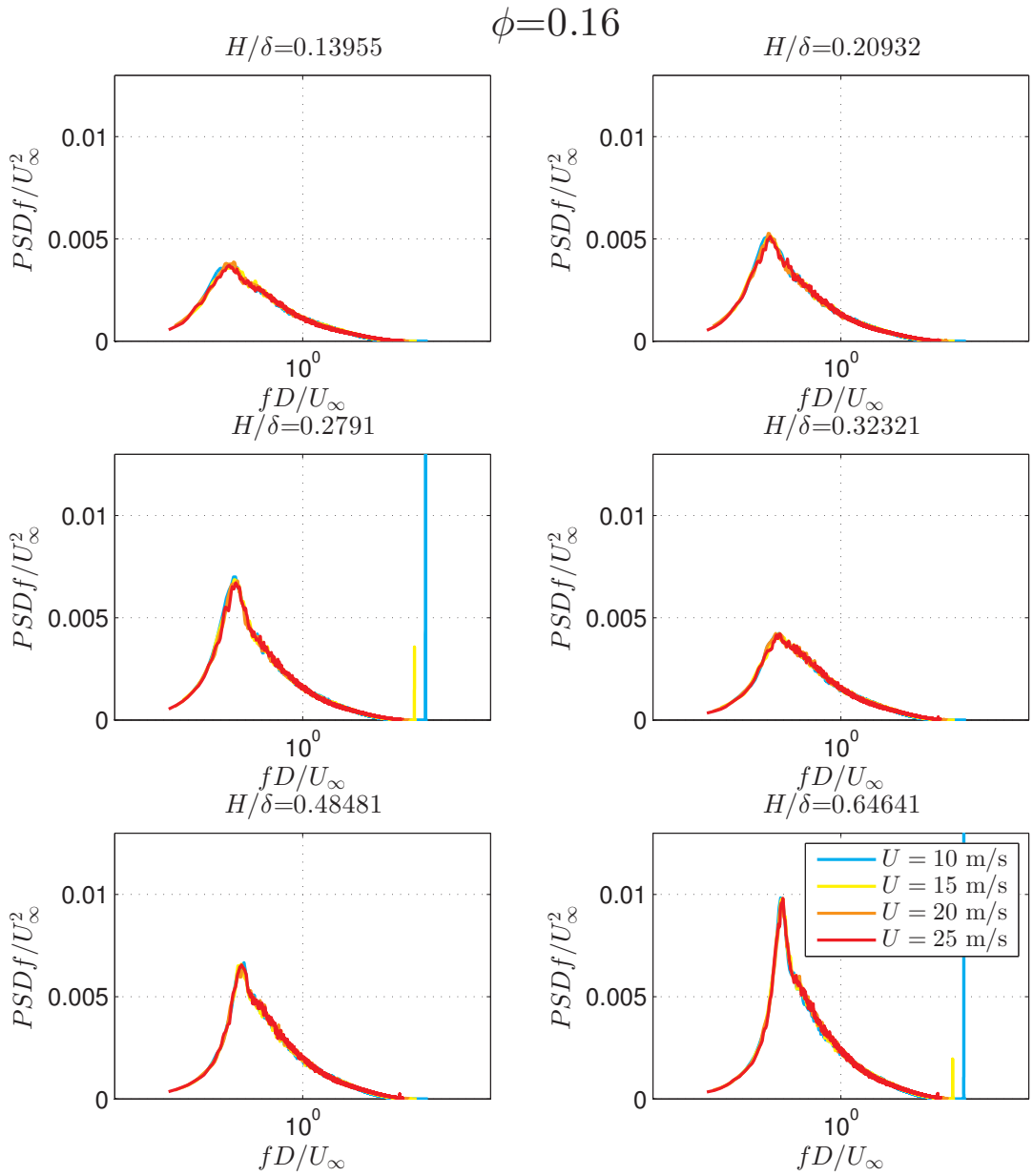

Figure B.4: Plots of premultiplied spectra for ϕ = 0.16 (i.e. C_{64}) at different H/δ for four different freestream velocities.

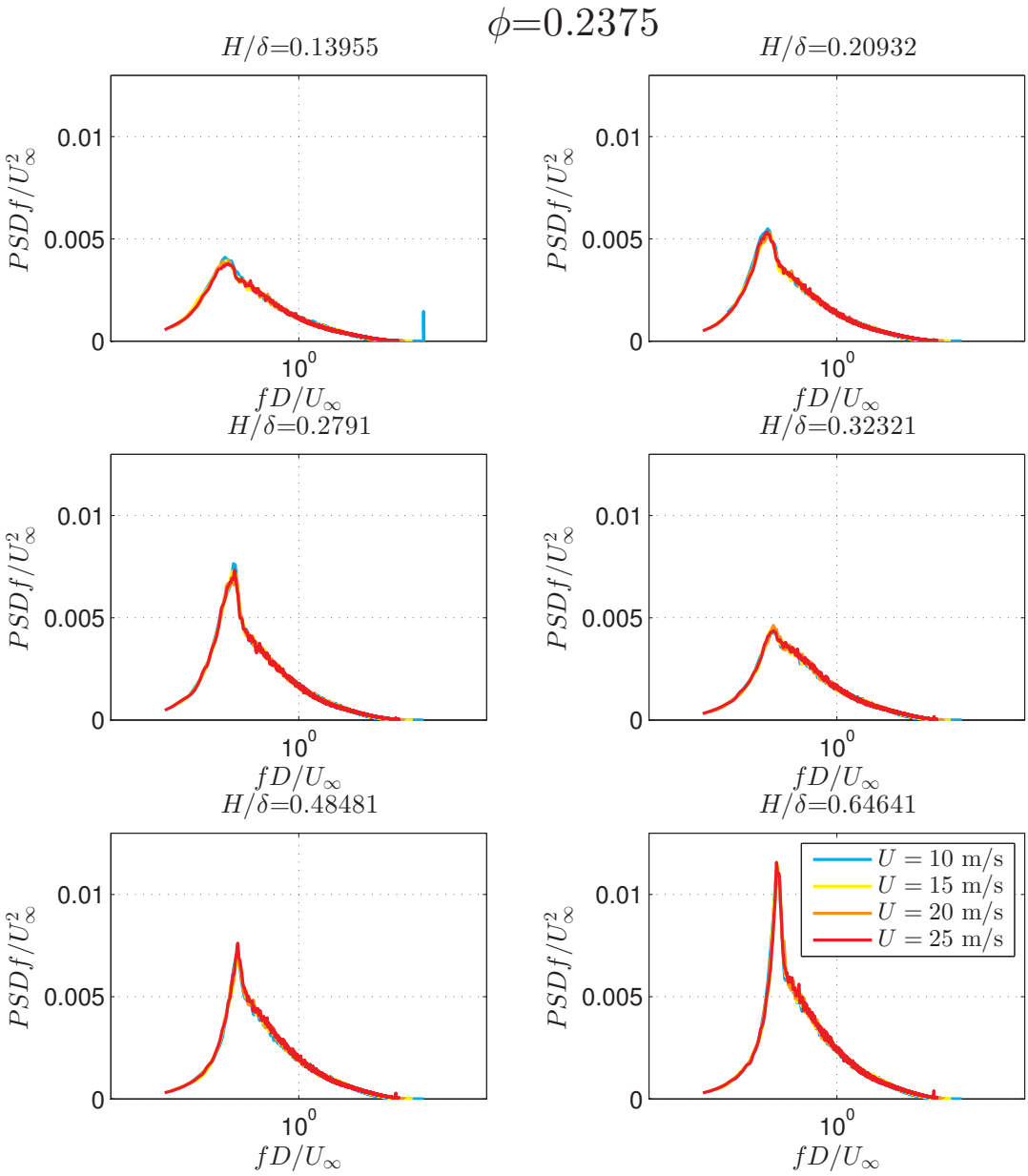

Figure B.5: Plots of premultiplied spectra for ϕ = 0.2375 (i.e. C_{95}) at different H/δ for four different freestream velocities.

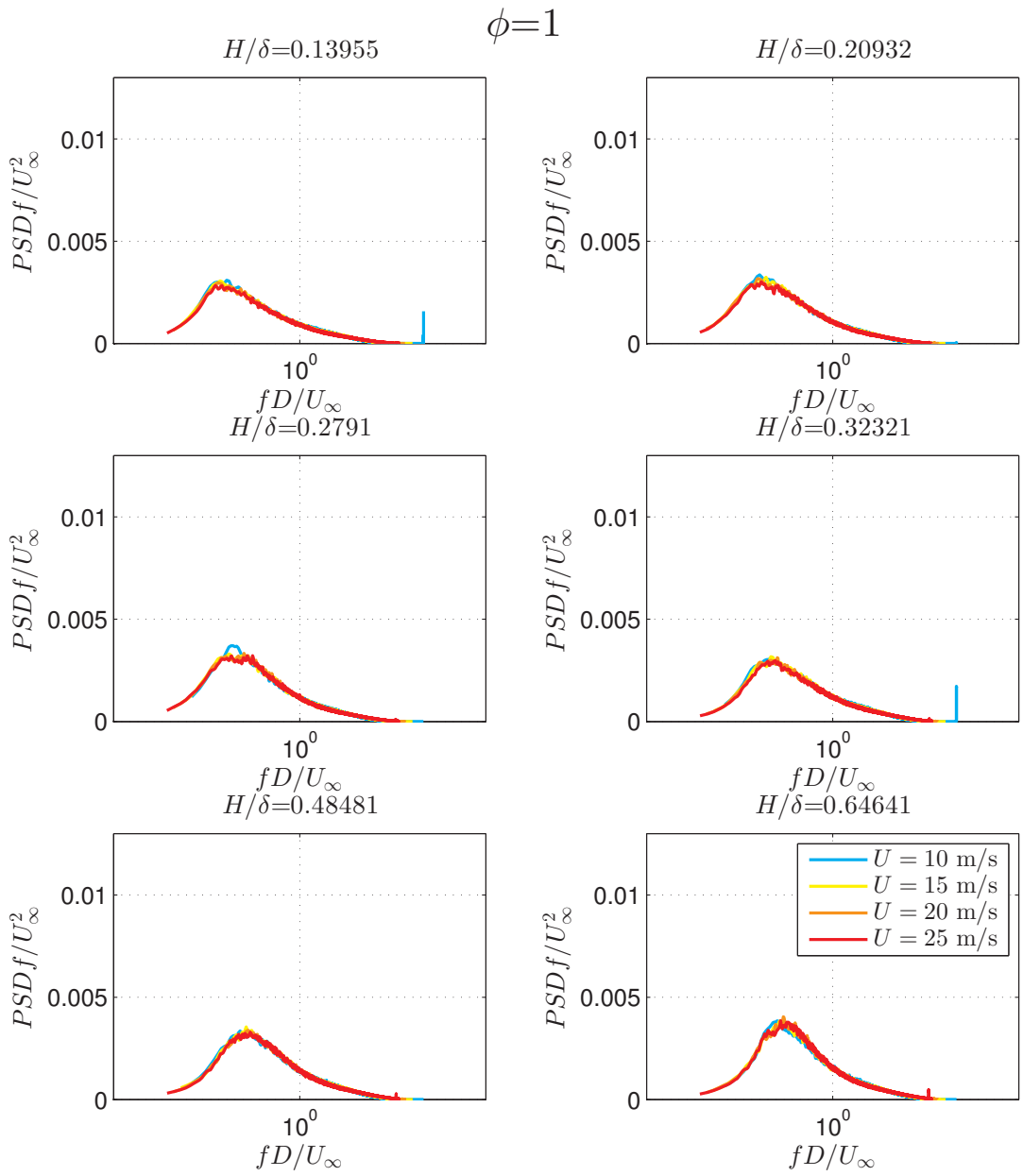

Figure B.6: Plots of premultiplied spectra for ϕ = 1 (i.e. C_S) at different H/δ for four different freestream velocities.

B.2 Free flow spectra at different velocities

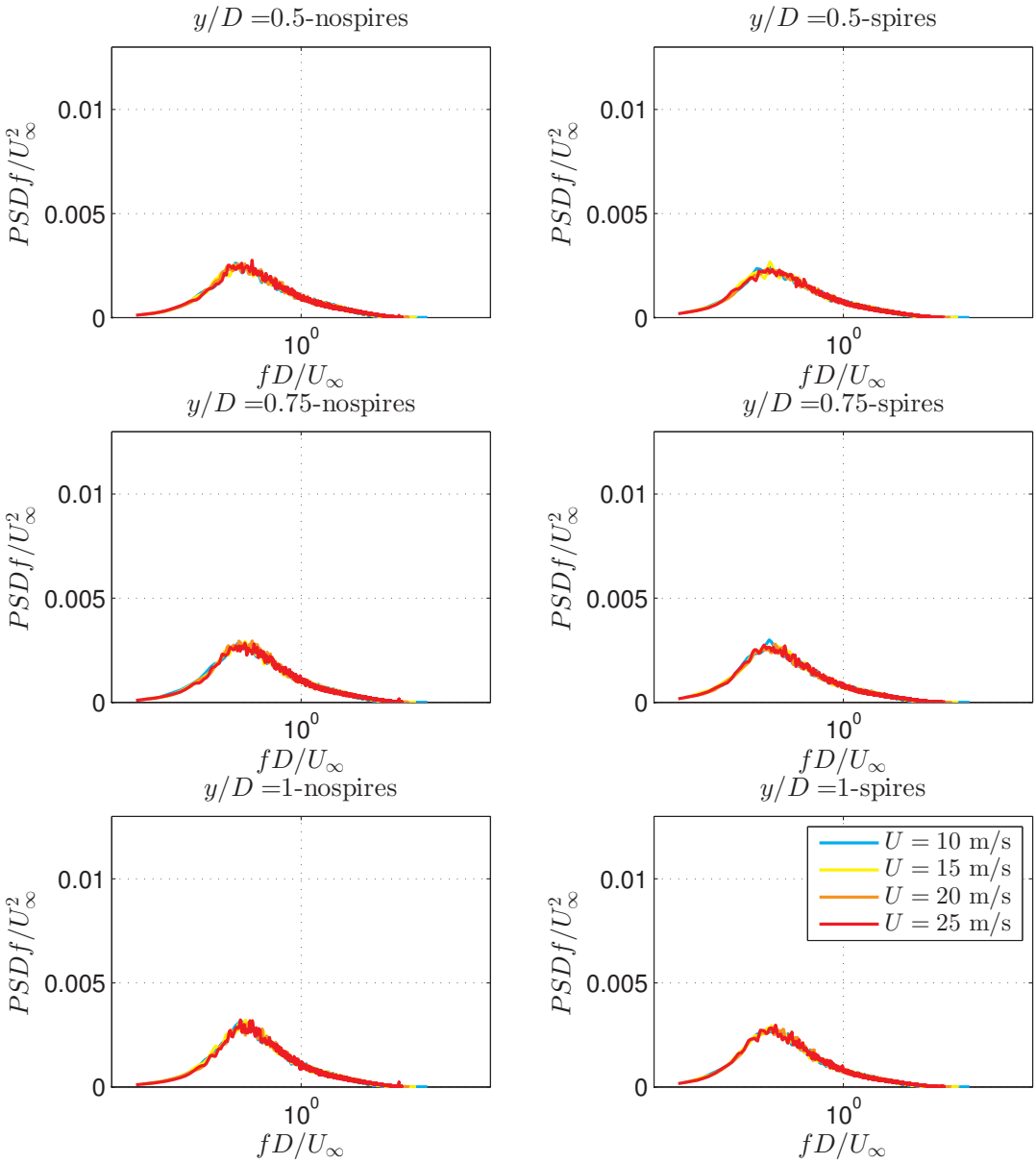

Figure B.7: Plots of premultiplied spectra for the freestream flow at different H/δ for four different freestream velocities. y/D is the height of the hot wire from the tunnel floor.

Appendix C

Additional plots

All the following plots are the plane view of the vector field and contours of various quantities. $U_{h/2}$ is the incoming velocity of the boundary layer at the plane of the measurements (y/D = 0.5). The vector field only indicates the flow direction, but not its intensity (the length of the vectors is not proportional to their intensity). Only one vector every 35 vectors is represented. The cylinders are represented in their actual configuration.

C.1 Horizontal PIV: mean lateral velocity

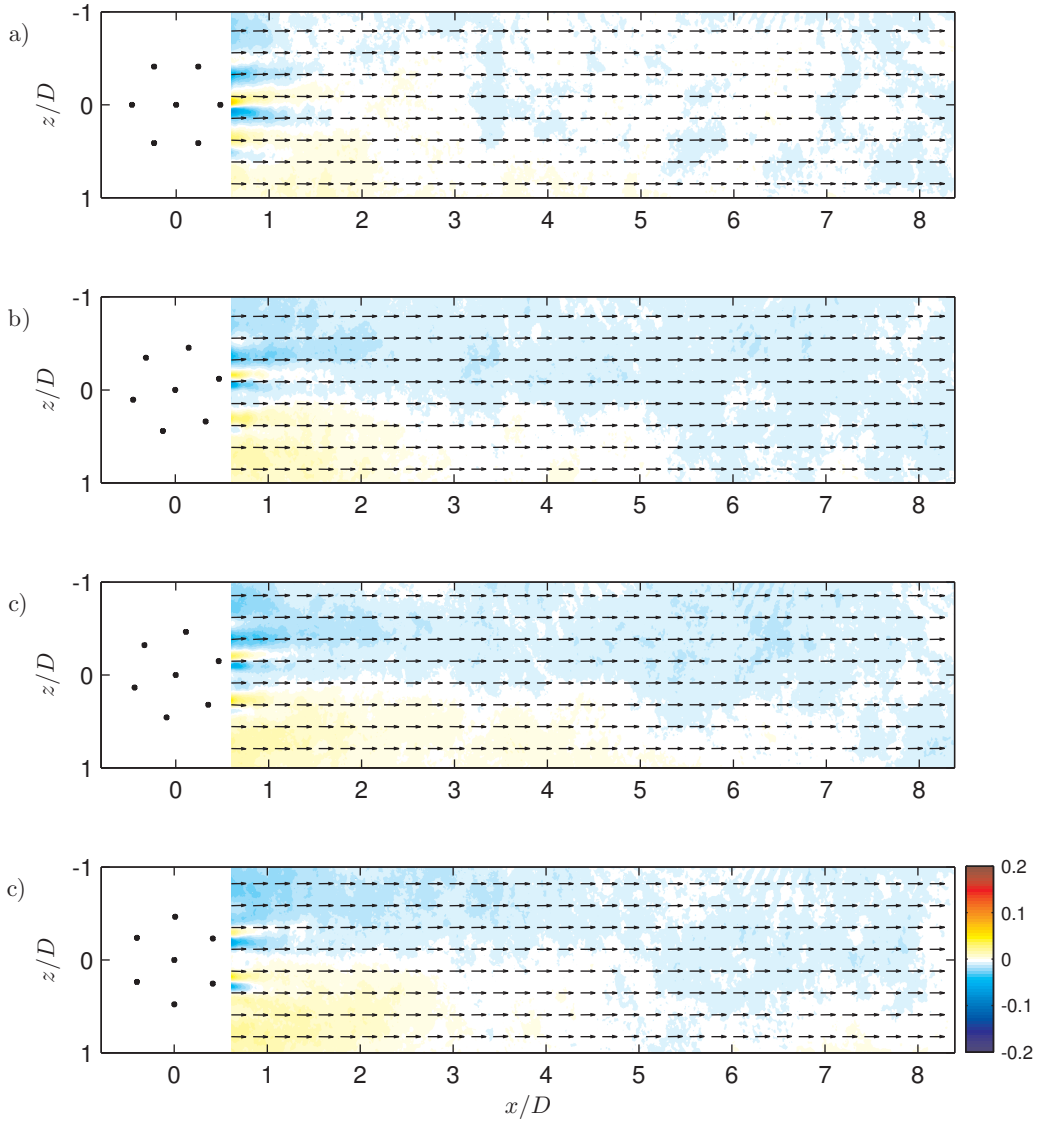

Figure C.1: Plots of $W/U_{y=H/2}$ (a) C_{7_0}, (b) $C_{7_{10}}$, (c) $C_{7_{20}}$ and (d) $C_{7_{30}}$.

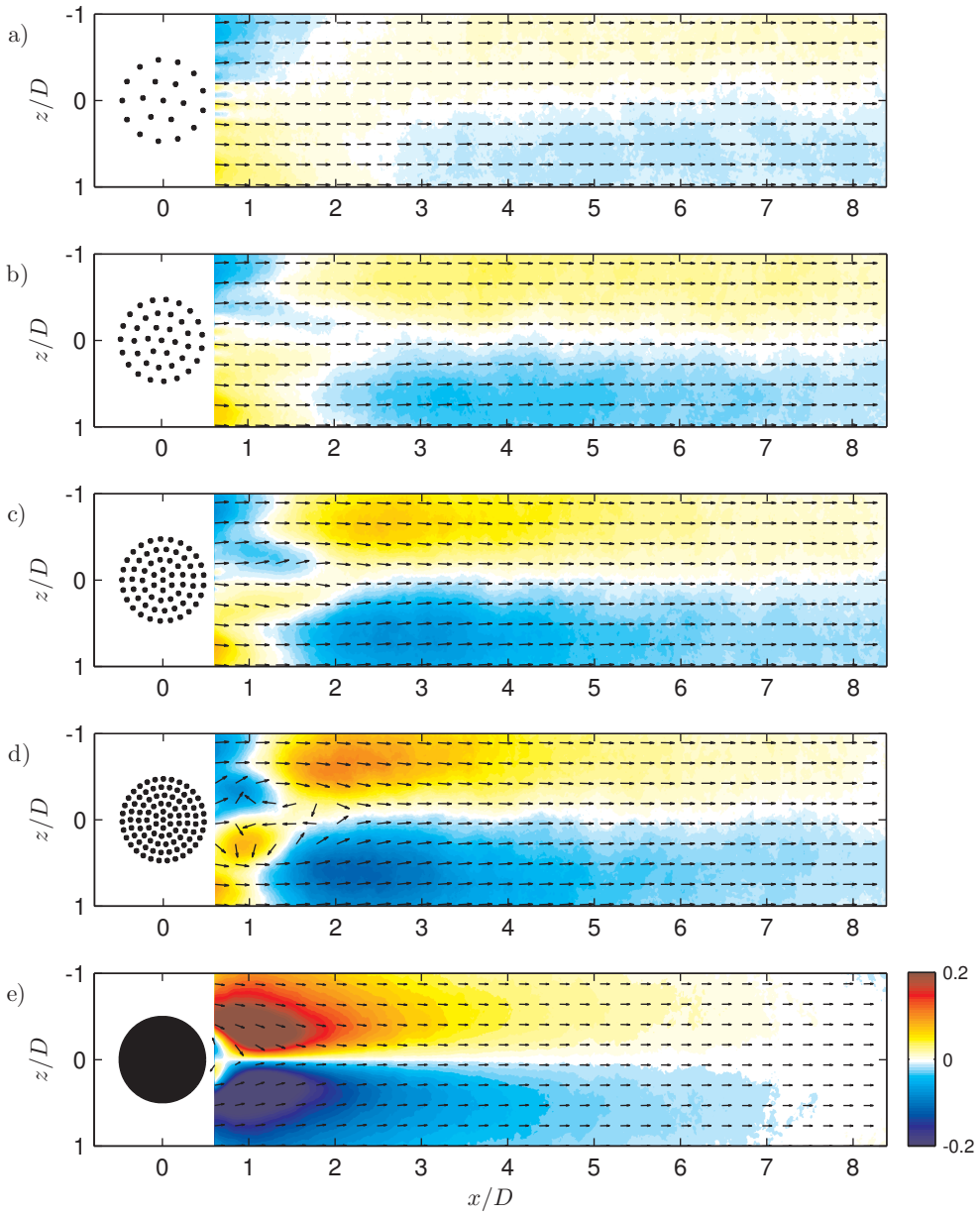

Figure C.2: Plots of $W/U_{y=H/2}$ (a) C_{20}, (b) C_{39}, (c) C_{64}, (d) C_{95} and (e) C_S.

C.2 Horizontal PIV: streamline velocity fluctuations

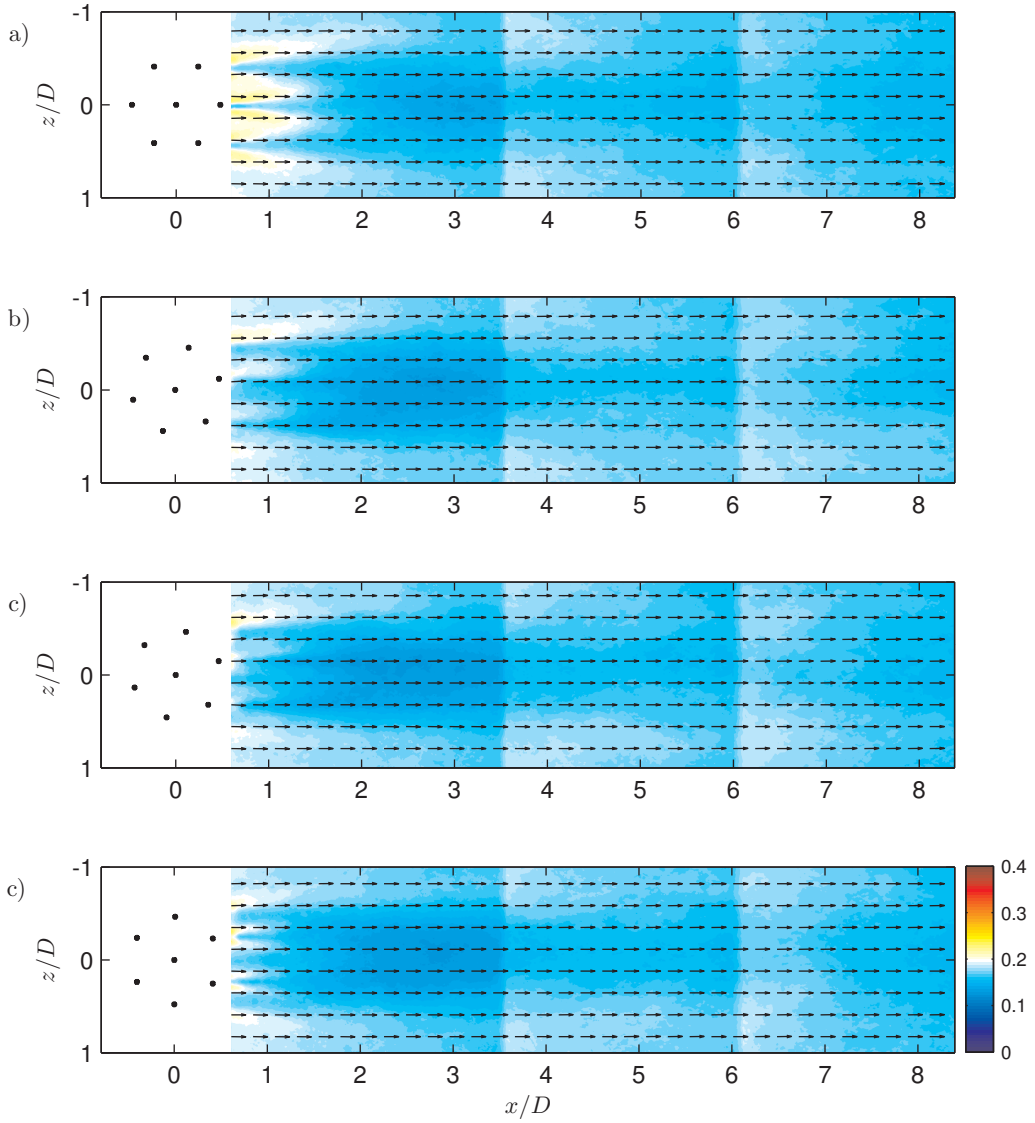

Figure C.3: Plots of $\sigma_U/U_{y=H/2}$ (a) C_{7_0}, (b) $C_{7_{10}}$, (c) $C_{7_{20}}$ and (d) $C_{7_{30}}$.

C.3 Horizontal PIV: lateral velocity fluctuations

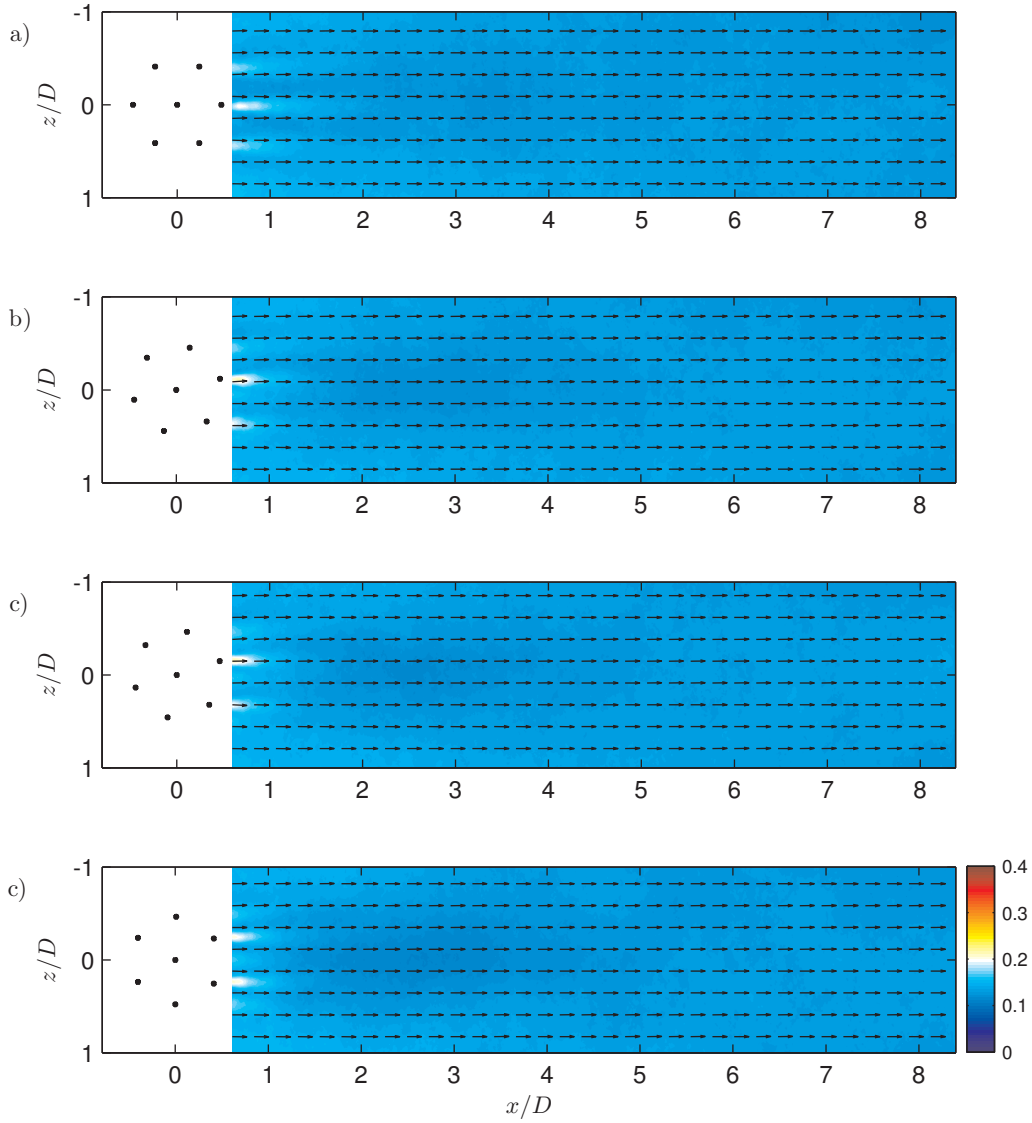

Figure C.4: Plots of $\sigma_W/U_{y=H/2}$ (a) C_{7_0}, (b) $C_{7_{10}}$, (c) $C_{7_{20}}$ and (d) $C_{7_{30}}$.

C.4 Horizontal PIV: Reynolds stress

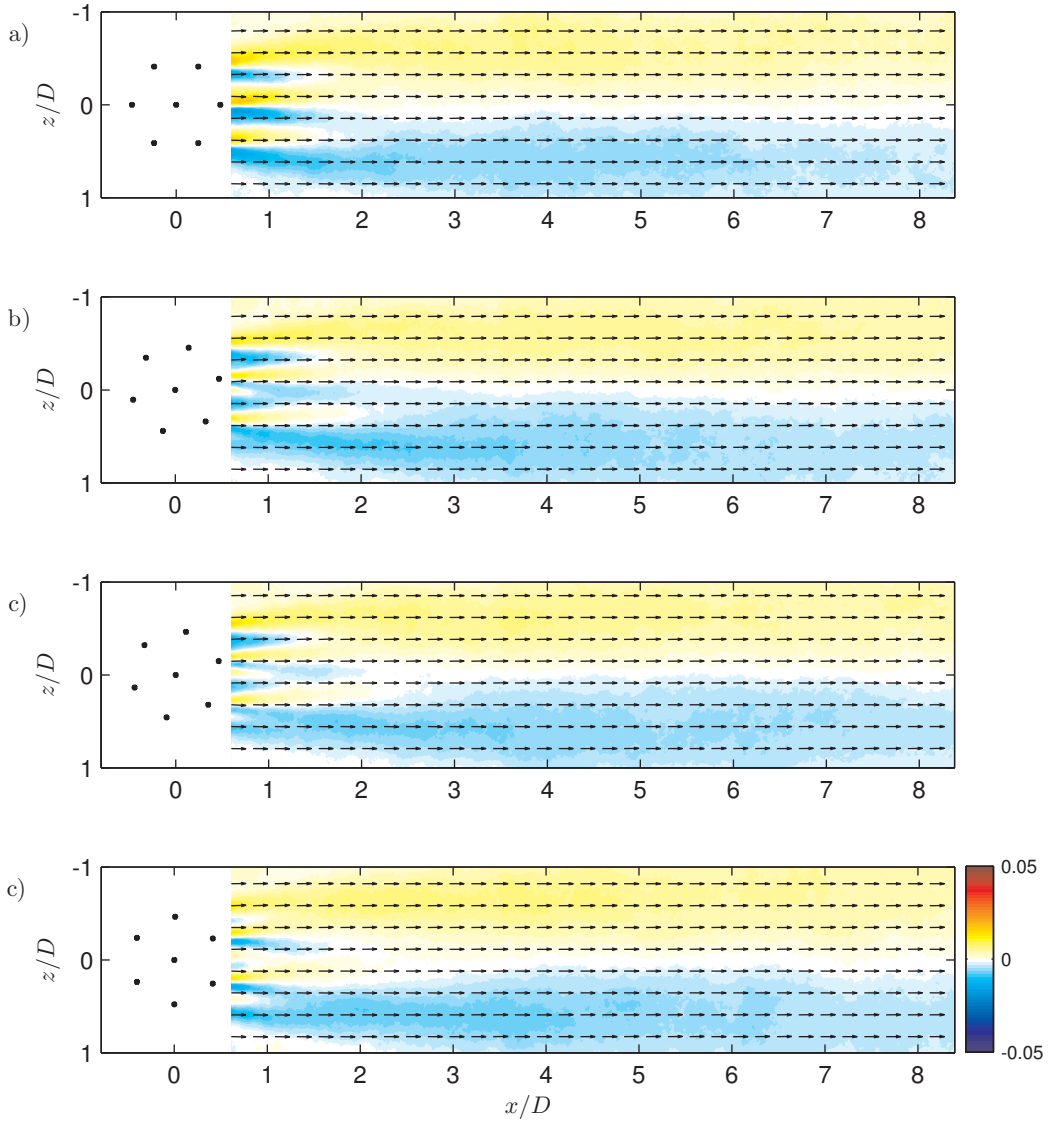

Figure C.5: Plots of $\overline{uw}/U^2_{y=H/2}$ (a) C_{7_0}, (b) $C_{7_{10}}$, (c) $C_{7_{20}}$ and (d) $C_{7_{30}}$.

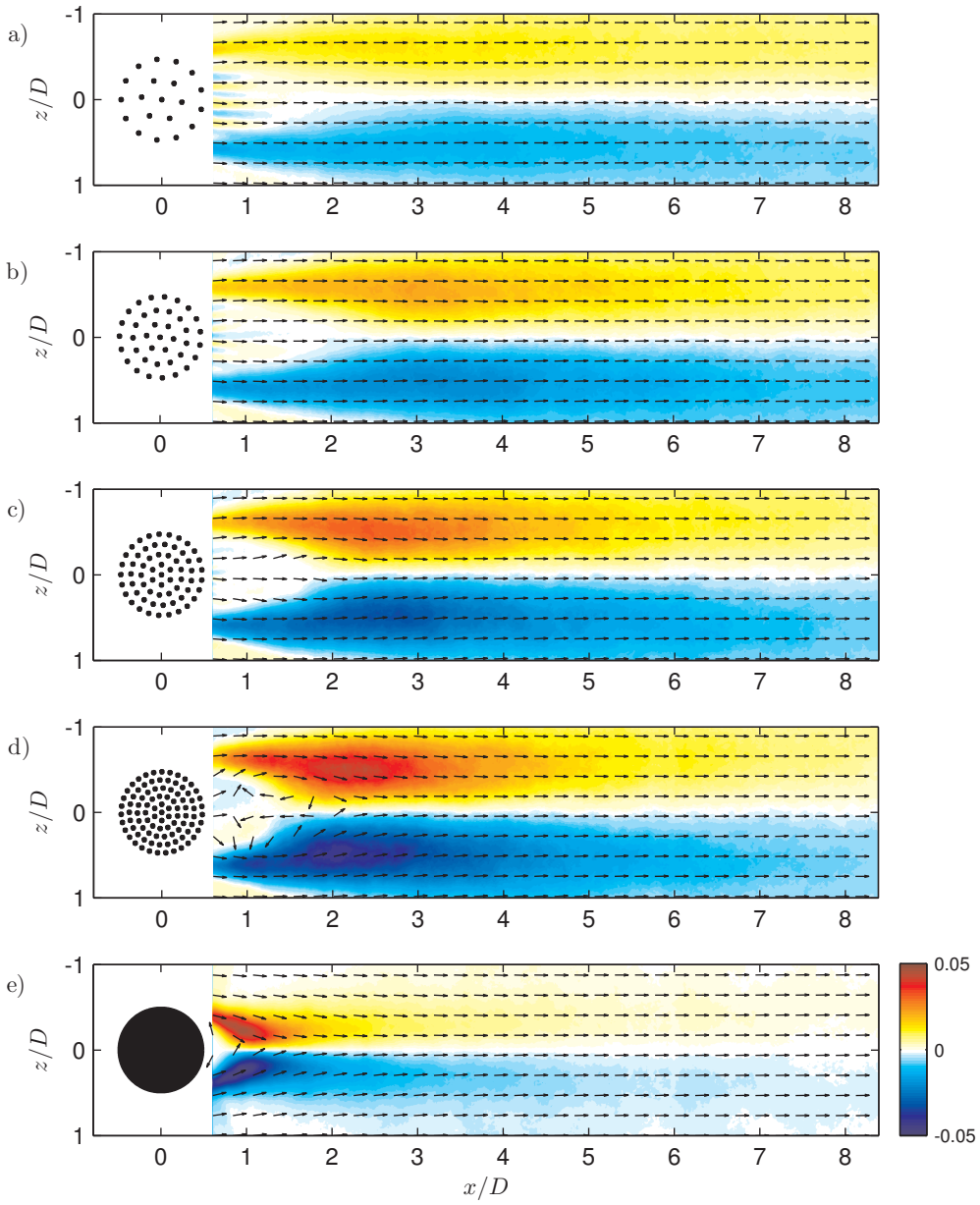

Figure C.6: Plots of $\overline{uw}/U^2_{y=H/2}$ (a) C_{20}, (b) C_{39}, (c) C_{64}, (d) C_{95} and (e) C_S.

C.5 Horizontal PIV: vorticity

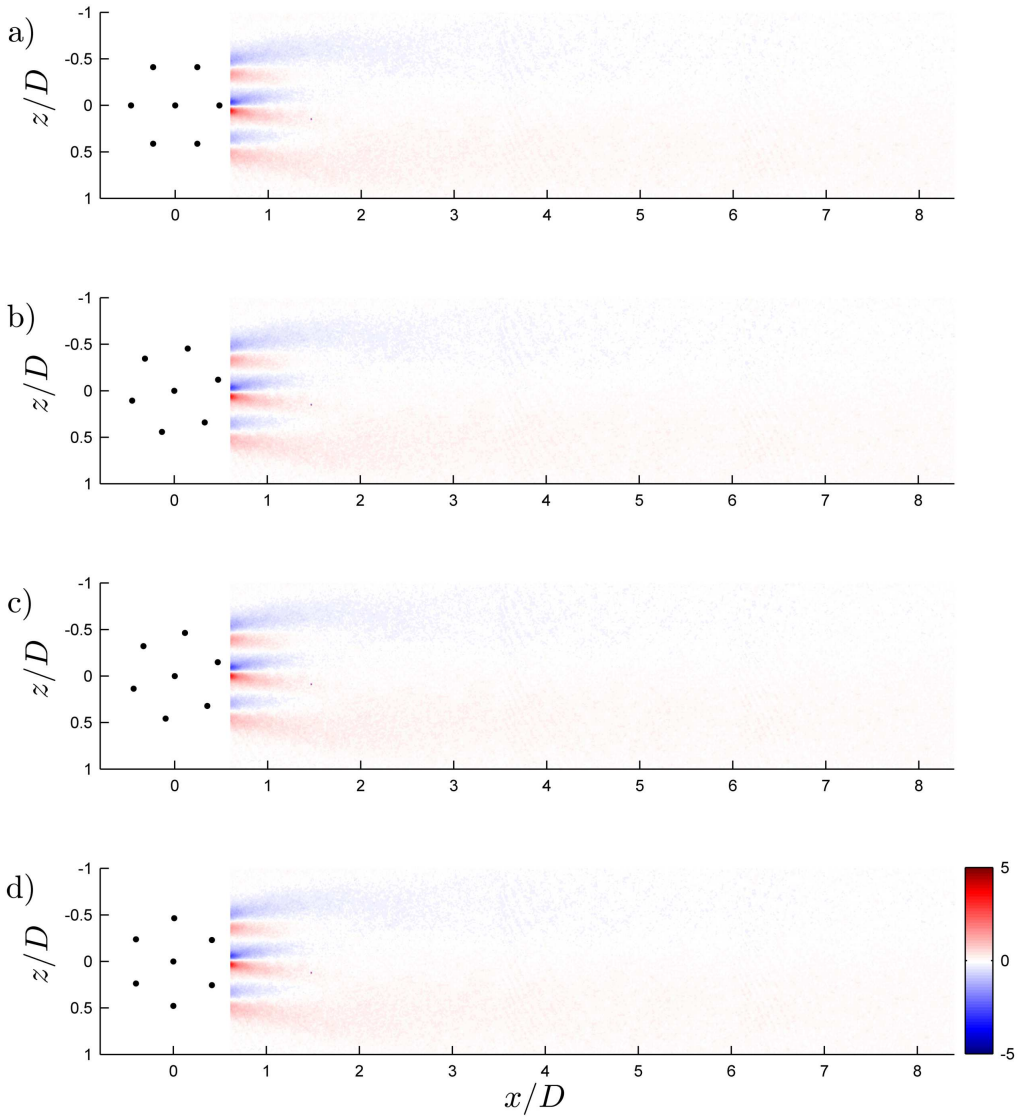

Figure C.7: Plots of $\omega_y D/U_\infty$ (a) C_{7_0}, (b) $C_{7_{10}}$, (c) $C_{7_{20}}$ and (d) $C_{7_{30}}$.

C.6 Vertical PIV: streamline velocity fluctuations

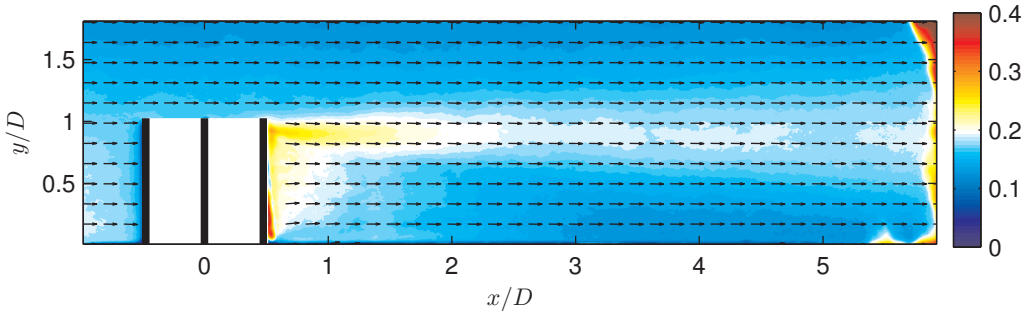

Figure C.8: Plots of $\sigma_U/U_{y=H/2}$ for C_7.

C.7 Vertical PIV: vertical velocity fluctuations

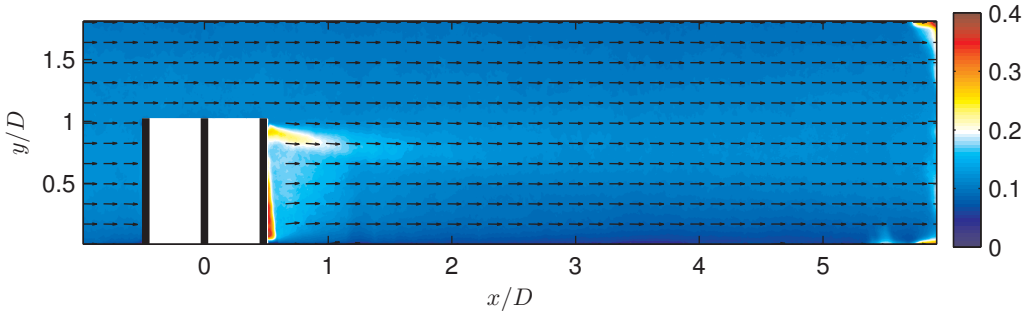

Figure C.9: Plots of $\sigma_V/U_{y=H/2}$ for C_7.

C.8 Vertical PIV: Reynolds stress

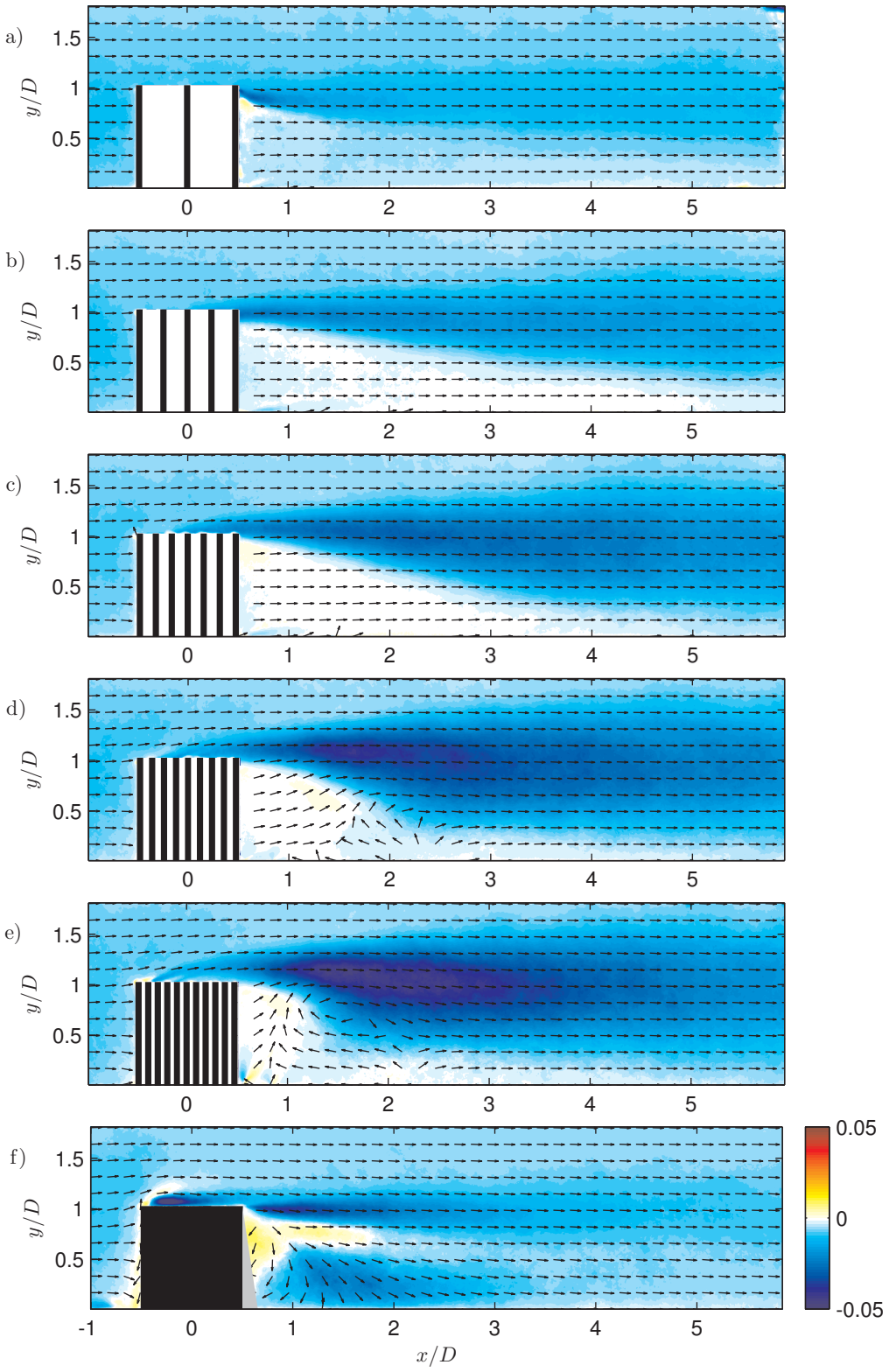

Figure C.10: Plots of $\overline{uv}/U^2_{y=H/2}$ (a) C_7, (b) C_{20}, (c) C_{39}, (d) C_{64}, (e) C_{95} and (f) C_S.

C.9 Vertical PIV: vorticity

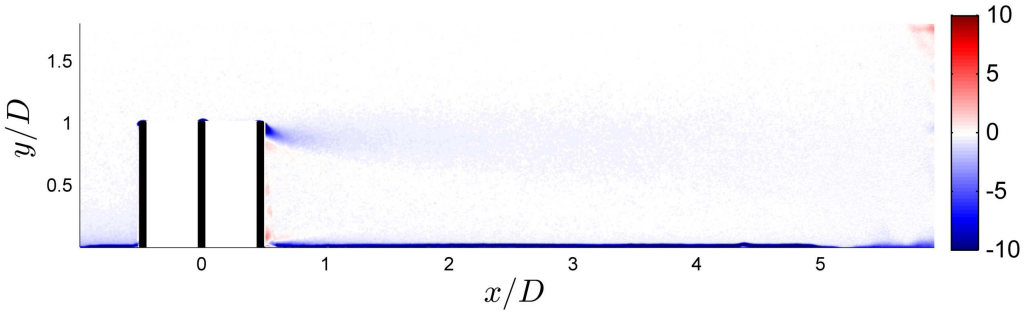

Figure C.11: Plots of $\omega_z D/U_\infty$ for C_7.

Appendix D

Comparison with 2-D data

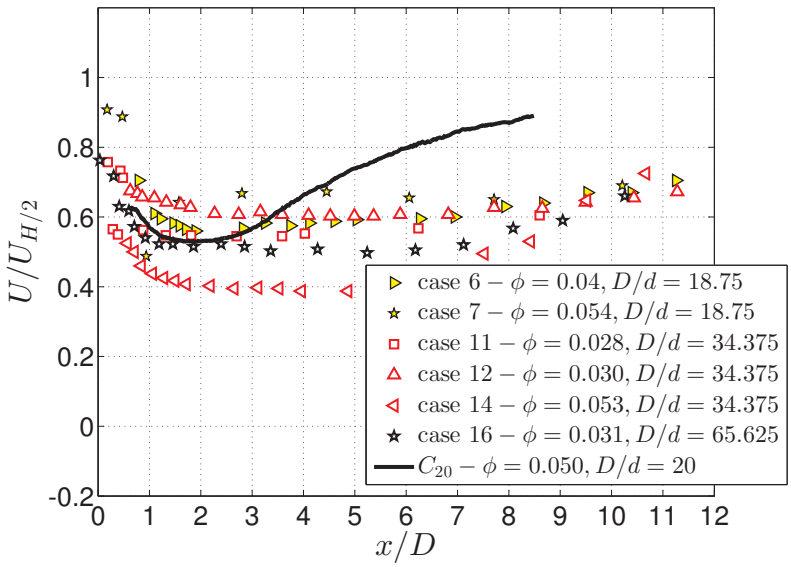

Figure D.1: Comparison of the centreline velocity $U/U_{H/2}$ with Chen et al. (2012) for the cases C_{20} (ϕ = 0.05, D/d = 20).

Figure D.1 shows the comparison for the case C_{20} with similar values of density, for different D/d. It is evident how, except for the case 14 from Chen et al. (2012), the minimum value of U in the present study is comparable with the 2D case. The steady region is present for this case, but shorter (up to almost x/D = 2.5, e.g. $2D$ after the end of the patch). Looking at the velocity recovery rate, it seems comparable only with case 14, while all the other cases show a slower trend. This is in agreement with the faster 3D wake development which was introduced in Section 6.3.

The effect of D/d seems to apparently "increase" the nominal density of the patch, so that it behaves as a patch with higher density. Somehow lower densities with higher D/d behaves as C_{20} model (e.g. case 11 and case 16), while similar densities with higher D/d show a higher velocity deficit (e.g. case 14).

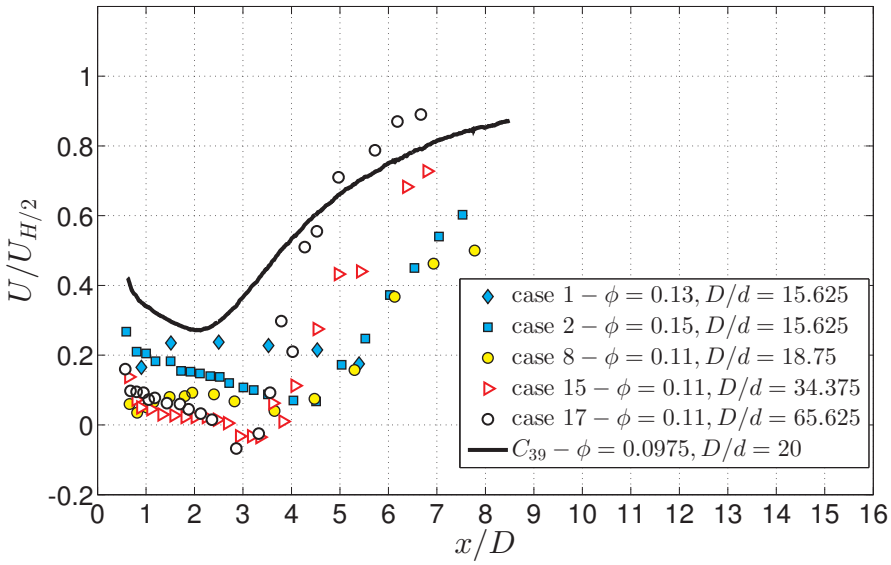

Figure D.2: Comparison of the centreline velocity $U/U_{H/2}$ with Chen et al. (2012) for the case C_{39} (ϕ = 0.0975, D/d = 20).

The data in Chen et al. (2012) did not include any data for densities between 0.05 and 0.11. Model C_{39} was compared with the closer values of densities from Chen et al. (2012) and it is shown in Figure D.2. The C_{39} case shows a short plateau between x/D = 2 and 2.2, and the rate of the recovery seems comparable with the cases from Chen et al. (2012). The minimum in the present case is close only to case 1 in Figure D.2 (which has higher density but lower D/d), while all other cases have lower peaks and all the cases show longer steady velocity regions which are due to the two dimensionality of the models.

The general effect of D/d is confirmed also from this plot, except for case 8 whose behaviour should have been closer to C_{39}.

Figure D.3 shows the comparison for the case C_{64} with similar values of density, for different D/d. For this case, the minimum in velocity decreases, being still comparable with the set of Chen data. There is no plateau and the velocity recovery starts immediately after the minimum. The rate of the recovery seems comparable with the cases from Chen et al. (2012). The velocity decay up to the minimum immediately downstream of the patch seems smoother for 2D data, and much more rapid for model C_{64}.

Again, the effect of D/d on the curves from Chen et al. (2012) is consistent, except for case 8. Case 10 (which has the same density of C_{64} but higher D/d) is misleading, because the minimum of the velocity profile was taken in correspondence of x/D = 4, and the fact that the velocity increases immediately downstream of the patch and then decreases is not what is expected. Probably there is an overestimation of the velocity in the range $0 < x/D < 3$.

Finally, Figure D.4 shows the comparison for the case C_{95}, with data from Chen et al. (2012), which they approximate as a solid 2D body. The behaviour is similar, especially for the case

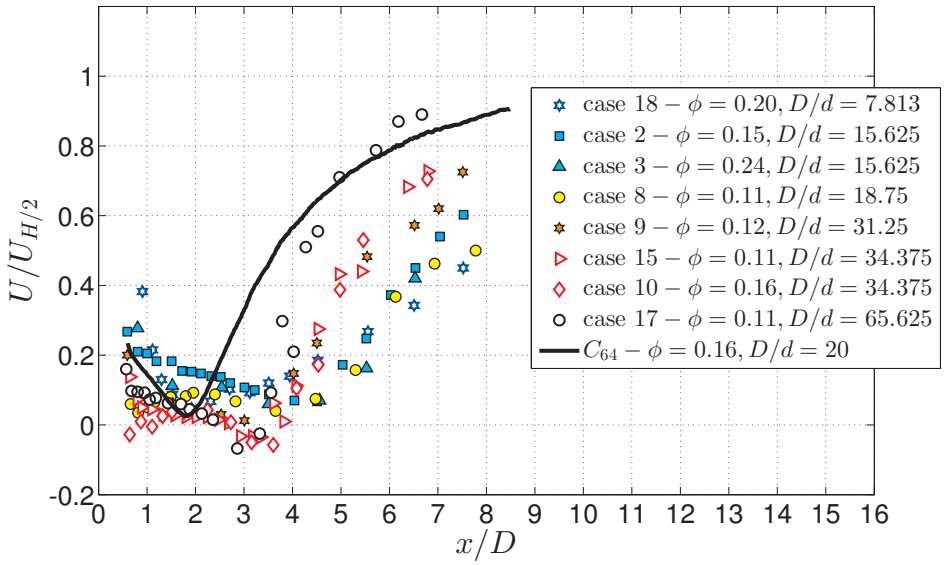

Figure D.3: Comparison of the centreline velocity $U/U_{H/2}$ with Chen et al. (2012) for the case C_{64} (ϕ = 0.16, D/d = 20).

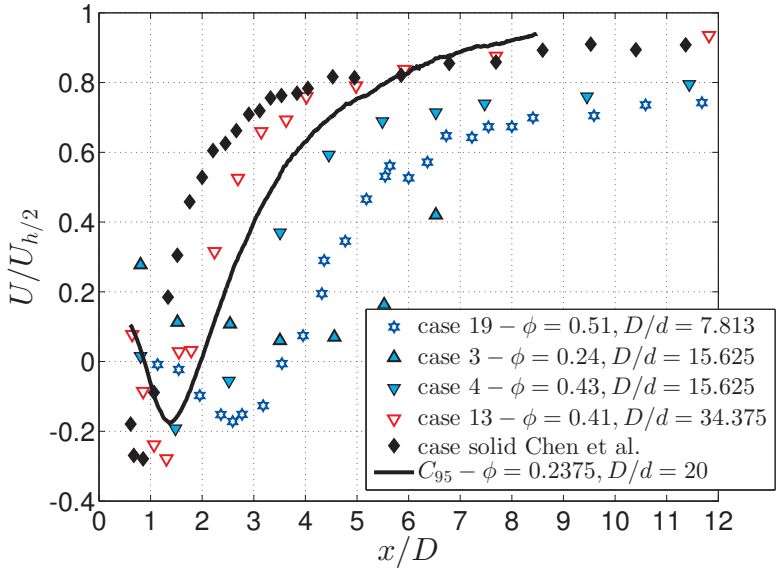

Figure D.4: Comparison of the centreline velocity $U/U_{H/2}$ with Chen et al. (2012) for the case C_{95} (ϕ = 0.24, D/d = 20).

4, which shows the same minimum in U; this minimum is the same also for case 19, while it reduces for the solid case and case 13. The rate of recovery is very similar to the one of a solid 2D cylinder, for all the cases it is linear with a comparable slope up to $U/U_{h/2}$ = 0.6. Beyond this value, the increase in U tends to be faster with increasing D/d, and, for the case C_{95}, it seems to be faster than all the other 2D cases. The effects of D/d are consistent also for these curves.

Accounting for the influence on D/d is not straightforward, since the density ϕ depends on

D/d itself ($\phi = N_c d^2/D^2$). What was found in the present study holds for a fixed D/d, varying the number of cylinders within the patch, and the relation between ϕ and N_c is linear. In order to investigate the effects of D/d only, the best option would be to fix the number of cylinders within the patch and vary extensively D/d. The experiments in Chen et al. (2012) are for patches with different values of N_c, so it is not possible to evaluate D/d effects from their data.

Appendix E

Horizontal-vertical PIV comparison at the centreline

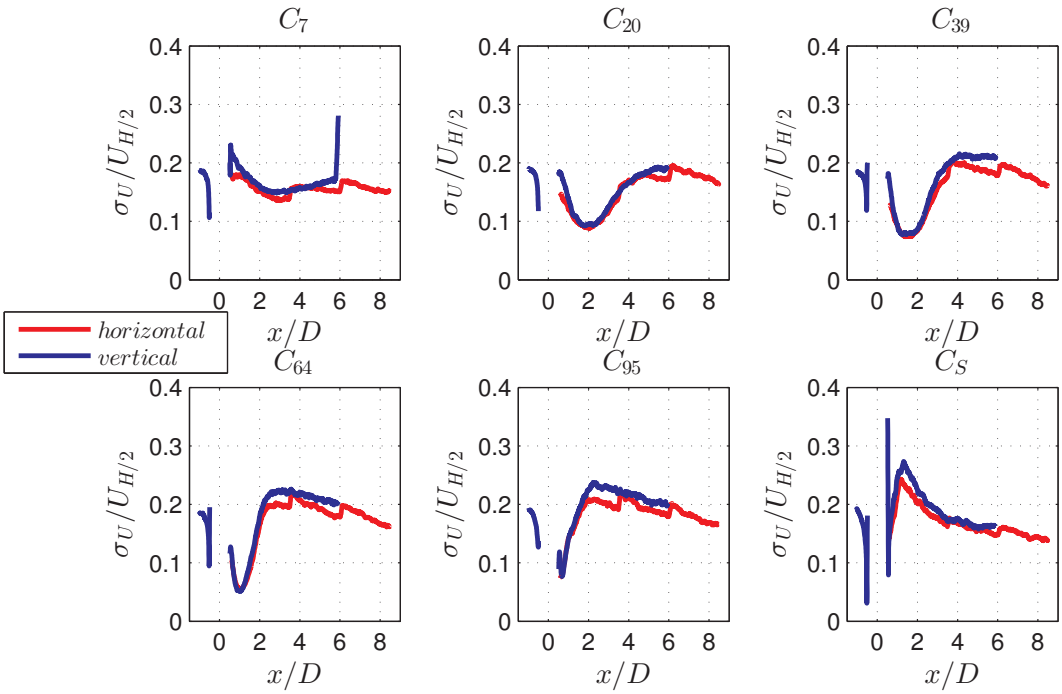

Figure E.1: $\sigma_U/U_{H/2}$ along x for all the patches: comparison between horizontal PIV results (red) and vertical PIV results (blue). $U_{H/2}$ is the freestream velocity at the measurements plane.

It is evident from Figure E.1 that the horizontal PIV measurements of the standard deviation of the streamline velocity component drop along each camera. The agreement between the two sets of measurements is good for the first part of the first horizontal camera, but then it shows a drop. At the junction with the second horizontal camera it seems to restart with the appropriate value, and then it drops again. The same is for the third horizontal camera. This could be due to a slight misalignment of the cameras, but no other mean quantity presents the

same behaviour (see subsequent figures). When it concerns data from σ_U, only the vertical PIV results will be used.

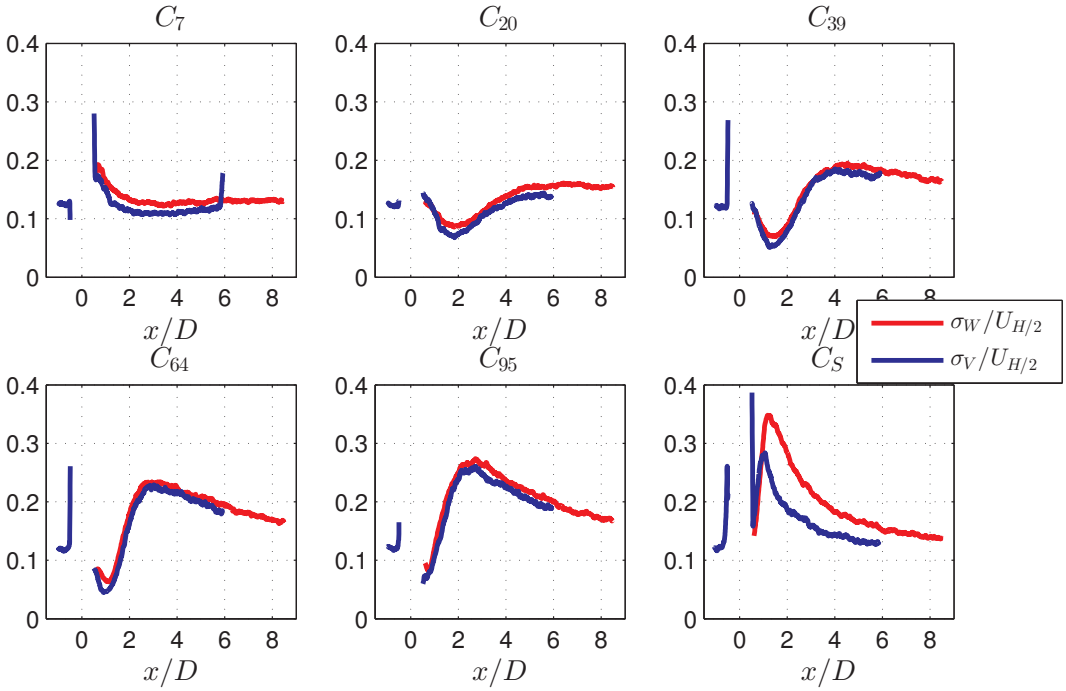

Figure E.2: $\sigma_W/U_{H/2}$ along x for all the patches for the horizontal PIV measurements and $\sigma_V/U_{H/2}$ along x for all the patches for the vertical PIV measurements. $U_{H/2}$ is the freestream velocity at the measurements plane.

Figure E.2 shows the standard deviation of the lateral and vertical velocity components, i.e. σ_W and σ_U, non dimensionalised with the freestream velocity at the measurements plane, i.e. $U_{H/2}$.

References

Adramola, M. S., Akinlade, O. G., Sumner, D., Bergstrom, D. J., and Schenstead, A. J. (2006). Turbulent wake of a finite circular cylinder of small aspect ratio. *Journal of Fluids and Structures*, 22:919–928.

Armitt, J. and Counihan, J. (1968). The simulation of the atmospheric boundary layer in a wind tunnel. *Atmospheric Environment (1967)*, 2:49–62, IN3, 63–71.

Ball, D. J., Stansby, P. K., and Alliston, N. (1996). Modelling shallow water flow around pile groups. *Proceedings of the ICE - Water Maritime and Energy*, 118:226–236.

Belcher, S. E., Jerrami, N., and Hunt, J. C. R. (2003). Adjustment of a turbulent boundary layer to a canopy of roughness elements. *Journal of Fluid Mechanics*, 488:369–398.

Blunden, L. S. (2009). *New approach to tidal stream energy analysis at sites in the English Channel.* Phd thesis, University of Southampton, School of Civil Engineering and the Enviroment.

Britter, R. E. and Hanna, S. R. (2003). Flow and dispersion in urban areas. *Annual Review of Fluid Mechanics*, 35:469–496.

Bruun, H. H., Nabhani, N., Fardad, A. A., and Al-Kayem, H. H. (1990). Velocity component measurements by x hot-wire anemometry. *Measurement Science and Technology*, 1(12):1314–1321.

Cassiani, M., Katul, G. G., and Albertson, J. D. (2008). The effects of canopy leaf area index on airflow across forest edges: large-eddy simulation and analytical results. *Boundary-Layer Meteorology*, 126:433–460.

Castro, I. P. (1971). Wake characteristics of two-dimensional perforated plates normal to an air-stream. *Journal of Fluid Mechanics*, 46:599–609.

Castro, I. P. (2007). Rough-wall boundary layers: mean flow universality. *Journal of Fluid Mechanics*, 585:469–485.

Castro, I. P. and Robins, G. (1977). The flow around a surface-mounted cube in uniform and turbulent streams. *Journal of Fluid Mechanics*, 79:307–335.

Chang, K. and Constantinescu, G. (2015). Numerical investigation of flow and turbulence structure through and around a circular array of rigid cylinders. *Journal of Fluid Mechanics*, 776:161–199.

Chen, Z., Ortiz, A., Lijun, Z., and Nepf, H. (2012). The wake structure behind a porous obstruction and its implications for deposition near a finite patch of emergent vegetation. *Water Resources Research*, 48.

Cheng, H. and Castro, I. P. (2002). Near wall flow over urban-like roughness. *Boundary-Layer Meteorology*, 104:229–259.

Coles, D. (1956). The law of the wake in the turbulent boundary layer. *Journal of Fluid Mechanics*, 1:191–226.

Connelly, J. S., Schultz, M. P., and Flack, K. A. (2006). Velocity-defect scaling for turbulent boundary layers with a range of relative roughness. *Experiments in Fluid*, 40:188–195.

Counihan, J. (1969). An improved method of simulating an atmospheric boundary layer in a wind tunnel. *Atmospheric Environment (1967)*, 3:197–200, IN1–IN2, 201–214.

Cucchi, V. and Bert, D. (2003). Wind-firmess in *Pinus pinaster* a´it. stands in southwest france: influence of stand density, fertilisation and breeding in two experimental stands damaged during the 1999 storm. *Annals of Forest Science*, 60:209–226.

Davidson, M. J., Snyder, W. H., Lawson Jr, R. E., and Hunt, J. C. R. (1996). Wind tunnel simulations of plume dispersion through groups of obstacles. *Atmospheric Enviroment*, 30:3715–3731.

Einian, M., Bergstrom, D. J., and Sumner, D. (2010). Numerical simulation of the flow around a surface-mounted finite square cylinder. *Proceedings of the ASME 2010 3rd Joint US-European Fluids Engineering Summer Meeting and 8th International Conference on Nanochannels, Microchannels, and Minichannels, August1fi5, 2010, Montreal, QC, Canada*, (FEDSM-ICNMM2010-30394):103–110.

Flack, K. A., Schultz, M. P., and Connelly, J. S. (2007). Examination of critical roughness height for outer layer similarity. *Physics of Fluid*, 19(095104).

Flack, K. A., Schultz, M. P., and Shapiro, T. A. (2005). Experimental support for townsend's reynolds number similarity hypothesis on rough walls. *Physics of Fluid*, 17(035102).

Florens, E., Eiff, O., and Moulin, F. (2013). Definig the roughness sublayer and its turbulence statistics. *Experiments in Fluids*, 54.

Folkard, A. M. (2011). Flow regimes in gaps within stands of flexible vegetation: laboratory flume simulations. *Enviromental Fluid Mechanics*, 11:289–306.

Fox, T. A. and West, G. S. (1993). Fluid-induced loading of cantilevered circular cylinders in a low-turbulence uniform flow. part 1: Mean loading with aspect ratios in the range 4 to 30. *Journal of Fluids and Structures*, 7:1–14.

Garrett, C. and Cummins, P. (2005). The power potential of tidal currents in channels. *Proceedings of Royal Society, A*, 461(2060):2563–2572.

Gu, Z. L., Jiao, J. Y., and Su, J. W. (2011). Large-eddy simulation of the wind field and plume dispersion within different obstacles arrays using a dynamic mixing legth subgrid-scale model. *Boundary-Layer Meteorology*, 139:439–455.

Huang, J., Cassiani, M., and Albertson, J. D. (2011). Coherent turbulent structures across a vegetation discontinuity. *Boundary-Layer Meteorology*, 140:1–22.

Irvine, M. R., Gardiner, B. A., and Hill, M. K. (1997). The evolution of turbulence across a forest edge. *Boundary-Layer Mereorology*, 84:467–496.

Irwin, H. (1981). The design of spires for wind simulation. *Journal of Wind Engineering and Industrial Aerodynamics*, 7(3):361–366.

Iungo, G. V., Pii, L. M., and Buresti, G. (2012). Experimental investigation on the aerodynamic loads and wake flow features of a low aspect-ratio circular cylinder. *Journal of Fluids and Structures*, 28:279–291.

Jackson, P. S. (1981). On the displacement height in the logarithmic velocity profile. *Journal of Fluid Mechanics*, 111:15–25.

Kappler, M., Rodi, W., Szepessy, S., and Badran, O. (2005). Experiments on the flow past long circular cylinders in a shear flow. *Experiments in Fluids*, 38:269–284.

Lim, H. C., Castro, I. P., and Hoxey, R. P. (2007). Bluff bodies in deep turbulent boundary layers: Reynolds-number issues. *Journal of Fluid Mechanics*, 571:97–118.

Manes, C., Poggi, D., and Ridolfi, L. (2011a). Turbulent boundary layers over permeable walls: scaling and near wall structure. *Journal of Fluid Mechanics*, 687:141–170.

Manes, C., Pokrajac, D., Nikora, V. I., Ridolfi, L., and Poggi, D. (2011b). Turbulent friction in flows over permeable walls. *Geophysical Research Letters*, 38.

Manes, C., Ridolfi, L., and Katul, G. (2012). A phenomenological model to describe turbulent friction in permeable-wall flows. *Geophysical Research Letters*, 39.

Marrè-Brunenghi, M. (2009). *Riproduzione sperimentale in galleria del vento dello Strato Limite Atmosferico (ABL).* Master thesis, University of Genoa, Faculty of Engineering.

Monin, A. and Yaglom, A. (1971). *Statistical Fluid Mechanics: Mechanics of Turbulence.* Number v. 1 in Dover books on physics. Dover Publications.

Myers, L. E. and Bhaj, A. S. (2012). An experimental investigation simulating flow effects in first generation marine current energy converter arrays. *Renewable Energy*, 37:28–36.

Nepf, H. M. (1999). Drag, turbulence, and diffusion in flow through emergent vegetation. *Water Resources Research*, 35:479–489.

Nepf, H. M. (2011). Flow over and through biota. In Wolanski, E. and McLusky, D., editors, *Treatise on Estuarine and Coastal Science*. Elsevier.

Nicolle, A. and Eames, I. (2011). Numerical study of flow throug and around a circular array of cylinders. *Journal of Fluid Mechanics*, 679:1–31.

Okamoto, T. and Yagita, M. (1973). The experimental investigation on the flow past a circular cylinder of finite length placed normal to the plane surface in a uniform stream. *Bulletin of the Japan Society of Mechanical Engineers*, 16:805–814.

Pattenden, R. J., Turnock, S. R., and Zhang, X. (2005). Measurements of the flow over a low-aspect-ratio cylinder mounted on a ground plane. *Experiments in Fluids*, 39:10–21.

Perry, A. E. and Li, J. D. (1990). Experimental support for the attached-eddy hypothesis in zero-pressure-gradient turbulent boundary layers. *Journal of Fluid Mechanics*, 218:405–438.

Pope, S. B. (2011). *Turbulent flows.* Cambridge University Press, Cambridge.

Princevac, M., Baik, J.-J., Li, X., Pan, H., and Park, S.-B. (2010). Lateral channeling within rectangular arrays of cubical obstacles. *Journal of Wind Engineering and Industrial Aerodynamics*, 98:377–385.

Raupach, M. R., Antonia, R. A., and Rajagopalan, S. (1991). Rough-wall turbulent boundary layers. *Applied Mechanics Reviews*, 44(1):1–25.

Rominger, J. T. and Nepf, H. M. (2011). Flow adjustment and interior flow associated with a rectangular porous obstruction. *Journal of Fluid Mechanics*, 680:636–659.

Rudnicki, M., Silins, U., and Lieffers, V. J. (2001). Measure of simultaneous tree sways and estimation of crown interactions amongo a group of trees. *Trees*, 15:83–90.

Sakamoto, H. and Arie, M. (1983). Vortex shedding from a rectangular prism and circular cylinder placed vertically in a turbulent boundary layer. *Journal of Fluid Mechanics*, 126:147–165.

Schultz, M. P. and Flack, K. A. (2005). Outer layer similarity in fully rough turbulent boundary layers. *Experiments in Fluids*, 38:328–340.

Sumner, D. (2013). Flow above the free end of a surface-mounted finite-height circular cylinder: A review. *Journal of Fluids and Structures*, 43:41–63.

Sumner, D., Heseltine, J. L., and Dansereau, O. J. P. (2004). Wake structure of a finite circular cylinder of small aspect ratio. *Experiments in Fluids*, 37:720–730.

Tanaka, S. and Murata, S. (1999). An investigation of the wake structure and aerodynamic characteristics of a finite circular cylinder (time-averaged wake structures behind circular cylinders with various aspect ratios). *JSME International Journal, Series B - Fluids and Thermal Engineering*, 42:178–187.

Taniguchi, S., Sakamoto, H., and Arie, M. (1981). Flow around circular cylinders of finite height placed vertically in turbulent boundary layers. *Bulletin of the Japan Society of Mechanical Engineers*, 24:37–44.

Tanino, Y. and Nepf, H. M. (2008). Laboratory investigation of mean drag in a random array of rigid, emergent cylinders. *Journal of Hydraulic Engineering-ASCE*, 134:34–41.

Tavoularis, S., Stapountzis, H., and Karnik, U. (1987). Vortex shedding from bluff cylinders in strongly sheared turbulent streams. *Journal of Wind Engineering and Industrial Aerodynamics*, 26:165–178.

Townsend, A. A. (1961). Equilibrium layers and wall turbulence. *Journal of Fluid Mechanics*, 11:97–120.

Tropea, C., Yarin, A. L., and Foss, J. F. (2007). *Spriger Handbook of Experimental Fluid Mechanics*. Springer.

Vennell, R. (2010). Tuning turbines in a tidal channel. *Journal of Fluid Mechanics*, 663:235–267.

Vennell, R. (2011). Tuning tidal turbines in-concert to maximise farm efficiency. *Journal of Fluid Mechanics*, 671:587–604.

Wang, H. F. and Zhou, Y. (2009). The finite-length square cylinder near wake. *Journal of Fluid Mechanics*, 638:453–490.

Wang, H. F., Zhou, Y., Chan, C. K., and Lam, K. S. (2006). Effect of initial conditions on interaction between a boundary layer and a wall-mounted finite-length-cylinder wake. *Physics of Fluids*, 18(065106).

Wang, H. F., Zhou, Y., Chan, C. K., Wong, W. O., and Lam, K. S. (2004). Flow structure around a finite-length square prism. *Proceedings of the 15th Australasian Fluid Mechanics Conference, The University of Sydney, Sydney, Australia*, (AFMC00189).

Wang, X. K., Gong, K., Zhang, J.-X., and Tan, S. K. (2013). Flow around four cylinders arranged in a square configuration. *Journal of Fluids and Structures*, 43:179–199.

Wygnanski, I., Champagne, F., and Marasli, B. (1986). On the large-scale structures in two-dimensional, small-deficit, turbulent wakes. *Journal of Fluid Mechanics*, 168:31–71.

Zong, L. and Nepf, H. (2012). Vortex development behind a finite porous obstruction in a channel. *Journal of Fluid Mechanics*, 691:368–391.